

Numerical Study of the Gap at the Base of the Bridge on the River Flow Parameters

Mohamadamin
Oyarhossein
Civil Engineering
Department,
University of
Aveiro, 3810-193
Aveiro, Portugal

Vahid Khiali
Civil Engineering
Department,
University of
Aveiro, 3810-193
Aveiro, Portugal

Kasra
Hosseinmostofi
Civil Engineering
Department,
University of
Aveiro, 3810-193
Aveiro, Portugal

Mostafa Adineh
Civil Engineering
Department,
University of
Aveiro, 3810-193
Aveiro, Portugal

Hamid Bayatghiasi
Civil Engineering
Department,
University of
Aveiro, 3810-193
Aveiro, Portugal

Abstract: In this study, substrate surface channel and bridge piers is modeled by utilization of Ansys Fluent. Continuity and Momentum equations is solved and for the pressure-velocity linkage SIMPLE algorithm is utilized. In order to model turbulence due to relatively high Reynolds value, K- ϵ is being used. Effect of wall shear stress, velocity magnitude and static pressure is being investigated at different heights thorough substrate longitudinal lines. It was found that different heights of longitudinal lines won't affect static pressure, while it affects velocity magnitude and wall shear stress significantly.

Keywords: Bridge, Scour, Shear stress , Numerical Study

1. INTRODUCTION

For bridges with piers sitting in the water, flood waters can cause scour at bridge foundations, undermining bridge structures by partially removing the supporting soil. The exposure of bridge foundations reduces the lateral load bearing capacity of bridges as well as the buckling resistance of pile foundations [1,2]. In addition to the reduced bridge capacity and stability, the exposure of bridge foundations also increases the flow-induced load acting on the bridge. Thus, a bridge that is subjected to scour becomes vulnerable in floods. For example, a large number of bridges in Taiwan have been significantly damaged due to the combined effects of scour and flow-induced loads since 2000 [3]. The damage includes tilted and tipped-over piers, dropped superstructures, pier settlements, and partial and complete collapses. The behavior of scoured bridges under flood conditions involves complex interactions between bridge structures, pile foundations, soils, and water. In recent years, a number of studies [4–12] have attempted to study the behavior of scoured bridges under flood conditions. Most of these studies have been conducted based on relatively simplified models or indirect approaches. Bennett et al. [4] studied the effect of scour depths on the behavior of a bridge pile group under flood conditions. McConnell and Can [5] investigated the influence of scour on the strength capacity of the substructure and superstructure of the Indian River Inlet Bridge. Lin et al. [6] proposed an integrated technique for analyzing bridge substructures and superstructures in an iterative fashion in order to assess the effect of scour on the bridge system performance. Ghadami et al. [38] studies the role of sensors in determining the structural health of the bridges along with efficient methods for sensor data transmission. Klinga and Alipour [7] investigated the influence of different types of scour, including local scour, general scour, aggradation, and degradation on the behavior of bridges. A common strategy for enhancing the lateral resistance of scour-critical pile supported bridges is to install additional piles to bridge foundations. However, the increased number of piles also adversely affects the bridge safety by inducing magnified flow-induced loads acting on the bridge. Hughes et al. [8,9] evaluated the influence of scour on the performance of

bridges with pile bents and investigated the effectiveness of bracing systems for mitigating the scour damage to bridges. The performances of X- braced bents with and without a horizontal bracing strut were examined. During flood events, authorities are faced with the challenge of making appropriate decisions regarding traffic control on bridges. If bridges can remain open, they can serve an important role in disaster recovery. Nevertheless, significant casualties and property loss can occur if bridges in danger of collapse are not closed in a timely Scour is the most serious waterway problem at which greater than 60% of the reported failures can be attributed to it [27]. There are many reports about bridges failure around the world due to scouring [10,17]. The mechanism of scouring around a bridge pier is very complex and has been reported by various investigators [9,15,16] and [5]. Abdelhafiz [3] studied the effect of pier shape and spacing on energy loss and scour around bridge piers. It was found that the maximum scour occurs upstream of the pier and the depth of scour hole increases as tail Froude number increases. Fotherby and Jones [8] used collars around bridge pier for reducing and controlling local scour depth. The authors recognized the potential usage of both a collar and a footing for scour reduction. In [37] Shahri et al. conducted a numerical study of sediment flow using Flow-3D. Experimental studies were applied using piers provided with slots and collars under different flow conditions by Kumar [13]. Kumar et al. [14] studied the efficiency of slots with different lengths and angles of attack. It was concluded that a slot can be effective in reducing scour, particularly if it extends into the bed, and that the slot is practically ineffective if the approach flow has a high obliquity with respect to the slot. Zarrati et al. [29] worked on the application of a collar to control the scouring around rectangular bridge piers having a rounded nose. It was found that collar effectiveness improves as the collar becomes wider and as the level at which it is positioned on the pier becomes lower. Reduction of local scour in the vicinity of circular bridge pier groups

using collars and riprap was studied by Zarrati et al. [30] The effect of triangular collar around bridge pier was studied experimentally by Mohamed et al. [19]. Different shapes and compound bridge piers. EL-Ghorab [6] studied

experimentally the local scour depth around bridge piers provided with slots. Torabi et al. at 2019 by using Finite Volume Method investigated the effect of geometry parameters on erosion and sedimentation in channel's junction [31]. The effect of pile cap thickness on the temporal evolution of the maximum scour depth and the development of equilibrium conditions was investigated by Ferraro et al.[7]. Sheppard et al. [26] performed an evaluation of the existing equations for the local scour at bridge piers. Nordila et al.[22] studied the local scour depth at wide bridge piers. In addition, laboratory studies of sacrificial piles for pier scour protection are reported by Shen et al. [25], Chang and Karim [4], Paice and Hey [23], and Singh et al. [27]. These studies showed up to 50% scour reduction due to the presence of the sacrificial piles. Laboratory studies on the use of sacrificial piles as a pier scour countermeasure are reported by Melville and Hadfield [18].

2. TRANSPORT EQUATIONS IN TURBULENCE MODEL $k - \epsilon$

All Realizable K- ϵ is being utilized to consider the effect of turbulence. Each term of K and ϵ is being illustrate separately by Zeidi et al. [32-34]. In the mentioned study the appropriate conditions in which realizable K- ϵ turbulence model is needed to used is clarified comprehensively by utilization of finite volume scheme.

$$\begin{aligned} \frac{\partial}{\partial t}(\rho k) + \frac{\partial}{\partial x_i}(\rho k u_i) &= \frac{\partial}{\partial x_i} \left[\left(\mu + \frac{\mu_t}{\sigma_k} \right) \frac{\partial k}{\partial x_j} \right] + G_k + G_b \\ &\quad - \rho \epsilon - Y_m + S_k \\ \frac{\partial}{\partial t}(\rho \epsilon) + \frac{\partial}{\partial x_i}(\rho \epsilon u_i) &= \frac{\partial}{\partial x_i} \left[\left(\mu + \frac{\mu_t}{\sigma_\epsilon} \right) \frac{\partial \epsilon}{\partial x_j} \right] + \rho C_1 S_\epsilon \\ &\quad - \rho C_2 \frac{\epsilon^2}{k + \sqrt{\nu \epsilon}} + C_{1\epsilon} \frac{\epsilon}{k} C_{3\epsilon} G_b \\ &\quad + S_\epsilon \\ C_1 &= \max \left[0.43, \frac{\eta}{\eta + 5} \right] \end{aligned}$$

In this equation, G_k represents the kinetic energy produced due to changes in the velocity gradient is calculated by the following equation:

$$G_k = -\rho \overline{u'_i u'_j} \frac{\partial u_j}{\partial x_i}$$

σ_k and σ_ϵ are the Prantel numbers for k and ϵ turbulence and t_{land} and t_ϵ are terms defined by the user. S is module average rate of strain tensor is defined as follows:

$$S = \sqrt{2 S_{ij} S'_{ij}}$$

3. MODELING

Given the importance of elements around the base of network quality and impact on the results, the network

boundary layer around the base are produced. This type of network is not used in numerical analysis scour, because it is difficult to establish the boundary layer in three-dimensional geometry. The advantage of this type of network elements control the size of the first layer around the base and determine the orderly growth of layers and number of layers. The first layer to the base height of 5 mm, the growth rate and the number of layers and layers 1/02 and 20 is selected and the size of the boundary layer 0/121487 meters.[35, 36]

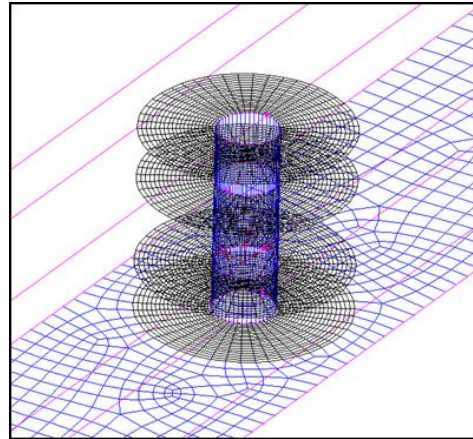
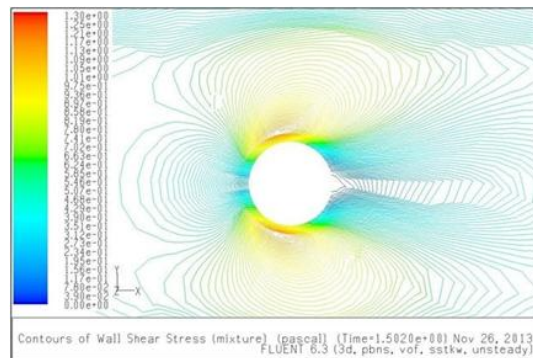
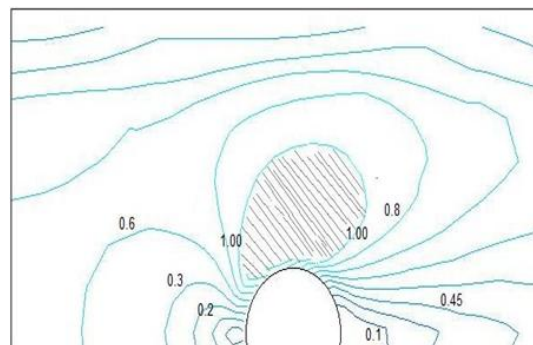


Fig 1: Meshing of substrate surface channel and bridge piers along the boundary layer



a: Numerical values of shear stress around the base



b: The numerical value of shear stress, ranging from basic scour

Fig 2: Numerical simulation of bridge piers

In this section original model to simulate the bridge pier has split within it. Catia geometry of three- dimensional modeling and computational domain has been done. The following parameters were used for the production of geometry.

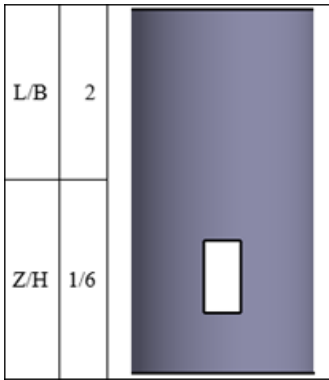


Table 1. gap size

L	The gap
B	Width of the gap
Z	Gap between floor of the bed
H	Height Paul

4. RESULT

The boundary conditions is set at the entrance of the Reynolds number equal to 200000 value that indicates a fully turbulent flow. To perform simulations from the powerful software which is used ansys fluent simulation capability is capable of streaming. For modeling turbulence RNG-ke model was used.

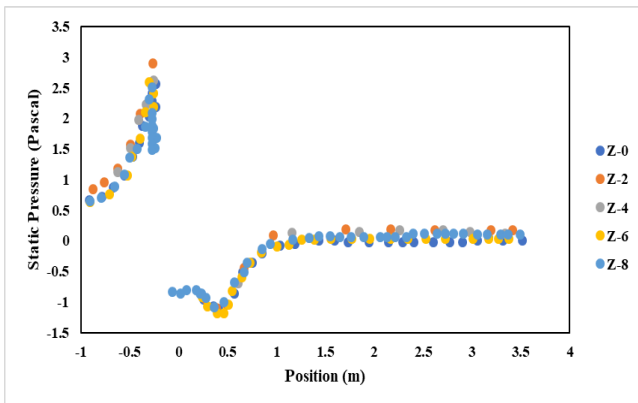


Fig 3: The pressure distributions on longitudinal lines at different heights from the substrate

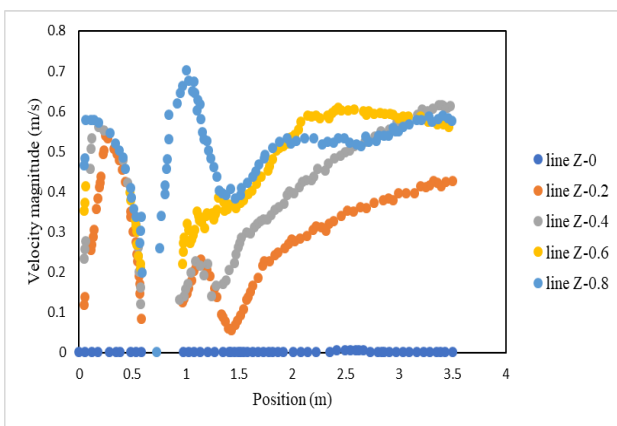


Fig 4: longitudinal lines velocity distribution at different heights from the substrate

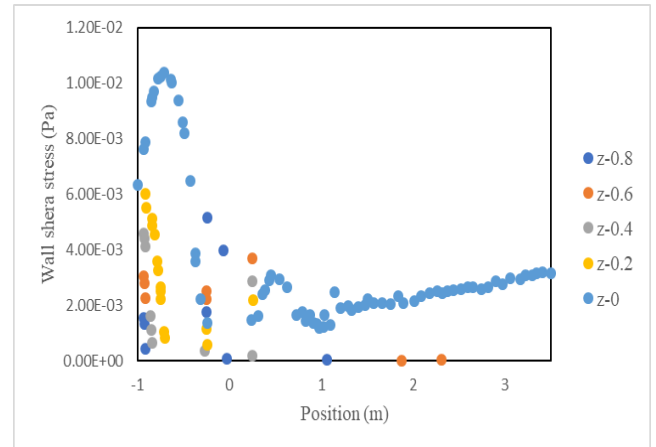


Fig 5: Distribution of shear stress on longitudinal lines at different heights from the the substrate

The shear stress distribution on longitudinal lines at different heights from the the substrate shows. Which, as can be seen from this graph almost at the height of bridge pier where there are gaps shear stress is the highest value and this is an indication that the bridge pier where there are gaps the reduced flow rate Scour the but occur more often and show the shear stress. At the end of the latest models created as another innovation with respect to a proposed recommendation, a hole with a diameter of 5 cm on the base and at a distance of half a meter from the bed has been created.

5. CONCLUSION

In this paper, modeling and simulation in the case of the pier with gaps and without gaps is being investigated. A model without gap is being used to validate the current simulation according to the previous authors. Also it is notable that presence of gap can affect wall shear stress and velocity magnitude as different heights is being considered. It was found that in presence of gaps, shear stress shows its highest value.

6. REFERENCES

- [1] G.M. Abdel-Aal, Y.A. Mohamed, O. Waheed E-Din, M. Elfolly, 2008. Local scour mitigation around bridge piles using protective plate (collar). Scientific Bulletin. Faculty of Engineering. Ain Shames University, Faculty of Engineering, Cairo, Egypt.
- [2] G.M. Abdel-Aal, Y.A. Mohamed, 2010. The effect of collar size and shape on scour depth around bridge piers. Scientific Bulletin, Faculty of Engineering, Ain Shames University, Faculty of Engineering, Cairo, Egypt, March.
- [3] E.A. Abdelhafiz, 1978. Some flow characteristics in water streams around bridge supports. Unpublished Thesis, Faculty of Engineering, Ain Shams University, Cairo, Egypt.

- [4] F.F.M. Chang, M. Karim, An experimental study of reducing scour around bridge piers using piles, Rep. South Dakota. (1972) 10.
- [5] B. Dargahi, Controlling mechanism of local scouring, J. Hydraul. Eng. ASCE 116 (10) (1990) 1197–1214.
- [6] E. EL-Ghorab, Reduction of scour around bridge piers using a modified method for vortex reduction, Alexandria Eng. J. 52 (2013) 467– 478.
- [7] D. Ferraro, A. Tafarojnoruz, R. Gaudio, A. Cardoso, Effects of pile cap thickness on the maximum scour depth at a complex pier, J. Hydraul. Eng. 139 (5) (2013) 482–491.
- [8] L.M. Fotherby, J.S. Jones, The influences of exposed footings on pier scour depths, in: Proceeding of Hydraulics Conference, ASCE, New York, 1993, pp. 22–927.
- [9] Hjorth, P., 1975. Studies on the nature of local scour, Dept. Water Res. Eng. Lund Inst. Technol. Bullet. Ser. A, No. 46.
- [10] P.A. Johnson, D.A. Dock, Probabilistic bridge scour estimates, J. Hydraul. Eng. ASCE 124 (7) (1998) 750–754.
- [11] U. Kothiyari, A. Kumar, Temporal variation of scour around circular compound piers, J. Hydraul. Eng. 138 (11) (2012) 945– 957.
- [12] Zahabi, H., Torabi, M., Alamatian, E., Bahiraei, M., & Goodarzi, M. (2018). Effects of Geometry and Hydraulic Characteristics of Shallow Reservoirs on Sediment Entrapment. *Water*, 10(12), 1725.
- [13] V. Kumar, Reduction of scour around bridge pier using protective devices. PhD Thesis, University of Roorkee, Roorkee, India, 1996.
- [14] V. Kumar, K.G. Ranga Raju, N. Vittal, Reduction of local scour around bridge piers using slots and collars J, Hydraul. Eng. ASCE 125 (12) (1999) 1302–1305.
- [15] B.W. Melville, Local scour at bridge sites, University of Auckland, NEWZEALAND, Ph.D. Thesis, Dept. of Civil eng. Rep. No. 117, 1975.
- [16] Torabi, M. A., & Shafieefar, M. (2015). An experimental investigation on the stability of foundation of composite vertical breakwaters. *Journal of Marine Science and Application*, 14(2), 175-182.
- [17] B.W. Melville, S.E. Coleman, Bridge Scour, Water Resources Publications, 1999.
- [18] B.W. Melville, A.C. Hadfield, Use of sacrificial piles as pier scours countermeasures, J. Hydraul. Eng. ASCE 125 (11) (1999)1221– 1224.
- [19] B.W. Melville, Y.M. Chiew, Time scale for local scour at bridge piers, J. Hydraul. Eng. ASCE 125 (1) (1999) 59–65.
- [20] Y.A. Mohamed, G.M. Abdel-Aal, A.M. Negm, A.A. Fathy, 2008. Effect of triangular collar width on local scour at bridge pier under very low Froude numbers, in: 9th International Congress of Fluid Dynamics and Propulsion, 18–21 December, Alexandria. Egypt.
- [21] A.M. Negm, G.M. Abdel-Aal, Y.A. Mohamed, A.A. Fathy, Control of local scour around bridge piers using current deflector, in: Proc. Of 13th IWTC, Hurghada, Egypt, 12–15 March, 2009.
- [22] Nordila, Ali M. Thamer, A. Faisal, Y. Badrunnisa, Local scour at wide bridge Piers, Int. J. Eng. Res. Technol. (IJERT) 3(1) (2014).
- [23] Paice, R. Hey, The control and monitoring of local scour at bridge piers, Proc. Hydr. Engrg. Conf., ASCE, New York, 1993, pp. 061–1066.
- [24] A.J. Raudkivi, R. Ettema, Clear- water scour at cylindrical piers, J. Hydraul. Eng. ASCE 109 (3) (1983) 338–350.
- [25] H.W. Shen, V.R. Schneider, S.S. Karaki, Mechanics of local scour, U.S. Department of Commerce, Nat. Bureau of Standards, Inst. Appl. Technol., 1966.
- [26] D. Sheppard, B. Melville, H. Demir, Evaluation of existing equations for local scour at bridge piers, J. Hydraul. Eng. 140 (1) (2014) 14–23.
- [27] K.K. Singh, D.V.S. Verma, N.K. Tiwari, 1995. Scour protection at circular bridge piers, in: 6th International Symp. on River Sedimentation, New Delhi.
- [28] Transit New Zealand, Bridge Inspection and Maintenance Manual, 2001.
- [29] A.M. Zarrati, H. Gholami, M.B. Mashahir, Application of collar to control scouring around rectangular bridge piers, J. Hydr. Res. 42 (1) (2004) 97–103.
- [30] A.M. Zarrati, M. Nazariha, M.B. Mashahir, Reduction of local scour In the vicinity of bridge pier groups using collars and riprap, J. Hydraul. Eng. ASCE 132 (2) (2006) 154–162.
- [31] Torabi, M., Hamedi, A, Alamatian, E., Zahabi, H. (2019). The Effect of Geometry Parameters and

- Flow Characteristics on Erosion and Sedimentation in Channel's Junction using Finite Volume Method. *International Journal of Engineering and Management Research (IJEMR)*, 9(2), 115-123.
- [32] Zeidi, S. M. J. and Mahdi, M. [2015], Evaluation of the Physical Forces Exerted on a Spherical Bubble Inside the Nozzle in a Cavitating Flow With an Eulerian/Lagrangian Approach, *European J. of Physics*, Vol. 136. No. 6, pp 065041; doi:10.1088/0143-0807/36/6/065041.
- [33] Zeidi, S. M. J. and Mahdi, M. [2014], Effects of Nozzle Geometry and Fuel Characteristics on Cavitation Phenomena in Injection Nozzles, The 22st Annual International Conference on Mechanical Engineering-ISME 2014, available online at http://www.civilica.com/EnPaper--ISME22_394.htmlhttp://www.civilica.com/EnPaper--ISME22_394.html.
- [34] Hamed, A., Mansoori, A., Shamsai, A., & Amirahmadian, S. (2014). Effects of End Sill and Step Slope on Stepped Spillway Energy Dissipation. *J. Water Sci. Res*, 6(1), 1.
- [35] Shafaie, M., & Mostofi, K. H. (2015). RIVER SEDIMENT MONITORING USING REMOTE SENSING AND GIS (CASE STUDY KARAJ WATERSHED). *International Archives of the Photogrammetry, Remote Sensing & Spatial Information Sciences*, 40.
- [36] Hosseini, D., Torabi, M., & Moghadam, M. A. (2019). Preference assessment of energy and momentum equations over 2D-SKM method in compound channels. *Journal of Water Resource Engineering and Management*, 6(1), 24-34.
- [37] Khoshnevis, S. A., Shahri, S. M. Z., Bina, K., & Aboutalebi, S. A. (2019). Numerical Study of Sediment Flow Over Bottom Intake Racks With Flow-3D. *International Journal of Scientific Research and Management*, 7(07), v7i7-ec02.
- [38] Ghadami Talkhouncheh, R., Khoshnevis, S. A., Aboutalebi, S. A., Surakanti, S. R., Embedding Wireless Intelligent Sensors Based on Compact Measurement for Structural Health Monitoring Using Improved Compressive Sensing-based Data Loss Recovery Algorithm. *International Journal for Modern Trends in Science and Technology*, 5(07) July 2019.

Static and Dynamic Analysis of Flight Control Circuit Mixing Unit in a Typical Light Helicopter

Anup Banakar K

Department of Mechanical Engineering
East Point College of Engineering And Technology
Bengaluru
India

Dinesh Kumar

Department of Mechanical Engineering
East Point College of Engineering And Technology
Bengaluru
India

Abstract: Conventional helicopter (single main rotor & tail rotor) has three flight control inputs called as the cyclic stick, collective stick and anti-torque / rudder pedals. The principle motivation behind the flight controls in helicopter is to change the pitch angles of main and tail rotor and enabling the pilots to control helicopter elevation, speed and direction. The contributions to the cyclic stick and collective stick control the main rotor pitch angles. The inputs to the pedals (rudder) control the tail rotor pitch angles. Main rotor controls comprise of Collective, Cyclic Longitudinal (Pitch) and Cyclic Lateral (Roll) channels, which together control the main rotor blade pitch angles. Cockpit controls for Pilot and Co-Pilot are cultivated utilizing torque tube/switches and control bars. The mixing of collective and cyclic is done at mixing unit. The main rotor mixing unit is required to guarantee that all control inputs are transmitted to the main rotor without loss of input or one influencing the other. A mixing unit keeps up the cyclic angle by mixing collective input with right lateral, left lateral, and fore/aft inputs into a summing bell crank. "The present work mainly focuses on the finite element idealization of the mixing unit, evaluation of the strength characteristics for the applied control loads and also estimation of free vibration characteristics of the mixing unit".

1. INTRODUCTION

About Helicopters: A helicopter is an aircraft that is lifted and driven by one or more horizontal rotors, each rotor consisting of two or more rotor blades. Helicopters are classified as rotor craft or rotary-wing aircraft to distinguish them from fixed-wing aircraft because the helicopter derives its source of lift from the rotor blades rotating around a mast. "Helicopter" is derived from the French hélicoptère, instituted by Gustave de Ponton d'Amécourt in 1861. It is connected to the Greek words' helix/helikos ("winding" or "turning") and pteron ("wing").

The helicopter utilizes rotating wings to give lift, drive, and control. The rotor blades rotate about a vertical axis, describing a disk in a horizontal or nearly horizontal plane. Aerodynamic forces are created by the relative motion of a wing surface with respect to the air. The helicopter with its rotational wings can produce these forces even when the velocity of the vehicle is zero, as opposed to fixed-wing airplane, which require a transnational motion to continue flight.

Helicopter controls: There are three noteworthy controls in a helicopter that the pilot must use amid flight. They are the collective pitch control, the cyclic pitch control, and the anti-torque pedals or tail rotor control. In addition to these main controls, the pilot must also use the throttle control, which is usually mounted directly to the collective pitch control to fly the helicopter. The collective is utilized to make changes angle of the main rotor blades and does this at the same time, or on the collectively, as the name implies.

The cyclic pitch control is generally anticipated upward from the cockpit floor, between the pilot's legs or between the two pilot seats in certain models. This essential flight control

enables the pilot to fly the helicopter toward any path of movement: forward, rearward, left, and right.

2. OBJECTIVES

The objectives of the present study are

1. Finite element idealization of the mixing unit assembly of a typical light helicopter flight control system.
2. Evaluation of strength characteristics of mixing unit for the applied control loads which were being felt during the jammed condition of controls.
3. Finding the free vibration characteristics (natural frequencies, mode shapes) of mixing unit.

3. DESCRIPTION

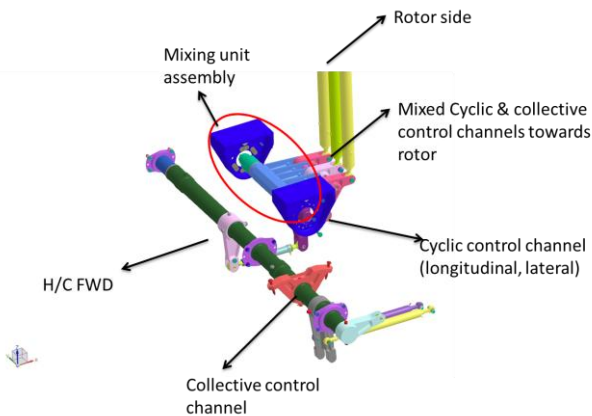
Finite element idealization of mixing unit assembly: The mixing unit assembly of a typical light helicopter is having the assembled parts of torque tube, lever input and brackets.

HYPERMESH software is used as preprocessor for discretizing the geometry domain to the finite elements. Individual CAD part (torque tube, lever, and brackets) models are imported into HYPERMESH.

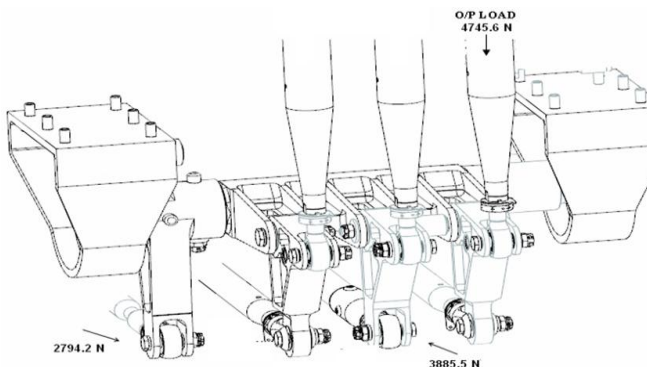
Static analysis of mixing unit assembly: In the present investigation MSC NASTRAN software utilized as finite element solver for taking care of static analysis problem. Figure 1 shows all components of Mixing circuit.

Details of the material used in the modeling

Part	MATERIAL	YOUNGS MODULUS (N/M2)	POISSON'S RATIO
Input lever	Al	7.00E+10	0.23
Torque tube assembly	SS	2.10E+11	0.23
Bracket LH-side	AL	7.00E+10	0.23
Bracket LH-side	Al	7.00E+10	0.23

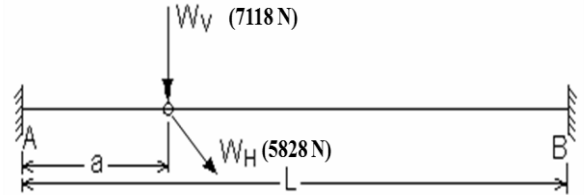


Torque tube and lever assembly: The pilot limit loads during jamming conditions are shown in Figure2. A factor of safety of 1.5 is used over these loads and these loads are applied to the torque tube and lever assembly FE model.



Ultimate load on the input lever = $2794.2 \times 1.5 = 4191.3 \text{ N}$
 Ultimate load on the torque tube $F_{z-ult} = 4745.6 \times 1.5 = 7118 \text{ N}$
 Ultimate load on the torque tube $F_{x-ult} = 3885.5 \times 1.5 = 5828 \text{ N}$

Bracket assembly: Loads on the brackets are estimated by idealizing the two support brackets at ends A and B with the torque tube AB of length L (296 mm) and a (92 mm) is being the distance of I/P and O/P levers as shown in the below figure. The reaction forces and moments which will come on to the bracket for the applied vertical and horizontal loads are calculated using standard empirical relations.



$$\begin{aligned}
 R_{AV} &= 5498 \text{ N} & R_{BV} &= 1620 \text{ N} \\
 M_{AV} &= -310.87 \text{ NM} & M_{BV} &= -139.1 \text{ NM} \\
 R_{AH} &= 4501 \text{ N} & R_{BH} &= 1326 \text{ N} \\
 M_{AH} &= -254.5 \text{ NM} & M_{BH} &= -113.9 \text{ NM}
 \end{aligned}$$

Free vibrations / Real Eigen value analysis: Free vibration analysis is utilized to decide the essential dynamic characteristics of the system.

In the case of damping is dismissed, the solution is known as undamped free vibration analysis. Real eigenvalue analysis is utilized to decide the basic dynamic characteristics of a structure.

Forced vibrations (Linear frequency response analysis): Forced vibrations frequency response analysis is an efficient strategy for finding the steady-state reaction to sinusoidal excitation.

Forced vibrations (Linear transient response analysis): Forced vibrations transient response analysis is the most general strategy for figuring the reaction to time-varying loads.

4. RESULT AND CONCLUSIONS

Finite Element idealization of mixing unit assembly (mixing collective input with right lateral, left lateral, and fore/aft inputs) of typical light helicopters main rotor flight control system is carried out. Static analysis of mixing unit is carried out for the applied pilot limit forces. Dynamic / Eigen analysis is carried out for evaluating the Eigen values of the mixing unit.

Based on the strength (static analysis) and stiffness (dynamics analysis) characteristics of the helicopter flight controls mixing unit assembly, it is concluded that

- 1) The strength margins of individual parts of the mixing unit assembly shows a good margin except the brackets where the safety margins are less.
- 2) The modified bracket where flange thickness is increased from 6mm to 8mm shows a significant increase in the strength margins.
- 3) The fundamental frequencies of the brackets, torque tube assembly, input lever is very high and above 2000 Hz which are well away from the dominant excitation frequencies of helicopter main rotor 1/rev and N/rev frequencies.

- 4) The fundamental frequencies of entire mixing unit assembly are above 500 Hz which are well away from the dominant excitation frequencies of helicopter main rotor 1/rev and N/rev frequencies and design is safe.
- 5) Design of the mixing unit is flight safe w.r.t the strength and stiffness characteristic as per the design limit pilot forces specified in Federal Aviation Regulations.

5. REFERENCES

- [1] John Watkinson, "The Art of the Helicopter", Elsevier Butterworth-Heinemann (2004).
- [2] Wayne Johnson, "Rotorcraft Aeromechanics", Cambridge university press 2013.
- [3] John M. Seddon, Simon Newman- "Basic Helicopter Aerodynamics", Aerospace Series, John Wiley (2011)
- [4] Venkatesan, C. "Fundamental of Helicopter dynamics" CRC Press 2015.
- [5] AMCP 706-201, engineering design handbook: helicopter engineering (part-1), preliminary design (30-aug-1974).
- [6] AMCP 706-202, engineering design handbook: helicopter engineering (part-2), detail design (20-jan-1976)

Design of Cross-Flow Turbine for Hydro-power Plant (Runner)

Cho Nwe Tun
Lecturer
Department of Mechanical
Engineering,
Technological University
(Thanlyin),
Yangon, Myanmar

Khin Nwe Zin Tun
Lecturer
Department of Mechanical
Engineering,
Technological University
(Thanlyin),
Yangon, Myanmar

Mya Thet Hnin
Lecturer
Department of Mechanical
Engineering,
Technological University
(Dawei),
Yangon, Myanmar

Abstract: In hydro-electric plants, water turbine is one of the most important parts to generate electricity. Cross-flow turbine is one of the simplest radial impulse turbine. In this paper, cross-flow turbine is designed to produce 5kW output power from head of 7m and the flow rate of 0.102 m³/s. For the given capacity, the dimensions of turbine diameter and length are 250 mm and 408 mm. The number of blades are used 28 blades, the thickness of each blades is 4.5 mm, the inner diameter of the runner is 166mm. According to these data, the important part of cross-flow turbine runner can be constructed. The detail design calculation of the runner is described in this study. And then detail drawing of 5kW cross-flow turbine is illustrated.

Keywords: cross-flow turbine, runner, hydro-power, flow rate, diameter.

1. INTRODUCTION

Nowadays, compact metal water turbines tend to be used instead of traditional water wheel. Water power is one of the major sources of energy. The other sources of energy being developed by the fuels such as coal, oil etc, and nuclear power are used for energy. Hydropower development is essential to utilize the hydraulic power proceed by the water flowing in a stream and to develop from it electric power through hydraulic (water) turbines coupled to electric generators. A hydropower plant requires no fuel and it is much simple to operate and maintain. So, the position of hydro-power plants becomes more and more important in today's global renewable technologies.

The Cross-Flow turbine is primarily impulse type. In the cross-flow turbine, the flow enters the runner from its circumferential direction, passes inside the runner and again passes through the runner blades toward the opposite direction before leaving the runner.



Figure.1 Cross-flow turbine runner

It is called cross-flow, since the water passage through the runner. The turbine consists of two parts, a nozzle and a turbine runner, Cross-flow is suitable for heads from 5 to 80 meters. The drum shaped runner of a cross-flow turbine is built of two parallel disks connected near the rim by a series of curved blades. The number of blades ranges between 26 to 30. This turbine is always installed with the shaft horizontal. The objective of this study are to study the about of micro hydropower plants thoroughly and to study the theory of cross-flow turbine. And then, it can be constructed the runner of cross-flow turbine by local material at small machine shop and to reduce the use of non renewable energy.

2. DESIGN CONSIDERATION OF RUNNER

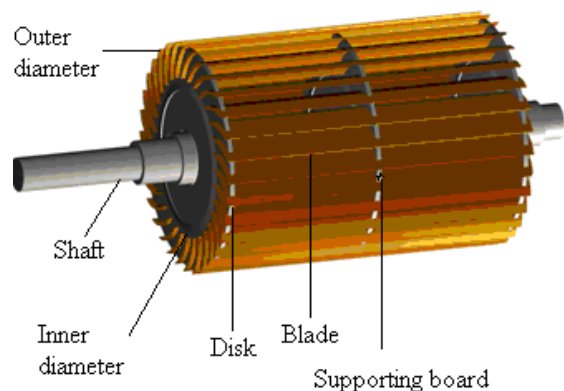


Figure.2 Cross-flow turbine runner[2]

The cross-flow turbine is primarily impulse type, the optimal speed of the runner primarily determined by the head. The runner speed of the cross-flow type is low as compared with other turbines. The heart of the turbine is the runner and is responsible for the conversion of water energy into mechanical energy. Cross-flow turbine runner is a cylindrical in shape with a long in axis direction and is built up of two parallel circular disks joined together at the rim with a series of curved blades as shown in Figure 2. Runner design is very critical for achieving good overall performance of the turbine. The diameter of the runner is an important and basic factor for the design of the runner. It can be determined from the speed and water head. From the turbine speed, generator can be selected depending on the synchronous speed.

In this paper, the inlet flow angle to the wheel is taken as 16° according to obtain the maximum efficiency. When considering the design of runner, the curvature of the blade, inlet blades angle, the value of pitch and the thickness of the runner. A cross-flow turbine has its runner shaft horizontal to the ground in all cases. Shaft transfers the generated torque to the generator or alternator. Bearing function is to hold the shaft rigidly on its position. At the same time it reduces the resistance to the rotation of the shaft and absorbs the axial forces on it. It includes one or two guide vanes depending on the inlet width. The function of the guide vane is to adjust and shut-off the water flow into the runner. A turbine with large maximum discharge has two guide vanes. The vanes lengths are 1/3 and 2/3 of the inflow width, respectively. When the discharge is small, only the shorter vane is used.

3. THEORETICAL CALCULATION OF CROSS-FLOW TURBINE RUNNER

The required design data for 5kW cross-flow turbine are as follow;

Net head, $H = 7$ m

Generator output, $P_G = 95\%$ of turbine output

Overall efficiency, $\eta_o = 0.75$

Design of water, $\rho = 1000$ kg/m³

Gravity, $g = 9.81$ m/s²

$C_v = 0.92 - 0.99$

The required discharge can be calculated,

$$P = \rho g Q H \eta_o$$

The total area of jets can be calculated,

$$V_1 = C_v \sqrt{2gH}$$

$$A = Q/V$$

The periphery velocity is $u = \pi DN/60$,

the range of specific speed for the cross-flow turbine is 40 to 200.

For this design, the specific speed is assumed $N_s = 80$ to calculated the rotational speed,

$$N_s = \frac{N\sqrt{P}}{H^{5/4}}$$

Where the wheel rotation is taken 400 rpm, thus the diameter of runner can be calculated as follows;

$$D_1 = \frac{60u}{\pi N}$$

So, Above the equation the runner diameter is used 25 mm.

Outer diameter of runner,

$$R_1 = D_1/2$$

Inner Radius ,

$$R_2 = D_1/3$$

Radius of blade shaped arc r,

$$r = \frac{(R_1^2 - R_2^2)}{2R_1 \cos \beta_1}$$

∴ the radius of blade shaped arc is 0.04 m.

$$\text{So, } r = 0.16 D_1$$

The radial rim width (a) was graphically ascertained from the intersection of the two curves.

$$a = R_1 - R_2$$

The diameter of the shaft can be calculated as follow,

$$d_s = 150 \sqrt[3]{\frac{P}{N}}$$

So the diameter of the shaft is used 35 mm.

The efficiency is equal to the ratio of the output and input power.

$$\text{Efficiency} = \frac{\text{output power}}{\text{input power}}$$

4. RESULT OF RUNNER

This table shows the calculated result for runner using above equation.

Table 1. Calculated result for 5kw cross-flow turbine

No.	Name	Symbol	Result (mm)
1.	Outer radius of runner	R_1	125
2.	Inner radius of runner	R_2	83
3.	Diameter of runner	D	92
4.	Width of runner	B	408
5.	Radius of curvature	r	40
6.	Radial rim width	a	42
7.	Shaft diameter	d_s	34.8
8.	Efficiency	η	87 %

Figure 3 shows the result drawing of 5kW cross-flow turbine runner. In the cross-flow turbine, runner is the important part for the whole part of the turbine .

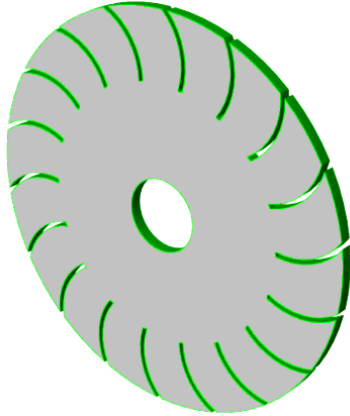


Figure.3 Drawing of runner (front view)

5. CONCLUSION

Hydroelectric power has been important in the provision of electricity. The future of hydroelectric power will depend on the demand of electricity and the provision of this using the most economical and environmental source available. In hydropower plant, turbine is one of the most important parts to generate electricity. The author has designed a runner of 5 kW cross-flow turbines for micro-hydropower plant. Unlike the other turbines, according to the water passes through the runner which is called cross-flow.

The cross-flow turbine designed for 7 m of head and 0.102 m³/s of flow rate to generate 5 kW. The author has designed the runner of this turbine and drawn the working drawing of turbine runner. The diameter of the runner is 92 mm. For that turbine, a synchronous generator 6 pole is used with direct coupling. The attack angle at the runner is taken as 16 degree to get optimal efficiency. The inlet blade angle is 30 degree. The number of blade is 28 and thickness is 4.5 mm, depending on the runner diameter.

6. ACKNOWLEDGMENT

The author is deeply grateful to her teachers, parents and friends for their noble support, encouragement, and guidance throughout her entire life.

7. REFERENCES

- [1] L.A.Haimeral., 1956 The cross flow turbine. Deutche Miller-Zeitung.
- [2] Pa Pa Min. 2007 Design and construction of 300W cross-flow turbine.
- [3] Nakase, Y., (1982): A study of Crossflow Turbine, Small Hydro Power Fluid Machinery, p. 13-18.
- [4] Khosrowpahan, S., (1984): Experimental Study of the Crossflow Turbine, Ph.D. Dissertation, Colorado State University, Fort Collins, CO.

- [5] Javed A. Chattha et. al. (2010): Design of a cross flow turbine for a micro-hydro power Application, Proceedings of the ASME 2010 Power Conference, July 13-15.
- [6] [http:// www.waterturbine.com](http://www.waterturbine.com)
- [7] [http:// www.microhydropower.net/turbine.html](http://www.microhydropower.net/turbine.html)
- [8] [http:// www.energymanagertraining.com](http://www.energymanagertraining.com)
- [9] [http:// www.hypo-info](http://www.hypo-info), “Hydropower”.

Design of Impeller for Centrifugal Compressor

Cho Nwe Tun
Lecturer
Department of Mechanical
Engineering,
Technological University
(Thanlyin),
Yangon, Myanmar

Khin Swe Swe Latt
Lecturer
Department of Mechanical
Engineering,
Technological University
(Thanlyin),
Yangon, Myanmar

May Kyi Tha
Lecturer
Department of Mechanical
Engineering,
Technological University
(Thanlyin),
Yangon, Myanmar

Abstract: This compressor is a dynamic compress which depends on a rotating impeller to compress the air. Impeller is the most important part of the centrifugal compressor components. Detail design calculation of centrifugal compressor impeller is described in this research. This study contains a complete set of detail drawing for blade profile of impeller. It can be used at sites which flow rate is $0.1275 \text{ m}^3/\text{s}$ and 45561 rpm. The required data are collected from Ahlone Power Station which is located in Yangon. For the given capacity, the inlet and outlet diameter are 0.054 m and 0.17 m and the number of blade is 19.

Keywords: Impeller, Pressure, velocity, centrifugal compressor

1. INTRODUCTION

Centrifugal compressor is one of the oldest turbo machinery, widely used in various industries like, aviation, oil and gas, refrigeration, etc. Centrifugal compressor is a radial turbomachine, which compresses air or gas with the action of centrifugal force. During the Second World War, the centrifugal compressors were used by British and American fighter aircrafts, as a part of early development of gas turbine engines. Later, during the 1950s, a large number of turboprop, turbofan, turbo-shafts and auxiliary power units started using the centrifugal compressors for air compression due to their high pressure raising capability in a single stage and their robustness in case of foreign object damage.

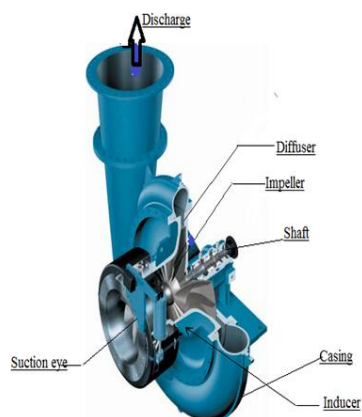


Figure.1. Basic Component of centrifugal compressor

Centrifugal compressors are a key piece of equipment for modern production. Among the components of the centrifugal compressor, the impeller is a pivotal part as it is used to transform kinetic energy into pressure energy. Impeller is an active part that adds energy to the fluid, its geometry plays a major role in the centrifugal compressors performance. An impeller is a wheel or rotor which is provided with a series of

backward curved blades or vanes. It is mounted on a shaft which is couple to an external source of energy which imparts the required energy to the impeller there by making it to rotate. The impellers may be classified as;

- Shrouded or closed impeller,
- Semi-open impeller and
- Open impeller.

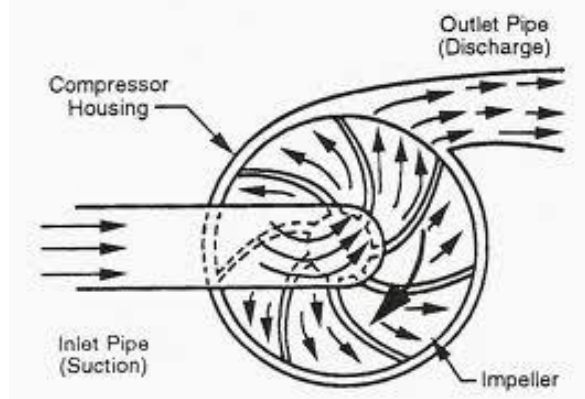


Figure.2. Working Principle of centrifugal compressor

2. SPECIFICATION DATA

Inlet pressure , $P_1 = 1030.765 \text{ kPa}$
Inlet temperature , $T_1 = 380 \text{ K}$
Rated speed , $N = 45561 \text{ rpm}$
Outlet pressure , $P_2 = 1799.6 \text{ kPa}$
Outlet temperature , $T_2 = 448 \text{ K}$
Capacity , $Q = 0.1275 \text{ m}^3/\text{s}$
Air mass flow rate , $\dot{m} = 1.5907 \text{ kg/s}$

Centrifugal compressor with this specifications has been installed on Ahlone Power Station at Ahlone Township, Yangon, Myanmar.

3. METHODOLOGY

The understanding of compressor operation is the ideal gas law, which is expressed in equation from the follows;

$$P_v = ZRT \quad (1)$$

The general form of the thermodynamic head equation for a polytropic process is

$$H_p = ZRT_1 \frac{n}{n-1} \left[\left(r_p \right)^{\frac{n-1}{n}} - 1 \right] \quad (2)$$

This equation drives from integrating the steady-state, steady flow work equation given by:

$$H_p = \int v dp \quad (3)$$

The polytropic process is of form:

$$PV^n = \text{constant} \quad (4)$$

3.1 Impeller Inlet Dimension

$$D_s = 3 \sqrt{\frac{16T}{\pi S_s}} \quad (5)$$

The eye diameter D_o may be found from the continuity equation:

$$\frac{\pi}{4} D_o^2 - \frac{\pi}{4} D_h^2 = \frac{Q}{V_o}$$

$$D_o = \sqrt{\frac{4 \times Q}{\pi \times V_o} + D_h^2} \quad (6)$$

The mean diameter of the vane inlet is made slightly greater than the impeller eye diameter.

Speed of sound of gas, a

$$a = \sqrt{k \times g \times R \times T_1} \quad (7)$$

The impeller inlet hub Mach number is 0.2 to 1 for compressible fluid. The value of Mach number is 0.3(assumed).

The impeller absolute velocity equation is

$$V_o = M \times a \quad (8)$$

The air enters the impeller eye to tip in the axial direction and prewhirl angle is zero, so that $V_{i1} = V_{t1}$ and is made slightly greater than V_o .

Impeller inlet width, b_1

$$b_1 = \frac{Q}{\pi \times V_1 \times D_1 \times \epsilon_1} \quad (9)$$

Impeller inlet velocity, U_1

$$U_1 = \frac{\pi D_1 N}{60} \quad (10)$$

3.2 Impeller Inlet Dimension

Impeller Outlet diameter, D_2

$$D_2 = \frac{60 \times \sqrt{H_p \times g}}{\pi \times n \times \sqrt{K'}} \quad (11)$$

Therefore

$$V_{t2} = V_{t1} \quad (12)$$

The outlet width is expressed by the following equation,

$$b_2 = \frac{Q}{\pi \times V_2 \times D_2 \times \epsilon_2} \quad (13)$$

The outlet vane thickness factor ϵ_2 can be calculated with following equation;

$$\epsilon_2 = \frac{\pi \times D_2 - \frac{z \times t}{\sin \beta_2}}{\pi \times D_2} \quad (14)$$

3.3 Enthalpy and Efficiency

The greater the number of vanes, the smaller the slip, i.e. the more nearly $V_{\omega 2}$ approaches U_2 . It is necessary in design to assume a value for the slip factor σ ;

$$\sigma = \frac{V_{\omega 2}}{U_2}$$

To find the number of number of blades, the following equation is used.

$$\sigma = 1 - \frac{0.63\pi}{z} \quad (15)$$

A relation between h and T, the most general form of h as $h=h(p,T)$, then

$$dh = \left(\frac{\partial h}{\partial T} \right)_p dT + \left(\frac{\partial h}{\partial p} \right)_T dp$$

Since the specific heat at constant pressure is defined as

$$c_p = \left(\frac{\partial h}{\partial T} \right)_p, \text{ then}$$

$$dh = c_p dT + \left(\frac{\partial h}{\partial p} \right)_p dp$$

An ideal gas h is a function of T only.

$$\text{Consequently, } \left(\frac{\partial h}{\partial p} \right)_T = 0 \text{ and}$$

$$dh = c_p dT \quad (16)$$

The efficiency defined on the basic of this ideal work is the compressor efficiency.

η_c =ideal work between the stagnation states/actual work

$$\eta_c = \frac{h_{02s} - h_{01}}{h_{02} - h_{01}} \quad (17)$$

Inlet blade angle, β_1

$$\beta_1 = \tan^{-1} \frac{V_1}{U_1} \quad (18)$$

Outlet blade angle, β_2

The compressor industry commonly uses a backward leading blade with angle, β_2 of between about 55-75 deg.

The blade outlet angle of 75 deg is maximum power position.

Therefore, the maximum design condition the outlet blade angle, $\beta_2 = 75$ deg.

H_p : polytropic head, kNm/kg

D_s : shaft diameter, m

D_o : eye diameter, m

D_1 : inlet diameter, m

D_2 : outlet diameter, m

a : speed of sound, m/s

M : mach number

b : width, m

ϵ_1 : inlet vane thickness factor(0.8 to 0.9)

z : number of blades

σ : slip factor

4. VALUE OF MACH NUMBER

The analytical design of impeller inlet result data are expressed by graphs.

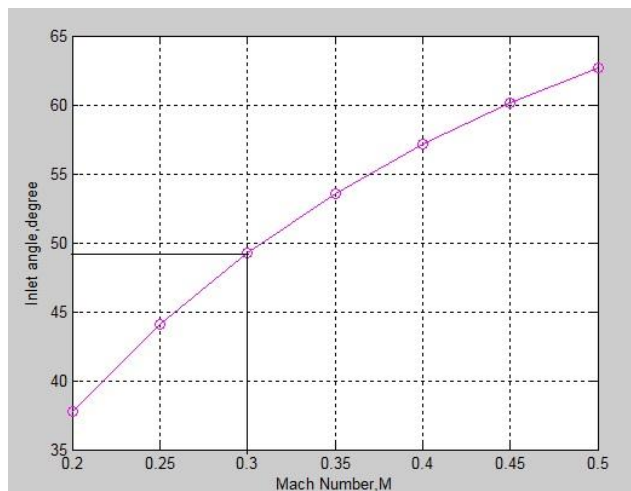


Figure.3. Mach number and Blade inlet angle

The relation between the blade inlet angle and Mach number are illustrated in Fig 2. This graph shows the larger the blade inlet angle, the higher the Mach number.

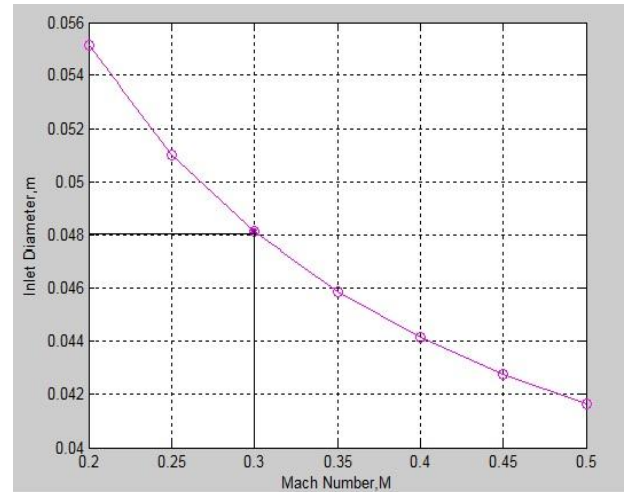


Figure.4. Mach number and Inlet diameter

The relation between the inlet diameter and Mach number are illustrated in Fig 3. This graph shows the smaller the inlet diameter, the higher the Mach number.

Based on these conditions Mach number, M is 0.3, at that point of data is nearly equal to the actual of the centrifugal compressor impeller inlet. Therefore, the design is satisfied for at that point of data.

5. THEORETICAL RESULTS

TABLE I
 CALCULATED DATA OF IMPELLER

no	Design Parameter	Symbol	Values	Units
1	Polytropic head	H_p	67.411	kNm/kg
2	Torque	T	32.906	N-m
3	Speed of sound	a	390.221	m/s
4	Mach number	M_1	0.3	-
5	Inlet velocity	U_1	103.283	m/s
6	Absolute velocity at inlet	V_1	119.993	m/s
7	Relative velocity at inlet	V_{r1}	158.322	m/s
8	Inlet blade angle	β_1	49.5	deg
9	Outlet velocity	U_2	346.22	m/s
10	Absolute velocity at outlet	V_2	336.209	m/s
11	Relative velocity at outlet	V_{r2}	124.226	m/s
12	outlet blade angle	β_2	75	deg
13	Outlet Mach no;	M_2	0.8	-
14	efficiency	η	94	%

TABLE II
 COMPARISON OF CALCULATED AND EXISTING DATA

	Design Parameter	Symbol	Unit	Calculated data	Actual data
1	Shaft diameter	D_s	m	0.02	0.0254
2	Hub diameter	D_h	m	0.0225	0.028
3	Eye diameter	D_o	m	0.047	0.053
4	Inlet diameter	D_1	m	0.048	0.054
5	Outlet diameter	D_2	m	0.161	0.17
6	Inlet width	b_1	m	0.009	0.0098
7	Outlet width	b_2	m	0.0021	0.0025
8	Number of vanes	z	-	19	19

The design of impeller in this paper is calculated inlet and outlet diameters and blade width and number of blades. The designed data of impeller inlet in this research are as well as the shaft diameter D_s is 0.02m, the hub diameter D_h is 0.0225m, Eye diameter D_o is 0.047m, Impeller inlet diameter D_1 is 0.048m, Impeller outlet diameter D_2 is 0.161m, Inlet width b_1 is 0.009m, Outlet width b_2 is 0.0021m. All of the calculated data are slightly smaller than the actual data. This calculated data can be accepted because this data are situated between 20% error. The number of impeller blade is same at these two data.

6. CONCLUSIONS

Centrifugal compressors are compressible flow machine. Centrifugal compressor from 'Ahlone Power Station' is designed in this paper. This paper is attempted to design a single stage centrifugal compressor from 'Ahlone Power Station'. The design of impeller in this paper is inlet and outlet diameter and number of blades and blade width. This paper describes the inlet and outlet velocity triangle. And this research shows the pressure and velocity distribution by using COMSOL Multiphysics software.

Types of compressor are used in many services and power generation. Centrifugal compressors compress air to raise pressure at high speed. This compressor use also main component in aircraft gas turbine. In this paper, the centrifugal compressor is designed with data from 'Ahlone Power Station'.

REFERENCES

- [1] Baliye, O.E: Turbomachines. New York: John Wiley and Sons, Inc., 1981.
- [2] Ronald P. Lapina P>E. Estimating Centrifugal Compressor Performance Process compressor thchnology. Vol-1. McGraw Hill Publications Co,1982
- [3] Ebara Hatakeyama Memorial Fund: Compressor Engineering. U.S.A. John Wiley and Sons, Inc., 1992.
- [4] Meherwan, P. Boyce: Gas Turbine Engineering Handbooks, Part-II,2nd .Ed., New Delhi: Gulf Professional Publishing Co.,2002.
- [5] Rama S.R.Gorla, Turbomachinery Design and Theory,Cleveland State University,Cleveland,Ohio, U.S.A 2003.
- [6] Beckers, J.: Uses of High-Speed Turbocompressors in Offshore Installations.
- [7] Woodhouse, H., Inlet Conditions of Centrifugal Compressor for Aircraft Engine Superchargers and Gas Turbines, 2006.

PIC and Sensors Based Automatic Car Washing System

Ei Ei Aung
Department of Electronic
Engineering
Technological University (Lashio),
Myanmar

Abstract: This paper describes the design and implementation of automatic car washing system for the exterior of the vehicles using PIC16F877A microcontroller. There are five main parts to implement the system; moving, washing, foaming, brushing and cleaning. To accomplish the system, conveyor, LDR sensor circuits, motor driver circuits, pumps and motors are comprised. The conveyor is used to carry the vehicle and moved from step to step. The sensor circuit sensed and input data to the PIC. The outputs of PIC are commands to drive motors and pumps.

Keywords: automatic; car washing; PIC; conveyor; LDR; motors; pumps

1. INTRODUCTION

Car washing system is a facility used to clean the exterior and, in some cases, the interior of motor vehicles. As the transportation section is developed, the most common problem often encountered while cleaning these vehicle is time consumption. Then automatic car washing system is an attractive solution to the problem.

Automatic car washing machine consists of tunnel- like building. In this system, a car enters a washing station and automatically gets cleaned up. This system design can provide reliability, safety and reducing time consumption. This paper is mentioned on the basic research of developing on car washing and can be realized the operation of the Automatic Car Washing System. This system is controlled by using programmable interface controller (PIC). There are five steps involved in car washing system namely moving, washing, foaming, brushing and cleaning. The various components used in this project are the conveyor belt, sensors, buzzer, dc motors, pumps and brushes.

Using this automatic car washing system, many cars can be washed and it will save time, energy and manpower. Automation of the process is having its own significance with the advancement of science and technology. As the technology is upgrading day by day and everyday it creating life easier, so take advantage of these advancements. Such systems can be installed anywhere such as malls, airports, railway stations etc. This process is based on cyclic process which provides more than 95% cleaning.

In this paper, there are mainly five sections to implement this control system. Firstly the system is introduced. The second section describes the system description of overall control system, and some detailed features of the Automatic Car Washing System. The third and fourth sections present the software and hardware implementation, test and result of the overall system. Conclusion is mentioned in the fifth section.

2. SYSTEM DESCRIPTION

The technical characteristic of an Automatic Car Washing System are designed as follows. The five processes are moving, washing, foaming, brushing and cleaning. Firstly the conveyor is on and the car is entered to the station. When the car reaches on LDR sensor1, sensor senses and the pump will spray the car with water. When the car reaches on LDR sensor2, sensor senses and the pump will spray the car with detergent water. When the car reaches on LDR sensor3,

sensor senses and the motor will brush the car with brusher. Finally, when the car reaches on LDR sensor4, the pump will clean the car for 10 seconds. After finishing all processes, the buzzer will sound for 2 seconds and then the conveyor belt will stop.

The block diagram of Microcontroller based Automatic Car Washing System is shown in Figure 1.

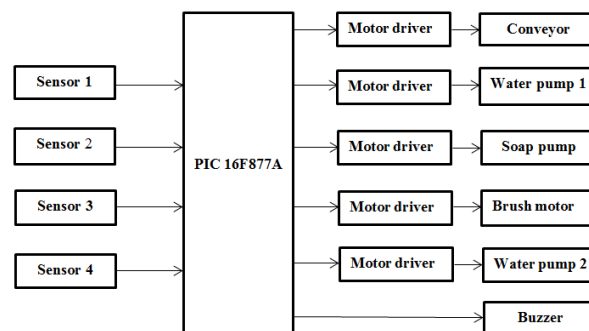


Figure 1. Block diagram of Automatic Car Washing System

2.1 Microcontroller

The major difference of a microcontroller compared to a microprocessor and microcomputer is that microcontroller consists of central processing unit (CPU), memory devices (ROM and RAM), input and output ports and timer embedded into a single chip. PIC 16F877A is mainly used to implement the automatic car washing design. It has many I/O ports such as PORTA, PORTB, PORTC, PORTD and PORTE. Speed of 4MHz crystal is used to carry out the algorithm. Six pins of PORTB is used as output pins to the motors and pumps, and other pins of PORTD are used as input pins to sense the car and input data to the PIC.

2.2 Sensor and Relay Driver Circuits

The 12V supply voltage supplies to all sensor circuits, motors, pumps and conveyor belt and then 5V supplies the PIC. When the car reaches on LDR sensor1, sensor senses and the incoming signal reaches to the base of transistor Q1 which collector is connected to the relay. The common point of relay is connected to the input pin of the PIC RD0. At the time the signal reaches the input pin RD0, the program runs. The signal from the output pin RB0 and RB1 enter through the base of transistor Q5 and Q6 which collector are connected to

the relay. The 12V supply voltage supplies to the common point of relay at the output. When the relay on, the conveyor belt and pump1 starts working. There are four sensor circuits with four motors or pumps respectively.

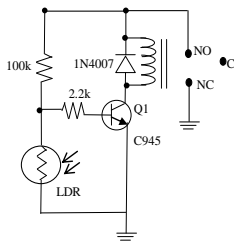


Figure 2. LDR sensor circuit

Design for one sensor circuit,

To saturate the transistor, V_B must be greater than $V_{BE(sat)}$. Using voltage divider formula, $V_B = (R_{LDR} / (R_1 + R_{LDR})) \times V_{CC}$, let $R_1 = 100k\Omega$. When LDR resistance is reached $10.4k\Omega$, V_B is 1.13V and I_B can calculate from $I_C(I_{relay})/h_{FE}$ and applying Kirchhoff's voltage law, $R_B = (V_B - V_{BE(sat)})/I_B$, the base resistor is $2.2k\Omega$.

Design for relay driver circuit,

When PIC output is 5V, $V_{BE(sat)}$ is 0.8V and I_B can calculate from $I_C(I_{relay})/h_{FE}$ and applying Kirchhoff's voltage law, $R_B = (V_B - V_{BE(sat)})/I_B$, the base resistor is $28k\Omega$ and choose $27k\Omega$ as a standard value.

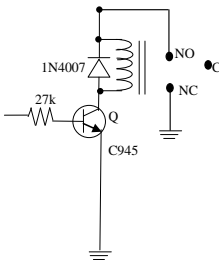


Figure 3. Relay driver circuit

2.3 Overall Circuit Diagram

The overall circuit diagram is illustrated in Figure 4.

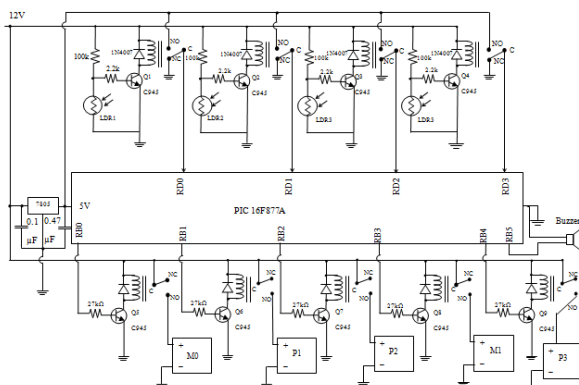


Figure 4. Overall Circuit of Automatic Car Washing System

In this circuit design, there are five main portions to implement the system. They are moving washing, foaming, brushing and cleaning. Then buzzer is alarm to know the process is complete. Based on the overall system design, the

simulation result is implemented by using mikroC Pro for PIC and Proteus software.

3. SOFTWARE IMPLEMENTATION

3.1 Flowchart of the System

When the car reaches on LDR sensor1, the conveyor is on and the water pump1 is on .When LDR sensor2 is active, the soap pump is on. When LDR sensor3 is detected the car, the brush motor is active to wash the car with brushes. Finally, when the car reaches on LDR sensor4, the water pump2 is on to clean the car for 10 seconds. After finishing all processes, the buzzer will sound for 2 seconds and then the conveyor belt will stop.

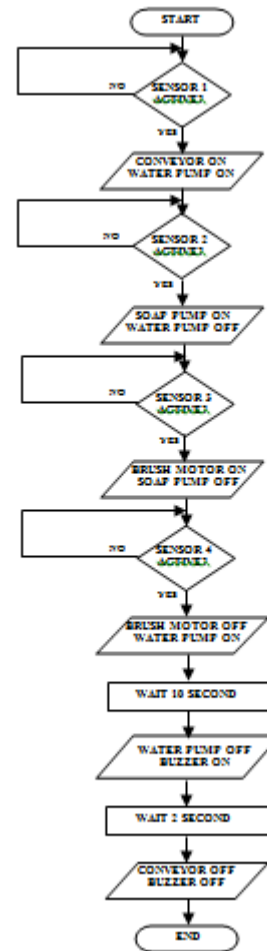


Figure 5. Flowchart of the system

3.2 Simulation and Compiling

Firstly, the C program to test the simulation must be written in the Notepad as C file. And then using mikroC Pro for PIC compiler software, program must be compiled. When the result is succeed, there are many files that created by the software. Among them, the HEX file is needed to link with the PIC. The circuit diagram with the PIC microcontroller is drawn and compiled with the HEX file. Finally simulation test is implemented with the Proteus software. If the result is satisfied, it is downloaded to PIC using Easy PIC kit. Figure 6 show the test result of compiled code is succeeded.

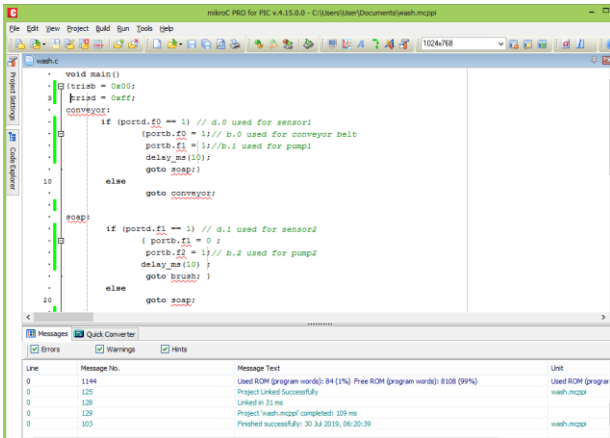


Figure 6. Testing software implementation

4. TEST AND RESULT

When the car reaches on LDR sensor1, the conveyor is on and the water pump1 also starts for washing as shown in Figure 7.



Figure 7. Washing the car

When the car reaches on LDR sensor2, the soap pump is on for foaming as shown in Figure 8.



Figure 8. Foaming the car with detergent liquid

When the car reaches on LDR sensor3, the brush motor is on for brushing as shown in Figure 9.



Figure 9. Brushing the car

When the car reaches on LDR sensor4, the water pump 2 is active for cleaning as shown in Figure 10.



Figure 10. Final cleaning the car

Complete system design is accomplished as shown in Figure 11. There are four sections except conveyor and their respective tanks; two water tanks and one soap tank.



Figure 11. Complete system of Automatic Car Washing System

5. CONCLUSION AND DISCUSSION

Car washing is a service that becomes essential role in most of cities currently in developing country. Automation was created to reduce manpower, to make production process easier and increase its quantities several times. The system aim to develop the required demand on reduces time consumption, less cost and reduces human errors. C language is used because of the short learning curve that most students have the basic of the C language, and now its wide distribution and its general- purpose nature have to be studied and linked with the PIC microcontroller technology. In addition drying and polishing can be extended. And cleaning of the interior in the vehicles is also expanded.

6. ACKNOWLEDGMENTS

The author would like to thank to her family and partners who have contributed towards development of this work.

7. REFERENCES

- [1] D.W Smith. 2002. "PIC in practice", Gutenberg Press Ltd.
- [2] Anonymous, 2003, "PIC16F87X Datasheet", Microchip Technology Inc.
- [3] Lucio Di Jasio, Tim Wilmshurst, Dogan Ibrahim, John Morton, Martin P. Bates, Jack Smith, D. W. Smith, Chuck Hellebuyck. 2008. "PIC Microcontrollers: know it all", Elsevier Inc.
- [4] Thomas L. Floyd. 2007. "Electronic Fundamentals: Circuit, Devices and Application".
- [5] Janik, A. Kupiec. 2007. "Trends in Modern Car Washing" Polish J. of Environ Stud. Vol.16, No.6.
- [6] M., Amir Hossein Daei Sorkhabi, "Manufacturing of Full Automatic Carwash Using With Intelligent Control Algorithms", IEEE Vol: 7, No: 3, 2013.
- [7] Muhammadali V.V. 2010. Programmable Controller, Principles and Applications, "Seminar on Automatic Car Washing System".
- [8] Irfan Anjum, Tarif Hussain, M. Fasial Mafeed. 2018. "PLC Based Automatic Car Wash System".

Single Axis Solar Tracking System

Ei Ei Aung
Department of Electronic
Engineering
Technological University (Lashio),
Myanmar

Abstract: This paper describes the analysis and implementation of solar tracking system to generate electricity from renewable energy. This is aim to recover the demand on electricity in the rural area. To get maximum energy, solar panel is tracked the path of sun using Arduino Uno, LDR sensors, stepper motor and solar panel. And the battery is used to store the energy from the solar panel through the charge controller and applied to the intended loads. Data analyzing is accomplished and compared to sunny day and cloudy on hour to hour.

Keywords: solar; tracking; Arduino Uno; LDR; stepper motor; charge controller, analysis

1. INTRODUCTION

In this day, renewable resource is one of the major concerns because of increasing more power demand but the quality and availability of conventional energy sources are not enough. Energy is essential factor for the development of any nations of all over the world. Most of the energy production depends on fossil fuel. The resources of the fossil fuels are limited, so that there are growing demand for energy from renewable resources like solar, geothermal and ocean tidal wave. Among all renewable systems, photovoltaic system is the one which has great chance to replace the conventional energy resources. To enhance the performance of solar panel the only way is to increase the intensity of light falling on it. Solar tracker is the best technology to increase the efficiency of solar panel by keeping panel aligned with the suns position. The advantage of using solar power for small power generation is its probability; it can be carried whenever or wherever small power generation is required.

In this research, a microcontroller based simple and easily programmed automatic solar tracker is presented. Design and construction of a prototype for solar tracking system detected the sunlight using Light dependent Resistors (LDR), is discussed in this work. The control circuit for the solar tracking system is based on Aurdino Uno. This is programmed to detect the sunlight through the LDRs and then actuate the stepper motor to position the solar panel where it receives maximum sunlight. Compared with any other type of motor, the stepper motor is more controllable, more energy efficient, more steady and having high tracking accuracy and suffering little environmental effect.

In this paper, there are mainly five sections to implement this control system. Firstly the system is introduced. The second section describes the system description of overall control system, and some detailed features of the Solar Tracking System. The third and fourth sections present the software, test and result of the overall system. Conclusion is mentioned in the fifth section.

2. SYSTEM DESCRIPTION

The propose system is the Arduino based variable and compactable system with a single axis solar tracking system. The Arduino gets the data from the two LDR sensors to rotate the solar panel to the lighting place by using the motor driver and the stepper motor. The voltage divider method is used as

the voltage sensor. The battery is used to store the energy from the solar panel and applied to the loads. The block diagram of single axis solar tracking system is shown in Figure 1.

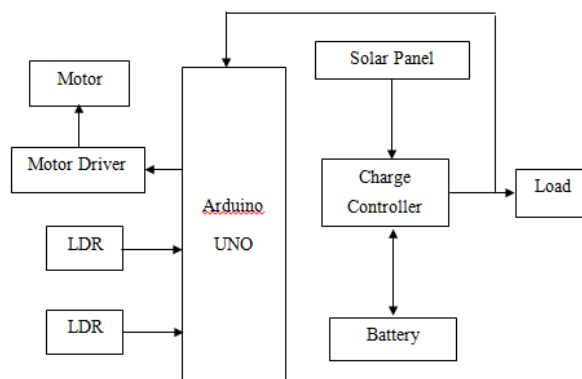


Figure 1. Block diagram of Solar Tracking System

2.1 Microcontroller

The Arduino Uno is a microcontroller board based on the ATmega328 (datasheet). It has 14 digital input/output pins (of which 6 can be used as PWM outputs), 6 analog inputs, a 16 MHz ceramic resonator, a USB connection, a power jack, an ICSP header, and a reset button. It contains everything needed to support the microcontroller; simply connect it to a computer with a USB cable or power it with an AC-to-DC adapter or battery to get started. The Uno differs from all preceding boards in that it does not use the FTDI USB-to-serial driver chip. Instead, it features the Atmega16U2 (Atmega8U2 up to version R2) programmed as a USB-to-serial converter.



Figure 2. Arduino Uno

2.2 Solar Cell

The photovoltaic cell is the basic building block of a photovoltaic system. The individual cells can vary from 0.5 inches to 4 inches across. One cell can however produce only 1 or 2 watts that is not enough for most appliances. Performance of a photovoltaic array depends on sunlight. Climatic conditions like clouds and fog significantly affect the amount of solar energy that is received by the array and therefore its performance. Most of the PV modules are between 10 and 20 percent efficient.



Figure 3. Solar cell

2.3 Stepper Motor

There are many types of motors AC; DC; Servo and Stepper motors. Stepper motors are DC motors that move in discrete steps. They have multiple coils that are organized in groups called "phases". By energizing each phase in sequence, the motor will rotate one step at a time. With a computer controlled stepping can achieve very precise positioning and/or speed control. For this reason, stepper motors are the motor of choice for many precision motion control applications.



Figure 4. Stepper motor

2.4 Motor Driver

This is a professional two-phase stepper motor driver. It supports speed and direction control. Driver's micro step and output current can be set with 6 DIP switch. There are 7 kinds of micro steps (1, 2 / A, 2 / B, 4, 8, 16, 32) and 8 kinds of current control (0.5A, 1A, 1.5A, 2A, 2.5A, 2.8A, 3.0A, 3.5A) in all. And all signal terminals adopt high-speed optocoupler isolation, enhancing its anti-high-frequency interference ability.

The features of stepper motor driver are:

- Support 8 kinds of current control
- Support 7 kinds of micro steps adjustable
- The interfaces adopt high-speed optocoupler isolation
- Automatic semi-flow to reduce heat
- Large area heat sink
- Input anti-reverse protection
- Overheat, over current and short circuit protection



Figure 5. TB-6600 stepper motor driver

2.5 LDR Sensors

The lighting sensor is composed the fixed resistor and the light dependent resistor (LDR). Supply voltage is 5V, and the voltage of LDR cannot be connected directly to the controller. So, voltage divider method is applied to read the voltage of LDR. The value of voltage difference between two LDRs is compared to the sensitivity, because the motor cannot be rotated every time on the whole day. The solar tracking system is designed to rotate CW or CCW directions according to the greater level of voltage when the voltages difference of two LDRs. When the voltage difference is greater than or not the sensitivity, the motor rotates to its respective direction.

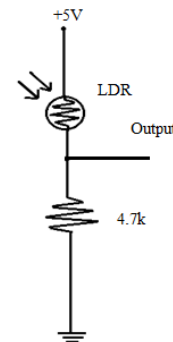


Figure 6. LDR sensor circuit

In the above circuit, a complementary resistor with a value of 4.7kΩ is used to get the desired output voltage signals. Regulated voltage supply is 5V.

The output voltages are calculated by using the following equation;

For maximum, let $R_1 = R_{LDR(max)} = 1M\Omega$,

Assume, $R_2 = 4.7k\Omega$, using voltage divider,

$V_{out} = [R_2 / (R_{LDR} + R_2)] \times V_{cc}$ and the output voltage is 0.02 V.

For midpoint, let $R_1 = R_{LDR(mid)} = 1k\Omega$,

Assume $R_2 = 4.7k\Omega$, the output voltage is 4.12V.

2.6 Overall Circuit Diagram

The overall circuit diagram is illustrated in Figure 7. There are three parts in the control systems; LDR sensor, microcontroller and stepper motor. The LDR sense the sunlight and send the data to the microcontroller. The microcontroller control TB-6600 motor drivers to drive the stepper motor change direction depend upon the signal on LDR sensors. The solar panel tracks the sunlight to have the maximum power. The charge controller is used to control the voltage charging to the battery.

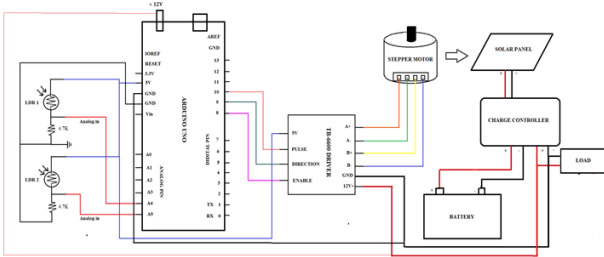


Figure 7. Overall Circuit of Single Axis Solar Tracking System

3. SOFTWARE IMPLEMENTATION

3.1 Program Flowchart of the System

Firstly the header files, the variable, input and output pins are considered to initialize. Then the data from LDRs are read. The difference between the two LDR and sensitivity are compared. If the measured difference between the set of sensors is greater than the sensitivity value, the direction pin on Arduino is HIGH. The motor rotates CW direction. Or the direction pin on Arduino is LOW and the motor rotates CCW direction.

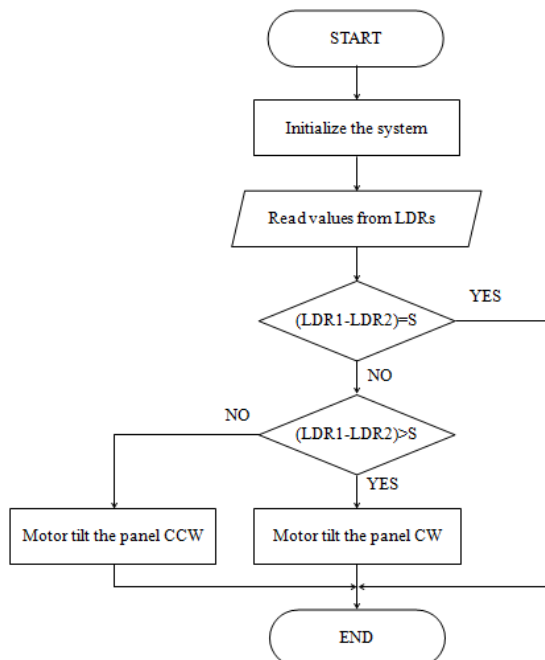


Figure 8. Program flowchart of the solar tracking

3.2 Simulation and Compiling

To simulate and compile the whole system, Arduino IDE software is established. Figure 9. shows the test result of compiled code is succeeded.

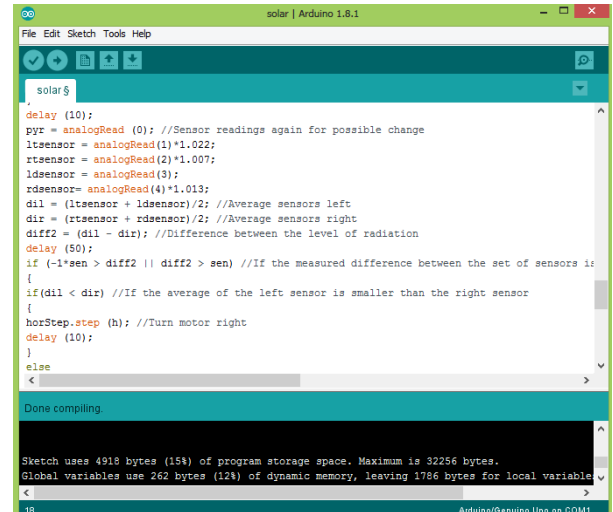


Figure 9. Compilation result of the program

4. TEST AND RESULT

Figure 10. shows the testing of microcontroller, BT-6600 motor driver and stepper motor. Implementation of the system is partially developed without solar panel.

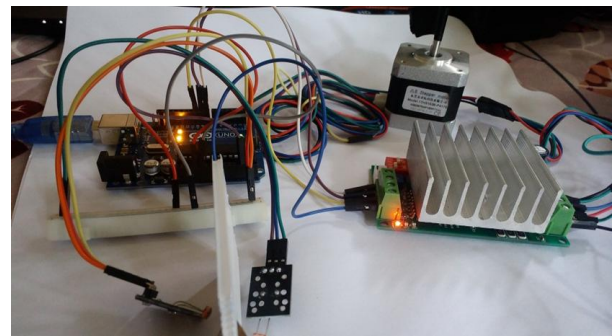


Figure 10. Testing of microcontroller, BT-6600 motor driver and stepper motor

Figure 11. shows implementation of the system is developed with solar panel.

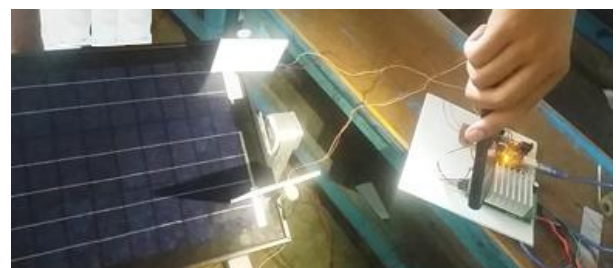


Figure 11. Testing of the whole system

4.1 Data Analysis

The data from the two LDRs are converted to analogue voltages and compared to hour by hour. But there are not much changed in the day. If here is no light, the system is switched off to reduce power consumption. Table 1. shows the comparison of the voltages on cloudy day.

Table 1. The comparison of the voltages on cloudy day

Time	LDR 1 Volt	LDR 2 Volt
8:00 Am	3.76	3.88

9:00 Am	3.96	4.22
10:00 Am	4.24	4.52
11:00Am	4.48	4.72
12:00 Am	4.78	4.75
1:00 Pm	4.69	4.64
2:00 Pm	4.60	4.65
3:00 Pm	4.32	4.36

To illustrate the voltages from the two LDRs, line chart is used as shown in Figure.

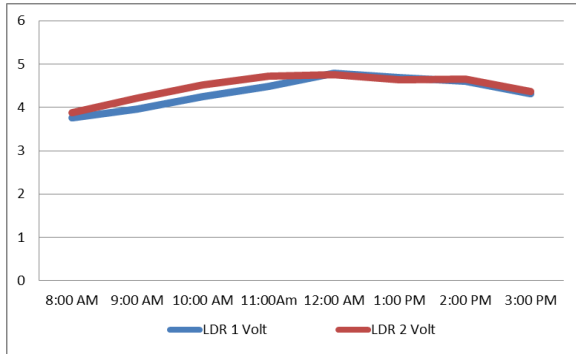


Figure 12. Line chart for the data from two LDRs in cloudy day

Table 2. shows the comparison of the voltages on sunny day.

Table 2. The comparison of the voltages on sunny day

Time	LDR1	LDR2
8:00 Am	1.55	1.61
9:00 Am	1.82	1.85
10:00 Am	2.40	2.52
11:00 Am	2.65	2.71
12:00 Am	2.89	3.08
1:00 Pm	3.02	3.14
2:00 Pm	2.75	2.86
3:00 Pm	2.42	2.54

To illustrate the voltages from the two LDRs, line chart is used as shown in Figure 13.

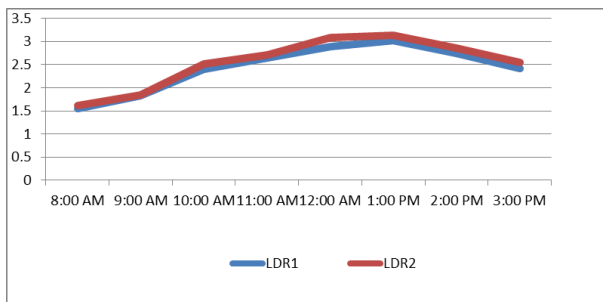


Figure 13. Line chart for the data from two LDRs in sunny day

From the data, it can be seen that the voltage from cloudy day is less as twice as the sunny day. But voltage difference of cloudy day is greater than the sunny day. So the motion of solar panel is infrequently changed in sunny day.

5. CONCLUSION

An Arduino based single axis solar tracking system was designed and constructed in the current work. LDR light sensors were used to sense the light intensity of the sun with the help of the photovoltaic cells. The stepper motor had enough torque to drive the panel. Stepper motors are noise free and are affordable, making them the best choice for the project.

The compact, cost effective and reliability of this solar tracker is intended to suitable for the rural usage. The purpose of renewable energy from this work offered advance in idea to help the people. This system can be designed to provide electricity to the entire home by changing solar panel, using more efficient sensors and designing the charge controller. Instead of single axis tracker, dual axis tracker are also performed and compared to the single axis. Solar car and solar motorbike can be developed for pollution problems without using resource from the world.

6. ACKNOWLEDGMENTS

The author would like to thank to her teachers, family and partners who have contributed towards development of this work.

7. REFERENCES

- [1] Anne Rosenblatt, Nicole Aaron. 2014. "SOLAR TRACKING SYSTEM", Project Report for Swarthmore College Engineering Department.
- [2] Oloka Reagan Otieno, 2009. "SOLAR TRACKER FOR SOLAR PANEL", University Of Nairobi.
- [3] Thomas L. Floyd.2007. "Electronic Fundamentals: Circuit, Devices and Application".
- [4] S. Armstrong, W.G Hurley. 2009. "Investigating the Effectiveness of Maximum Power Point Tracking for a Solar System", The IEEE Conference on Power Electronics Specialists.
- [5] Damm,J. 1990. "An active solar tracking system", Home Brew Magazine, Issue # 17.
- [6] Simon Monk. 2011. " Programming Arduino: Getting Started with Sketches".
- [7] J.A. Beltran, J.L.S. Gonzalez Rubio, C.D. Garcia Beltran. 2007. " Design, Manufacturing and Performance Test of a Solar Tracker Made by Embedded Control, CERMA, Mexico
- [8] David Cooke. 2011. " Single vs. Dual Axis Solar Tracking", Alternate Energy eMagazine.
- [9] Kumar Lokhande. 2014. "AUTOMATIC SOLAR TRACKING SYSTEM", International Journal Of Core Engineering & Management (IJCEM), Volume 1, Issue 7.

Performance Evaluation of Virtual Traffic Light (VTL) Algorithm Vs Traffic Light System (TLS) in SUMO

Tin Maung Wynn
Department of Information Technology,
Technological University(Thanlyin)
Yangon, Myanmar

Wah Wah Kyaw
Department of Electronic Engineering,
Technological University(Toungoo)
Toungoo, Myanmar

Abstract: In future, all the vehicles will be the connected vehicles and they can communicate with each other. At that time, physical traffic light systems will be replaced with Virtual Traffic Light systems. The Virtual Traffic Light (VTL) is a self-organizing traffic control system without requiring road infrastructures. However, the major weakness of the existing VTL allows only one vehicle crossing the intersection at a time and considers only straightforward direction of vehicles. This paper implements a VTL algorithm for road intersections on Simulation of Urban Mobility (SUMO) that allows more vehicles to cross the intersection without collisions and considers the vehicle's other directions such as turn left or turn right rather than go straight. For performance evaluation, the CO₂ emission of vehicles applying the proposed VTL is compared to that of physical traffic light system (TLS) in SUMO. According to comparison result, the average CO₂ emission of vehicles applying the proposed VTL algorithm significantly decreases compared to traffic light system in SUMO.

Keywords: ITS, VTL, TLS, SUMO

1. INTRODUCTION

As Smart Vehicles (SVs) become more common, the traffic control strategies that are currently used for human drivers will likely have to be re-thought. An important example is that of intersection management (IM): in a typical traffic light setting, vehicles are not allowed to cross the intersection if the light corresponding to their lane is red, even in the absence of conflicting vehicles. This often results in many vehicles unnecessarily idling, and can significantly increase their CO₂ emissions. Fully leveraging the capacities of smart vehicles, various autonomous IM (AIM) techniques that do not require a signal-based approach have been proposed in [1]. One of the approaches is to implement VTL system for smart vehicles.

Nowadays, traffic lights currently control only a limited number of intersections, and increasing the number of traffic lights is clearly infeasible due to the high cost of deployment and maintenance [2]. To overcome this challenge, the first distributed VTL algorithm for Vehicular Ad-hoc NETWORKS (VANETs) has been described in [3], where simulation results showed up to 60% increase in the average flow rate in the reference city of Porto. The adopted algorithm is based on the definition of cluster of vehicles, cluster head, and VTL leader. The vehicles on the same road form a cluster and the one which is nearest to the intersection is the cluster head. The cluster head that is farther from the intersection is then elected as the VTL leader and is responsible for determining the priorities of vehicles and broadcasting the virtual traffic light messages. Once the VTL leader leaves the intersection, a new VTL leader is elected.

The same algorithm has been in many subsequent studies. The distributed VTL algorithms introduced in [2, 4] exchange information between smart vehicles using both broadcast messages for signaling and unicast messages for precedence definition and traffic light decisions. The algorithm has been implemented and tested through low cost IEEE 802.11p devices, using open source software. But, the distributed VTL algorithms in [4] and [2] are designed with the assumption that they are not able to infer the future movements of each SV and only one SV can cross the intersection at a time, even though there will be no possibility

of collision between SVs. For example, two SVs approaching the intersection from opposite directions with the intent to go straight would not need to stop at the intersection.

Although some VTL algorithms were introduced for VANETs, they allow only one vehicle to cross the junction at a time. While a vehicle from one road segment is crossing the junction, the vehicles from the other three road segments cannot cross the junction. Moreover, the VTL algorithms consider only straightforward directions of vehicles.

In this study, a VTL algorithm for road intersection is proposed to optimize the existing VTL algorithm. The proposed VTL algorithm enables more than one vehicle crossing the intersection simultaneously without collision and considers the vehicle's other directions such as turn left or turn right rather than go straight. The algorithm is intended for intersections where the deployment of real traffic lights is not cost-effective. The algorithm was implemented and tested in SUMO. As a simulation result, the CO₂ emission of vehicles using the proposed VTL algorithm is compared with the TLS in SUMO.

The rest of this paper is organized as follows: The proposed VTL algorithm is mentioned in detail in Section 2. In Section 3, the implementation of the proposed VTL algorithm is described and the simulation result and discussion is shown in Section 4. Finally, the conclusion is drawn in Section 5.

2. THE PROPOSED VIRTUAL TRAFFIC LIGHT ALGORITHM

The proposed VTL algorithm is based on the first coming, the first crossing principle for the initial coordination.

2.1 Assumptions of Original VTL algorithm

The VTL algorithm knows the position of each vehicle from the SUMO's built-in localization system. By using this information, the VTL algorithm gets the updated positions of vehicles and is able to calculate the priority to cross the intersection.

The VTL algorithm is based on the following key concepts:

- Each smart vehicle (SV) is assigned a priority in order to cross the intersection. The priority is calculated based on the distance between SV and the intersection.
- For each road segment, the SV that is closest to the intersection is denoted as leader and the others as followers. One of the leaders is elected as the intersection leader and it has the priority to cross the intersection.
- If the vehicles are driving in opposite directions or the same road segment with the intersection leader, these vehicles can cross the intersection simultaneously.
- If the vehicles with priorities to cross the intersection have passed the junction, the priority is granted to the vehicles from another road segment.

Figure 1 shows the example of the virtual traffic light, in which the intersection leader, leaders and follower can be seen.

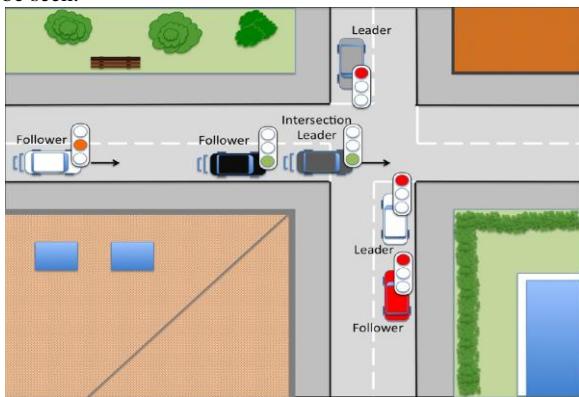


Figure 1. Virtual traffic light example scenario [2]

2.2 Working Procedure of the proposed VTL Algorithm

In order to implement the proposed VTL algorithm in real world, each smart vehicle must be equipped with a global navigation satellite system such as Global Positioning System (GPS) and short range wireless communication system based on IEEE 802.11p technology. Each SV knows its own position using GPS and broadcasts to neighbour vehicles via short range wireless communication system.

The proposed VTL algorithm starts when the vehicles enter the VTL area. In this study, the VTL area's threshold value is denoted as eighty meters (VTL area's diameter of 160 meters) from the junction because the packet loss rate using IEEE 802.11p remains lower at distances up to 200 meters when SVs communicate each other. For longer distances, packet loss rate increases. The algorithm executes the following steps.

- Step 1) Update the positions of vehicles and calculate the distance from the vehicles to the junction.
- Step 2) If the vehicle's distance to the junction is less than eighty meter, set the vehicle's VTL as Orange (Orange VTL) and move to Step 3. Otherwise, return to Step 1.
- Step 3) Separate the vehicles based on road segment ID. (There can be at most four vehicles group for a junction.)
- Step 4) Sort vehicles on each road segment (N-North, S-South, W-West and E-East) according to their distance from the junction.

Assign the vehicle that is closest to the junction as the leader and the others as followers.

- Step 5) Define two priority zones NS (vehicles from N and S road segments) and WE (vehicles from W and E road segments).
- Step 6) Get leader from each road segment and form a leaders set.
- Step 7) Sort the vehicles from the leaders set based on their distance from the junction. Set the first vehicle from the sorted leaders set as the intersection leader. (If all the leaders are equal distances from the junction, the intersection leader is elected based on road segments.)
- Step 8) If a vehicle is intersection leader, set the vehicle's VTL as Green (Green VTL) and move to Step 10. Otherwise, move to Step 9.
- Step 9) Set the vehicle's VTL as Red (Red VTL) and slow down the vehicle.
- Step 10) If the intersection leader is in NS zone, set the vehicles' VTLs in NS as Green (Green VTLs) and define VTL priority as 'ns', then move to Step 14. Otherwise, move to Step 11.
- Step 11) Set the vehicles' VTLs in WE as Green (Green VTLs) and define VTL priority as 'we'. Move to Step 14.
- Step 12) If the VTL priority is 'ns' and there is no vehicle in NS zone, set the vehicles' VTLs in WE as Green (Green VTLs) and move to Step 14. Otherwise, move to Step 13.
- Step 13) If there is no vehicle in WE zone, set the vehicles' VTLs in NS as Green (Green VTLs) and move to Step 14.
- Step 14) Calculate the priorities of the two vehicles attempting to cross the junction from the opposite directions. (The working procedure to calculate the priority is described in the following).

In order to calculate the priorities, the two conditions, non-collision condition and possible collision condition of two opposite vehicles (SV1 and SV2) are defined as shown in Figure 2 and Figure 3.

Non-collision Condition			①	②
	SV1	SV2		
1	Straight	Straight		
2	Turn-Left	Turn-Left		
3	Turn-Right	Turn-Right		
4	Straight	Turn-Right		
5	Turn-Right	Straight		

Figure 2. Non-collision condition of two opposite vehicles

Possible Collision Condition		
	SV1	SV2
1	Straight	Turn-Left
2	Turn-Left	Straight
3	Turn-Right	Turn-Left
4	Turn-Left	Turn-Right

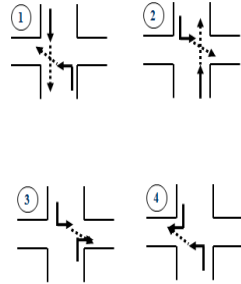


Figure 3. Possible collision condition of two opposite vehicles

Calculation of the priorities of the two vehicles attempting to cross the junction from the opposite directions includes the following steps:

- Step 1) Get the two vehicles' signals for directions (Straight, Turn-Left, Turn-Right).
- Step 2) If the two vehicles are in the non-collision condition, they can cross the junction simultaneously. Otherwise, move to Step 3.
- Step 3) Calculate the distance of the two vehicles to the junction.
- Step 4) If one vehicle whose distance to junction is lower than the other, move to Step 5. Otherwise, move to Step 6.
- Step 5) Give the priority to the nearest vehicle to the junction and the other vehicle needs to slow down until the prioritized vehicle pass the junction.
- Step 6) If the two vehicles are in the same distance to junction and in one of the possible collision conditions, follow the right-of-way rules.

3. IMPLEMENTATION

The proposed VTL algorithm was developed using Matlab, SUMO traffic simulator and Traffic Control Interface for Matlab (TraCI4Matlab).

To implement the proposed VTL algorithm in SUMO, the scenario road network file is created using NETEDIT application. In this simulation, a road network with a junction that contains four road segments is created. Then, the route file is created to add vehicles and to define their routes. In this scenario, the proposed VTL algorithm is tested with twelve smart vehicles with their respective directions as in Figure 4(a), and the proposed VTL is represented with vehicle's colour as shown in Figure 4(b).

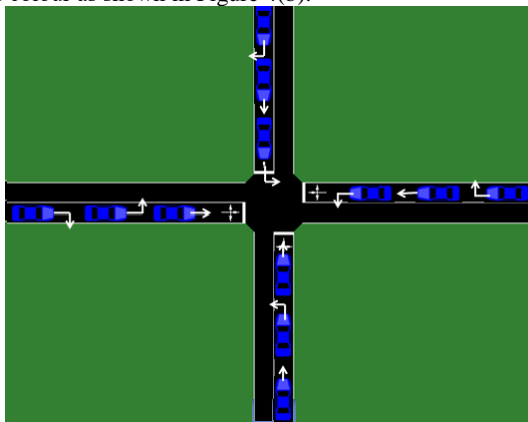


Figure 4(a). Simulation of the proposed VTL with 12 SVs

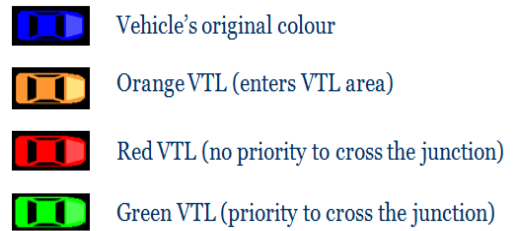


Figure 4(b). Definition of vehicle's colour in the proposed VTL

When the simulation starts, the vehicle's colour is set to blue. When a vehicle enters the VTL area, the vehicle's colour is changed from blue to orange (Orange VTL), and then green (Green VTL) or red (Red VTL).

In Figure 5, twelve SVs are approaching the junction from four different road segments (N, S, W and E). SV1, SV4, SV7 and SV10 are leaders of four different road segments and the other eight vehicles will be followers when they enter the VTL area. Then the SVs are sorted on each road segment according to their distance to the junction and the algorithm define two priority zones NS (SV4, SV5, SV6, SV10, SV11, SV12) and WE (SV1, SV2, SV3, SV7, SV8, SV9). Among four leaders, SV10 in S is closest to the junction and it is elected as intersection leader. The algorithm defines VTL priority as 'ns'. The algorithm sets SV10 as Green VTL which means that SV10 can cross the junction and sets the vehicles from NS zone as Green VTL because the intersection leader is in NS zone and calculate the priorities of vehicles. Then, the algorithm sets the vehicles from WE zone as Red VTL as shown in Figure 6. The speed of Red VTL vehicles is decelerated.

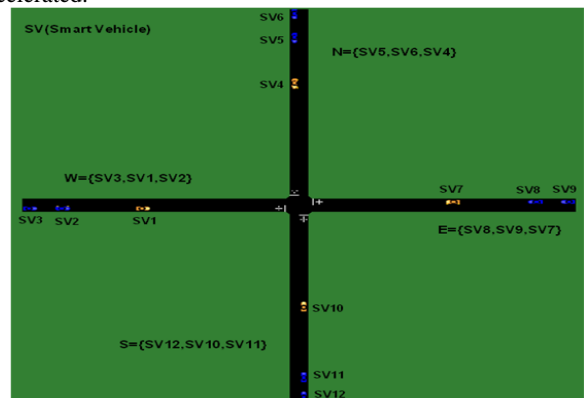


Figure 5. Example scenario of proposed VTL

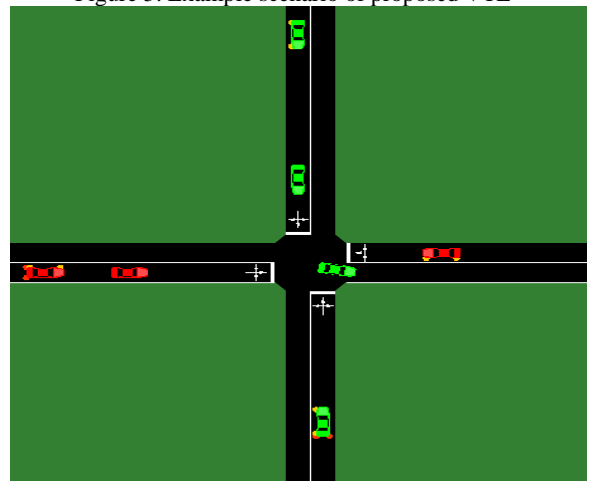


Figure 6. The state of VTL priority in 'ns'

If the VTL priority is 'ns' and there is no vehicle in NS zone, the algorithm sets the vehicles from WE zone as Green VTL as shown in Figure 7, defines VTL priority as 'we' and calculate the priorities of vehicles.

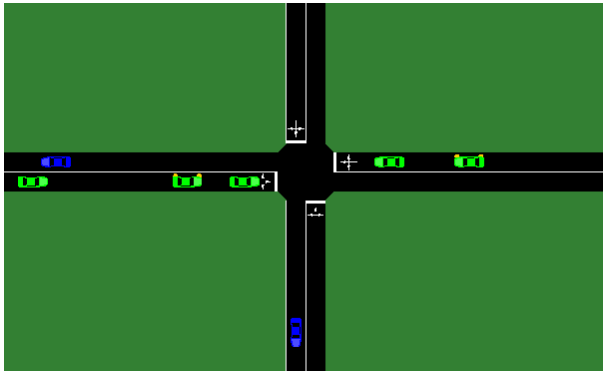


Figure 7. The state of VTL priority in 'we'

4. RESULTS AND DISCUSSIONS

To evaluate the proposed VTL algorithm compared with physical traffic lights, another simulation with twelve vehicles using SUMO's traffic lights (TLS) is implemented and tested as shown in Figure 8. The default green phase length of 33 seconds is used in TLS in SUMO.

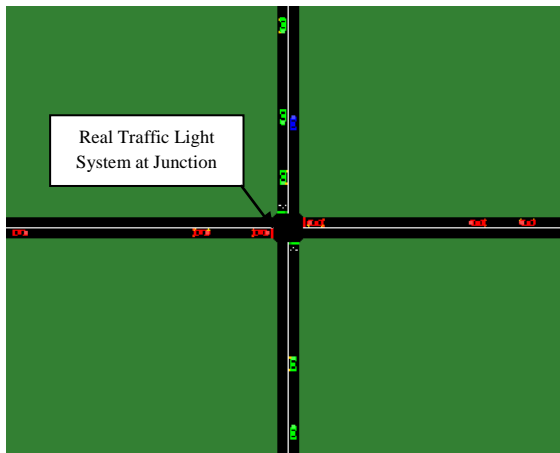


Figure 8. Traffic light simulation with twelve SVs

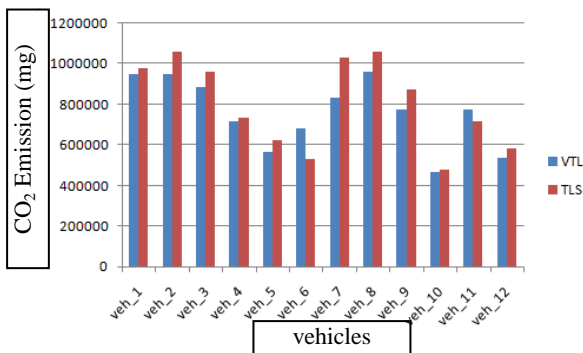


Figure 9. CO₂ Emission of vehicles

In order to compare the proposed VTL algorithm with physical traffic light system in SUMO, the CO₂ emission of each vehicle is obtained from the simulations.

When the CO₂ emission of each vehicle and their average CO₂ emission are examined, all vehicles (except SV6 and SV11) using proposed VTL are lower than real traffic light system as shown in Figure 9. On average, the CO₂ emission of all vehicles using proposed VTL algorithm is 750278 milligram (mg) and 802120 mg in physical traffic light system. Thus, the proposed VTL algorithm decreases CO₂ emission almost 7% without having any infrastructure like in real traffic light system. The proposed VTL algorithm saves time, in relation to real traffic light system due to the effectiveness of the algorithm and reduces time wasting at the junction. There is no risk yet in the current simulations although the proposed VTL considers not only the vehicles' straight forward directions but also turn left and turn right directions. One of the most significant findings is that the proposed VTL algorithm enables more vehicles to cross the intersection at the same time without collisions.

5. CONCLUSIONS

In this study, a VTL algorithm for road intersection was presented. The algorithm is intended for intersections where the deployment of real traffic lights is not cost-effective. The proposed VTL algorithm allows more than one vehicle to cross the intersection at the same time without collision by considering various vehicles' directions. The average CO₂ emission using proposed VTL algorithm was compared to that of physical traffic light system in SUMO. The algorithm's effectiveness was validated through the implementation of physical traffic light system and virtual traffic light system in SUMO. The simulation results also proved the system's efficiency.

6. ACKNOWLEDGMENTS

The author thanks the any anonymous reviewers for helpful comments on the manuscript. I am also grateful to my colleagues for helping in my work. My special thanks go to my Department for allowing me to use the Lab facility.

7. REFERENCES

- [1] Chen, L., Englund, C.: 'Cooperative intersection management: a survey', *IEEE Trans. Intell. Transp. Syst.*, 2015, **PP**, (99), pp. 1–17.
- [2] A. Bazzi, A. Zanella, and B. M. Masini, "A distributed virtual traffic light algorithm exploiting short range V2V communications," *Ad Hoc Networks*, vol. 49, p. 42–57, 2016.
- [3] M. Ferreira, R. Fernandes, H. Conceição, W. Viriyasitavat, O.K. Tonguz, "Self-organized traffic control," 7th ACM International Workshop on Vehicular InterNetworking, in: VANET '10, ACM, New York, NY, USA, 2010, p. 85–90.
- [4] A. Bazzi, A. Zanella, B. Masini, G. Pasolini, "A distributed algorithm for virtual traffic lights with IEEE 802.11p," *Networks and Communications (EuCNC)*, 2014 European Conference on, 2014, p. 1–5.

GAP Analysis of Good Manufacturing Practice on Lobster Supply Chain in Lombok

Hamdanul Fain

Departement of Aquatic
Product Technology
Bogor Agricultural University
Bogor, Indonesia

Ruddy Suwandi

Departement of Aquatic
Product Technology
Bogor Agricultural University
Bogor, Indonesia

Tri Wiji Nurani

Departement of Fisheries
Resources Utilization
Bogor Agricultural University
Bogor, Indonesia

Abstract: Lobster is one of the fishery commodities to develop. The implementation of a good manufacturing practice (GMP) is important. The level of implementation of GMP in the lobster supply chain in Lombok is unknown. Therefore, a gap analysis is needed for the application of GMP in the lobster supply chain in Lombok. The application of Good Aquaculture Practice (GAP) at the level of enlargement fisher and Good Handling Practice (GHP) at the level of catchers is included in category C or quite well. In the same case the collectors level is in category A or very good. The application of *Good Transportation Practice* (GTP) in lobster supply chain in Lombok is quite well. However, improvements in the application of GAP, GHP, and GTP are required. Improvement in GTP is included in improvement of GAP and GHP.

Keywords: lobster; handling; aquaculture; fishermen; improvement; good manufacturing practice

1. INTRODUCTION

Lobster is one of the economically valuable fishery commodities. The export value produced can reach US \$ 11 777 954 per year (KKP RI, 2012). Lobster prices doubled in 2015 compared to 2009 which originally sold for 150 000 per kilogram. This increase in selling prices is an opportunity for fishermen in East Lombok, West Nusa Tenggara. Lobster production in this area reached 146 tons in 2011. Although in the following years it decreased to 47.9 tons in 2014. Opportunities to maximize production can be seen from the many available seeds in Lombok waters. Jones et al (2010) reported that in Lombok had two peak harvest seasons of lobster seeds (puerulus phase), namely in August-September and April-May. The lowest number of seeds is 25 000 and the highest number is 70 000. Increased production is supported by the existence of the PERMEN KP No 1 of 2015 which requires a minimum size of lobster exports so that export of seeds is not allowed. Thus the fishermen are very helpful to get lobster seeds.

Putro (2008) states that aspects of quality and food safety have an important role in supporting export competitiveness. The quality aspect of lobster depends on how it is handled along the lobster supply chain. The implementation of a good manufacturing practice (GMP) in an important supply chain is to be implemented. The level of implementation of GMP in the lobster supply chain in Lombok is unknown. Therefore, a gap analysis is needed for the application of GMP in the lobster supply chain in Lombok. A gap analysis is a process comparing two different situation so that we can formulate a solution to bridge the different (Ritchey, 2013).

2. METHOD

GAP Analysis Assess based on Decree of the Minister of Maritime Affairs and Fisheries Number 2 of 2007 concerning the method of good fish cultivation or Good Aquaculture Practice (GAP), Indonesian National Standard (SNI) 7792: 2013 for Good Handling Practice (GHP) at the fishing catcher level, and SNI 4488.3: 2011 for Good Handling Practice (GHP) at the container level, assessment of GAP and GHP

related to lobster transportation is then used to describe the application of Good Transportation Practice (GTP) in the supply chain descriptively

3. DISCUSSION

3.1 Lobster Handling and Application of Good Aquaculture Practice (GAP) at Enlargement Fisherman Level

Handling lobster at the level of enlargement consists of five stages. First, enlargement fishermen purchase seeds according to their needs, KJA capacity, and financial capacity. Seeds are purchased from seed catchers in Batunampar, Awang, Bumbang and Gerupuk areas. Enlargement fishermen who lack capital can also buy seeds in the reservoir. The consequence of the purchase in the container is the sale after harvest must be carried out in the same container. Next, the seeds purchased were kept in one hole measuring 6x3x3 m³ for two months. Enlarged fishermen call this process a quarantine process before being stocked into a maintenance pit. Seedlings are given one glass of 220 ml rebon shrimp feed. Feeding is done once, morning or evening. The average number of seeds maintained in one KJA unit reached 694.

Furthermore, the seeds that have been quarantined for 2 months are sorted first. Sort it so that the lobsters that are stocked in the maintenance pit are uniform in size and do not have a striking difference. The lobster is then stocked into a 3x3x3 m³ maintenance hole. Maintenance is carried out separately with a stocking density of 100 - 125 tails. The feed given at this stage of maintenance is trash fish cut to a size of 1-2 cm. The size of the pieces of trash fish is adjusted to the size of the lobster that is increasing every month. An alternative feed for lobster if there is no trash fish is a rice slug. Feeding is done twice a day, in the morning or evening. Some fishermen also provide feed once a day.

Harvesting is carried out after 12 months of maintenance starting from the purchase of seeds. Harvesting can be done by enlarging fishermen or collectors who buy lobsters. The harvesting process at KJA by container is sorting, stunning,

weighing and packaging. Direct purchase by the container makes it easier for fishermen to enlarge in selling their crops and the quality is more maintained. Harvesting carried out by fishermen enlargement has the disadvantage that lobster is only placed in a plastic bucket container during distribution to the container. The entire process carried out by fishermen enlargement is shown in Figure 1.

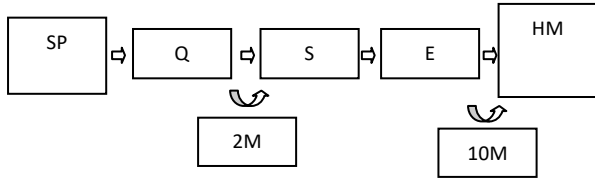


Figure 1 Process carried out by lobster enlargement fishermen

Image Description:

- SP : Seed procurement
- Q : Quarantine
- S : Sorting
- E : Enlargement
- HM : Harvesting and marketing
- 2M : Two month process
- 10M : Ten month process

The application of Good Aquaculture Practice (GAP) to lobster enlargement is very important to maintain the quality of lobster. The application of GAP to fishermen enlargement in Lombok is still quite a lot of non-conformity. The results of the assessment of nonconformities are shown in Table 1. Nonconformities in fishing enlargement consisted of 14 minor deviations and 16 major deviations.

Table 1. Incompatibility handling on enlargement fisherman

SNI	Real Condition
Minor The cultivation business unit is in a suitable environment where the risk of food safety from chemicals, biological and physical is minimized Cultivation units have good water sources and supply water is protected from pollution sources Feeding is carried out in efficiency according to the recommended dosage Feed labeled / has information that includes the composition, expiration date, dosage and method of administration clearly in Indonesian Harvesting is well prepared to avoid the influence of high temperatures At harvest time, efforts are made to avoid deterioration and contamination Handling of fish is carried out hygienically and efficiently so as not to cause physical damage The dead product is	Business units still exist in inadequate waters Water sources directly from the waters where some are vulnerable to pollution Feeding is sometimes less than needed The dominant feed is obtained from nature in the form of trash fish Harvesting is done improbably Some fishermen harvest without any effort to avoid quality degradation and contamination Handling is still less hygienic and efficient

immediately cooled and the temperature is close to 0 ° C in all parts The product temperature during transport is close to temperature (13 ° C - 15 ° C) in all parts of the product Live lobsters are handled and maintained in conditions that do not cause physical damage or contamination Recorded the type and origin of feed (manufacturer's feed) and raw materials for fish (for homemade feed) Record keeping of use of fish drugs, chemicals and biological materials or other treatments during the maintenance period Record water quality (source water, supply water, maintenance water and liquid waste) as needed Record keeping of disease events that might have an impact on food safety of fishery products Major The cultivation business unit has a design and layout that can prevent cross contamination Toilets, septic tanks, warehouses and other facilities are separate and do not have the potential to contaminate aquaculture products The cultivation unit has a liquid or solid waste disposal facility that is placed in the appropriate area Efforts to filter water or settling are carried out and ensure the quality of water that is suitable for cultivated fish Monitor source water quality regularly to ensure the quality of water that is suitable for cultivated fish The seeds are stocked in healthy conditions and come from certified hatchery units and do not contain dangerous diseases or fish medicine. Fish feed used has a registration number / certificate issued by the Director General or a guarantee letter from a competent institution Medicines for fish, chemicals and biology are stored properly according to specifications.	No temperature drop is approached to close to 0 ° C Some fishermen carry out transportation without trying to maintain temperature It still allows physical damage There is no recording of the type and origin of raw materials No storage of records of drugs, chemicals and other biological materials is carried out There is no water quality record There are no records of disease events The design and layout still allows cross contamination Toilet and warehouse are not separate Do not have liquid or solid waste disposal facilities Water directly from the waters Water quality monitoring is not carried out Seeds not certified Direct food is obtained from nature No storage is carried out according to specifications Tests are not carried out to detect drug and chemical residues Ice is not from an approved
---	---

<p>Tests are carried out to detect drug and chemical residues below the threshold Ice only comes from approved suppliers and uses drinking water / clean water Equipment and equipment are easy to clean and maintain in clean and hygienic conditions Equipment and equipment for handling results are easy to clean and disinfect (if necessary) and always kept clean Equipment and transportation facilities used are easy to clean and always be kept clean (boxes, containers, etc.) Waste (liquid, solid and dangerous) is managed (collected and disposed of) in a hygienic and sanitary manner to prevent contamination Corrective actions (on the danger of food safety) are carried out as routine and controlled activities. The corrective action is carried out correctly and immediately according to the problem found. Owners of business units or conscious and trained workers (training, seminars, workshops, outreach, etc.) in preventing and controlling food safety hazards in aquaculture.</p>	<p>supplier</p> <p>Poor maintenance of equipment</p> <p>Poor maintenance of equipment</p> <p>Transportation equipment is poorly maintained</p> <p>Waste is discharged directly into the water</p> <p>There are no routine corrective actions</p> <p>The owner is not trained in preventing and controlling food safety hazards</p>
---	--

3.2 Lobster Handling And Implementation of Good Handling Practice (GHP) at Catcher Fisherman Level

Handling lobster at the fishing catcher level is done simply. Handling is carried out, namely: handling before arrest, handling during arrest, and handling post-arrest. Handling before the arrest is done is the preparation and inspection of equipment. Next, handling when catching is done when removing the net at a depth of 25-40 meters. The net is released in a circle around the coral reef. Then the catch is brought up and placed in styrofoam containers containing fine sand. The catch collected in styrofoam is distributed to reservoirs by land.

The application of Good Handling Practice (GHP) in lobster fishing in Lombok is very important to maintain the quality of lobsters. Lobster that has good quality will provide more benefits than lobster that is less qualified. The incompatibility of GHP implementation with catching fishermen is shown in Table 2. Deviations carried out by lobster fishermen in Lombok consist of 5 major deviations, and some aspects that are not available in terms of ship design and layout. This is because most lobster catchers use small capacity boats or

boats. Lack of capital causes fishermen not to be able to buy or rent larger vessels.

Table 2. Incompatibility on catcher fisherman

SNI	Real Condition
<p>Minor (Not Available) Ship space used for direct contact has a design that can prevent contamination. Awake handling design of disease-spreading animals Walls and floors are made of material that is smooth, does not absorb water and is easy to clean The ship is designed so that laundry waste flows directly into the sea and there is no hot water Minor Equipment consists of: container (hatch or insulated box), aerator, salinometer, thermometer, water pump. All equipment and equipment used in handling live lobsters have a smooth and flat surface, do not peel, do not rust, do not constitute a source of contamination of microorganisms, are not cracked and are easy to clean. Measurement of clean seawater parameters according to the parameters of live lobster media Salinity and temperature of water are maintained according to lobster habitat The number of lobsters is adjusted to the capacity of the container</p>	<p>Has no design that can prevent contamination</p> <p>It still allows interference from disease-spreading animals Does not have a design as specified in SNI</p> <p>Do not have a sewage disposal system</p> <p>Sometimes it is not equipped with a salinometer, thermometer, aerator and water pump Less attention to the surface of the equipment used</p> <p>No measurements are taken</p> <p>Lack of maintaining water temperature and salinity Less attention to container capacity</p>

3.3 Handling of Lobster and Application of Good Handling Practice (GHP) at Container Level

The container in Lombok has implemented GHP well. This condition should be maintained and developed so that lobster containers in Lombok can directly export lobster. The results of the assessment of nonconformities in containers are shown in Table 3.

Table 3. Incompatibility on container

SNI	Real Condition
<p>Minor The shelter business unit has a design and layout that can prevent cross contamination Major Shelter business units have liquid or solid waste disposal facilities placed in the appropriate area</p>	<p>The design and layout still allows cross contamination</p> <p>Disposal directly to the coast or waters around the shelter</p>

The container gets the lobster in two ways, namely: first, the lobster is delivered directly to the shelter by fishermen catching or fishing enlargement, the container also gets lobster by coming directly to harvest with the owner of KJA. Handling in both ways of getting lobster supplies is no different.

Handling carried out by container consists of several stages, namely: sorting, stunning, weighing, packaging, and distribution of sales. Sort is done to find out the number of lobsters with different types. Separation of lobster based on the type is based on the desire of the customer. Stunning is done by placing lobster in a plastic container filled with water. The water temperature is lowered slowly to 10-15 ° C. The lobster is soaked for 15 minutes until it faints. Fainting lobsters are dried with fine sand. Then the lobster is weighed and packaged using newspaper and then placed in styrofoam containers with a capacity of 18-20 kg. Styrofoam is equipped with ice cubes which are packed with plastic bottles and placed in all four corners. The styrofoam cover is glued with duct tape and then weighed. Next styrofoam is given a label to mark the contents of the type, weight and origin and destination of lobster delivery.

The results of the general assessment of nonconformities in the three main lobster supply chain actors are shown in Table 15. The application of GAP at the level of fishery enlargement is included in the fairly good category. The application of GHP at the catcher level is included in the fairly good category. The container is included in the very good category in the application of GHP.

3.4 Good Transportation Practice (GTP) In Lobster Supply Chains in Lombok

The application of Good Transportation Practice (GTP) is needed in every process of transferring lobster from one actor to the next. The application of GTP at the catcher level is quite good because lobsters are packed using styrofoam and given coolers in the form of ice cubes in a bottle container measuring 1.5 L. The application of GTP at the fishing level enlargement still needs improvement. Transporting lobsters to containers using inadequate equipment is still found in Lombok. Poor transportation only uses plastic containers which are sometimes not closed. Handling during this kind of transportation is found when enlargement fishermen sell not much. If sales are carried out in large quantities, the container will take directly to KJA.

Transportation carried out by containers has implemented good GTP. The procedure used has followed SNI 4488.2: 2011 and SNI 4488.3: 2011. Packaging is done with Styrofoam which has been given ice cubes so that it stays cool during transportation. The amount of ice cube used during

transportation is 4 bottles of drinking water measuring 1.5 L in each corner of Styrofoam. The capacity of each styrofoam reaches 18-20 kg with the number of lobsters 72-85 tails with an average weight of 200-250 gr.

The delivery time from the container location to the airport is around 1 hour. Shipping using ordinary cars without special insulation. The time during shipping on the plane takes 1-2 hours.

4. CONCLUSION

The application of Good Aquaculture Practice (GAP) at the level of enlargement fisher and Good Handling Practice (GHP) at the level of catchers is included in category C or quite well. In the same case the collectors level is in category A or very good. The application of *Good Transportation Practice* (GTP) in lobster supply chain in Lombok is quite well. However, improvements in the application of GAP, GHP, and GTP are required. Improvement in GTP is included in improvement of GAP and GHP.

5. ACKNOWLEDGMENTS

Our thanks to all sponsor for this research.

6. REFERENCES

- [1] [BSN] Badan Standardisasi Nasional. 2011. SNI 4488.2:2011. Lobster (*Panulirus spp*) hidup untuk konsumsi-bagian 2: persyaratan bahan baku. Jakarta (ID): BSN.
- [2] [BSN] Badan Standardisasi Nasional. 2011. SNI 4488.3:2011. Lobster (*Panulirus spp*) hidup untuk konsumsi-bagian 3: penanganan. Jakarta (ID): BSN.
- [3] [BSN] Badan Standardisasi Nasional. 2013. SNI 7792:2013. Penanganan ikan di atas kapal – lobster hidup (*Panulirus spp*). Jakarta (ID): BSN.
- [4] Jones CM, Long NV, Hoc DT, Priyambodo B. 2010. Eksploitation of puerulus settlement for the development of tropical spiny lobster aquaculture in the Indo-West Pacific. *J Mar Biol*. 52(2):292-303.
- [5] [KKP] Kementerian Kelautan dan Perikanan. 2007. Keputusan Menteri Kelautan dan Perikanan Republik Indonesia Nomor KEP.02/MEN/2007 tentang Cara Budidaya yang Baik. Jakarta (ID): KKP.
- [6] [KKP] Kementerian Kelautan dan Perikanan Republik Indonesia. 2012. Statistik ekspor hasil perikanan 2011 buku I. Jakarta (ID): KKP.
- [7] Putro S. 2008. Peran mutu dalam menunjang ekspor udang nasional. *Squalen*. 3(1): 1-6.
- [8] Ritchey, Tom. 2013. Morphological Gap-Analysis Using GMA to Find The Delta. *Acta Morphologica Generalis*. 2(2).

Design of Runner for Cross-Flow Turbine (10 kW)

Khin Swe Swe Latt
Lecturer
Department of Mechanical
Engineering,
Technological University
(Thanlyin),
Yangon, Myanmar

Cho Nwe Tun
Lecturer
Department of Mechanical
Engineering,
Technological University
(Thanlyin),
Yangon, Myanmar

Khin Nwe Zin Tun
Lecturer
Department of Mechanical
Engineering,
Technological University
(Thanlyin),
Yangon, Myanmar

Abstract: Electricity demand is increasing worldwide. Water power is one of the major sources of energy. In hydro power plants, water turbine is one of the most important parts to generate electricity. This runner of Cross-flow, Banki-Mitchell turbine is designed to produce 10kW electric power from head of 14m and the flow rate of 0.123 m³/s. For the given capacity, the dimensions of turbine diameter and width are 150 mm and 320 mm. According to these data, the important part of cross-flow turbine runner can be constructed.

Keywords: runner, microhydro-power, flow rate, cross-flow turbine,

1. INTRODUCTION

The hydroelectric power generation is the availability of a source of water with a very large amount of hydraulic energy. Hydropower is a clean, domestic and renewable source of energy. Hydropower plants provide inexpensive electricity and produce no pollution. Hydropower requires no fuel and the machine to produce is much simpler, and also simple to operate and maintain. The other sources of energy being developed by the fuels such as coal, oil etc, and nuclear power are used for energy. Hydropower development is essential to utilize the hydraulic power proceed by the water flowing in a stream and to develop from it electric power through water turbines coupled to electric generators. The Cross-Flow turbine is primarily impulse type. In the cross-flow turbine, the flow enters the runner from its circumferential direction, passes inside the runner and again passes through the runner blades toward the opposite direction before leaving the runner.

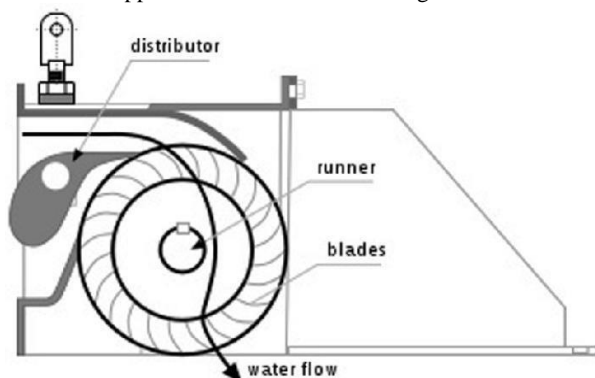


Figure.1 Working Principle of Cross-flow turbine

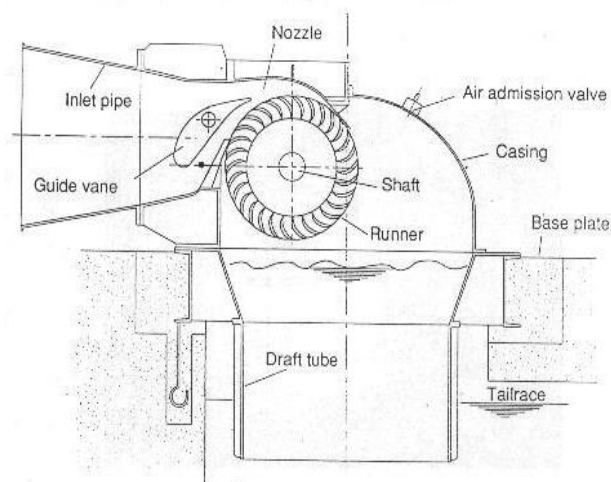


Figure.2 Cross-flow turbine

Also called a Michell-Banki turbine a cross-flow turbine has a drum-shaped runner consisting of two parallel discs connected together near their rims by a series of curved blades. A cross-flow turbine always has its runner shaft horizontal. In operation a rectangular nozzle directs the jet onto the full length of the runner. The water strikes the blades and imparts most of its kinetic energy. It then passes through the runner and strikes the blades again on exit, impacting a smaller amount of energy before leaving the turbine. High part-flow efficiency can be maintained at less than a quarter of full flow by the arrangement for flow portioning. At low flows, the water can be channeled through either two-thirds or one third of the runner, thereby sustaining relatively high turbine efficiency.

2. DESIGN CONSIDERATION OF RUNNER

The cross-flow turbine is primarily impulse type, the optimal speed of the runner primarily determined by the head. The runner speed of the cross-flow type is low as compared with other turbines. The heart of the turbine is the runner and is responsible for the conversion of water energy into mechanical energy. Cross-flow turbine runner is a cylindrical in shape with a long in axis direction and is built up of two parallel circular disks joined together at the rim with a series of curved blades as shown in Figure 2. Runner design is very critical for achieving good overall performance of the turbine.

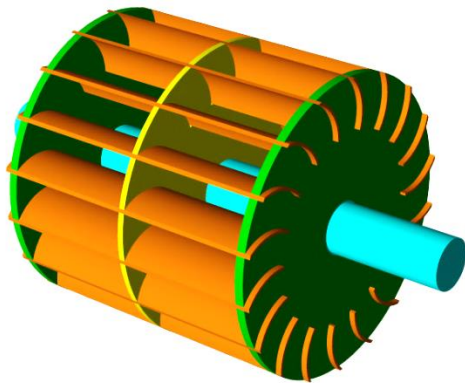


Figure.3 Cross-flow turbine runner[5]

The diameter of the runner is an important and basic factor for the design of the runner. It can be determined from the speed and water head. From the turbine speed, generator can be selected depending on the synchronous speed. In this paper, the inlet flow angle to the wheel is taken as 16° according to obtain the maximum efficiency. When considering the design of runner, the curvature of the blade, inlet blades angle, the value of pitch and the thickness of the runner. A cross-flow turbine has its runner shaft horizontal to the ground in all cases. Shaft transfers the generated torque to the generator or alternator. Bearing function is to hold the shaft rigidly on its position. At the same time it reduces the resistance to the rotation of the shaft and absorbs the axial forces on it. It includes one or two guide vanes depending on the inlet width. The function of the guide vane is to adjust and shut-off the water flow into the runner. A turbine with large maximum discharge has two guide vanes. The vanes lengths are $1/3$ and $2/3$ of the inflow width, respectively. When the discharge is small, only the shorter vane is used.

3. DESIGN CALCULATION OF CROSS-FLOW TURBINE RUNNER

The required design data for 5kW cross-flow turbine are as follow;

Net head, $H = 14$ m

Discharge, $Q = 0.123$ m³/s

Generator output, $P_G = 95\%$ of turbine output

Overall efficiency, $\eta_o = 0.65$

Design of water, $\rho = 1000$ kg/m³

Gravity, $g = 9.81$ m/s²

The required discharge can be calculated,

$$P = \rho g Q H \eta_o$$

The total area of jets can be calculated,

$$V_1 = C_v \sqrt{2gH}$$

$$A = Q/V$$

The periphery velocity is $u = \pi DN/60$,

the range of specific speed for the cross-flow turbine is 40 to 200.

The number of blades ranges between 20 and 33. When the number of blades is increased, the manufacturing difficulties for small workshops become progressively more serve.

For this design, the specific speed is assumed $N_s = 80$ to calculate the rotational speed,

$$N_s = \frac{172.556}{H^{0.425}}$$

Where the wheel rotation is taken 400 rpm, thus the diameter of runner can be calculated as follows;

$$D_1 = \frac{60u}{\pi N}$$

So, Above the equation the runner diameter is used 25 mm.

Outer diameter of runner,

$$R_1 = D_1/2$$

Inner Radius ,

$$R_2 = 2 \times \frac{D_1}{3} \times \frac{1}{2}$$

Therefore, 28 blades are chosen for this design. Outer diameter D of runner is the basic parameter for design. Diameter of the blade stands for its inner surface. In this design, thickness of blade can be chosen 3.2 mm.

\therefore the radius of blade shaped arc is 0.04 m.

$$\text{So, } r = 0.16 D_1$$

The radial rim width (a) was graphically ascertained from the intersection of the two curves.

$$a = R_1 - R_2$$

The diameter of the shaft can be calculated as follow,

$$d_s = 150 \sqrt[3]{\frac{P}{N}}$$

So the diameter of the shaft is used 35 mm.

4. RESULT OF RUNNER CALCULATION

This table shows the calculated result for runner using above equation.

Table 1
Calculated result for 10kw cross-flow turbine for
micro-hydro power plant

No.	Name	Symbol	Result (m)
1.	Outer radius of runner	R_1	0.75
2.	Inner radius of runner	R_2	0.05
3.	Diameter of runner	D	0.15
4.	Width of runner	B	320
5.	Radius of curvature	r	40
6.	Radial rim width	a	0.105
7.	Shaft diameter	d_s	0.249

- [4] Modi, P.N., and Seth, S.M. 1982. Hydraulics and Fluid Mechanics. 5th Edition, University of Roorkee.
- [5] Robert, L.Mott, P.E. 1985. Machine Elements in Mechanical Design. University of Dayton.
- [6] [http:// www.waterturbine.com](http://www.waterturbine.com)
- [7] [http:// www.microhydropower.net/turbine.html](http://www.microhydropower.net/turbine.html)
- [8] <http://www.home.carolina.rr.com/microhydro/turbine.html>

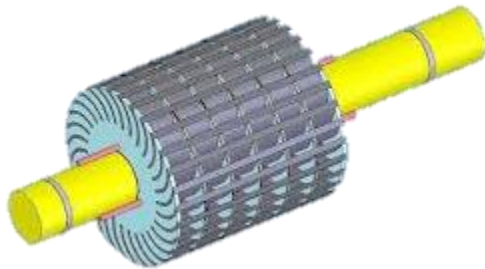


Figure.4 Two Dimensional Drawing

5. CONCLUSION

Water energy is renewable sources suitable technology needs to obtain these natural resources. In hydropower plant, turbine is one of the most important parts to generate electricity Cross-flow turbine is the best for low head to generate electricity. This type of turbine will be useful for micro hydro project because different sizes of turbine can be constructed easily for different kinds of require power. In this study, cross-flow turbines was designed a runner of 10 kW for micro-hydropower plant. The cross-flow turbine designed for 14 m of head and 0.53 m³/s of flow rate to generate 10 kW. The diameter of the runner is 150 mm and length is 320 mm. For that turbine, a synchronous generator 6 pole is used with direct coupling. The attack angle at the runner is taken as 16 degree to get optimal efficiency. The number of blade is 28 and thickness is 3.2 mm, depending on the runner diameter.

6. REFERENCES

- [1] L.A.Haimeral., 1956 The cross flow turbine. Deutche Miller-Zeitung.
- [2] Seiroku Sajiki, Hitoshi Yamamoto., 1983. "Commercialization of Cross-Flow Hydraulic Turbines and Their Power Generating Systems", series No.68, No.2.
- [3] Allen R. Inversin, 1986. Micro Hydropower Source Book.

Design of Impeller for Centrifugal Compressor

Khin Swe Swe Latt
Lecturer
Department of Mechanical
Engineering,
Technological University
(Thanlyin),
Yangon, Myanmar
khinswe2latt77@gmail.com

Cho Nwe Tun
Lecturer
Department of Mechanical
Engineering,
Technological University
(Thanlyin),
Yangon, Myanmar
chonwehtun229@gmail.com

Khin Nwe Zin Tun
Lecturer
Department of Mechanical
Engineering,
Technological University
(Thanlyin),
Yangon, Myanmar
khinnwezintun@gmail.com

Abstract: This study deals with the flow analysis of centrifugal compressor impeller. The impeller design based on parameters flow analysis using air as the working fluid shows that a 0.162m diameter centrifugal compressor with a blade outlet width of 0.0021m gives a static pressure ratio of 4:1. In this design, the impeller blade have exit angle 65° with inlet blade angle 37.74° . So, this compressor is backward-curved blades. The number of blades having 19 equally spaced vanes with the profile is used to improve compressor efficiency. This is the single stage compressor. Theme of centrifugal compressor is to atomize diesel. So, it can more ignite in combustion chamber.

Keywords: Centrifugal compressor, Impeller, velocity, Diameter, width.

1. INTRODUCTION

Compressor are used in many industrial application. A compressor is a piece of machinery that compresses a fluid, a liquid or a gas that flows in the compressor into greater pressure. Compressors are widely used in construction, power plants, process industry, assembly plant, refineries, air conditioning, and refrigeration, to mention some of the applications. It is a power conversion machines, like pumps and electric motors. Centrifugal compressors are second only to reciprocating compressor in services. However, the centrifugal compressor established its hold on the market in an era of cheap energy when power cost was rarely evaluated. This compressor has been around for quite a long time. Originally, it was used in process applications at relatively low-pressure, high-volume services.

Centrifugal compressor used in small gas turbines. These compressors are the driven units in most gas turbine compressor trains. The function of a compressor is to admit vapor from a low pressure region, compress it and deliver it to high pressure region.

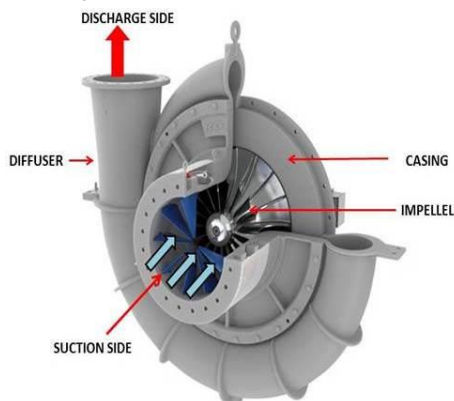


Figure.1 centrifugal compressor

Centrifugal compressor consists of a stationary casing containing an impeller that imparts a high velocity to the air

and a number of diverging passages, in which air is decelerated with a consequent rise in static pressure. The centrifugal compressor is designed for the most demanding applications where a reliable air supply is required. It is perfect for automotive, commercial and industrial applications. The maximized operating pressure, increased air flow, and extended duty cycle are required.

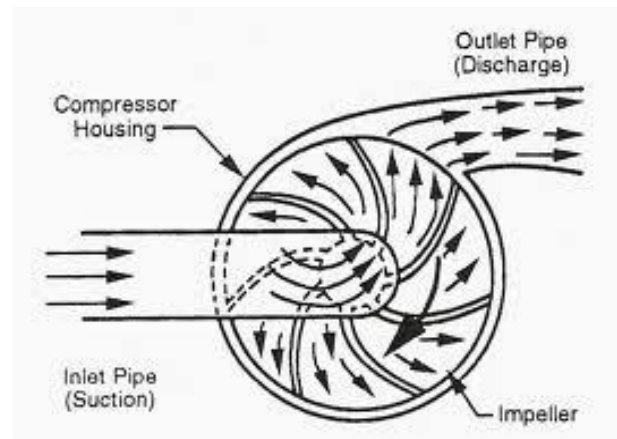


Figure.2 Working Principle of centrifugal compressor

Advantages of the Centrifugal compressor are that it is longer service life than other rotaries and it can often increase the pressure enough for efficient combustion with only one stage. But higher initial cost and air flow is sensitive to change in ambient conditions. However, the airflow for a Centrifugal compressor is much lower than for an axial, and its pressure ratio is generally lower than axial compressor and it is much less effective for creating thrust and less fuel efficient. Hence, it is more often seen in small engines. Centrifugal compressors have two functions: single and multistage.

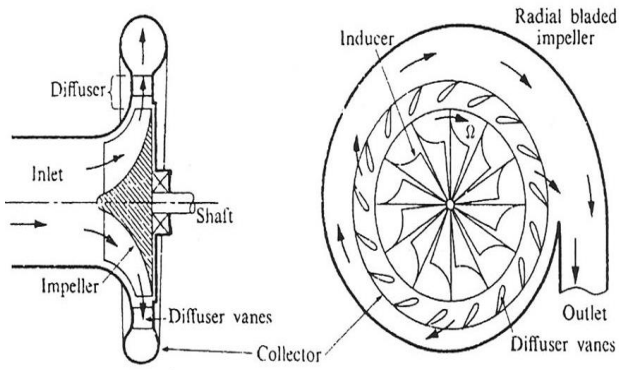


Figure.3 Component of centrifugal compressor

2. SPECIFICATION DATA

Inlet pressure , P_1	= 1030.766 kPa
Inlet temperature , T_1	= 380 K
Rated speed , N	= 45561 rpm
Outlet pressure , P_2	= 1799.6 kPa
Outlet temperature , T_2	= 448 K
Capacity , Q	= 0.1275 m ³ /s
Air mass flow rate , m°	= 1.5907 kg/s
Shaft diameter , D_s	= 0.0254 m
Hub diameter , D_h	= 0.028m
Eye diameter , D_o	= 0.053m
Inlet diameter , D_1	= 0.054 m
Outlet diameter , D_2	= 0.17m
Inlet width , b_1	= 0.0098m
Outlet width , b_2	= 0.0025 m
Number of vanes , z	=19

3. FLOW SIMULATION

In this study, the SolidWorks simulation is used to analyze the pressure and velocity distribution of centrifugal compressor impeller. The first step of simulation is the user would work with a impeller assembly model in SolidWorks, accessing SolidWorks flow simulation via a menu heading in SolidWorks and follow these steps. The Wizard is selected from the SolidWorks flow simulation menu and firstly chooses the configuration for the analysis as well as the unit system requirement. To determine the boundary condition at inlet and outlet of impeller cover, the inlet boundary condition is the inlet mass flow rate and outlet boundary condition is the discharge pressure. Next, choose the working fluid, which in this case is air. The program has a library of commonly used liquids and gases from which to choose. Finally select the resolution of result on a scale from one to eight. The higher the number, the more refined the mesh will be and the more accurate the results.

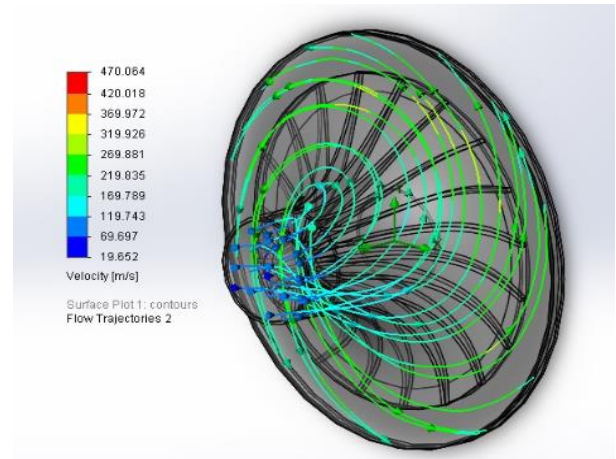


Figure.4 Velocity distribution of centrifugal compressor impeller (flow trajectories)

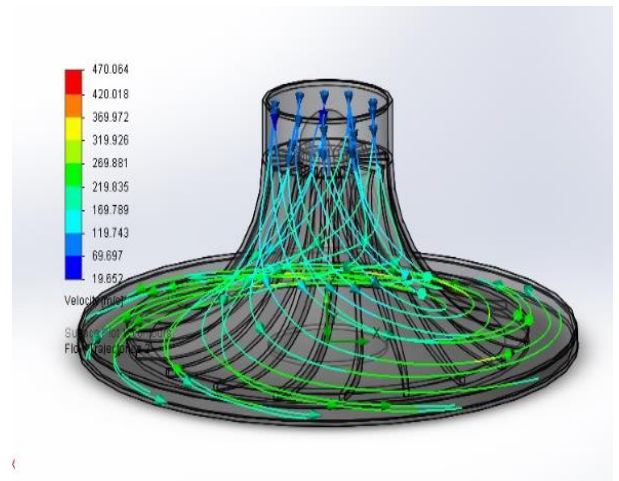


Figure.4 Velocity distribution of centrifugal compressor impeller (flow trajectories- side view)

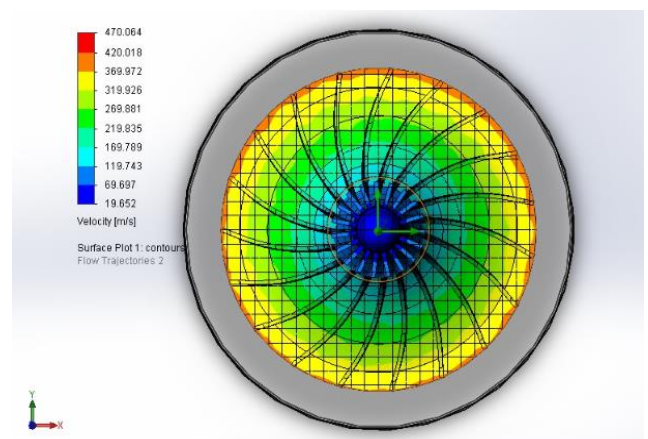


Figure.5 Velocity distribution of centrifugal compressor impeller (surface plots - top view)

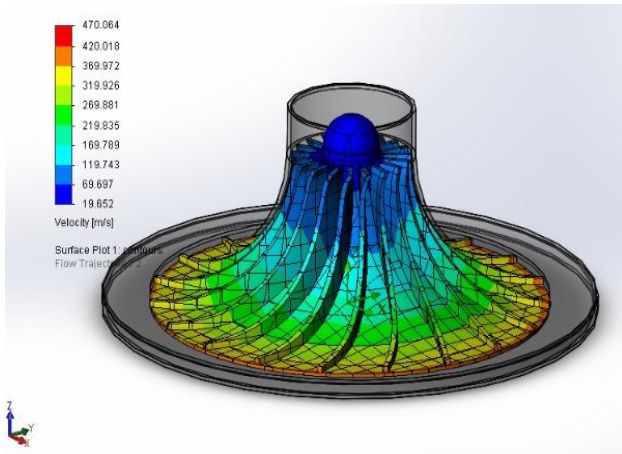


Figure.6 Velocity distribution of centrifugal compressor impeller (surface plots - side view)

Figure 4, 5 and 6 illustrate the velocity distribution of centrifugal compressor impeller by using SolidWorks software. The inlet boundary condition is the inlet mass flow rate. The value of inlet mass flow rate is 1.5907 kg/s. The outlet boundary condition is the outlet pressure. The value of outlet pressure is 1799.595 kPa. The theoretical result of impeller inlet velocity V_1 is 117.566 m/s and outlet velocity V_2 is 338.664 m/s. The numerical result of inlet velocity rate is 69.697 to 119.743 m/s and outlet velocity rate is 319.926 to 369.972 m/s. So, theoretical result of impeller inlet and outlet velocity are nearly the same with numerical result.

4. CONCLUSIONS

Centrifugal compressors are compressible flow machine. Centrifugal compressor used in small gas turbines. This study can also be improved to gain a better understanding of the relationship between velocities and blade shape by using suitable theory. This research can support the production of centrifugal compressor impeller. Moreover, the flow simulation procedure is described in detail. . And this study shows the velocity distribution by using SolidWorks software. The existing value of impeller inlet and outlet flow are nearly equal with numerical research value.

5. REFERENCES

- [1] Baliye, O.E: Turbomachines. New York: John Wiley and Sons, Inc., 1981.
- [2] Ronald P. Lapina P>E. Estimating Centrifugal Compressor Performance Process compressor thchnology. Vol-1. McGraw Hill Publications Co,1982
- [3] Ebara Hatakeyama Memorial Fund: Compressor Engineering. U.S.A. John Wiley and Sons, Inc., 1992.

- [4] Meherwan, P. Boyce: Gas Turbine Engineering Handbooks, Part-II.2nd.Ed., New Delhi: Gulf Professional Publishing Co.,2002.
- [5] Rama S.R.Gorla, Turbomachinery Design and Theory,Cleveland State University,Cleveland,Ohio, U.S.A 2003.
- [6] Akhtar, M.S.2001. Selection and Optimization of Centrifugal Compressor for oil gas applications, February 2007

Traffic Flow Theory for One Dimension and Formation of Shock Speed

Wah Wah Aung
Department of Engineering
Mathematics
Technological University
(Thanlyin)
Myanmar

Mya Thida Hlaing
Department of Engineering
Mathematics
Technological University
(Thanlyin)
Myanmar

Zaw Min Tun
Department of Engineering
Mathematics
West Yangon Technological
University (Hlaing Tharyar)
Myanmar

Abstract: This paper presents the necessary background on traffic flow theory and the existing macroscopic mathematical models for single-lane, one-dimensional space traffic flow. The derivation of traffic flow theory based on conservation of mass and the relationships between velocity and density are presented. The exact and weak solutions to the scalar traffic flow Partial Differential Equation, and the shock wave, rarefaction wave, and the admissibility of a solution are considered.

Keywords: Conservation Laws, Boundary Conditions, Traffic Flow, Weak Solutions. Car Following Model.

1. INTRODUCTION

In traffic flow problem, nonlinear hyperbolic conservation laws have been studied for many years. Traffic flows are classified according to traffic conditions, roadway conditions and traffic network structures. Traffic flows are considered inhomogeneous when the roadway has different parameters at different locations. A mathematical model for fluid dynamic flows on road networks is based on conservation laws. In this paper, we considered the first order traffic flows model. The first order model is based on the conservations of cars and is described by a single equation in conservation form. The main assumption of the car following models is that an individual car's motion only depends on the car ahead. As traffic jams display sharp discontinuities, there is a correspondence between traffic jams and shockwaves. We used the conservation laws model on the roads with time varying traffic distribution coefficients. In order to obtain a unique solution of the Riemann problem at junctions, we need to assume some rules, so we can construct solutions via wave-front tracking technique. To describe a road network as a finite collection of roads meeting at some junctions that play a key role, since the system at a junction is under-determined even after imposing the conservation of cars. Traffic models are represented by minimization of congestions, accidents, pollution, and the maximization of safety. Shock and rarefaction waves are the basic solutions to a Riemann problem for such a conservation law.

The paper is organized as follows. In section 2, the model for traffic flow on a road network is described. Section 3 deals with weak solutions, scalar Riemann problem and Numerical Method use for the traffic flow problem. Finally we discuss the shock formation.

2. VELOCITY FIELD

Consider a car moving along a highway. Since there is no passing and cars cannot move through each other, the order of the cars is preserved, although they can move at slightly different speeds. Let the velocity of car " i " be v_i . If the x -axis coincides with the road and position of this car is $x_i(t)$ at time t , then

$$v_i(t) = \frac{dx_i}{dt}, \quad i=1,2,\dots, N,$$

with N cars there are different velocities, $v_i(t)$, $i=1,\dots, N$, each depending on time.

3. TRAFFIC DENSITY

Traffic density $\rho(x, t)$ is the average number of cars per unit length at the position x and time t . The flow can be written as

$$f(x, t) = \rho(x, t)v(x, t), \quad (1)$$

where ρ is the density of cars, V is the mean velocity and f is the traffic flow.

As the density increases, the velocity of cars diminishes. Thus we make the hypothesis that the velocity of cars at any point of the road is a strictly decreasing function of the density:

$$v = v(\rho).$$

If there are no other cars on the highway, then the car would travel at the maximum speed V_{\max} ,

$$v(0) = v_{\max}.$$

V_{\max} is sometimes referred to as the "mean free speed" corresponding to the velocity cars would travel if they were free from interference from other cars. At a certain density cars stop before they touch to each other. The maximum density ρ_{\max} , usually corresponds to what is called bumper-to-bumper traffic:

$$v(\rho_{\max}) = 0.$$

In our case the flux is the following

$$f(\rho) = v_{\max} \rho \left(1 - \frac{\rho}{\rho_{\max}} \right),$$

where we set for simplicity $\rho_{\max} = 1 = v_{\max}$, thus it reads:

$$f(\rho) = \rho(1 - \rho).$$

4. CAR FOLLOWING MODEL

To derive the one-dimensional model, first assume cars cannot pass each other. Then the idea is that a car in one-dimension can move and accelerate forward based on two parameters; the headway distance between the current car and the one in front, and their speed difference. Hence, it is called car following, where a car from behind follows the one in front, and this is the anisotropic property. Suppose the n^{th} car location is $x_n(t)$, then the nonlinear model is given by

$$\ddot{x}_n(t) = c \frac{\dot{x}_n(t) - \dot{x}_{n-1}(t)}{x_n(t) - x_{n-1}(t)}. \quad (2)$$

The acceleration of the current car $\ddot{x}_n(t)$ depends on the front car speed and location, c is the sensitivity parameter. Integrating the above yields

$$\dot{x}_n(t) = c \ln(x_n(t) - x_{n-1}(t)) + d_n.$$

Since by the definition of the density (number of cars per unit area)

$$\frac{1}{\rho(x,t)} = x_n(t) - x_{n-1}(t), \quad (3)$$

and the integration constant d_n is chosen such that at jam density ρ_{\max} , the velocity is zero. Then for steady-state we get

$$v = -c \ln \frac{\rho}{\rho_m}. \quad (4)$$

It can be seen that $\rho \rightarrow 0$ traffic densities are low, car speed is the maximum allowed speed, hence we can assume $v = v_{\max}$, which is the maximum allowed speed.

4.1 Traffic Flow

The average number of cars passing per time unit is called the traffic flow $f = f(x, t)$. Suppose there is a road with cars moving with constant velocity v_0 , and constant density ρ_0 such that the distance between the cars is also constant as shown in the Figure. 1(a). Now let an observer measure the number of cars per unit time t that pass him (i.e. traffic flow f). In t time, each car has moved $v_0 t$ distance, and hence the number of cars that pass the observer in t time is the number of cars in $v_0 t$ distance, see in Figure. 1(b).

Since the density ρ_0 is the number of cars per unit area and there is $v_0 t$ distance, then the traffic flow is given by

$$f = \rho_0 v_0. \quad (5)$$

This is the same equation as in the time varying case,

$$f(\rho, v) = \rho(x, t) v(x, t). \quad (6)$$

To show this, we consider the number of cars that pass point $x = x_0$ in a very small time Δt . In this period of time the cars have not moved far and hence $\rho(x, t)$ and $v(x, t)$ can be approximated by their constant values at $x = x_0$ and $t = t_0$. Then, the number of cars passing the observer occupies a short distance, and they are approximately equal to, $\rho(x, t) v(x, t) \Delta t$ where the traffic flow is given by Equation 6.

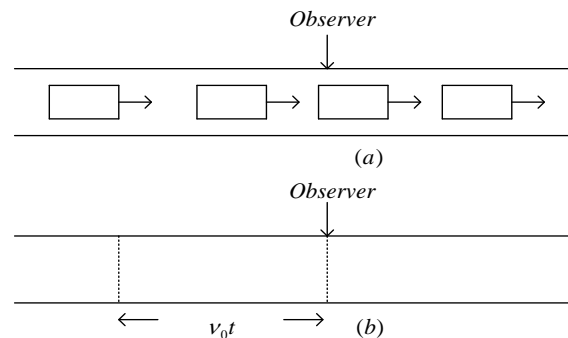


Figure .1 (a) Constant Flow of Cars

(b) Distance Traveled in Hours for a Single Car t

4.2 Conservation Law

The models for traffic, whether they are one-equation or system of equations, are based on the physical principle of conservation. When physical quantities remain the same during some processes, these quantities are said to be conserved. Putting this principle into a mathematical representation will make it possible to predict the densities and velocities patterns at future time. In our case, the number of cars in a segment of a highway $[x_1, x_2]$ is our physical quantities, and the process is to keep them fixed (i.e., the number of cars coming in equals the number of cars going out of the segment). Consider a stretch of highway on which cars are moving from left to right as shown in Figure 2. It is assumed here that there are no exit or entrance ramps. The number of cars within $[x_1, x_2]$ at a given time t is the integral of the traffic density given by

$$N = \int_{x_1}^{x_2} \rho(x, t) dx. \quad (7)$$

The number of cars can still change (increase or decrease) in time due to cars crossing both ends of the segment. Assuming no cars are created or destroyed, and then the change of the number of cars is due to the change at the boundaries only. Therefore, the rate of change of the number of cars is given by

$$\frac{dN}{dt} = f_{in}(\rho, v) - f_{out}(\rho, v), \quad (8)$$

since the number of cars unit time is the flow $f(\rho, v)$. Combining Equations 7, and 8, yields the integral conservation law

$$\frac{d}{dt} \int_{x_1}^{x_2} \rho(x, t) dx = f_{in}(\rho, v) - f_{out}(\rho, v). \quad (9)$$

This equation represents the fact that change in number of cars is due to the flows at the boundaries. Let the end points are independent variables (not fixed with time), then the full derivative is replaced by partial derivative to get

$$\frac{\partial}{\partial t} \int_{x_1}^{x_2} \rho(x, t) dx = f_{in}(\rho, v) - f_{out}(\rho, v). \quad (10)$$

The change in the number of cars with respect to distance is given by

$$f_{in}(\rho, v) - f_{out}(\rho, v) = - \int_{x_1}^{x_2} \frac{\partial f}{\partial x}(\rho, v) dx, \quad (11)$$

and by setting the last two equations equal to each other, we get

$$\int_{x_1}^{x_2} \left[\frac{\partial \rho}{\partial t}(x, t) + \frac{\partial f}{\partial x}(\rho, v) \right] dx = 0. \quad (12)$$

This equation states that the definite integral of some quantity is always zero for all values of the independent varying limits of the integral. The only function with this feature is the zero function. Therefore, assuming $\rho(x, t)$ and $f(x, t)$ are both smooth, the one-dimensional conservation law is found to be

$$\frac{\partial}{\partial t} \rho(x, t) + \frac{\partial}{\partial x} f(\rho, v) = 0. \quad (13)$$

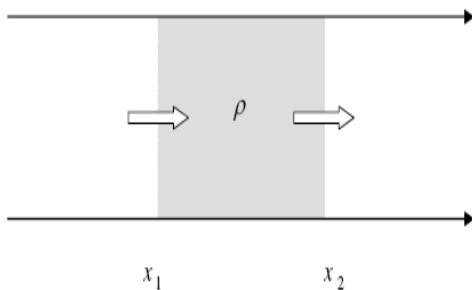


Figure 2. One Dimension Flow

4.3 Weak Solutions

The function ρ is needed to interpret as a solution in a weak sense of the initial-value problem Equation 14. In particular, assume we use method of characteristics to see that even for smooth initial conditions the strong solutions cannot be extended in time indefinitely. In fact, even smooth initial conditions can lead to discontinuous solutions in finite time.

In this case, it can be used test function $\phi \in C_0^1(\mathfrak{R} \times \mathfrak{R})$.

C_0^1 is the space function that are continuously differentiable with compact support. $\phi(x, t)$ is identically zero outside of some bounded set, and so the support of the function lies in a compact set.

$$\left. \begin{aligned} \phi: \mathfrak{R} \times [0, \infty) &\rightarrow \mathfrak{R}, \\ \phi &\in C_0^\infty(\mathfrak{R} \times [0, \infty)), \end{aligned} \right\} \quad (14)$$

by parts and we call ϕ is a test function. Then multiply the equation $\rho_t + f(\rho)_x = 0$ by ϕ and integrate:

$$\begin{aligned} \int_0^{+\infty} \int_{-\infty}^{+\infty} (\rho_t + f(\rho)_x) \phi dx dt \Big|_{t=0} &= 0 \\ - \int_0^{+\infty} \int_0^{+\infty} \rho \phi_t dx dt - \int_{-\infty}^{+\infty} \rho \phi dx \Big|_{t=0} &= 0 \\ - \int_0^{+\infty} \int_{-\infty}^{+\infty} f(\rho) \phi_x dx dt &= 0. \end{aligned}$$

Using the initial condition $\rho(x, 0) = \rho_0(x)$ on $\mathfrak{R} \times \{t=0\}$, we have

$$\int_0^{+\infty} \int_{-\infty}^{+\infty} \rho \phi_t + f(\rho) \phi_x dx dt + \int_{-\infty}^{+\infty} \rho_0 \phi(x, 0) dx = 0. \quad (15)$$

4.4 Scalar Riemann Problem

Scalar Riemann problem is the Cauchy problem for the scalar conservation law where the initial data is a piecewise constant function with only two values. In both cases there will be two different values on both sides of $x=0$ at time $t=0$. In one case the left hand side value will be lower in the other it will be higher than the right hand side value.

The initial value problem

$$\begin{aligned} \frac{\partial}{\partial t} \rho(x, t) + f'(\rho) \frac{\partial}{\partial x} \rho &= 0, \\ \rho(x, 0) &= \rho_0, \end{aligned}$$

with the piecewise constant initial function

$$\rho(x, 0) = \begin{cases} \rho_l, & \text{if } x < 0, \\ \rho_r, & \text{if } x > 0, \end{cases}$$

is called Riemann's problem for the scalar conservation law. $\rho_r, \rho_l \in \mathfrak{R}$ are the left and right initial states, with $\rho_l \neq \rho_r$.

(i) If $\rho_l > \rho_r$, from the lax entropy condition of the for convex fluxes, the unique entropy solution of the Riemann problem is

$$\rho(x, t) = \begin{cases} \rho_l, & \text{if } x < st, \\ \rho_r, & \text{if } x > st, \end{cases} \quad (16)$$

where $x \in \mathfrak{R}$, $t > 0$ and s is given by the Rankine-Hugoniot condition;

$$s = \frac{(\rho_l + \rho_r)}{2} \quad (17)$$

is the shock speed, the speed at which the discontinuity travels

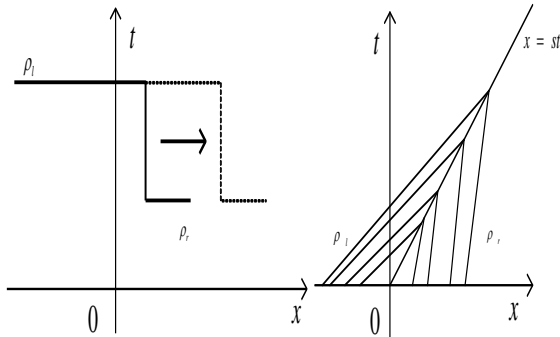


Figure 3. Shock Wave

(ii) If $\rho_r > \rho_l$, the unique entropy solution of the Riemann's problem

$$\rho(x,t) = \begin{cases} \rho_l & \text{if } \frac{x}{t} < f'(\rho_l), \\ (f')^{-1}\left(\frac{x}{t}\right) & \text{if } f'(\rho_l) < \frac{x}{t} < f'(\rho_r), \\ \rho_r & \text{if } \frac{x}{t} > f'(\rho_r), \end{cases} \quad (18)$$

where $x \in \mathbb{R}, t > 0$.

(iii) If $\rho_l = \rho_r$, there exists a unique entropy solution of the Riemann problem, that is the constant state $\rho(x,t) = \rho_l = \rho_r$.

Therefore in each case we can give an explicit expression of the solution of the Riemann's problem.

In the first case the two constant states ρ_l and ρ_r are separated by a shock wave with constant speed s . In the other case the two states are separated by a rarefaction wave. The rarefaction solution is continuous in $\mathbb{R} \times (0, \infty)$. From a physical point of view it corresponds to expansive states of fluids and it is commonly known as the rarefaction wave.

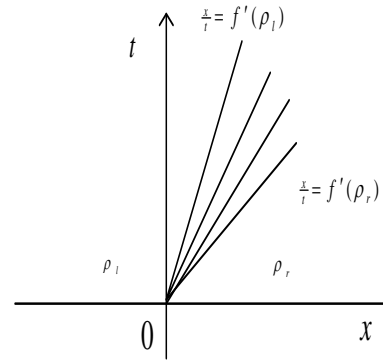
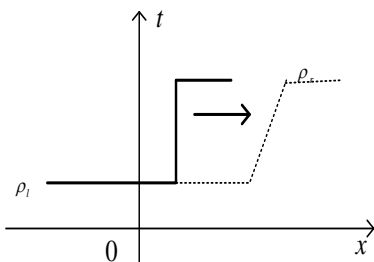


Figure 4. Rarefaction Wave

4.5 Shock Speed

The propagating shock Equation 18 is a weak solution to Burgers' Equation only if the speed of propagation is given by Equation 17. The same discontinuity propagating at a different speed would not be a weak solution. The speed of propagation can be determined by conservation. If M is large compared to st then by Equation.10,

$$\int_{-M}^M \rho(x,t) dx \text{ must increase at the rate}$$

$$\begin{aligned} \int_{-M}^M \rho(x,t) dx &= f(\rho_l) - f(\rho_r) \\ &= \frac{1}{2}(\rho_l + \rho_r)(\rho_l - \rho_r) \end{aligned} \quad (19)$$

$$\begin{aligned} \int_{-M}^M \rho(x,t) dx &= f(\rho_l) - f(\rho_r) \\ &= \frac{1}{2}(\rho_l + \rho_r)(\rho_l - \rho_r) \end{aligned} \quad (20)$$

for Burger's equation. On the other hand, the Equation 16 has

$$\int_{-M}^M \rho(x,t) dx = (M + st)\rho_l + (M - st)\rho_r \quad (21)$$

so that

$$\frac{d}{dt} \int_{-M}^M \rho(x,t) dx = s(\rho_l - \rho_r). \quad (22)$$

For arbitrary flux function $f(\rho)$ this same argument gives the following relation between the shock speed s the states ρ_l and ρ_r , called the Rankine- Hugoniot (R-H) jump condition:

$$f(\rho_r) - f(\rho_l) = s(\rho_r - \rho_l). \quad (23)$$

For a scalar conservation law the shock speed is

$$s = \frac{f(\rho_l) - f(\rho_r)}{\rho_l - \rho_r}$$

$$= \frac{[f]}{[\rho]} \quad (24)$$

where $[\cdot]$ indicates the jump in some quantity across the discontinuity. Note that any jump is allowed, provided the speed is related Equation 24.

For systems of equations, $\rho_l - \rho_r$ and $f(\rho_r) - f(\rho_l)$ are both vectors while S is still a scalar. We cannot always solve for S to make Equation 23 holds. Only certain jumps $\rho_l - \rho_r$ are allowed, those for which the vectors $f(\rho_r) - f(\rho_l)$ and $\rho_l - \rho_r$ are linearly dependent.

For a linear system

$$f(\rho_r) - f(\rho_l) = s(\rho_r - \rho_l), \quad (25)$$

$\rho_l - \rho_r$ must be an eigenvector of the matrix and S is the associated eigenvalue. For a linear system, these eigenvalues are the characteristic speeds of the system. Thus discontinuities can propagate only along characteristics, a fact that we have seen for the scalar case.

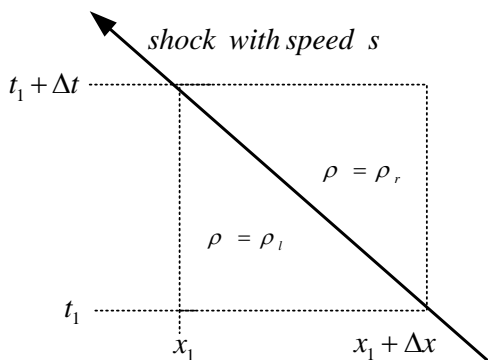


Figure 5. Region of Integration for Shock Speed Calculation

4.6 Vehicle Path

The velocity of vehicles is independent of traffic wave velocity. Once a vehicle a distance D encounters traffic wave which moves with velocity $-V_{max}$, the car will begin to move. The density in the expansion fan is

$$\rho(x, t) = \rho_{max} \left(\frac{v_{max} t - x}{2 v_{max} t} \right). \quad (26)$$

The velocity of a car is $v = v_{max} \left(1 - \frac{\rho}{\rho_{max}} \right)$.

The path $x(t)$ of the car thus satisfies

$$\frac{dx}{dt} = v_{max} \left(1 - \frac{1}{\rho_{max}} \left[\rho_{max} \left(\frac{v_{max} t - x}{2 v_{max} t} \right) \right] \right).$$

5. CALCULATED RESULT FOR SHOCK SPEED

Let $f = 60\rho \left(1 - \frac{\rho}{300} \right)$ in miles/ hours units. We

suppose that $t = 0$ the density on road is given by

$$\rho(x, 0) = \begin{cases} 40, & \text{for } x < 0 \\ 40(1 + 3x), & \text{for } 0 < x < 1 \\ 160, & \text{for } x > 1. \end{cases}$$

.Since $v(\rho) = 60 \left(1 - \frac{\rho}{300} \right)$, the characteristics are

$$x = \begin{cases} 30t + x_0, & \text{for } x_0 < 0, \\ 60 \left(\frac{2}{3} - x_0 \right) t + x_0, & \text{for } 0 < x_0 < 1, \\ -10t + x_0, & \text{for } x_0 > 1. \end{cases}$$

In the transition region characteristics are thus given by

$$x = 60 \left(\frac{2}{3} - x_0 \right) t + x_0. \text{ At time } t = \frac{1}{60}, \text{ these}$$

characteristics intersect at $x = \frac{2}{3}$ mile, and a shock forms.

The shock velocity is given by

$$\begin{aligned} v_{shock} &= \frac{d\xi}{dt} = \frac{[f(\rho_l) - f(\rho_r)]}{[\rho_r - \rho_l]} \\ &= 60(1 - (40 + 160)/300) \\ &= 20 \text{ mph.} \end{aligned}$$

Consider what happens to the car at $x = -1$ when $t = 0$.

The speed of the car is initially

$$60(1 - 40/300) = 52 \text{ mph. At } t = \frac{1}{60}, \text{ it has}$$

reach $x = 0$ and the shock forms at $x = \frac{2}{3}$. Since the car's

path is given by $x_{car} = 40t - 1$ and the shock path by $x_{shock} = 20(t - 1/60) + 2/3$ the car will meet the

shock when $x_{car} = x_{shock}$ or $t = \frac{1}{15}$ hours. Once through

the shock, the car moves at velocity

$$60 = \left(1 - \frac{160}{300}\right) = 28mph..$$

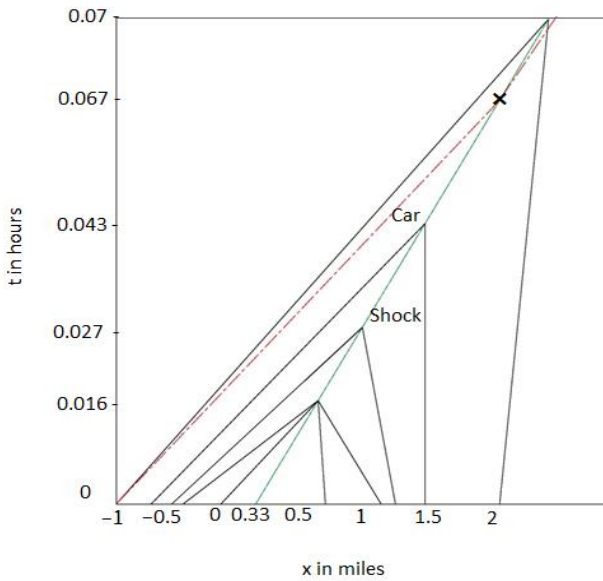


Figure 6. Shock Formation from the Initial Density

6. CONCLUSIONS

In this paper, we focused on road networks, where on each road the scalar conservation laws model and car following models determines the evolution of the car traffic. Then we calculated for the shock speed.

7. ACKNOWLEDGMENT

The authors would like to acknowledge the support of the papers for their references.

8. REFERENCES

- [1] Kac, P.: Optimal and Feedback Control for Hyperbolic Conservation Laws, Faculty of the Virginia Polytechnic Institute and States University, Virginia, (2007)
- [2] Bretti, G., and Piccoli, B.: Traffic Flow on Road Networks, SIAM Journal on Mathematical Analysis 36, (2005) pp. 1862- 1886
- [3] Leveque, R.J.: Finite Volume Methods for Hyperbolic Problems, Cambridge Texts in Applied Mathematics, Cambridge University Press, (2002).
- [4] Piccoli, B.: Numerical Approximations of a Traffic Flow Models on Networks, Networks and Heterogeneous Media, No. 1, (206) pp. 57-84.
- [5] Klar, A., and Rasche, M.: Derivation of Continuum Flow Traffic Models from Microscopic Follow the Leader Models, SIAM J. Appl. Math., (2002) pp. 259.
- [6] Randall J. Le Veque: Numerical Methods for Conservation Laws, Second Edition.

Performance Analysis of Overhead Transmission Line Design

Aye Aye Maw

Department of Electrical Power Engineering
Technological University (Mawlamyine)
Mawlamyine, Myanmar

Abstract: An overhead transmission line may be used to transmit or distribute electric power. The purpose of this paper is to transmit optimum power at a given power factor, over a given distance and voltage regulation. The design and analyze of a three phase, 50Hz, 160km long overhead line supplies 150MW at 230kV, 0.9 power factor lagging are presented. In the mechanical design includes types of tower, span, ground clearance, tension and sag for different spans with poles at equal height. And also electrical design consists of choice of conductor, percentage voltage regulation and efficiency of transmission line. The system performance can be developed by correcting the power factor shunt capacitor bank.

Keywords: transmission line, mechanical design, electrical design, voltage regulation, transmission efficiency, capacitor bank

1. INTRODUCTION

The purpose of a transmission network is to transfer electric energy from generating unit to various locations to the distribution system which ultimately supplied the load. Conductor, insulator and support are the main parts of transmission system. Resistance, inductance and capacitance are constants for electrical design of the transmission line.

There are two types of transmission line which are AC transmission line and DC transmission line. The transmission voltages levels are 66kV, 132kV, 230kV and 500kV. The suitable method is to employ three phase three wire AC system for transmission systems.

Power factor correction (PFC) is a technique of counteracting the undesirable effects of electric loads that create a power factor that is less than one. Power factor correction may be applied either by an electrical power transmission utility to improve the stability and efficiency of the transmission. Therefore, shunt capacitors are widely used in power factor correction applications.

2. PERFORMANCE OF POWER TRANSMISSION LINE

The fundamental purpose of the electric utility transmission system is to transmit power from generating units to the distribution system that ultimately supplies the loads. This objective is served by transmission lines that connect the generators into the transmission network, interconnect various areas of the transmission network, interconnect one electric utility with another, or deliver the electrical power from various areas within the transmission network to the distribution substations. Transmission system design is the selection of the necessary lines and equipment which will deliver the required power and quality of service for the lowest overall average cost over the service life. The system must also be capable of expansion with minimum changes to existing facilities.

2.1 Classification of Overhead Line

A transmission line has three contents R, L, C distributed uniformly along the whole length of the line. The resistance and inductance form the series impedance. The capacitance existing between the conductors for a single phase line or from a conductor to neutral for a three phase line forms a shunt path throughout the length of the line. Therefore, capacitance effects introduce complications in transmission line calculations. Depending upon the manner in which capacitance is taken into account; the overhead transmission lines are classified as:

(i) Short Transmission Line

(ii) Medium Transmission Line

(iii) Long Transmission Line

2.1.1 Short Transmission Line

When the length of an overhead transmission line length is less than 30 miles, or the line voltage is not over < 33 kV, it is usually considered as a short transmission line. Due to smaller length and lower voltage, the shunt capacitance and conductance effects are small and hence can be neglected. Therefore, while studying the performance of a short transmission line, only inductance and resistance of the line are taken to account.

2.1.2 Medium Transmission Line

When the length of an overhead transmission line is about 30-80 miles and the line voltage is moderately high (> 33 kV and 66 kV), it is considered as a medium transmission line. Due to sufficient length and voltage of the line, the capacitance effects are taken into account. For purpose of calculation, the distributed capacitance of line is divided and lumped in the form of the condensers shunted across the line at one or more points.

2.1.3 Long Transmission Line

When the length of an overhead transmission line is more than 80 miles and line voltage is very high (> 66 kV), it is considered as a long transmission line. For the treatment of such a line, a line constants are considered uniformly distributed over the whole length of the line.

3. MECHANICAL DESIGN OF TRANSMISSION LINE

The successful operation of an overhead line depends to a great extent upon the mechanical design of the line. While constructing an overhead line, it should be ensured that mechanical strength of the line is such so as to provide against the most probable weather conditions.

3.1 Supports of Transmission Line

The different types of structure (poles or towers) used for supporting the overhead transmission lines or wires, such types are called line supports. The line support plays a major role in power transmission. It kept the proper spacing between the conductors and maintained the conductor at the distance from its ground parts. It also maintained the specified ground clearance. Requirement of the line supports is low cost, low maintenance and long life. The line supports are made of wood,

concrete, steel or aluminum. It is mainly classified into two types;

- (i) Electrical Pole
- (ii) Electrical Tower

3.2 Overhead Insulators

The overhead line conductors should be supported on the poles or towers in such a way that currents from conductors do not flow to earth through supports i.e. line conductors must be properly insulated from supports. This is achieved by securing line conductors to supports with the help of insulators. The insulators provide necessary insulation between line conductors and supports and thus prevent any leakage current from conductors to earth. The insulators are made of porcelain, glass and polymer. There are mainly types of insulator used as overhead insulator likewise;

- (i) Pin Insulators
- (ii) Shackle Insulators
- (iii) Strain Insulators
- (iv) Egg/Stay Insulators
- (v) Suspension Disc Insulators

3.3 Sag in Overhead Line

The difference in level between points of supports and the lowest point on the conductor is called sag. There are two different levels.

3.3.1. Supports are at equal levels

Consider a conductor between two equal level supports A and B with O as the lowest point as shown in Figure (1). It can be proved that lowest point will be at the mid-span.

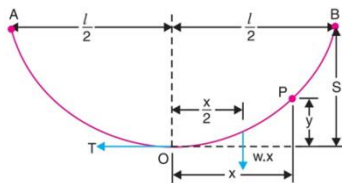


Figure1. Sag at Normal Ground Level two supports

$$\text{Sag } (S) = \frac{Wl^2}{8T} \quad (1)$$

where, W = unit weight of conductor (kg/m)

l = span (m)

T = horizontal tension of conductor (kg)

3.3.2. Supports are at unequal levels

In hilly areas, we generally come across conductors suspended between supports at unequal levels. In Figure (2), shows a conductor suspended between two supports A and B which are at different level. The lowest point on the conductor is O.

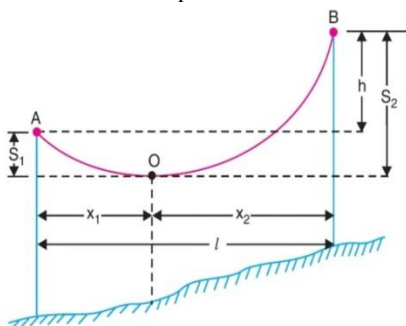


Figure2. Sag at Unbalance Ground Level two supports

If W is the weight per unit length of the conductor, then,

$$\text{Sag, } S_1 = \frac{Wx_1^2}{2T} \quad (2)$$

$$\text{Sag, } S_2 = \frac{Wx_2^2}{2T} \quad (3)$$

Where, l = Span length

h = Difference in levels between two supports

x_1 = Distance of support at lower level A from O

x_2 = Distance of support at higher level B from O

3.4. Effect of Wind Loading

The worst weather conditions expected which will be the case occurred wind pressure, temperature, conductor tension expected when the weather is fine. Cable operation (Stringing work) must be calculated in advance what to do. In the severe weather condition,

Let Temperature = t_1
 Conductor tension = T_1
 Actual length of conductor = L

$$L_1 = l + \frac{W_1^2 l^3}{24T_1^2} \quad (4)$$

In the good weather condition,

At starting stringing progress, the temperature and tension will change.

Temperature = t_2
 Conductor tension = T_2
 Actual length of conductor = L

And also changing the load on conductor W_2 ,

$$L_2 = l + \frac{W_2^2 l^3}{24T_2^2} \quad (5)$$

Different between two weather conditions, the length of conductor are Changing.

Solve equation (1) and (2),

$$\Delta L = \frac{W_2^2 l^3}{24T_2^2} - \frac{W_1^2 l^3}{24T_1^2} \quad (6)$$

T_1 = max: working Tension

= 3500 kg (35% of UTS = 10000 kg)

W_1 = weight of conductor at bad weather

W_2 = conductor weight only

Other way, calculating the of changing of conductor length

$$\Delta L_1 = \frac{(T_2 - T_1)l}{EA} \quad (7)$$

Where, E = Young's Modulus of elasticity

A = Sectional area of conductor

And also changing of conductor by t_1 and t_2 , form of temperature coefficient

$$\Delta L_2 = \alpha l (t_2 - t_1) \quad (8)$$

Temperature coefficient (coefficient of linear expansion) = α

Equation (7) + (8),

$$\Delta L = \frac{(T_2 - T_1)l}{EA} + \alpha l (t_2 - t_1) \quad (9)$$

Simplify equation (6) and (9),

$$\frac{W_2^2 l^3}{24T_2^2} - \frac{W_1^2 l^3}{24T_1^2} = \frac{(T_2 - T_1)l}{EA} + \alpha l (t_2 - t_1)$$

$$\frac{W_2^2 l^2 E}{24T_2^2} - \frac{W_1^2 l^2 E}{24T_1^2} = \frac{T_2}{A} - \frac{T_1}{A} + \alpha tE$$

$$\frac{W_2^2 l^2 E}{24T_2^2} = \frac{T_2}{A} - \frac{T_1}{A} + \frac{W_1^2 l^2 E}{24T_1^2} + \alpha tE$$

$$\frac{W_2^2 l^2 E}{24} = T_2^2 \left[\frac{T_2}{A} - \left(\frac{T_1}{A} - \frac{W_1^2 l^2 E}{24T_1^2} - \alpha tE \right) \right]$$

$$M = \frac{W_2^2 l^2 E}{24} \quad (10)$$

$$K = \frac{T_1}{A} - \frac{W_1^2 l^2 E}{24T_1^2} \quad (11)$$

$$M = T_2^2 \left[\frac{T_2}{A} - (K - \alpha tE) \right] \quad (12)$$

$$S = \frac{W_2 l^2}{8T_2} \quad (13)$$

$$\text{Ground clearance} = \text{Tower height} - \text{Sag} \quad (14)$$

4. ELECTRICAL DESIGN OF TRANSMISSION LINE

Transmission of electric power is done by 3-phase, 3-wire overhead lines. An a.c. transmission line has resistance, inductance and capacitance uniformly distributed along its length. These are known as constants or parameters of the line. The performance of a transmission line depends to a considerable extent upon these constants. For instance, these constants determine whether the efficiency and voltage regulation of the line will be good or poor.

4.1. Conductors

Transmission line conductors are normally made from aluminum with certain reinforcements. Copper is not usually at high voltage because of its costs even though it has a very low resistance. The conductors are made of aluminum strands which are reinforced by another material. The reinforcement, by steel for instance, provides a ratio of high strength to weight. Aluminum conductors are classified as follows:

AAC = All Aluminium Conductor

ACSR = Aluminium Conductor Steel Reinforcement

AAAC = All Aluminium Alloy Conductor

4.2. Reactance of Transmission Line

Inductance and capacitance of transmission lines is calculated per phase. Inductance consists of self inductance of the phase conductor and mutual inductance between the conductors. Capacitance is considered the actual outside radius of the conductor.

4.2.1 Inductance of Symmetrical Three-Phase Line

In symmetrical three-phase line, all the conductors are placed at the corners of the equilateral triangle. Such an arrangement of conductors is also referred to as equilateral spacing. It is shown in the diagram below.

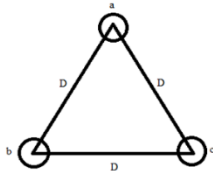


Figure 3. Symmetrical Three-Phase Line

D is the geometric mean of the three spacing of the three phase line and the radius of each conductor, r.

$$\text{GMD, } D_m = \sqrt[3]{D_{ab}D_{ac}D_{bc}}$$

$$\text{GMR, } D_s = 0.7788r$$

$$L = 2 \times 10^{-7} \ln \frac{\text{GMD}}{\text{GMR}} \quad [\text{H/m}]$$

$$L = 2 \times 10^{-7} \ln \frac{D_m}{D_s} \quad [\text{H/m}] \quad (15)$$

$$X_L = 2\pi fL \quad \Omega/\text{phase} \quad (16)$$

where, GMR is the geometric mean radius and GMD is the geometric mean distance.

4.2.2. Capacitance of Symmetrical Three-Phase Line

The three conductors a, b and c of the 3-phase overhead transmission line having charges Q_a , Q_b and Q_c per metre length respectively. Let the conductors be equidistant (D metres) from each other. The capacitance from line conductor to neutral in this symmetrically spaced line is calculated per phase.

$$C_N = \frac{1}{8 \times 10^9 \ln \left(\frac{D_m}{r} \right)} \quad \text{F/m} \quad (17)$$

$$X_C = \frac{1}{2\pi f C_N} \quad \Omega/\text{phase} \quad (18)$$

4.3. General Formula for Long Transmission Line

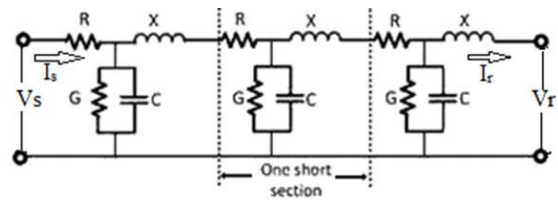


Figure 5. Circuit Diagram of Long line

$$V_s = AV_r + B I_r \quad (19)$$

$$I_s = CV_r + DI_r \quad (20)$$

Where, V_s = Sending end voltage per phase

I_s = Sending end current

V_r = Receiving end voltage per phase

I_r = Receiving end current

A, B, C and D are constants and generally complex number.

$$\text{For constant A, } A = 1 + \frac{ZY}{2} \quad (21)$$

$$\text{For constant B, } B = Z \left[1 + \frac{ZY}{6} + \frac{Z^2 Y^2}{120} + \dots \right] \quad (22)$$

$$\text{For constant C, } C = Y \left[1 + \frac{ZY}{6} + \frac{Z^2 Y^2}{120} + \dots \right] \quad (23)$$

$$\text{For constant D, } D = 1 + \frac{ZY}{2} \quad (24)$$

Where, Y = Shunt admittance of the line

Z = Series impedance of the line

For series impedance Z ,

$$Z = R + jX_L \quad \Omega/\text{phase} \quad (25)$$

For shunt admittance Y ,

$$Y = j2\pi f C_N \quad \text{S}/\text{phase} \quad (26)$$

4.4. Effect of Load Power Factor on Voltage Regulation and Efficiency

The regulation and efficiency of a transmission line depend to a considerable extent upon the power factor of the load.

4.4.1. Effect on regulation

The performance of a transmission line is desirable to determine its voltage regulation the difference in voltage at the receiving end of a transmission line between conditions of no load and full load is called voltage regulation and is expressed as a percentage of the receiving end voltage. When a transmission line is carrying current, there is a voltage drop in the line due to resistance and inductance of the line. The result is that receiving end voltage (V_r) of the line is generally less than the sending end voltage (V_s). This voltage drop ($V_s - V_r$) in the line is expressed as a percentage of receiving end voltage V_r and is called voltage regulation. Mathematically,

$$\% \text{ Voltage Regulation, } VR = \frac{V_s - V_r}{V_r} \times 100 \% \quad (27)$$

4.4.2. Effect on transmission efficiency

The power obtained at receiving end of a transmission line is generally less than the sending end power due to losses in the line resistance. The power delivered to the load depends upon the power factor.

$$P = 3V_r I \cos \phi \quad (\text{For 3-phase line})$$

∴

$$I = \frac{P}{3V_r \cos \phi_r} \quad (28)$$

Power losses, $P_L = 3I^2R$

$$\begin{aligned} \text{\% Transmission Efficiency, } \eta &= \frac{\text{Receiving end power}}{\text{Sending end power}} \times 100 \\ (29) \quad &= \frac{V_r I_r \cos \phi_r}{V_s I_s \cos \phi_s} \times 100 \\ &= \frac{3V_r I_r \cos \phi_r}{3V_r I_r \cos \phi_r + \text{Losses}} \times 100 \end{aligned}$$

Where V_r , I_r and $\cos \phi_r$ are receiving end voltage, current and power factor while V_s , I_s and $\cos \phi_s$ are sending end voltage, current and power factor.

5. POWER FACTOR IMPROVEMENT

The system performance can be improved by correcting the power factor. The system power factor is given by:

$$\text{Power Factor} = \text{kW/kVA} \quad (30)$$

Where kW and kVA are the real and apparent power, respectively. The power factor of any operating system can be lagging or leading. The direction of active and reactive power can be used to determine the nature of the power factor. If both the real and reactive power flow are in the same direction, then the power factor is lagging. If the reactive power flows in the direction opposite to that of the real power, then the power factor is leading.

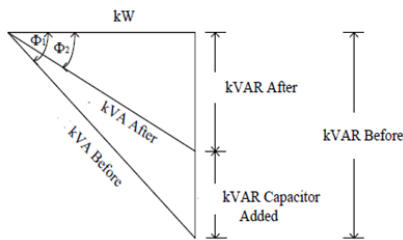


Figure 4. Power Factor Correction Triangle

If power factor is raised to $\cos \phi_2$,
Desired kVA Demand, $kVA_2 = \text{Present load/ Desired power factor}$

Desired kVA Demand, $kVA_2 = \text{kW/ } \cos \phi_2$

$$\begin{aligned} \text{kVAR}_2 \text{ at power factor } \cos \phi_2 &= kVA_2 \times \sin \phi_2 \text{ or} \\ &= \sqrt{(kVA_2^2 - kW^2)} \end{aligned}$$

Capacitor rating = $\text{kVAR}_1(\text{Uncorrected}) - \text{kVAR}_2(\text{Corrected})$

6. CALCULATION OF POWER TRANSMISSION LINE

The high voltage overhead transmission line has a various span between level supports. In the central regions of Myanmar, the most powerful air pressure is 66kg/m^2 and in that time the temperature is 28°C .

The following data are obtained from Thaton-Mawlamyine power transmission line to design shunt capacitor bank for power factor correction. In this design calculation, suitable size of shunt capacitor bank is installed.

Present load, kW = 150MW

Present $kVA_1 = 166.67\text{MVA}$

Present $\text{kVAR}_1 = 72.649\text{MVAR}$

Present Power Factor = 0.9

Desired Power Factor = 0.95

Voltage = 230kV

If power factor is raised to 95%,

Desired kVA Demand,

$kVA_2 = \text{Present load/ Desired power factor}$

$$= 150/0.95 = 157.895\text{MVA}$$

The size of the capacitor required to accomplish this is determined from the KVAR at the two values of power factor as follows:

$$\text{kVAR} = \sqrt{(kVA^2 - kW^2)}$$

At 90% power factor,

$$\begin{aligned} \text{kVAR}_1 &= \sqrt{(kVA_1^2 - kW^2)} = \sqrt{(166.67^2 - 150^2)} \\ &= 72.649\text{MVAR} \end{aligned}$$

At 95% power factor,

$$\begin{aligned} \text{kVAR}_2 &= \sqrt{(kVA_2^2 - kW^2)} \\ &= \sqrt{(157.895^2 - 150^2)} = 49.303\text{MVAR} \end{aligned}$$

Capacitor rating = $\text{kVAR}_1(\text{Uncorrected}) - \text{kVAR}_2(\text{Corrected})$

$$= 72.649\text{MVAR} - 49.303\text{MVAR}$$

$$= 23.346\text{MVAR}$$

Table 1. Results of Sag, Tension and Ground Clearance (GC) for Transmission Line

Types of Conductor (ACSR)	Tower Height (m)	Span (m)	Tension (kg)	Sag (m)	GC (m)
346.4mm ² (DUCK)	20	344	2209	7.8	9.75
	58	678.35	2104	31.71	23.84
	58	643	2109	28.43	27.12
374.7mm ² (GROSBE AK)	20	344	2237	8.6	8.95
	58	678.35	2186	34.18	21.37
	58	643	2188	30.68	24.87

Table 2. Results of Voltage Regulation and Transmission Line Efficiency for 0.9 Power Factor

Type of Conductor (ACSR)	Current (A)	V drop (kV)	Diame ter (mm)	V.R (%)	Line η (%)
346.4 mm ²	418.37	18.366	24.21	13.8	95.18
374.7 mm ²	418.37	17.927	25.15	13.45	95.44

Table 3. Result of Transmission Line Performance for After Power Factor Correction

Types of conductor (ACSR)	power factor					
	0.9 (Lagging)			0.95 (Lagging)		
	V drop (kV)	V.R (%)	Line η (%)	V drop (kV)	V.R (%)	Line η (%)
346.4 mm ²	18.37	13.8	95.18	14.36	10.8	95.57
374.7 mm ²	17.93	13.5	95.44	13.96	10.5	95.81

[5] HadiSaadat,InternationalEdition,WCB 1999,Power System Analysis,Milwaukee School of Engineering,McGraw-Hill.

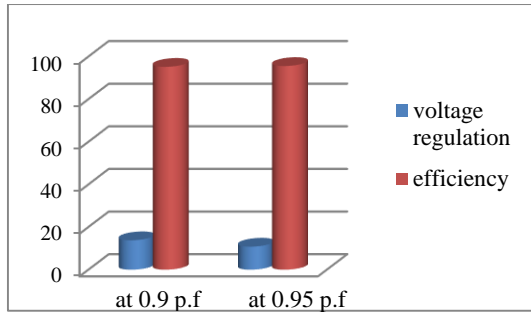


Figure 6.Results from 346.4mm²ACSR(DUCK) Conductor

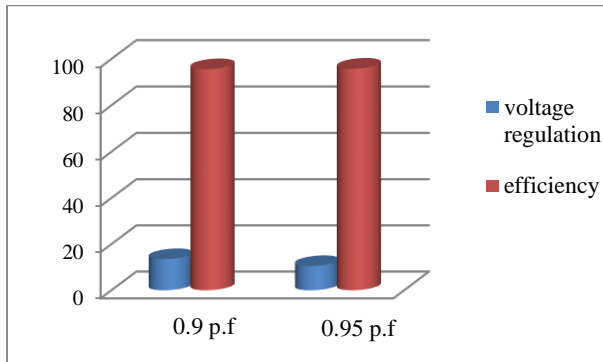


Figure 7. Results from 374.7mm²ACSR(GROSBEAK) Conductor

7. CONCLUSIONS

In this paper, the line conductor and tower are determined and calculated voltage regulation and transmission efficiency to design the transmission line. Overhead transmission lines depend on area of installation, the design of these lines requires maximum clearances to be observed to maintain safety. Sag and tension for different span at equal height are calculated with two types of conductor size and temperature. Shunt capacitors are widely used in power factor correction applications. This paper illustrated the basis issues related to power factor improvement by using shunt capacitor banks for transmission system. The performance of results are presented by the table.

8. ACKNOWLEDGMENT

I would like to express thankful thank to my friend, for her great advices and kindly co-operation in finding of manuscripts and helps, till the completion of this paper. And then specially, I am deeply grateful to my family, who initially got my interested in learning to be educated and have supported and guided my throughout my life.

9. REFERENCES

- [1] V.K. Mehta & Rohit Mehta, "Principles of Power System", 4th Revised Edition, 2008
- [2] Transmission Line Training of Ministry of Electrical and Energy, Myanmar, 2010
- [3] No.2, Sag and Tension Paper for Ministry of Electricity and Energy, Myanmar, 2011
- [4] George G. Karady, "Transmission System", Electrical Power Engineering Handbook, 2001

Secure Data Transfer using RSA and Steganography

Zo Nun Khuma
Department of Information Technology,
West Yangon Technological University
Myanmar

Abstract: Today, transferring sensitive information via secure methods and protecting information privacy are becoming critically important, the two ways for securing and transferring messages and data are cryptography and steganography. Steganography is used for hiding messages in innocuous media (carriers) such as text, image, audio, video and protocol. Amongst these different carriers, digital images are the most popular because of their frequency on the internet. To be more robust in security, steganography can be combined with cryptographic techniques. In this paper, we propose Secure Data Transfer using RSA and Steganography in order to obtain a secure system. The system will be implemented by Java programming language.

Keywords: Cryptography, RSA, Secure Data Transfer, Image Carriers, Steganography

1. INTRODUCTION

Since the rise of the Internet one of the most important factors of communication and information technology has been the security of information. It is necessary to protect this information while communicated over insecure channels. Thus, a need exists for developing technology that will help protect the integrity of digital content and secure the intellectual property rights of owners. This has resulted in an explosive growth of the field of information hiding. In addition, the rapid growth of publishing and broadcasting technology also requires an alternative solution in hiding information. To overcome this problem, some invisible information can be embedded in the digital media in such a way that it could not be easily extracted without a specialized technique [1]. One and most widely used for securing data is Steganography. The word steganography is derived from the Greek words “*stegos*” meaning “cover” and “*grafia*” meaning “writing” defining it as “covered writing” [2]. Today, steganography is mostly used on computers with digital data being the carriers and networks being the high speed delivery channels. It is a performance that inserts secret messages into a cover file, so that the existence of the messages is not apparent. Research in information hiding has tremendous increased during the past decade with commercial interests driving the field [3].

For security enhancement, this system can be made by combining with another method for securing data, called Cryptography. Cryptography was created as a technique for securing the secrecy of communication and many different methods have been developed to encrypt and decrypt data in order to keep the message secret.

2. RELATED WORK

Recently, there is a growing interest in the information security to the problems in the current data communication domain. Steganography is the idea of hiding private or sensitive data or information within something that appears to be nothing out of the ordinary.

The paper [4] pointed out that “some specific image based steganography techniques and show that an observer can indeed distinguish between images carrying a hidden message and images which do not carry a message.” And the paper [5] also figures out that “given an image is believed to contain a

secret message, identify where the message is hidden. We treat this problem as outlier detection”. Moreover, the paper [6] pointed out that “The strength of steganography can be thus amplified by combining it with cryptography”.

On the other hand, applying encryption algorithm on the message can enhance the security. And it is an important tool to protect information from attackers. To overcome this problem, the need is to add security mechanism in our system. To improve the performance of this proposed system, steganographic and cryptographic techniques are combined to implement the system.

3. STEGANOGRAPHY

3.1 Different Kinds of Steganography

Almost all digital file formats can be used for steganography, but the formats that are more suitable are those with a high degree of redundancy. Figure 1 shows the categories of steganography.

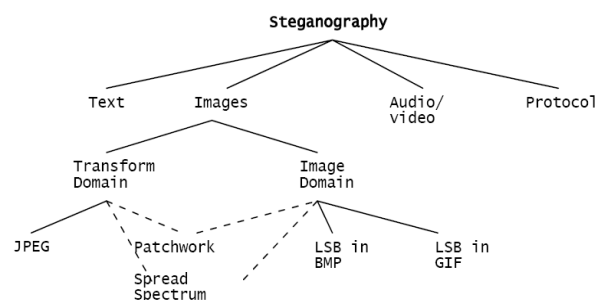


Figure 1 Categories of Steganography

Hiding information in text is historically the most important method of steganography. Text steganography using digital files is not used very often since text files have a very small amount of redundant data. The large amount of redundant bits presents in the digital representation of an image, so images are the most popular cover objects for steganography.

To hide information in audio files similar techniques are used as for image files. One different technique unique to audio steganography is masking, which exploits the properties of the human ear to hide information unnoticeably. A faint, but audible, sound becomes inaudible in the presence of another louder audible sound [3]. Although nearly equal to images in

steganographic potential, the larger size of meaningful audio files makes them less popular to use than images [7].

The protocol steganography refers to the technique of embedding information within messages and network control protocols used in network transmission [8]. In the layers of the OSI network model, there exist covert channels where steganography can be used [9].

3.2 Image Steganography

Images are the most popular cover objects used for steganography. For the different image file formats, different steganographic algorithms exist. For these different image file formats different steganography algorithm exist.

Image steganography techniques can be divided into two groups: those in the Image Domain and those in the Transform Domain [10]. Image – also known as spatial – domain techniques embed messages in the intensity of the pixels directly, while for transform – also known as frequency – domain, images are first transformed and then the message is embedded in the image [11]. Image domain techniques encompass bit-wise methods that apply bit insertion and noise manipulation and are sometimes characterized as “simple systems”. The image formats that are most suitable for image domain steganography are lossless and the techniques are typically dependent on the image format.

Steganography in the transform domain involves the manipulation of the algorithms and image transforms. These methods hide messages in more significant areas of the cover image, making it more robust. Many transform domain methods are independent of the image format and the embedded message may survive conversion between lossy and lossless compression.

3.3 Embedding data into an image

To a computer, an image is an array of numbers that represent light intensities at various points, or pixels. In digital, images are represented with the numerical values of each pixel where the value represents the color and intensity of the pixel. These pixels make up the image’s raster data. Digital images are typically stored in either 24-bit or 8-bit per pixel files. 24-bit images are known as true colour images. Obviously, a 24-bit image provides more space for hiding information as compared to 8 bit image [12].

3.4 Least significant bit insertion

The least significant bit insertion method is probably the most well-known image steganography technique. It is a common, simple approach to embed information in a graphical image file. This is the most common method used in this the data to be hidden is inserted into the least significant bits of the pixel information In digital, images are represented with the numerical values of each pixel where the value represents the color and intensity of the pixel. In 24 bit image we can embed 3 bits in each pixel while in 8-bit we can embed only 1 bit in each pixel. To hide an image in the LSBs of each byte of the 24- bit image, one can store 3 bits in each pixel. A 1024 x 768 image has the potential to hide a total of 2,359,296 bits of information. For e.g., the letter A can be hidden in three pixels. The binary value of A is 10000011.

The original raster data of 3 pixels may be:

(00100111 11101001 11001000)
 (00100111 11001000 11101001)

(11001000 00100111 11101001).

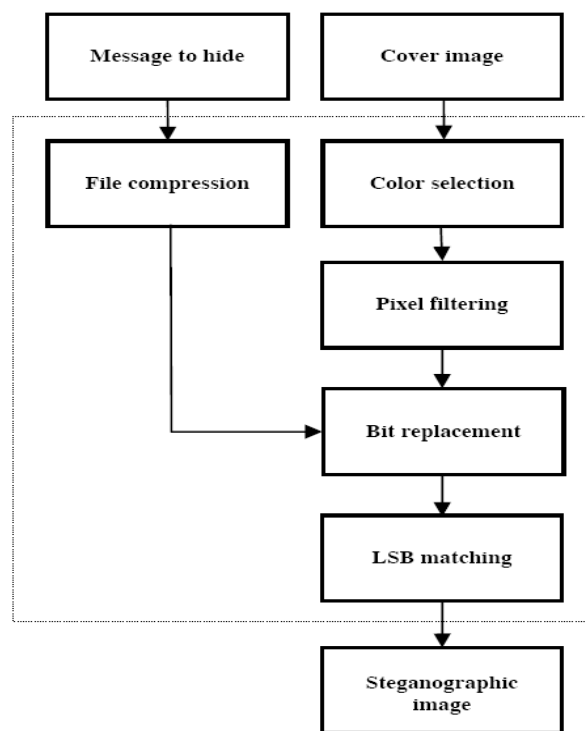


Figure 2 Structure of the Algorithm SLSB

After inserting the binary value for A.

(00100111 11101000 11001000)
 (00100110 11001000 11101000)
 (11001000 00100111 11101001)

The highlighted bits are the only three actually changed in the 9 bytes of data. One can hide data in the least and second least significant bits and still the human eye would not be able to discern it. In this proposed algorithm we generate random number initialized with a stego-key and its output is combined with the input data, and this is embedded to a cover image. The usage of a stego-key is important, because the security of a protection system should not be based on the secrecy of the algorithm itself, instead of the choice of a secret key.

4. CRYPTOGRAPHY

Cryptography is an important element of any strategy to address message transmission security requirements. Cryptography is the study of methods of sending messages in disguised form so that only the intended recipients can remove the disguise and read the message. It is the practical art of converting messages or data into a different form, such that no-one can read them without having access to the 'key'. The message may be converted using a 'code' (in which case each character or group of characters is substituted by an alternative one), or a 'cypher' or 'cipher' (in which case the message as a whole is converted, rather than individual characters). Cryptology is the science of 'breaking' or 'cracking' encryption schemes, i.e. discovering the decryption key. Cryptographic systems are generically classified along three independent dimensions [13]. If both sender and receiver use the same key, the system is referred to as symmetric, single-key, secret-key, or conventional encryption. If the sender and receiver each use a different key, the system

is referred to as asymmetric, two keys, or public-key encryption.

4.1 Asymmetric Encryption

Asymmetric algorithm also called as public-key algorithm rely on one key (public key) for encryption and a different by related key (private key) for decryption as shown in Figure 3. Each recipient has a private key that is kept secret and a public key that is published for everyone. The sender looks up or is sent to the recipient's public key and uses it to encrypt the message. The recipient uses the private key to decrypt the message and never publishes or transmits the private key to anyone. Thus, the private key is never in transit and remains invulnerable [14].

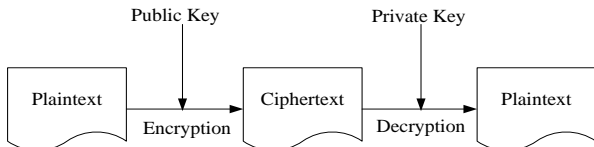


Figure 3 Public-Key Encryption Scheme

4.2 RSA ALGORITHM

The RSA algorithm is named after Ron Rivest, Adi Shamir and Len Adleman, who invented it in 1977[15]. The basic technique was first discovered in 1973 by Clifford Cocks [16] of CESG (part of the British GCHQ) but this was a secret until 1997. The patent taken out by RSA Labs has expired.

The RSA cryptosystem is the most widely-used public key cryptography algorithm in the world. It can be used to encrypt a message without the need to exchange a secret key separately.

The RSA algorithm can be used for both public key encryption and digital signatures. Its security is based on the difficulty of factoring large integers.

Party A can send an encrypted message to party B without any prior exchange of secret keys. A just uses B's public key to encrypt the message and B decrypts it using the private key, which only he knows. RSA can also be used to sign a message, so A can sign a message using their private key and B can verify it using A's public key.

4.2.1 Detailed Description of RSA Encryption Algorithm

In the encryption and decryption algorithm, converting plaintext to ciphertext the cryptographic algorithm is called encryption and converting ciphertext back to plaintext using cryptographic algorithm is called decryption. Each encryption scheme can be divided into three stages.

- Key Generation Stage
- Encryption Stage
- Decryption Stage

The security of any public-key algorithm, whether based on the difficulty of factoring large the numbers or the difficult of taking discrete logarithms of large numbers, depends on the size of those large numbers. If the number is small enough, we have no security. If the number is large enough, we have security all the computing power in the world working from now until the sun goes nova. We have a choice of key length, and it is an important choice. What follows is an analysis of different key lengths and their susceptibility to factoring, both today and in the near future.

The encryption key consists of the pair of integers (e, n), and the decryption key is (d, n) as shown in Figure 4. The starting point in finding keys for this RSA algorithm is to select a value of n. The value of n should be quite large, a product of two primes p and q. Both p and q should be large themselves. Typically p and q are approximately 100 digits each, so that n is approximately 200 digits long. This length effectively inhibits factoring n to infer p and q.

Next a relatively large integer e is chosen so that e is relatively primed to (p-1)*(q-1). (Recall that “relatively prime” means that e has no factors in common with (p-1)*(q-1)). An easy way to guarantee that e is relatively prime to (p-1)*(q-1) is to choose e as prime that is larger than both (p-1)*(q-1).

Finally, it is needed to select d such that $e*d \equiv 1 \pmod{(p-1)*(q-1)}$ as illustrated in Figure 5.

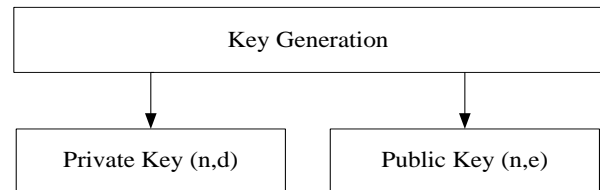


Figure 4 Block Diagram of Key Generation

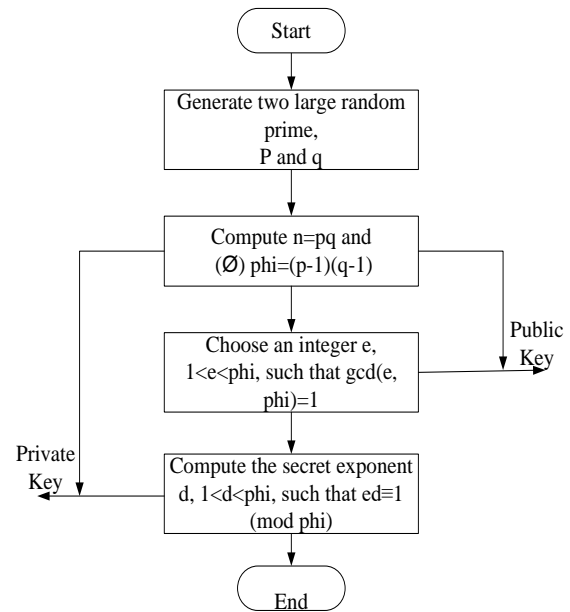


Figure 5 Block Diagram of RSA Key Generation Algorithm

4.2.2 Small Example of RSA Method

Consider the case $p = 53, q = 61, n = p * q = 53 * 61 = 3233$ and $d = 791$ then $\phi(3233) = 52 * 60 = 3120$ and e can be computed as $e = \text{inv}(791, 3233)$. Therefore, $e = 71$, the multiplicative inverse (mod 3233) of $d = 791$.

With $n = 3233$ can be encoded two letters per block, substitution a two-digit numbers for each letter:

blank = 00, A = 01, B = 02, C = 03, D = 04, E = 05, F = 06,....., Z = 26

Thus, the message $M = \text{RENAISSANCE}$

Becomes RE | NA | IS | SA | NC | E |

is encoded: 1704 1800 0818 1800 1302 0426

The first block, (M = 1704) is enciphered ...

$M71 = 3106 \pmod{3233}$

The whole message is enciphered as:

3106 0100 0931 2691 1984 2927

The reader can check those deciphering words:

$3016791 = 704 \pmod{3233}$, etc....

To encrypt and decrypt efficiently, use the fast exponentiation algorithm [17]. It is called "exponentiation by repeated squaring and multiplication".

5. PROPOSED SYSTEM

As shown in Figure 6, two ways of securing method are used in this proposed system: Steganography and Cryptography.

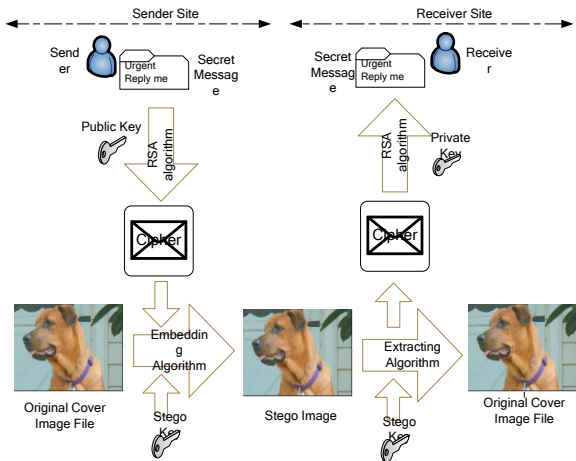


Figure 6 Proposed System Design

In the first step, at the sender site, the plaintext (secret message) is encrypted with the help of RSA, popular algorithm and then the cipher text is produced as in Figure 7. Because it is an asymmetric key algorithm, the Public Key is applied for encryption and Private Key for decryption.

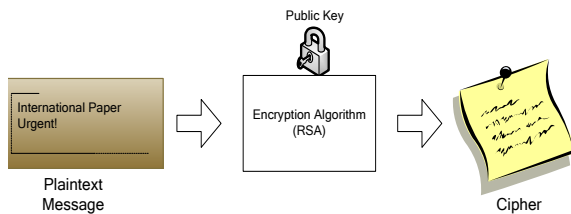


Figure 7 Encrypting the Message

Here we embed the message (Cipher) into the carrier image by using Least Significant Bit (LSB) insertion method. After embedding a secret message into the cover-image, a so-called stego image is obtained. The size of information to be hidden relatively depends on the size of the cover-image. Any image

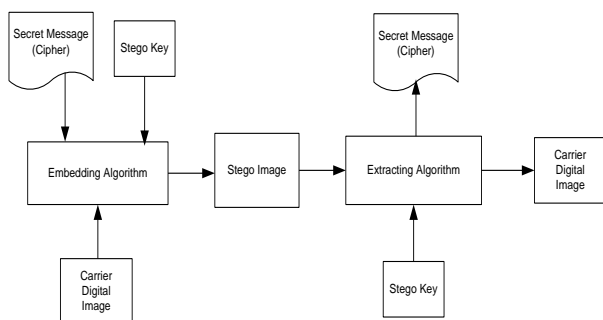


Figure 8 Embedding and Extracting the Message (Cipher)

file can hide the message of size of one – eight the size of original cover file, e.g if cover image is 128 bytes then it hide 16 bytes of message without any distortion.

After this process, at the receiver site, the embedded message is extracted from the stego image file and obtained the cipher text again as depicted in Figure 8.

The resulting cipher text is decrypted by using RSA algorithm with the receiver's Private Key. Finally, the receiver obtains the sent message (plaintext) as shown in Figure 9.

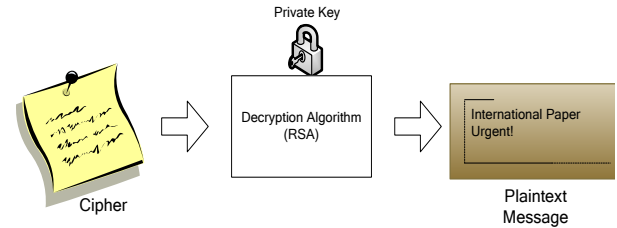


Figure 9 Decrypting the Message

6. PROS AND CONS

Table 1 Steganography Vs Cryptography

Steganography	Cryptography
Unknown message passing	Known message passing
Steganography prevents discovery of the very existence of communication	Encryption prevents an unauthorized party from discovering the contents of a communication
Little known technology	Common technology
Technology still being developed for certain formats	Most of algorithm known by all
Once detected message is known	Strong current algorithms are currently resistant to attack, larger expensive computing power is required for cracking
Steganography does not alter the structure of the secret message	Cryptography alter the structure of the secret message

7. TEST AND RESULT

Firstly, the system is implemented by using StegoJava. User

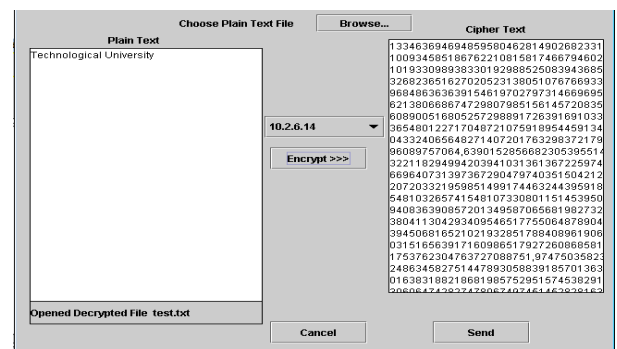


Figure 10 Encrypting the Message with RSA Algorithm

need to enter the message or choose the text file from Browse first. Figure 10 shows the encryption process with RSA algorithm.

The resulting cipher message is fetched to the embedding mode and is embedded the GIF image which is used as a cover image as in Figure 11 by the help of LSB.



Figure 11 The Cover Image

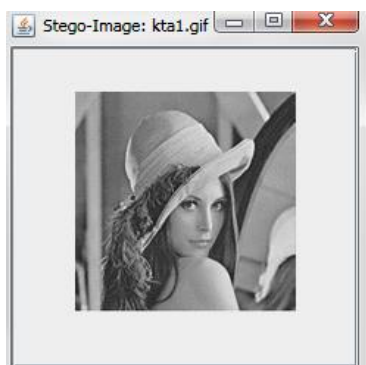


Figure 12 The Stego-image

Finally, the resulting cipher message extracting from the stego-image is decrypted to get the original message as shown in Figure 13.

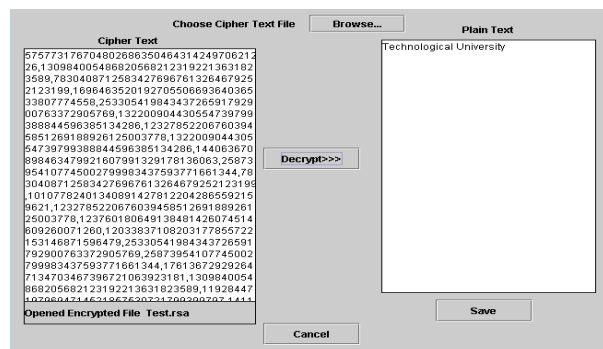


Figure 13 Decrypting the Cipher Message with Private Key

8. CONCLUSION

Till now, information hiding techniques received very much less attention from the research community and from industry than cryptography. Steganography has its place in security. It is not intended to replace cryptography but supplement it. In this paper we give an idea to enhance the security of system by combining the two techniques. It can enhance integrity and

confidentiality of information and provides a means of communicating privately. Here message is first encrypted and then embed in image file with the help of steganographic system. There are infinite number of steganography applications for digital image including copyright protection, feature tagging, and secret communication. This paper explores a tiny fraction of the art of steganography. It goes well beyond simply embedding text in an image.

9. REFERENCES

- [1] Dunbar, B. "Steganographic techniques and their use in an Open-Systems environment", *SANS Institute*, January 2002
- [2] Moerland, T. "Steganography and Steganalysis", *Leiden Institute of Advanced Computing Science*, www.liacs.nl/home/tmoerl/privtech.pdf
- [3] Silman, J. "Steganography and Steganalysis: An Overview", *SANS Institute*, 2001
- [4] Chandramouli, R. & Nasir Memon, "Analysis of LSB Based Image Steganography techniques", 2001 IEEE
- [5] Ian Davidson & Goutam Paul, "Locating Secret Messages in Images", *KDD'04*, Seattle, Washington, USA, August 22-25, 2004
- [6] Morkel, T., JHP Eloff and MS Olivier, "An Overview of Image Steganography," in *Proceeding of the fifth Annual Information Security South Africa Conference (ISSA 2005)*, Sandton, South Africa, June/July 2005 (Published electronically)
- [7] Artz, D. "Digital Steganography: Hiding Data within Data", *IEEE Internet Computing Journal*, June 2001
- [8] Ahsan, K. & D Kundur, , "Practical Data hiding in TCP/IP", *Proceedings of the Workshop on Multimedia Security at ACM Multimedia*, 2002
- [9] Handel, T. & M. Sandford, "Hiding data in the OSI network model", *Proceedings of the 1st International Workshop on Information Hiding*, June 1996
- [10] Silman, J. "Steganography: and Steganalysis: An Overview", *SANS Institute*, 2001
- [11] Lee, Y.K. & L.H. Chen, "High capacity image steganographic model", *Visual Image Signal Processing*, 147:03, June 2000
- [12] Lin E.T. and E.J. Delp, "A Review of Data Hiding in Digital Images", JUNE 2001
- [13] Stinson, D. "Cryptography: Theory and Practice"
- [14] Cox, C., Killian, J., Leighton, T. and Shamoon, T., "Secure Spread Spectrum Communication for Multimedia", N.E.C. Research Institute, 1995
- [15] Rivest, R., Shamir, A. and Adleman, L., "A Method for Obtaining Digital Signatures and Public-Key Cryptosystems", *Communications of the ACM*, 21 (2), pp. 120-126, February 1978
- [16] Clifford Cocks, "A Note on 'Non-Secret Encryption'", *CESG Research Report*, 20 November 1973
- [17] Johnston, P., "RSA Encryption Algorithm", No Date

Application of Laplace Transform for RLC Circuit

Mya Thida Hlaing
 Department of Engineering
 Mathematics
 Technological University
 Thanlyin, Myanmar

Wah Wah Aung
 Department of Engineering
 Mathematics
 Technological University
 Thanlyin, Myanmar

Thae Thae Htwe
 Department of Engineering
 Mathematics
 Technological University
 Pathein, Myanmar

Abstract: In this paper, Laplace transform is discussed and electric circuit problem as second order nonhomogeneous linear ordinary differential equation with constant coefficients is formulated. Then, this problem is solved by using Laplace transform method and analytical method. And then, ELC circuit acting over a time-interval will be solved by applying only Laplace transform method.

Keywords: Laplace transform. Ordinary differential equation. Electric circuit. Kirchhoff's Voltage Law. Time-shifting.

1. INTRODUCTION

The Laplace transform is an integral transform in mathematics. The transform has many applications in science and engineering such as first order ODE modeling (RL & RC) circuits with no AC source and with a DC source, second order ODE modeling (series & parallel RLC) circuits with no DC source and with AC source, and so on. Laplace transform of unit step function is suitable for solving ODEs with complicated right sides of considerable engineering interest such as single waves, inputs (driving forces) act for some time only. Laplace transforms are usually restricted to functions of t with $t \geq 0$. Laplace transformation from the time domain to the frequency domain transforms second order ordinary differential equations into algebraic equations. The required solutions are obtained by applying definition and some properties of Laplace transform as follows.

1.1 Definition of Laplace transform:

Let $y(t)$ be a function of t specified for $t > 0$, then the integral $\int_0^{\infty} e^{-st} y(t) dt$ is called Laplace transform of $y(t)$ and is denoted by $L\{y(t)\}$ or $Y(s)$.

$$\text{i.e. } L\{y(t)\} = \int_0^{\infty} e^{-st} y(t) dt = Y(s)$$

1.2 Properties of Laplace transform:

Linearity property:

If $f(t)$ and $g(t)$ are any functions of t , a and b are any constants, then

$$L\{af(t) + bg(t)\} = aL\{f(t)\} + bL\{g(t)\}.$$

Laplace transform of derivatives:

If $L\{y(t)\} = Y(s)$, then

$$L\{y^{(n)}(t)\} = s^n Y(s) - s^{n-1}y(0) - s^{n-2}y'(0) - \dots - y^{(n-1)}(0).$$

Inverse Laplace transform:

If $L\{y(t)\} = Y(s)$, then $y(t) = L^{-1}\{Y(s)\}$ is called inverse Laplace transform of $Y(s)$.

S-shifting property:

$$\text{If } L\{y(t)\} = Y(s), \text{ then } L\{e^{at}y(t)\} = Y(s - a).$$

Laplace transform of unit step function:

The unit step function is a typical engineering function made to measure for engineering applications, which often involve functions are either “off” or “on”.

$$u(t - a) = \begin{cases} 0 & \text{if } t < a \\ 1 & \text{if } t > a \end{cases}$$

is also called Heaviside function.

T-shifting Property:

$$\text{If } L\{y(t)\} = Y(s), \text{ then } L\{y(t - a)u(t - a)\} = Y(s)e^{-as}$$

which is often modeled in a RLC circuit by a voltage source in series with a switch.

2. APPLICATION OF LAPLACE TRANSFORM ON ODES

This section, the definition of ordinary differential equation and the application of Laplace transform on second order linear ODE are described.

An ordinary differential equation (ODE) is a differential equation containing one or more functions of one independent variable and the derivatives of those functions.

The Laplace transform is a useful method in solving linear ODE with constant coefficients.

Consider second order nonhomogeneous initial value problem

$$y'' + ay' + by = r(t), \quad y(t_0) = k_0, y'(t_0) = k_1 \quad (1)$$

If Laplace transform on both sides of (1) is taken, the Laplace transform of derivatives and initial conditions are used, then algebraic equation is got. And then, the required solution is obtained by applying the inverse Laplace transform and s-shifting property.

Example: $y'' + 4y' + 20y = 120, y(0) = 0, y'(0) = 0.$

Solution: Taking Laplace transform on both sides

$$L\{y''\} + 4L\{y'\} + 20L\{y\} = L\{120\}$$

Using Laplace transform of derivatives and initial condition

$$(s^2 + 4s + 20)Y = \frac{120}{s}$$

$$\therefore Y(s) = \frac{120}{s(s^2 + 4s + 20)}$$

By using partial fraction method, inverse Laplace transform, and s-shifting property

$$y(t) = 6t - 6e^{-2t} \cos 4t - 3e^{-2t} \sin 4t.$$

3. MODELING RLC CIRCUIT

This section, the definition of electric circuit, Kirchhoff's Voltage Law and modeling to RLC circuit according to KVL are presented.

An electric circuit is a path in which electrons from a voltage or current source flow. The point where those electrons enter an electric circuit is called the source of electrons high-voltage direct current transmission uses big converters.

Kirchhoff's Voltage Law states that the sum of all voltages around a closed loop in any circuit must be equal to zero. This is a consequence of charge conservation and also conservation of energy.

Consider the circuits are basic building blocks of such networks. They contain three kinds of components, a resistor of resistance $R \Omega$ (ohms), an inductor of inductance L H(henrys) and a capacitor of capacitance C F(farads) are wired in series circuit, the same current flows through all components of the circuit, and connected to a generator or an electromotive force $E(t)$ V(volts), sinusoidal as in following figure

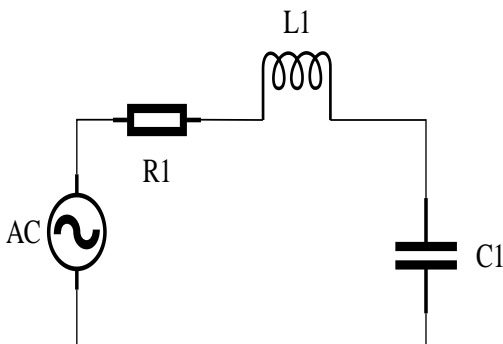


Figure1. RLC-circuit

The circuit is a closed loop, and the impressed voltage $E(t)$ equals the sum of the voltage drops across the three elements R, L, C of the loop.

According to Kirchhoff's Voltage Law, the above figure for an RLC-circuit with electromotive force

$$E(t) = E_0 \sin \omega t (E_0 \text{ constant}) \text{ as a model}$$

$$E_L + E_R + E_C = E(t) \quad (2)$$

$$Li' + Ri + \frac{1}{C} \int i dt = E(t) = E_0 \sin \omega t$$

$$\text{or } q'' + Rq' + \frac{1}{C}q = E_0 \sin \omega t \quad (3)$$

here q is the charge on the capacitor, i is the current in the

$$\text{circuit : } i(t) = \frac{dq}{dt} \text{ or } q(t) = \int i(t) dt$$

and differentiate (3)

$$Li'' + Ri' + \frac{1}{C}i = E_0 \cos \omega t. \quad (4)$$

This equation is a modeling RLC circuit as a second-order non-homogeneous linear ODE with constant coefficients.

4. APPLICATION TO RLC- CIRCUIT

Many science and technical problems are built as mathematical model in various fields. These models are solved by applying kinds of mathematical methods. Among them, now present modeling RLC circuit as second order non homogeneous linear ODE with constant coefficients by applying the analytical method and Laplace transform method. And then, solve RLC circuit problem given time interval by applying Laplace transform of time shifting property.

4.1 Analytical and Laplace transform methods application to RLC-circuit problem

A circuit has in series an electromotive force of 600 V, a resistor of 24Ω , an inductor of 4 H, and a capacitor of 10^{-2} farads. If the initial current and the initial charge on the capacitor are both zero, Find the charge and the current at time $t > 0$.

According to Kirchhoff's Voltage Law

$$E_L + E_R + E_C = E(t)$$

$$Lq'' + Rq' + \frac{1}{C}q = 600$$

$$q'' + 6q' + 25q = 150 \quad (5)$$

is second-order non homogeneous linear ODE.

Applying Analytical method

The corresponding homogeneous linear ODE of (5) is

$$q'' + 6q' + 25q = 0 \quad (6)$$

the corresponding characteristic equation of (6) is

$$\lambda^2 + 6\lambda + 25 = 0 \text{ and } \lambda = -3 \pm 4i$$

the general solution of (6) is

$$q_h(t) = e^{-3t}(A \cos 4t + B \sin 4t)$$

using the method of undetermined coefficients, $q_p(t) = 6$

then, the general solution of (5) is

$$q(t) = e^{-3t}(A \cos 4t + B \sin 4t) + 6 \quad (7)$$

differentiating (7) and using initial condition, the charge:

$$q(t) = 6 - 6e^{-3t} \cos 4t - 4.5e^{-3t} \sin 4t$$

and the current: $i(t) = 37.5e^{-3t} \sin 4t$.

Applying Laplace transform method

Taking Laplace transform on both sides of (5)

$$L\{q''\} + 6L\{q'\} + 25L\{q\} = L\{150\}$$

using Laplace transform of derivative and initial condition

$$Q(s) = \frac{150}{s(s^2+6s+25)}$$

by partial fraction method,

$$Q(s) = \frac{6}{s} - \frac{6(s+3)+18}{(s+3)^2+4^2}$$

applying inverse transform and s-shifting property,

the charge:

$$q(t) = 6 - 6e^{-3t} \cos 4t - 4.5e^{-3t} \sin 4t$$

and the current: $i(t) = 37.5e^{-3t} \sin 4t$.

4.2 Output of an RLC-circuit to a sinusoidal input acting over a time interval

An inductance of 0.4 henry, a resistor of 12 ohms and a capacitor of 0,0125 farad are connected in series with an electromotive force of $220 \sin 10t$ volts. At $t = 0$, the charge on the capacitor and current in the circuit is zero. Find the current where $E(t)$ is sinusoidal, acting for a short time interval

$$E(t) = \begin{cases} 220 \sin 10t & \text{if } 0 < t < 2\pi \\ 0 & \text{if } t > 2\pi \end{cases}$$

Modeling by KVL,

$$Li'' + Ri' + \frac{1}{C}i = E', \quad i(0) = 0, i'(0) = 0$$

$$i'' + 30i' + 200i = 550 \times 10 \cos 10t.$$

The above equation is second-order nonhomogeneous linear ODE.

Applying Laplace transform of derivative and time shifting property

$$\begin{aligned} [s^2 I(s) - si(0) - i'(0)] + 30[sI(s) - i(0)] + 200I(s) \\ = 5500 \left[\frac{s}{s^2+10^2} (1 - e^{-2\pi s}) \right] \end{aligned}$$

using initial conditions and partial fraction method,

$$I(s) = \frac{22}{s+20} - \frac{27.5}{s+10} + \frac{5.5s}{s^2+10^2} + \frac{165}{s^2+10^2} (1 - e^{-2\pi s})$$

Applying the inverse Laplace transform on both sides and t-shifting property, the current is

$$i(t) = 22(e^{-20t} - e^{-20(t-2\pi)}) - 27.5((e^{-10t} - e^{-10(t-2\pi)}),$$

5. CONCLUSIONS

Through this paper, we present the application of Laplace transform and RLC-circuit is modeled as second order nonhomogeneous linear ODE. When RLC-circuit problem is solved by applying the two methods, the charge and the current of this problem are the same in subsection 4.1. But, RLC-circuit acting over time interval can be solved by applying only Laplace transform method in subsection 4.2. Therefore, linear ordinary differential equations with constant coefficients can be easily solved by the Laplace Transform method without finding the general solution, particular solution and the arbitrary constants as analytical method. Thus, Laplace transform method is more effective tool to solve complex problems than the analytical method in various fields.

6. ACKNOWLEDGMENTS

First, the authors would like to acknowledge the support of the papers for their references. The authors are deeply grateful to their adorable benefactor parents and teachers who gave their knowledge, useful discussions, powerful encouragement, invaluable suggestions and interest help through their life.

7. REFERENCES

- [1] Laplace Transforms, "Murray. R. Spiegel," Higher Engineering Mathematics, Mc-Graw Hill Publication.
- [2] Ordinary Differential Equations, "Shepley L.Ross," Third Edition ("John Wiley & Sons," New York, 1980).
- [3] Advanced Engineering Mathematics, "Erwin Kreyszig," 9th Edition (John Wiley & Sons, New York, 2006).
- [4] Engineering Mathematics Volume II, "Madhumangal Pal and Anita Pal," 2011.
- [5] Advanced Differential Equations, "Wilsky Erasmus," India, 2014.
- [6] Electric Circuit, 9th Edition, "James W. Nilsson and Susan A. Riedel."

Design and Implementation of E-Tendering System

Aye Thida
Information Technology Engineering
Technological University(Thanlyin),
Myanmar

Aye Thu Hlaing
Information Technology Engineering
Technological University(Taungoo),
Myanmar

Abstract: E-tendering is one of the information technology tools that has been highlighted by construction industry experts to assist in changing the industry's culture and improving its processes. E-Tendering System is an internet based process wherein the complete tendering process; from advertising to receiving and submitting tender-related information are done online. This enables firms to be more efficient as paper-based transactions are reduced or eliminated, facilitating for a more speedy exchange of information. E-tendering Systems can significantly reduce the numbers of hours and bureaucracy to create and award a tender. The aim of this paper is to provide tendering services easily and conveniently for city-staff and company, to create tender for bidding their requirements and for the users who want to bid opening tender related to their company, to automate manual activities currently performed in the tendering process. E-tendering System can significantly improve the efficiency and time taken to complete a purchasing process, many of the activities listed above can be managed efficiently. It is implemented by Struts, Spring, Hibernate framework based on Web Application Features. Java platform provides all of the tools and technologies that are needed to build distributed web application. Java is the dominant Web programming language today, and is used extensively by the Open Source community. In this paper, Fedora redhat linux OS is used to implement the web design for E-tendering Services. This system is Web application system depends on this framework concept and uses Hibernate Query Language to test the database. With the achievement of this paper, it is easy to understand how to create E-tendering services with linux administration approaches.

Keywords: E-tendering; Open Source; Fedora redhat linux Operating System; Hibernate Query Language; Struts; Spring

1. INTRODUCTION

E-Tendering system is a web based application intended for online users for replacing the manual paper-based tender processes. The E-Tender system is to provide the interface between the tender buyers and the sellers on the internet. E-tendering is the process where the physical tendering activity is carried out online using the internet and associated technologies. Our E-tendering system consists of four-Users: Admin, City Staff, Company and Citizen.

This system allows tender board Admin to manage tenders through a web site. Companies can submit bids online and upload documents. The companies can modify their bids till the tender bid submission closing by the admin. The Admin subsystem is to give services for city-staff (tender-board who create tenders. All the citizens can see the information of the published tenders by visiting our E-tendering web-site.

The main objective of this system is to provide tendering services easily and conveniently for city-staff and company. Admin must be to create, update, delete the tender and decide the winner for the tender. The current manual system the company has decided to automate the current system into the computer application as the website.

Company has an opportunity to bid the tender by putting the bidding price and the application document. And so process for registration and the searching the tenders becomes easy and fast. So the system helps to save the time at the both site. Other users can browse the tender-information and winner company information for all disclose tender (which means the winner company is chosen for that tender).

2. ARCHITECTURE DESIGN

This system is implemented by Struts, Spring and Hibernate framework based on Web Application Features. This is an

open-source framework that in combination with standard Java Technologies like Java Servlets, Java Beans, and XML helps in effective development of web application. This system is Web application system depends on this framework concept and uses Hibernate Query Language to test the database.

2.1 Advantage of Linux Operating System in Networking

Linux is open source operating system first developed and released to the world by in 1991. Linux has been adapted to include support for non-Intel processor and even multiple processors, sophisticated TCP/IP networking facilities. And Versions of Linux are now available for many computer models. Linux is distinguished from many popular operating systems in three important ways. The first is that Linux is a cross-platform operating system. The second fact is that Linux is free: Linux is free or nearly free in an economic sense. And then Linux and many Linux applications are distributed in source form. This makes it possible for users to modify or improve Linux. Because of this freedom, Linux is being constantly improved and updated. The key advantage of Linux operating system is network configuration. The most important and fundamental configuration for a server is network configuration [1].

2.2 Functional Requirement

The online tendering system consists of four sub-systems. One is the *City Staff* subsystem that all cities will use this system to create tender for bidding their requirements. One is the *Company* Subsystem that they can bid opening tender related to their company. Another is the *Citizen* that they can see which company is winner after tender disclosed. Another one is the *Admin* that they can control all of the system and can decide the winner after tender closed.

3. SYSTEM DESIGN

There are four main processes in e-tendering system. The overall system design for proposed system is shown in Figure 1 and actor in use case diagram is shown in Table 1.

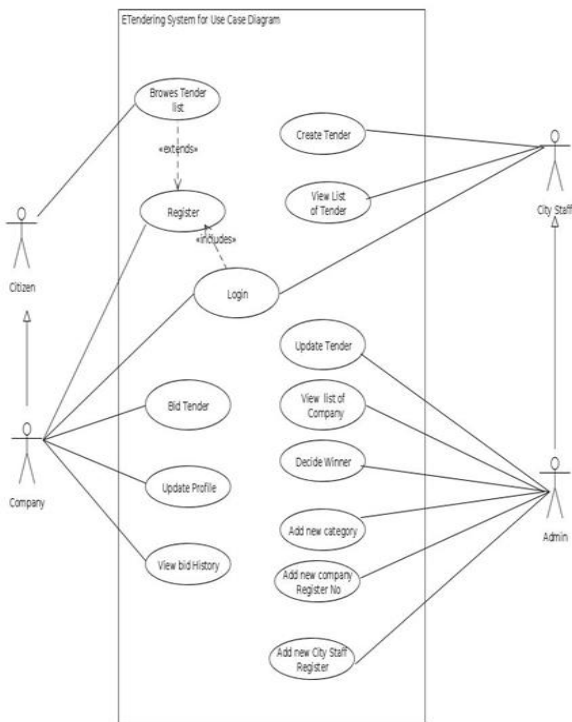


Figure 1. Use Case Diagram for E-tendering System

Table 1. Actor in Use Case Diagram

No	User	Description
1	Company	Company must be view tender list the E-Tendering system to make and create tender by making registration to the system.
2	City Staff	City Staff must be registered user, authorized person in your universities or Companies who can make tender submission.
3	Admin	Admin must be registered user, authorized person in your universities or companies who has the admin role and this system to choose winner company.
4	Citizen	All citizens in the country who view tender list and winner company list of disclosed tender.

3.1 Database Design

E-Tendering system needs four users in general. The following things are that they can do in the system.

User can do: Registration as member, Login if member, Search tender by category/ subcategory, View Bid History, View Profile, Update Profile Logout.

City Staff can do: Login, Create Tender, View List of Tender, Update City Staff Profile, Logout.

Admin can do: Login, List of Tender, Add category/ subcategory, Create Tender, Update Tender, List of City Staff, List of Company, Add City Staff, Add Company Registration Number, Decide Winner, List of Winner, J Free Chart, Logout.

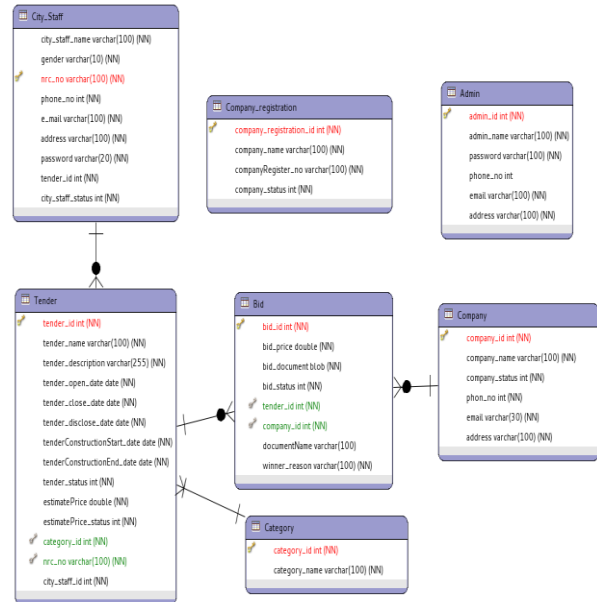


Figure 2. Entity Relationship Diagram for E-Tendering System

3.1.1 CRUD Matrix

CRUD stand for Create, Refer, Update and Delete is four basic functions of persistent storage and it is used for bottom-up data modeling to analyze when and what events happens to each entity and its attribute. CRUD matrix for e-tendering system is shown in Table 2.

Table 2. CRUD Matrix for E-tendering System

User	Citizen	Company	Admin	City Staff
Entity				
company registration	-	-	C,R,U,D	-
city-staff	-	-	C,R,U,D	R,U
Bid	-	C,R	R,D	R
tender	R	R	R,U,D	C,R,U
category	R	R	C,R,U,D	R
company	-	C,R,U	R,D	R

4. IMPLEMENTATION OF PROPOSED SYSTEM DESIGN

When the user is entered the client URL of the application in the browser, the home page of the application will be occurred where search menu bars and the list of open status tenders are displayed.

User can search the desired tender in three ways; by choosing the category or by selecting open date or close date as shown in Figure 3. The user can see the tender name, tender category, status, open date, close date and Disclose date in the list of tender. A link to show the tender detail information is also provided.



Figure 3. Citizen Home page with Search Menu Bar

The open tender detail page is shown in Figure 4. The user can view the detail information of specific tender without register for login. Whenever user wants to bid the tender, he has to login as the first task. If he click “Bid” button, login page will appeared as shown in figure 5.



Figure 4. Open Tender Detail Page

A new user can make registration by clicking the registration link as shown in Figure 5. In Figure 6, the “***” beside the label indicates the required field for successful registration on the site.

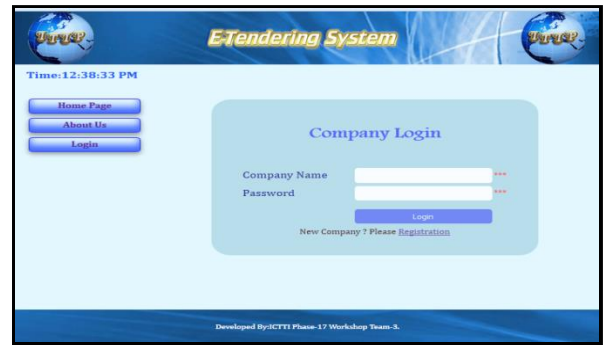


Figure 5. Company Login Page for Bid



Figure 6. Company Registration Page

If the user fills the required information completely and correctly, user can click the “Register” Button and confirmation page will appear and registration successful page will be displayed as shown in Figure 7.



Figure 7 - Citizen Registration Successful Page

When the user clicks the save button, the user information is submitted for registration and our system reply the congratulation mail to successfully registered company and will displayed “Congratulation Message”.

The company (user) can enter into the system by inserting correct login name and password. If the login process is success, the user can see the company home page of his/her

account and the company user can view bid history, view their profile and update their profile as shown in Figure 8.



Figure 8. Welcome Page for Company

In the list of tender, a detail link will show the detail information of tender. In detail information, “count” shows how many number of company already bid this tender. For further information, company can see the list of company through the count link.

For disclosed tenders, the system will describe the winner in the list of company as shown in Figure 9. The company (user) can see the “Bid” button to bid the open tender. And then, the user can bid the interested tender by offering bid price and uploading document.



Figure 9. Bid History Page for Company

At the city staff home page, the user who is the city staff can see latest 10 tenders list with their status and he/she can also click “First”, “Prev”, “Next”, “Last” link to see another tenders. City staff can search tender by Category Name, Tender Name, Tender Open Date and Close Date. City staff can view each interested tender detail information by clicking “Detail” link. The city staff can view the list of tenders that he/she created by clicking “View List of Tender” link. The city staff can also update information of tender when the status is in “Create” state as shown in Figure 10.



Figure 10. City Staff Home Page

The admin can do all the operations of city-staff together with admin operations such as: add company information, add new category and city staff information as shown in Figure 11. Moreover, Admin can block the black list company and the dismissed city staff and also unblock them if needed. Admin can also view the city-staff member list. Admin can see the all list of tender as available in our system. Admin can update and delete tender when tender is “create” status through the “List of Tender” link. Admin can retrieve and view the chart for tender report by year through ‘Jfree Chart’ link as shown in Figure 12.



Figure 11. Admin Home Page

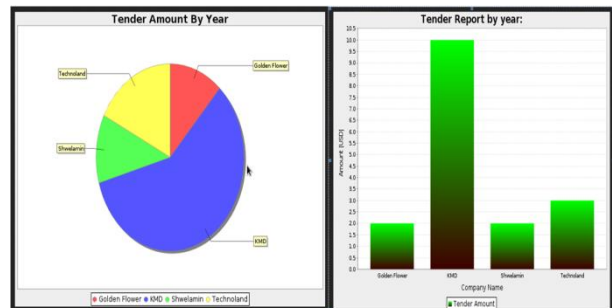


Figure 12. Pie Chart and Bar Chart for Tender Report

5. CONCLUSION AND DISCUSSION

The e-tendering system is a web based system that can be accessible by all city-staff to prepare their tenders and publish

them using the system. Moreover, the companies can also view the available tenders on-line and submit their bid on-line. Winner Company can receive an e-mail from our e-tendering system. Furthermore, all the citizens who do not involve in tendering process can view the tender information and winner information of the tenders. The system makes the tendering process more convenient for both the city-staff and companies. All the necessary data for the tendering process is stored on an RDBMS at the server side. The server processes all of user requests based on the user type and give appropriate response according to the requests. This system was designed into four modules; first one for the client who wishes to access the system as viewers (citizens), the second one is bidders (company). Third is for the city-staff who can create the tenders and fourth module is the admin who manage the tenders and city-staff. The e-tendering system is the most widely used and popular in this current day. The system can be used easily and have many benefits. In the next year, the system can be widely expressed and convenient for tender management process for tender board staff and admin and bidding process for companies.

6. ACKNOWLEDGMENTS

The author would like to thank to her family and partners who have contributed towards development of this work.

7. REFERENCES

- [1] Y.Kogure, T.D. Phyu, E.E. Khin, 2008, “Fundamental Linux”, ICTTI Union of Myanmar.
- [2] Betts, M., Black, P., Christensen, S., Dawson, E., Du, R., Duncan, W. Foo, E. & Gonzalez, J. (2006) Towards Secure and Legal E-tendering. IT con, Vol.11, Special Issue e-commerce in construction, pg. 89–102.
- [3] BCIS (2006) 2006 eTendering Survey Report, RICS, 2006.
- [4] BCIS (2009) 2009 eTendering Survey Report, RICS, 2009.
- [5] Booty, F. (2004) “Does E-Tendering Represent the Future Marketplace?” Available at: www.rics.org/ricsms/bin/show?class=Feature&template=/includes/feature (Accessed 16 September 2008).
- [6] Brown, C. (2006) The Role of Electronic Documentation Improving Production Line Efficiencies. Available at: <https://aerade.cranfield.ac.uk/bitstream/1826/1625/1/Brown-2006.pdf> (Accessed 10 October 2008).
- [7] Horsman, L. (2001) “Electronic Tendering System from the OGC”. Available at: www.sourceuk.net/articles/a01619.html (Accessed 10 October 2008).

Design of Centrifugal Pump Volute-Type Casing

Khin Sandi Cho
Department of Mechanical
Engineering
Technological University
Hpa-an, Myanmar

Aye Thida San
Department of Mechanical
Engineering
Technological University
Patein, Myanmar

Soe Myat Thu
Department of Mechanical
Engineering
Technological University
Mawlamyine, Myanmar

Abstract: Every centrifugal pump has four main components, namely, casing, impeller, suction pipe and discharge pipe. The important principles and fluid mechanics theories on centrifugal pump are introduced in firstly. The detailed design procedure for volute type pump casing is carried out.

In this paper, various kinds of pumps and operational sequences are described. And then, application and characteristics of centrifugal pump are also expressed. This paper relates to the design of casing of single-suction centrifugal pump that can develop a head of 30m and discharge 1.7m³/min of water at the speed of 1880 rpm. The designed impeller has 115 mm inlet diameter, 256 mm outlet diameter, 19.5° inlet vane angle and 22.5° outlet vane angle. The number of vanes is 6. The outlet width is 15mm. The discharge diameter is 3in (96mm) to operate the designed head and capacity. The maximum efficiency of the pump is 72 %. The designed single-suction centrifugal pump can fulfil the requirements of agricultural processes.

Keywords: Centrifugal pump; Fluid mechanic; Volute type casing; Single-suction pump; Pump casing design.

1. INRODUCTION

Centrifugal pump is the device for converting of mechanical energy of the drive shaft to hydraulic energy of the handling fluid to get it to the required place or height by the centrifugal force of the impeller blade and the change in pressure and velocity in the volute casing. The input power for centrifugal pump is the mechanical energy of the drive shaft driven by the prime mover such as electrical motor. The output energy is hydraulic energy of the fluid being raised or carried. So, its purpose is to provide the necessary pressure to move the fluid at the desired rate.

The centrifugal pump moves liquid by rotating one or more impellers inside a volute casing. The liquid is introduced through the casing inlet to the eye of the impeller where it is picked up by the impeller vanes. The rotation of the impeller at high speeds creates the centrifugal force that throws the liquid along the vanes, causing it to be discharged from its outside diameter at a higher velocity. This velocity energy is converted to pressure energy by the volute casing prior to discharging the liquid to the system.

2. GENERAL DESCRIPTION OF CENTRIFUGAL PUMP

The centrifugal pump is so called because the pressure increase within its rotor due to centrifugal action is an important factor in its operation.

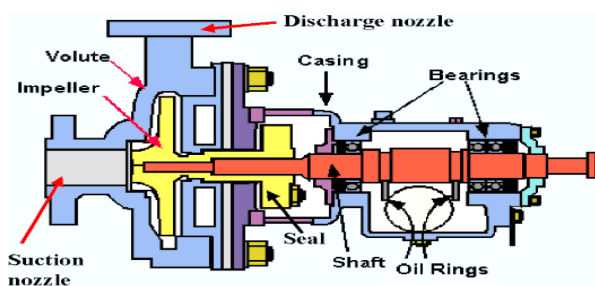


Figure 1. Single-suction Centrifugal Pump

In the single suction pump, the water enters the impeller from only one side. Because of this action, a single-suction

centrifugal pump impeller is exposed to a large axial hydraulic thrust force resulting from the unbalanced hydraulic pressure on the impeller. This force tends to move the impeller away from the suction side. “Figure 1” shows a single-suction pump.

2.1 Volute-Type Centrifugal Pump Casing

In a volute casing, the impeller discharges into a single casing channel of gradually increasing area called a volute, and the major part of the conversion takes place in the conical discharge nozzle. The volute centrifugal pump has no diffusion vane but instead of the casing and is of a spiral type. The casing is as shown in “Figure 2”. So it makes as to produce an equal velocity of flow at all sections around the circumference and also to gradually reduce the velocity of the water as it flows from the impeller to the discharge pipe. The spiral is often called the nozzle. A centrifugal pump volute increases in area from its initial point until it encompasses the full 360 degrees around the impeller and then flares out to the final discharge opening. The wall dividing the initial section and the discharge nozzle portion of the casing called the tongue of the volute, or the cut-water.

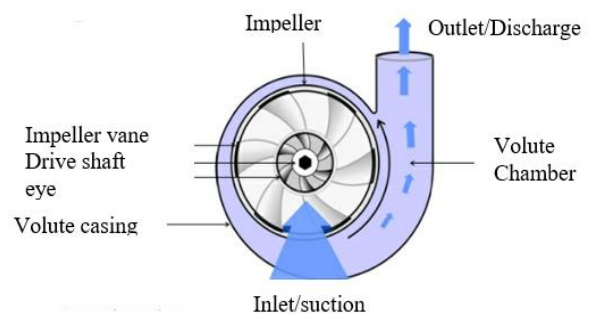


Figure 2. Volute Casing

3. DESIGN CONSIDERATION OF CENTRIFUGAL PUMP VOLUTE CASING

The hydraulic design of an end section single-stage centrifugal pump casing for fresh water is considered by the following:

3.1 Specific Speed

Using equation, we can calculate the specific speed, n_s (rpm) is considered,

$$n_s = n \frac{\sqrt{Q}}{H^{3/4}} \quad (1)$$

Pump efficiency η is assumed by using “Figure 3”. And also the diameter of suction pipe D_s (or d_s) can be estimated from this chart. The discharge pipe diameter D_d (or d_d) is usually selected equal to or one size smaller than that of the suction pipe. Thus, velocities in these pipes are given by

$$V_s = \frac{Q_s}{\pi \frac{D_s^2}{4}} \quad (2)$$

$$V_d = \frac{Q_s}{\pi \frac{D_d^2}{4}} \quad (3)$$

The inner diameter, ID corresponding to D_s or D_d shown in “Table 1” is substituted for D_s or D_d in the above equations to calculate each of these velocities.

3.2 Input Power

The input power, L (W) is considered by

$$L = \frac{\rho Q_s g H}{\eta} \quad (4)$$

Rated output of an electric motor, L_r (KW) is decided from the following equation.

$$L = \frac{(1 + F_a) \times L}{\eta_{tr} \times 1000} \quad (5)$$

Where, F_a is the allowance factor, and 0.1~0.4 for an electric motor and larger than 0.2 for engines. η_{tr} is the transmission efficiency, and 1.0 for direct coupling and 0.9~0.95 for belt drive. If an electric motor is used for driving a pump, “Table 2” is used for its selection.

3.3 Hub and Shaft Diameters

The diameter of the end of main shaft d_c is calculated from the next equation.

$$d_c \geq 0.3653 \sqrt[3]{\frac{L_h/n}{\tau_{al}}} \approx k \sqrt[3]{\frac{L_h}{n}} \quad (6)$$

The shaft diameter at the hub section d_{sh} is selected so as to satisfy $d_{sh} > d_c$. The dimension of hub at the impeller eye are usually decided from

$$\text{Diameter: } D_h = (1.5 \sim 2.0) d_{sh}$$

$$\text{Length: } L_h = (1.0 \sim 2.0) d_{sh}$$

The diameter of impeller eye D_o is calculated from the following equation.

$$D_o = \sqrt{\frac{4Q_s}{\pi V_{mo}} + D_h^2} \quad (7)$$

Where the velocity at the eye section is given by

$$V_{mo} = K_{mo} \sqrt{2gH} = (1.5 \sim 3.0) \leq V_{m1} \quad (8)$$

$$K_{mo} = (0.7 \sim 0.11) + 0.00023n_s$$

3.4 Impeller

3.4.1 Stepanoff Chart

The stepanoff chart shown in “Figure 5” is widely used to decide the impeller geometry. If the blade outlet angle β_{b2} near 22.5° is selected. The parameters K_u (speed constant),

K_{m1} , K_{m2} , and $\frac{D_1}{D_2}$ are obtained, since n_s is given. Thus,

$$U_2 = K_u \sqrt{2gH} \quad (9)$$

$$V_{m1} = K_{m1} \sqrt{2gH} \quad (10)$$

$$V_{m2} = K_{m2} \sqrt{2gH} \quad (11)$$

3.4.2 Impeller Outlet

The outlet diameter D_2 is decided considering the following relationship;

$$D_2 = \frac{U_2 \times 60}{\pi \times n} \quad (12)$$

The blade exit angle is set by the following,

$$\beta_{b2} = 22.5 \text{ (15 deg } \sim 35 \text{ deg)}$$

3.4.3 Impeller Inlet

The inlet diameter is considered from $D_1 = D_2 \left(\frac{D_1}{D_2} \right)$.

Thus, the peripheral velocity at the inlet is:

$$U_1 = \frac{\pi D_1 n}{60} \quad (13)$$

The blade inlet angle β_{b1} (deg) is considered by,

$$\beta_{b1} = \tan^{-1} \left(\frac{K_{b1} V_{m1}}{U_1} \right) \approx \tan^{-1} \left(\frac{V_{m1}}{U_1} \right) + (0 \sim 6) \quad (14)$$

where, $K_{b1} = 1.1 \sim 1.25$

3.4.4 Blade number

The number of impeller blade Z is decided by the following,

$$Z = 6.5 \frac{D_2 + D_1}{D_2 - D_1} \sin \left(\frac{\beta_{b1} + \beta_{b2}}{2} \right) \quad (15)$$

When the impeller is made of bronze (e.g BC6), the minimum blade thickness is 2.0 mm and shroud thickness is 2.5 mm for an impeller having the diameter less than 200 mm. They are 2.5 and 3.0 mm respectively, if D_2 is greater than 200 mm.

3.4.5 Passage width

The width at the inlet b_1 and that of outlet b_2 are respectively decided based on the following equations where smooth variation in velocity is considered.

$$b_1 = \left[\frac{Q_s}{\pi D_1 V_{m1}} \right] \left[\frac{\pi D_1}{\pi D_1 - s_1 Z} \right] \text{ or } \left[\frac{Q_s}{\pi D_1 V_{m1}} \right] \quad (16)$$

$$s_1 = \frac{\delta_1}{\sin \beta_{b1}}, \quad s_2 = \frac{\delta_2}{\sin \beta_{b2}}$$

where, δ_1 = blade thickness near the leading edge (mm)
 δ_2 = blade thickness near the trailing edge (mm)

$$b_2 = \left[\frac{Q_s}{\pi D_2 V_{m2}} \right] \left[\frac{\pi D_2}{\pi D_2 - s_2 Z} \right] \quad (17)$$

3.5 Casing

3.5.1 Average Flow Velocity in the Volute Casing

The average volute velocity V_v is determined from the relationship;

$$V_v = K_v \sqrt{2gH} \quad (18)$$

where, V_v = average flow velocity in the volute casing (m/s)

K_v = experimental design factor
 g = gravitational acceleration (m/s²)
 H = head required (m)

So, to find the average flow velocity in the volute at the cut water, it is required to know the values of K_v , required head (H). The gravitational acceleration is 9.81 m/s².

The value of K_v varies with the specific speed of the design pump. It is determined by using the Volute Constants Chart as shown in "Figure 4". This chart is the value of specific speed versus the values of K_v , volute angle α_v , and the ratio of $(D_3 - D_2)/D_2$.

3.5.2 Volute Areas

Since the volute casing is divided into eight volute sections of 45° angular spacing, which increase in proportion from cut-water to discharge nozzle and the average velocity in the volute at the cut-water V_v is used, the A_v is the volute area at the throat. It can be estimated by,

$$A_v = \frac{Q_s}{V_v} \quad (19)$$

where, A_v = volute area at throat (m²)
 Q_s = flow rate per second (m³/s)
 V_v = average flow velocity in the volute at the throat (m/s)

The value of Q_s is estimated by;

$$Q_s = \frac{Q}{60}$$

Since the volute casing is divided into eight sections A_v is the volute area at the throat and it is denoted by A_{v8} representing the area of volute section 8. Then, other volute sections are estimated by,

$$A_{vi} = A_v \times \frac{i}{8} \quad (20)$$

Where, the value of i is from 1 to 8 representing the volute sections.

3.5.3 Other Requirements for Laying out Volute Casing

Other requirements are the values of ρ_{vi} , r_{vi} for laying out the cross-sectional shapes of volute sections.

The relationship between A_{vi} , ρ_{vi} and b_v is:

$$A_{vi} = 0.367 \rho_{vi}^2 - 0.604 b_v \quad (21)$$

where, A_{vi} = volute section area (mm²)

b_v = volute width (mm)

ρ_{vi} = parameter for laying out cross-sections of volute areas (mm)

Thus, after solving for ρ_{vi} ;

$$\rho_{vi} = \sqrt{\frac{A_{vi} + 0.604 b_v^2}{0.367}} \quad (22)$$

For, $i = 1$, i.e, for drawing the cross-sectional shape of the first volute section.

The relationship between r_{vi} and ρ_{vi} is:

$$r_{vi} = 0.206 \rho_{vi} \quad (23)$$

where, r_{vi} = the radius of volute tangent circle (mm)

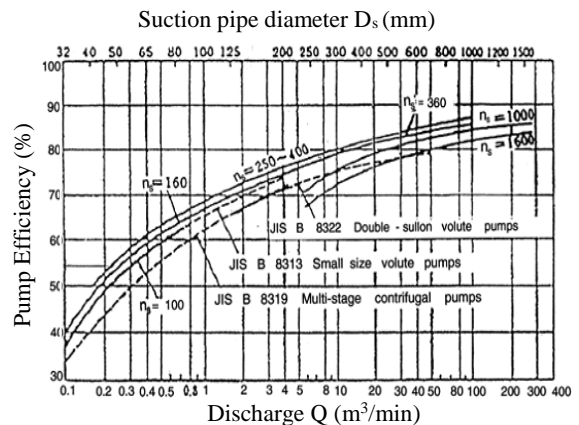


Figure 3. Pump Efficiency versus Discharge with vary Specific Speed

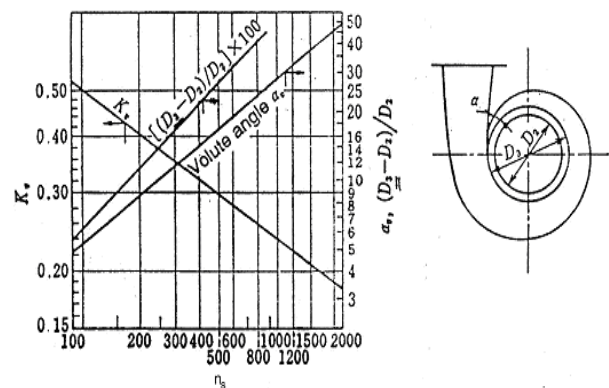


Figure 4. Volute Constant Chart

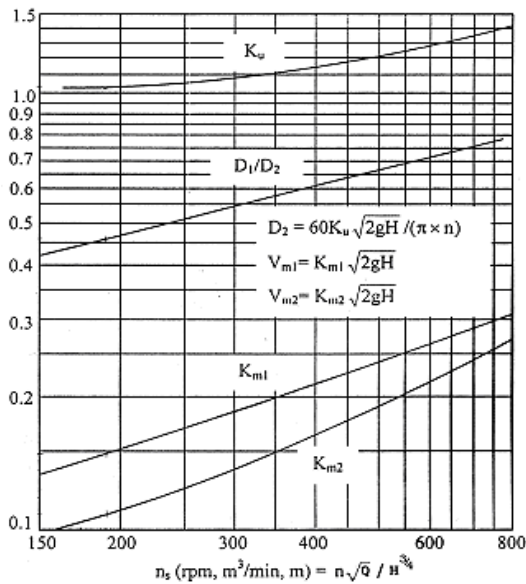


Figure 5. Stepanoff Chart

Table 1. Dimensions of Steel Pipe (S.G.P)

Nominal Pipe Size: A	Nominal Pipe Size: B	ID (mm)
40	1.5	41 6
50	2.0	52 9
65	2.5	67 9
80	3.0	80 7
100	4.0	105 3
125	5.0	130 8
150	6.0	155 2
200	8.0	204 7
250	10	254 2
300	12	304 7
400	16	390.6
500	20	492.2

Table 2. Rated Output of Electric Motor

Rated output (KW)	Allowance factor Fa
0.4	0.4
0.75	
1.5	
2.2	0.4-0.25
3.7	
5.5	
7.5	0.25-0.15
11	
15	
18.2	
22	
30	
37	

4. DESIGN CALCULATION OF CENTRIFUGAL PUMP VOLUTE CASING

The known parameters from impeller calculation are:

Flow rate, $Q = 1.7 \text{ m}^3/\text{min}$
 Head, $H = 30 \text{ m}$
 Specific speed, $N_s = 191.22 \text{ rpm}$
 Suction pipe diameter, $D_s = 128 \text{ mm}$
 Impeller diameter at outlet, $D_2 = 256 \text{ mm}$
 Shroud thickness, $= 3 \text{ mm}$
 Impeller outlet width, $b_2 = 15 \text{ mm}$

4.1 Calculation of Average flow velocity

The average flow velocity can be calculated by the Equation (18).

From "Figure 4", $K_v = 0.41$

$$V_v = K_v \sqrt{2gH}$$

$$= 0.41 \sqrt{2 \times 9.81 \times 30}$$

$$= 10 \text{ m/s}$$

4.2 Calculation of Volute Areas

The volute areas can be calculated by the Equation (19).

$$A_v = \frac{Q_s}{V_v}$$

$$= \frac{1.7}{10 \times 60}$$

$$= 2.833 \times 10^{-3} \text{ m}^2$$

$$= 2833 \text{ mm}^2$$

From Equation (20),

$$A_{vi} = A_v \times \frac{i}{8}$$

For $i = 1$

$$A_{v1} = A_v \times \frac{1}{8}$$

$$= 2833 \times \frac{1}{8}$$

$$= 354.125 \text{ mm}^2$$

4.3 Calculation of Volute Base Circle Diameter

The volute base circle diameter, D_3 can be determined by ratio;

$$\text{ratio} = \frac{(D_3 - D_2)}{D_2} \times 100$$

From "Figure 4",

The value of this ratio is 11 at $n_s = 191.22 \text{ rpm}$.

$$D_3 = \frac{\text{ratio} \times D_2}{100} + D_2$$

$$= \frac{11 \times 0.256}{100} + 0.256$$

$$= 284.16 \text{ mm}$$

4.4 Calculation of Volute Width

Volute width can be estimated in two ways.

The first method,

$b_v = b_2 + 2 \times \text{shroud thickness} + 2 \times \text{clearance on each side of impeller}$

$$= 15 + (2 \times 3) + (2 \times 4.5) = 30 \text{ mm}$$

Clearance on each side of impeller is according to the designer's choice.

The second method,

For low specific speed pump i.e ($100 \leq N_s \leq 500$)

$$b_v = 2 b_2 = 2 \times 15 = 30 \text{ mm}$$

So, b_v is taken as 30 mm.

4.5 Calculation of Volute Angle

Volute angle is read from volute constant chart if specific speed of the design pump is known.

The specific speed N_s being 191.22 in this design.

So, the volute angle $\alpha_v = 8.5^\circ$.

4.6 Calculation of Volute Wall Thickness

Volute wall thickness is chosen according to suction pipe diameter by using the following "Table 3".

Table 3. Suction Pipe Diameter versus Volute Wall Thickness

Suction pipe diameter (mm)	40~80	100~250	300	400	500
Mini-thickness (mm)	5	6	8	10	12

Since the suction pipe diameter is 128 mm in this design.

So, the volute wall thickness $t_v = 6$ mm

4.7 Calculation of Other Requirements for Laying out Volute Casing

Other requirements are the values of ρ_{vi} , r_{vi} for laying out the cross-sectional shapes of volute sections.

ρ_{vi} can be calculated by the Equation (22).

$$\rho_{vi} = \sqrt{\frac{A_{vi} + 0.604b_v^2}{0.367}}$$

For $i = 1$,

$$\rho_{v1} = \rho_1 = \sqrt{\frac{A_{v1} + 0.604b_v^2}{0.367}}$$

$$\rho_1 = \sqrt{\frac{(354.125 + 0.604 \times 30^2)}{0.367}} = 49.458 \text{ mm}$$

Similarly, the same calculation procedure is repeated for the values of i from 1 to 8.

r_{vi} can be calculated by the Equation (23).

$$r_{vi} = 0.206 \rho_{vi}$$

For $i = 1$,

$$r_{v1} = 0.206 \rho_{v1}$$

$$= 0.206 \times 49.458 = 10.188 \text{ mm}$$

This calculation procedure is repeated according to the volutes of i from 1 to 8 all volute sections. The overall calculated results are shown in following "table 4".

Table 4. Volute Areas and Parameters for Laying out Cross-sectional Shapes of Volute Sections

i	A_{vi} (mm ²)	ρ_{vi} (mm)	r_{vi} (mm)
1	354.125	49.458	10.188
2	708.250	58.404	12.031
3	1062.375	66.151	13.627
4	1416.500	73.081	15.055
5	1770.625	79.409	16.358
6	2124.750	85.268	17.656
7	2478.875	90.750	18.695
8	2833.000	95.919	19.759

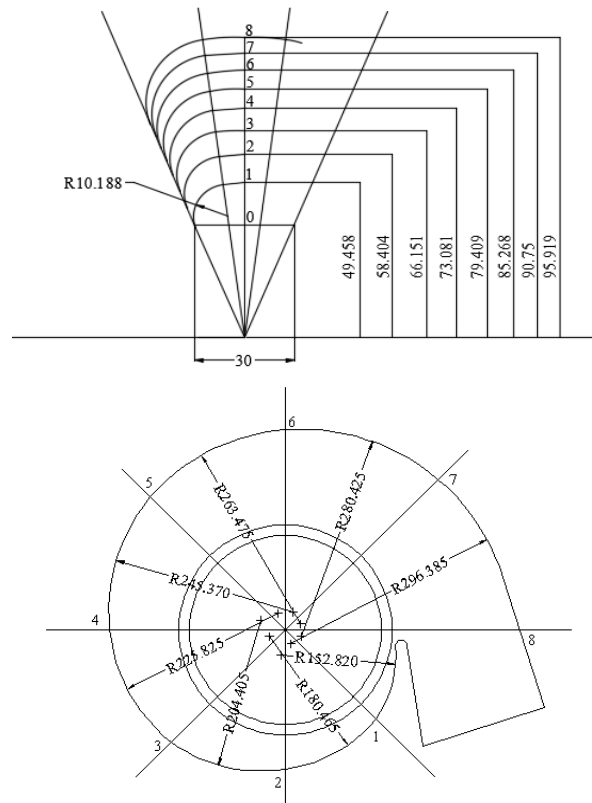


Figure 6. The Layout of Centrifugal Pump Volute Casing

4.8 Results and Discussion

In this paper, the casing is designed for the end-suction single stage centrifugal pump for fresh water.

The design pump is 18 hp motor drive single state centrifugal pump. The designed pump can develop a head at 1880 rpm. The designed impeller has 115 mm inlet diameter, 256 mm outlet diameter, 19.5° inlet vane angle and 22.5° outlet vane angle. The number of vanes is 6. And then, the outlet width is 15 mm. The diameter of discharge flange is 3 in 96 mm. The maximum efficiency of this pump may be obtained in 72%.

The design of volute is calculated depending on the impeller outlet diameter and impeller outlet width. In the design, the volute base circle diameter is 284 mm and it is used the laying out the volute casing. Volute width is 30 mm to draw the start of volute casing. According to suction pipe diameter, the volute wall thickness is 6 mm because the suction pipe diameter is 128 mm.

In this design, the volute casing is divided into eight volute sections of 45° angular spacing, which increase in proportion from cut-water to discharge nozzle. The design of volute areas or sections is very important in designing the volute casing. So, the volute area at the throat is calculated for eight volute sections from the value of average flow velocity in the volute casing. Volute angle is 8.5° and it is read from volute constant chart. After design calculation procedure, the layout of pump casing is drawn with AutoCAD. The results of calculated and existing are not much different. These are expressed in the following “table 5”.

Table 5. Comparison of Calculated and Existing Results

Type	D ₁ (mm)	D ₂ (mm)	D ₃ (mm)	b _v (mm)
Calculating Result	115	256	284	30
Existing Result	119	265	295	31
Percentage Error	3%	3%	4%	3%

5. CONCLUSION

The design pump is a single stage single-suction centrifugal pump. In Myanmar, this type is used in irrigation of farmland. It has advantage of simple construction rationally. It is easy for installation, operation and maintenance. So this type is chosen for the paper.

According to the table 5, it can be seen that the error percentages are little difference between the calculation and existing results. It is due to system of unit conversion (SI or old unit SI). As a result, tables and figures cannot be read definitely and base design may be low or high in range. However, design calculation results of volute casing of centrifugal pump are satisfied in design.

6. ACKNOWLEDGMENTS

The author wishes to thank and always ready to acknowledge to all who support her to do this paper.

7. REFERNECES

- [1] Higgins, 1926, “Centrifugal Pumps their Design, Operation and Testing”.
- [2] Frank A. Kristal and F. A. Annett, 1953, “Pumps Types, Selection, Installation, Operation and Maintenance”, Second Edition, Mcgraw-Hill Book Company, Inc.
- [3] Stepanoff , A.J. 1957, “Centrifugal and Axial flow Pumps”, John Willy and Sons, Inc.
- [4] Igor. J. Karassik and Roy Carter 1960, “Centrifugal Pumps Selection, Operation and Maintenance”, Megraw-Hill Book Company.
- [5] Igor. J. K, William.C. K, Warren. H.F and Joseph. P.M. 1976, “Pump Handbook”.
- [6] Haman, Dorota Z., Fedro S. Zazuteta and forrest T. Izuno.

- 1994, “Selection of Centrifugal Pumping Equipment”, <http:// www. edis. ifas. Ufl.dea>.
- [7] Kyushu Institute of Technology. 1996, “Fluid Mechanics of Turbomachinery”.
- [8] Khin Maung Aye, U. December, 2000, “Fluid Machinery for Mechanical Engineers”.
- [9] Robert L, Daugherty and Joseph B. Franzini. 2001, “Fluid Mechanics with Engineering Application”, Sixth Edition, Mcgraw-Hill Book Company.
- [10]Raymond C. Binder. 2002, “Fluid Mechanics”, Fourth Edition, Constable and Company Ltd.
- [11]Tyler G. Hicks and T.W. Edwards. 2003, “Pump Application Engineering”, Mcgraw- Hill Book Company.

Thermal Calculation for Converted CNG Engine (Radiator)

Khaing Thida
Department of Mechanical
Engineering,
Technological University
Thanlyin, Myanmar

Aye Nwe Moe
Department of Mechanical
Engineering,
Technological University
Thanlyin, Myanmar

Phyo Wai Lynn
Department of Mechanical
Engineering,
Technological University
Thanlyin, Myanmar

Abstract: Natural gas has been considered as one of the most promising alternative fuel for Transportation due to its ability to reduce regulated pollutants, cost and as safe as other fuels like gasoline and diesel. This thesis expresses about cooling system of converted CNG engine. In converted CNG engine, the engine cooling system has been increased because a medium working temperature has been increased. Engine cooling system is closely related with overall performances of an engine, including reduction of fuel consumption, decrease of air pollution, and increase of engine life. Radiator is the heart of cooling system. Compact heat exchangers have been widely used in various applications in thermal fluid systems including automotive thermal management systems. Radiators for engine cooling systems, evaporators and condensers for heating ventilation and air conditioning (HVAC) systems, oil coolers, and intercoolers are typical examples of the compact heat exchangers that can be found in ground vehicle. Among the different types of heat exchangers for engine cooling applications, cross flow compact heat exchangers with flat tube and flat plate fins are of special interest because of their higher rejection rate capability with the lower flow resistance.

Keywords: Converted CNG Engine, Water Cooling system, Thermal calculation, Radiator, Fin

1. INTRODUCTION

Natural Gas Vehicle (NGVs) that operate on compressed natural gas (CNG) fuel expected to find widespread use from the standpoint of promoting global environment protection and effective utilization of energy resources. This is because NGVs can be effective in preventing air pollution and global warming and also in coping with the future depletion of oil resources.

The union of Myanmar is endowed with plenty of natural resources. Petroleum and natural gas are among the rich terrestrial and aquatic resources and there lie a large deposit of them inland a well a off-shore. At such a time like this, it is good news that there is an abundant reserve of natural gas and that CNG engines can be used in place of petrol and diesel engines. Myanmar possesses many natural gas fields. As Myanmar can produce enough gas for vehicles, the CNG substitution plan is in accord with the nation's requirements.

CNG as an alternative fuel in an engine could be divided into three main types; Dual Fuel (Diesel-CNG), Bi-Fuel (Gasoline-CNG) and Dedicated/Mono Fuel. In our country, the dedicated conversion system is more useful. In converted CNG engine, cooling system has been increased because a medium working temperature has been increased.

As shown in **figure (1)** the CNG fuelled operation generated higher coolant temperature for all engine speeds compared to that of gasoline engine. These results demonstrated that CNG generated higher heat load into the cooling system compared to that of gasoline for all engine speeds. The higher coolant temperature of the CNG occurred presumably due to the higher auto ignition temperature. The CNG has 630°C of auto ignition temperature compared to that

of gasoline in the value of 315.60°C. At engine speed 1500 rpm, the coolant temperature for the CNG operation is 84.50°C compared to the gasoline with 83.40°C. The similar condition occurred at 3500 rpm of engine speed, coolant temperature for CNG operation can go up until 90.50 °C compared to that of gasoline at 89.10 °C.

2. OVERVIEW OF COOLING SYSTEM

All internal combustion engines are equipped with some type of cooling system because of the high temperatures they generate during operation. Fuel burning engines produce enormous amounts of heat; temperatures can reach up to 4,000 degrees F when the air-fuel mixture burns. However, normal operating temperature is about 2,000 degrees F. The cooling system removes about one-third of the heat produced in the combustion chamber. The purpose of the engine's cooling system is to remove excess heat from the engine, to keep the engine operating at its most efficient temperature, and to get the engine up to the correct temperature as soon as possible after starting. Ideally, the cooling system keeps the engine running at its most efficient temperature no matter what the operating conditions are.

As fuel is burned in the engine, about one-third of the energy in the fuel is converted into power. Another third goes out the exhaust pipe unused, and the remaining third becomes heat energy. A cooling system of some kind is necessary in any internal combustion engine. If no cooling system were provided, parts would melt from the heat of the burning fuel, and the pistons would expand so much they could not move in the cylinders called seize.

On the other hand, if an engine runs at too low a temperature, it is inefficient, the oil gets dirty (adding wear

and subtracting horsepower), deposits form, and fuel mileage is poor-- not to mention exhaust emissions! For these reasons, the cooling system is designed to stay out of the action until the engine is warmed up.

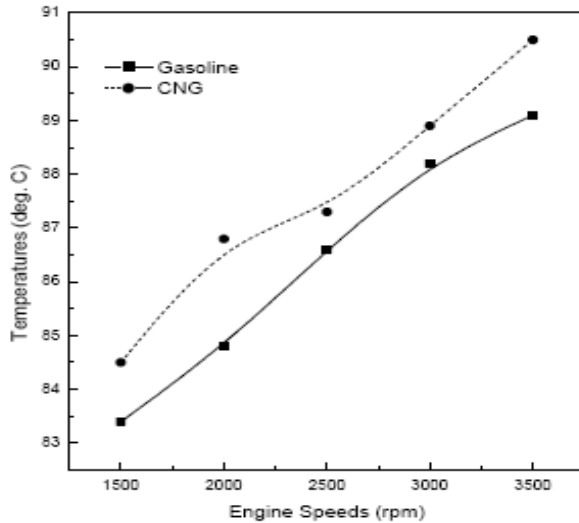


Fig (1) Cooling temperature profile for all speeds

2.1 Heat transfer

Heat transfer occurs when a temperature difference exists. As a result of combustion, high temperatures are produced, inside the engine cylinder. Considerable heat flow occurs from gases to the surrounding metal walls. However, the heat transfer on this account is quite small. Hence, the cylinder wall must be adequately cooled to maintain safe operating temperatures in order to maintain the quality of the lubricating oil.

Heat transfer from gases to the cylinder wall may occur predominantly by convection and radiation whereas the heat transfer through the cylinder wall occurs only by conduction. Heat is ultimately transferred to the cooling medium by all the three modes of heat transfer.

The cooling system works on the principle of heat transfer. Heat will always travel from a hotter to cooler object. Heat transfer is in three ways

1. Conduction
2. Convection
3. Radiation

2.2 Method of Heat Removal

When fuel is burned in an engine, a great deal amount of heat is produce. The rest of heat, the excess heat, must be removed to prevent engine damage from overheating. Excess heat is removed from engine in three ways.

1. Some heat leaves the cylinders with the hot exhaust gases. These are the burned and unburned gases that remain after combustion.

2. Some heat is removed by lubricating oil. After the hot oil drops down into the oil pan, the oil gives up some of its heat to the air passing under the oil pan.
3. The remaining heat is removed by the engine cooling system. This is about one-third of the heat produced in the combustion chambers by the burning fuel.

2.3 The Purpose of Cooling System

The cooling system keeps the engine at its most efficient temperature at all speeds and operation conditions. Burning fuel in the engine produces heat. Some of this heat is taken away before damages engine parts. This is one of the three jobs performed by the cooling system. It also helps bring the engine up to normal operating temperature as quickly as possible.

3. THERMAL CALCULATION

Thermal calculation of a spark ignition engine to be calculated in 2L Converted CNG engine is given bellow.

Initial data;

the rate power	$N_b = 70$ hp
the crankshaft speed	$n = 4200$ rpm
the number cylinder	$i = 4$
the compression ratio	$\epsilon = 10:1$

Physical constant; composition of CNG –fuel

(By volume) $CH_4=90.6$

$C_2H_6=5.4$ %

$C_3H_8=1.52$ %

$C_4H_{10}=1.6$ %

$C_5H_{12}=0.88$ %

(By mass) $C = 75\%$

$H = 25\%$

Higher heating value $H_H = 50$ MJ/kg

Lower heating value $H_L = 45$ MJ/kg

3.1 Design Consideration

In internal combustion engines, the oxygen necessary for combustion is contained in the air introduced into the cylinder during admission. Since there is about 23 per cent oxygen in the air by mass and 21 per cent by volume, we obtain correspondingly the theoretical amount of required for the combustion of one kilogram of fuel.

The theoretical amount of air required for the combustion of one mole or one cubic meter of gaseous fuel.

$$a_{th} = \frac{1}{0.23} \left[\frac{8}{3} C + 8H - O_r \right] \quad (1)$$

$$A_{th} = \frac{1}{0.21} \sum \left(m + \frac{n}{4} - \frac{r}{2} \right) C_n H_m O_r \quad (2)$$

The number of moles of fresh mixture is determined by:

$$M_1 = 1 + \alpha A_{th} \quad (3)$$

The lack of oxygen causes some of carbon to burn to CO. The amount of individual components of the combustion products are determined by the following equations:

$$M_{CO_2} = \sum n (C_n H_m O_r) \quad (4)$$

$$M_2 = M_{CO_2} + M_{H_2O} + M_{O_2} + M_{N_2} \quad (5)$$

The theoretical coefficient of molar change is

$$\mu_{th} = \frac{M_2}{M_1}$$

$$\eta_v = \frac{\epsilon P_a T_0}{(\epsilon - 1) P_0 (1 + \gamma_{res}) T_a} \quad (7)$$

There are two parameters we have to find for the compression. The first parameter is the pressure at the end of compression, P_c and the second parameter is the temperature at the end of compression, T_c .

$$P_c = P_a \epsilon^{n_1} \quad (8)$$

$$T_c = T_a \epsilon^{n_1 - 1} \quad (9)$$

3.2 Combustion Parameters

The actual coefficient of molar change, we use the following equation:

$$\mu_{act} = \frac{M_2 + \gamma_{res} M_1}{M_1 (1 + \gamma_{res})} \quad (10)$$

The maximum design pressure at the end of the combustion,

$$P_z = \mu_{act} \times \frac{T_z}{T_c} \times P_c \quad (11)$$

$$P'_z = 0.85 P_z \quad (12)$$

For CNG engine, the pressure at the end of expansion, P_b is determined by the following equation:

$$P_e = \frac{P_z}{\epsilon^{n_2}} \quad (13)$$

The temperature at the end of expansion can be calculated from the equation:

$$T_e = \frac{T_z}{\epsilon^{n_2 - 1}} \quad (14)$$

4. RADIATOR

A radiator is a heat exchanger that removes heat from coolant passing through it, thereby maintaining the engine temperature. This is done by heat transfer from hot coolant coming from engine cooling jacket, flowing into the tubes via the Inlet tank. Heat rejected from coolant to the tube is transferred to the ram air (ambient) flowing over the fins.

The radiator is the most important element of the cooling system and has the critical function of reducing temperature of the passing coolant. The “cooled” coolant continues recirculating throughout the engine, removing heat waste. The coolant carrying the heat waste from the engine moves into the radiator core via the inlet hose.

In **Fig (3)**, the automotive radiator has three main parts. These are a radiator core and inlet and outlet tanks. In the past, the entire radiator was made of copper. Now the cores are

usually made of aluminum while the tanks may be made of plastic or metal.

The radiator core has two sets of passage, a set of tubes and a set of fins attached to the tubes. The tubes run from the inlet tank to the outlet tank. Coolant flows through the tubes and air flows between the fins. Heat transfers from the hot coolant, through the tubes, to the fins. The outside air passing between the fins picks up and carries away the heat. This lowers the temperature of the coolant.

This process is called heat exchange in this case, heat is exchanged from the coolant, to air, this is called a liquid to air heat exchanger, note that the coolant flows through the tubes and air flows through the air fins.

Radiators are classified by the direction in which the tubing is assembled in the core; two types of radiators are commonly used in the automobile.

- Down flow radiator
- Cross-flow radiator

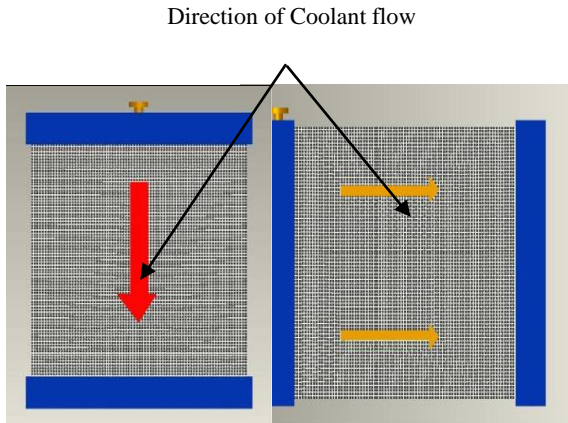


Fig (3) Down flow radiator and Cross flow radiator

4.1. Calculation of Heat Dissipation Surface of Radiator

Calculation of a radiator consists in determining the heat dissipation surface for the selected design of the radiator, as well as the velocities of the water and the air. It is assumed that all the heat rejected to the cooling system should be dissipated by the radiator surface.

4.1.1 The amount of heat received by cooling water,

$$Q_w = \eta_w H_l G_f \quad \text{J/hr} \quad (15)$$

Where Q_w = Amount of heat received by cooling water, J/hr

H_l = Lower heating value of fuel, J/kg

ρ_w = Percentage of heat going to cooling water
(Assume $\rho_w = 25\%$)

G_f = Consumption of fuel, kg/hr.

The design amount of heat dissipated by the radiator surface,

To allow for reduction of the heat transfer coefficient as a result of clogging of the radiator face and of scale deposits on the internal surfaces of the tubes, and for deviations of the data used in the calculations from actual conditions, the design amount of the heat is increased by 10 percent, and $Q_{rad} = 1.1 Q_w$ (16)

Where Q_{rad} = the design amount of heat dissipated by the radiator surface

4.1.2 Flow rate of Cooling water

$$G_w = Q_w / (C_w \rho_w / \Delta T_w) \quad (17)$$

where, G_w = Volume flow rate of cooling water, m³/sec

ΔT_w = drop in water temperature in the radiator,
= 6-12 K

C_w = specific heat capacity of water, 4187 J/kg.K

ρ_w = density of water, 1000 kg/m³

4.1.3 Velocity of Coolant water

$$v_w = G_w / A = 1.5662 \text{ m/sec} \quad (18)$$

$$A = \frac{\pi}{4} D_{inw}^2 = 0.000792 \text{ m}^2 \quad (19)$$

Where, D_{inw} = Water pump outlet diameter, ($D_{inw} = 1.25$ in or 0.03175m)

V_w = velocity of coolant water, m/sec

4.1.4 Calculation of Hydraulic diameter of Cool side and Hot side

(i) Calculating the water stream hydraulic diameter of a tube

Wetted circumference a single tube is calculate by this equation,

$$P_{tw} = 2\pi(r_t - x_{twt}) + 2(x_{tw} - x_{tt}) \quad (20)$$

Where, P_{tw} = wetted circumference of a single tube

r_t = tube outer radius

x_{tw} = width of tube

x_{tt} = thickness of tube

x_{twt} = tube wall thickness

Area of water cross section in tube,

$$A_{tcs} = \pi(r_t - x_{twt})^2 + (x_{tw} - x_{tt})(x_{tt} - 2x_{twt}) \quad (21)$$

$$= 28.731 \text{ mm}^2$$

Hydraulic Diameter of Tube,

$$D_{hw} = \frac{4A_{tcs}}{P_{tw}} \quad (22)$$

$$= 2.31 \text{ mm}$$

(ii) Calculating the air stream hydraulic diameter of a tube

External Tube Surface Area,

$$A_{teu} = [2\pi r_t + 2(x_{tw} - x_{tt})]x_{fp} \quad (23)$$

$$= 156.85 \text{ mm}^2$$

The unit fin surface area for four surface,

$$A_{feu} = 4(x_{fil}) \sqrt{\left(\frac{x_{fp}}{2}\right)^2 + (x_{fw})^2} \quad (24)$$

$$= 647.3 \text{ mm}^2$$

The total area exposed to air stream is,

$$A_{au} = A_{teu} + A_{feu} \quad (25)$$

$$= 804.15 \text{ mm}^2$$

Where, x_{fp} = Fin pitch

x_{fil} =Fin unit length

x_{fw} =Fin width of a unit cell

x_{tp} =tube pitch

The wetted Perimeter of external tube,

$$P_{aw} = x_{fp} + 2 \sqrt{\left(\frac{x_{fp}}{2}\right)^2 + (x_{fw})^2} \quad (26)$$

$$= 13.44 \text{ mm}$$

Unit Fin Cross section Area,

$$A_{acs} = \frac{x_{fp}}{2} \times x_{fw} = 7.5 \text{ mm}^2 \quad (27)$$

Hydraulic diameter of the air channel

$$D_{hz} = \frac{4A_{acs}}{P_{aw}} = 2.2324 \text{ mm} \quad (28)$$

4.1.5 Air temperature raise given by heat transfer

$$D_{fan} = 0.4 \text{ m}$$

$$A_{fan} = \frac{\pi}{4} D_{fan}^2 = 0.126 \text{ m}^2 \quad (29)$$

$$m_a = v_a \times A \times \rho_a = 1.8588 \text{ kg/sec} \quad (30)$$

$$\Delta T_a = \frac{Q_{rad}}{m_a \cdot c_{pa}} = 27.75 \text{ K} \quad (31)$$

Where, D_{fan} = diameter of fan

m_a =mass flow rate of air

ΔT_a =air temperature raise

ρ_a =air density (at 35C)

c_{pa} =specific heat capacity of air (at 35C)

4.1.5 Calculate the overall heat transfer coefficient of radiator

In order to calculate the overall heat transfer coefficient, the thermal resistance concept is employed in this study. As illustrated in Fig., the heat is rejected from the coolant to the air through four major thermal resistances:

(a) Convection from the coolant to the inner surface of the tube

(b) Resistance by fluid impurities, rust formation, or other reactions between the fluid and the wall material, R_f (Fouling factor)

(c) Conduction through the tube wall

(d) Convection from the outer surface of the tube to the air via the fins.

Those thermal resistances are in series as shown in Fig.

$$U = \left(\frac{1}{h_w} + R_f + \frac{t_t}{k_t} + \frac{1}{\eta_o h_a} \right) \quad (32)$$

Where, U = overall heat transfer coefficient of radiator, W/m² K

h_w = convection heat transfer coefficient for coolant side, W/m² K

t_t = thickness of tube, m

k_t = thermal conductivity of tube, W/m K

h_a = convection heat transfer coefficient for air side, W/m² K

η_o = overall surface efficiency of the fins

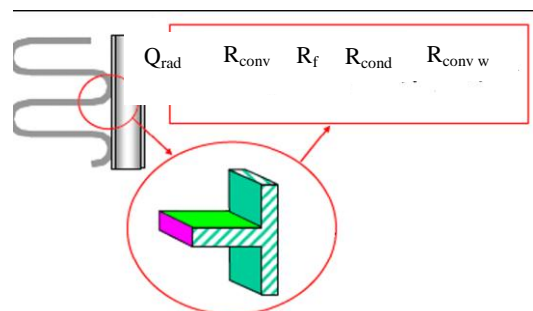


Fig (4) Thermal resistance of in series

(i) Convection Heat Transfer coefficient for the Coolant Side

The convection heat transfer coefficient for the coolant side (h_w) is calculated using the following formula:

$$Nu_w = \frac{h_w D_h}{k_w}$$

Where, Nu_w = Nusselt number for coolant side

h_w = convective coefficient of water, W/ m²K

D_h = Hydraulic diameter of tube, m

V_w =velocity of water in tube, 0.7 m/sec (assume)

ρ_w =density of water ,1000 kg/m³

(ii) Convection Heat Transfer Coefficient for Air side

The air side convective heat transfer coefficient is calculated by this equation,

$$Nu_a = \frac{h_a \times D_h}{K_a}$$

$$Nu_a = 0.664 Re^{1/2} Pr^{1/3} \quad (Pr \geq 0.6)$$

$$= 24.72$$

$$h_a = 297.8 \text{ W/m}^2 \text{ K}$$

(iii) Overall surface efficiency of fin

The overall surface efficiency of the fin

$$\eta_0 = 1 - \frac{A_{feu}}{A_{au}} (1 - \eta_f)$$

$$\eta_f = \frac{\tanh(mL)}{mL}$$

Fin length,

$$L = \sqrt{\left(\frac{x_{fp}}{2}\right)^2 + x_{fw}^2} = 5.22 \text{ mm}$$

$$m = \sqrt{\frac{2h_a}{Kt}} = 122.61$$

$$h_f = 0.8826 = 88.26\%$$

$$h_0 = 0.9055 = 90.55\%$$

R_f =fouling factor =0.000175 for engine jacket water

$U_{\text{overall}} =$

$$\left[\frac{1}{1564.85} + 0.000175 + \frac{0.4 \times 10^{-3}}{396.2} + \frac{1}{0.9055 \times 297.8} \right]^{-1}$$

$$= 221.07 \text{ W/m}^2 \text{ K}$$

5. CONCLUSION

In this thesis, study on engine cooling system and design of radiator. Engine cooling system is closely related with overall performances of an engine, including reduction of fuel consumption, decrease of air pollution, and increase of engine life. Radiator is the heart of cooling system. Compact heat exchangers have been widely used in various applications in thermal fluid systems including automotive thermal management systems. So, radiator design is calculated by at maximum water temperature flow out from water pump.

6. ACKNOWLEDGMENTS

I greatly appreciate to all teachers from the Department of Mechanical Engineering, Technological University (Thanlyin) who work in Renewable Energy Research.

7. REFERENCES

1. A. Kolchin and V. Demidov, 1984, Design of Automotive Engines
2. M. Khovakh, 1971, Motor Vehicle Engine (Part. I), MIR Publisher, Moscow
3. Frank Kreith, Heat and Mass Transfer
4. Frank P. Incropera and David P. DeWitt, Fundamentals of Heat and Mass Transfer
5. Heywood John B., 1989, Internal Combustion Engine Fundamentals, International Edition, New York, McGraw-Hill.
6. U Sein Win, 2003, Internal Combustion Engine Part I and II.
7. Mardani, 2004, Development of advanced intake system for optimum Compressed Natural Gas (CNG) Fuelled SI Engine Performances
8. Franciscus Xavierus Laubscher, 2005, A Model to Predict the Effect of Radiator Core and Ambient Conditions on the Performance of Cooling System of Rally

Freshwater Microalgae (*Chlorella* sp.): Pure Culture and Crude Oil Extraction for Biodiesel

Hnin Hnin Htun,
Department of
Biotechnology, Mandalay
Technological University,
Mandalay, Myanmar.

Thin Thandar Ko
Department of
Biotechnology, Mandalay
Technological University,
Mandalay, Myanmar.

Saw Myint Thu
Department of
Biotechnology, Mandalay
Technological University,
Mandalay, Myanmar

Abstract: *Chlorella* sp. was cultivated with Conwy medium, BG-11 medium and MN medium at microalgae laboratory. The pure strain with different media and pH were observed within one month. There are various methods for extracting the oil from freshwater microalgae, such as physical factors, mechanical pressing and solvent extraction etc. Solvent extraction method was used for extracting of crude oil from algae biomass by using n-hexane. In this study, crude oil extract of *Chlorella* sp. was identified and interpreted by Fourier Trans-form Infra-Red spectroscopy (FT-IR) to employ as a fast and reliable analytical technique for the quantification of various fatty acids esters and refined oil spectra in the produced biodiesel. This research has been focused on growing pure algae with high oil content and then extracting the potential of biodiesel from it.

Keywords: Microalgae, *Chlorella* sp., Solvent extraction, n-hexane, Oil extract, Fourier Trans-form Infra-Red spectroscopy (FT-IR)

1. INTRODUCTION

The term “algae” encompasses many different groups of living organisms. Algae have been commonly regarded as simple plants. Others, such as cyanobacteria, are more closely related to higher plants or animals in character. Algae have been part of the pattern of life on earth science primeval period and range from small single-celled organisms’ too much larger multicellular organisms that are related to plants, but without a vascular system, roots, stems leaves or embryos (fruits and seeds). They are mainly aquatic and are the primary producers in the aquatic food chain [1].

Depending on the species and cultivation conditions, algae can contain extremely high percentages of lipids or carbohydrates that are easily converted into a whole range of biofuels including biodiesel or bioethanol. Furthermore, the remaining biomass, mostly protein and carbohydrate, may be processed into many other products such as: foods, chemicals, medicines, vaccines, minerals, animal feed, fertilizers, pigments, salad dressings, ice cream, puddings, laxatives and skin creams (Edwards 2008) [2].

The use of fossil fuels is not sustainable and known petroleum reserves are estimated to be depleted in less than 50 years at the present rate of consumption (Sheehan et al., 1998) [3].

Algae technology has enormous potential, not only for algae based-biofuel, but also for food, feed, renewable chemicals and many other products that are critical for a more sustainable society. Algae have recently received a lot of attention as a new biomass source for the production of renewable energy. Some of the main characteristics which set algae apart from other biomass sources are that algae (can) have a high biomass yield per unit of light and area, can have a high oil or starch content, do not require agricultural land, fresh water is not essential and nutrients can be supplied by wastewater and CO₂ by combustion gas [4].

pH is another important growth factor for algae. Different algal species have different favorite pH ranges and outside the optimal range the growth is affected resulting in slower specific growth rates. Both *Chlorella* and *Botryococcus* are growing very well at around pH6. *Scenedesmus* prefer alkaline medium between pH 9 to 10. In addition, algae can

also change the pH of the medium during cultivation. When using CO₂ as carbon source, rapid growth of algae can cause the pH to rise due to photosynthetic uptake of inorganic C [5].

Lipids are one of the main components of microalgae; depending on the species and growth conditions 2–60 percent of total cell dry matter (Wijffels, 2006), as membrane components, storage products, metabolites and storages of energy. Among the biofuels, biodiesel represents an alternative to petroleum-based diesel fuels. Chemically speaking, biodiesel is a mixture of mono-alkyl esters of fatty acids, most often obtained from extracted plant oils and/or collected animal fats (Usta et al., 2005)[6]. These hydrocarbons are mainly accumulated on the outside of the cell, making extraction easier than when the cell wall has to be passed to reach the organics inside the cell (Wijffels, 2006)[7].

Most microalgae biomass contains three main components such as (1) lipids, (2) proteins, and (3) carbohydrates and/or hydrocarbons. Microalgae produce and store lipids in the form of fatty acids, phospholipids, glycolipids and it can be used as feedstock for biodiesel production by trans-esterification reaction in the presence of acid or base with methanol [8].

The aim of this paper is to study the mass cultivation, oil extraction and potential of freshwater microalgae for biodiesel production.

2. MATERIALS AND METHODS

2.1 Sample Collection

The freshwater microalgae (*Chlorella* sp.) sample was brought from Sal Taw drainage, in front of Mandalay Technological University, Mandalay, Myanmar. The strain was treated with enrichment culture for the favor of the rapid increase in number of a desired species of the microalgae. And then, they were kept in algae laboratory.

2.2 Preparation of Microalgae Culture

15ml of microalgae sample was taken from enrichment culture in each of four centrifuge tubes. These tubes were centrifuged at 5000 rpm for 5 minutes. After removing the supernatants, the cells will be suspended in distilled water in each tube. Centrifugation and washing were repeated for three

times to expel most of the microorganisms presented in algal sample. Washed microalgae were allowed to streak through loop on nutrient agar plates under axenic condition and to keep for at least 2 weeks to grow microalgae. Repeated streak-plating was carried out to peak up single colony from earlier streaked plates and to make free from bacteria.

From last streak plates, the single colonies were picked up by loop and allowed to grow in glass bottles for inoculum. Before putting in the 50 ml test tubes, the single cell growth and purity of single specie was confirmed after observing under microscope. Then, the pure culture of microalgae strain was maintained in 50ml test tubes, and placed onto the lighted shelf. And then, the test tube 10ml was transferred into the glass bottle 50ml by adding 40ml distilled water and nutrient with the ratio of 1ml/1L at room temperature and were cultured 15 days for inoculum.

After that, 50ml algae strain was cultured 20 days, with 200ml distilled water and nutrient. The cell density of strain was counted with Haemocytometer (x10) one day interval for one month. After one month culturing, they were turned over to 220 liter aquarium for two months with blower. The optical densities of microalgae were measured by using UV Spectrophotometer one day interval during the culture period (2 months).

2.3 Harvesting and Drying Process

The freshwater microalgae biomass was harvested by sedimentation. It was dewatered by filtration with a filter. And then, the wet microalgae biomass was collected from the filter with a spatula and taken in beaker. The biomass was dried at room temperature for 5days. The total biomass was weighted and stored at room temperature for extracting microalgae oil.

2.4 Pretreatment of Microalgae Biomass for Extraction Crude Oil

Before extraction, dried algal biomass was kept in freezer at 4°C overnight. And then, freezing biomass was grinded by mortar and pestle for disrupting the cell wall and enhance the efficiency of the lipid extraction process (Figure 1). Disrupting the cell wall for easier recovery of the intercellular lipids, resulted data was rapidly and increased efficiencies in lipid extraction.



Figure1. Pretreatment of Biomass by Mortar and Pestle

2.5 Solvent Extraction Method

Solvent Extraction Method was selected by using n-hexane as a solvent. Soxhlet extractor was prepared in the laboratory. 5 gm of dry biomass was wrapped in thimble and placed in the extractor. Three hundred milliliter of n-hexane solvent was used for extraction. The extraction was done by many cycles for 10 hours. The solvent-oil mixture was

separated by simple distillation for recovering of n-hexane solvent. Simple distillation was operated at 80°C because the boiling point of n-hexane was (50-70) °C.

2.6 Simple Distillation Method

After extracting, the solvent-crude oil mixture was placed into pre-weighed flask for evaporation. In the laboratory setup, the solvent and crude oil mixture was exposed to a vacuum and then heated at 80°C by using simple distillation because the boiling point of n-hexane was (50-70) °C. After distillation, the flask was weighed again and compared with first weight. In this way, the weight of the crude oil content was calculated. And then, the obtained microalgae oil was kept in tube at room temperature. The percentage of crude oil extraction was calculated by the following formula:

$$\% \text{ of total crude oil recovered} = \frac{\text{Weight of Crude Oil Extract}}{\text{Weight of Microalgae Biomass}} \times 100$$

2.7 Quantitative Analysis of Microalgae Crude Oil (FT-IR) Analysis

Fourier Transform Infra-Red spectroscopy (FT-IR) is an analytical technique that collects spectra based on the temporal coherence measurements from an infrared source. FT-IR identified the functional group present in the molecules.

3. RESULTS AND DISCUSSIONS

For obtaining the best growth rate of *Chlorella sp.* with BG-11 medium was tested in optimum culture condition such as nutrient, pH, temperature and so on. For optimum pH value, *Chlorella sp.* culture with BG11 medium was tested by adjusting three different pH values in 500ml glucose bottles (Figure 2). And also, *Chlorella sp.* was tested with three different media Conwy medium, BG-11 medium and MN medium which are shown in figure 3. And then, the *Chlorella sp.* was cultured with BG11 medium at room temperature for a month period. The resulted data of microalgae cells were counted by haemocytometer one day interval was showed in Figure 4.

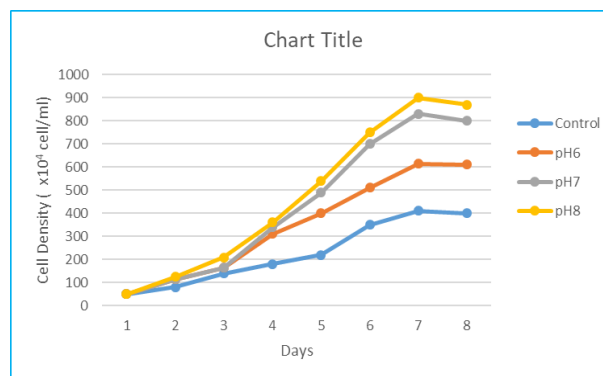


Figure 2. Growth Curve of *Chlorella sp.* Culture with Three Different pH Values by Measuring Haemocytometer

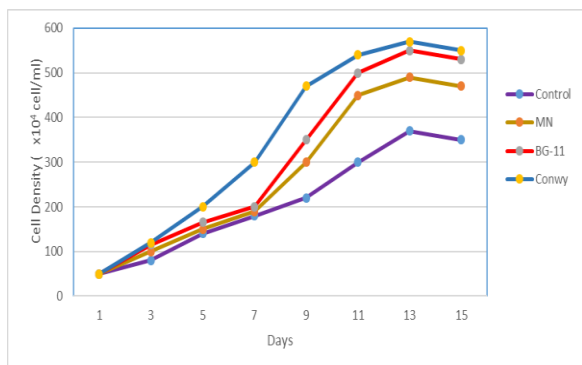


Figure 3. Growth Curve of *Chlorella sp.* Culture with Three Different Media by Measuring Haemocytometer

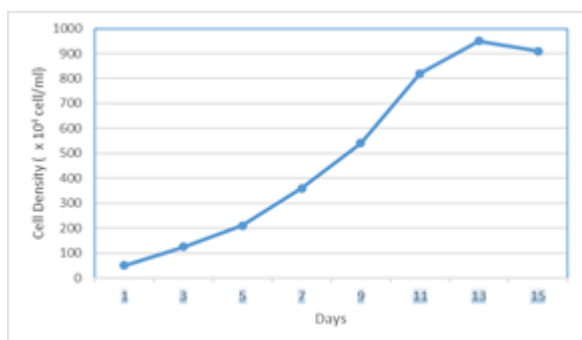


Figure 4. Growth curve of *Chlorella sp.* Culture with BG11 Medium by Measuring Haemocytometer

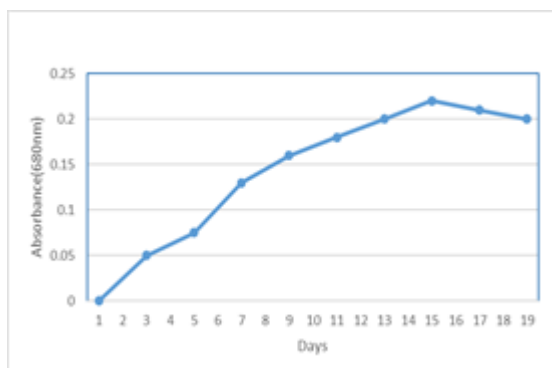


Figure 5. Growth Curve of *Chlorella sp.* Mass Culture with BG11 Medium by Measuring with UV Spectrophotometer (680nm).



Figure 6. Mass Culture of *Chlorella sp.* (200L)

It has been observed their growth conditions within one month. The resulted data of microalgae cells was counted by UV spectrophotometer (680nm) one day interval during culture period was showed in Figure 5. For mass culture of *Chlorella sp.* was cultured with BG11 medium for two months at outdoor condition as shown in Figure 6.

A. Biomass Processing

Microalgae biomass was harvested by sedimentation, dewatering and filtration. The harvested biomass was dried at room temperature and weighted. The result of 30gm was harvested from the maximum growth rate of *Chlorella sp.* (220 liters) (Figure 7).



Figure 7. Dried Biomass Harvested from the Cultivation of *Chlorella sp.*

B. Extraction of crude oil

From extraction oil of microalgae (*Chlorella sp.*) 5gm of microalgae dry weight, by soxhlet extraction method using n-hexane as solvent, the extract microalgae was approximately 1% (w/w) of dried *Chlorella sp.* biomass. The soxhlet extraction with n-hexane solvent was able to extract (18-20) % of crude oil present in the algae. The extract microalgae oil was showed in Figure 8.



Figure 8. Crude Oil Extract of *Chlorella sp.*

C. Quantitative Analysis of Microalgae Crude Oil (FT-IR) Analysis

Fatty acid ester content of extracted microalgae crude oil was analyzed by IR spectrum to identify microalgae crude oil used as feedstock for biodiesel production. It was used under the following condition: 4000-400cm⁻¹. Methoxy compounds, including methyl carboxylic esters, exhibit a weak band in the 2860- 2800cm⁻¹. Region of the infrared spectrum, which is diagnostic for the methoxyl group. The band occurs at a lower frequency than that of the main C-H absorption [9]. IR spectra of crude oil of *Chlorella sp.* strain was shown in figure 9. According to reference [9],[10] in figure 9, the characteristic absorption bands for the vibrations of C-H band, around 2923.25 cm⁻¹ and 2853.81 cm⁻¹ corresponding to the asymmetric and symmetric vibration modes of methyl groups respectively, was detected.

Rather subtle differences can be observed between the spectra, since the product of the transesterification process (FAME) is chemically similar to its precursor (the refined oil). In the

region from 1800-1700 cm^{-1} , it can be observed peaks that can be attributed to the stretching of C=O, typical of esters, and thus are common in both FAME and refined oil spectra [11].

The C=O absorption band of saturated aliphatic esters (except formates) is in the 1750-1735 cm^{-1} region. The C=O absorption bands of formates, α , β -unsaturated, and benzoate esters are in the region of 1730-1715 cm^{-1} . The C=O stretch, 1771 cm^{-1} : this is higher frequency than that from a normal ester C=O stretch 1740 cm^{-1} [9].

So, the intense C=O stretching band of aliphatic esters, benzoate esters, typical of esters and refined oil spectra appeared around 1740.83 cm^{-1} and 1715.76 cm^{-1} in figure 9.

There is a sharp peak for OCH₃ between 1500 cm^{-1} and 900 cm^{-1} , known as “fingerprint” region. The peak at 1459.21 cm^{-1} correspond to the asymmetric stretching of OCH₃ present in the biodiesel spectrum in figure 9.

The properties of biodiesel are largely determined by the structure of its component fatty acid esters (Knothe, 2005)[12].

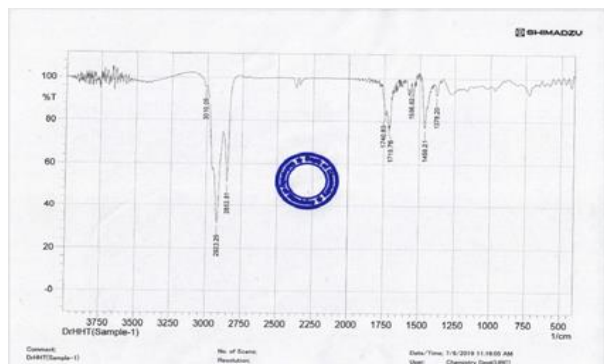


Figure 9. IR Spectra of Crude Oil Extract from *Chlorella* sp.

4. CONCLUSIONS

In this research, *Chlorella* sp. was successfully cultivated and grown with optimum culture condition such as nutrient (BG11medium), pH8, room temperature and so on. The microalgae strain gave more crude oil content amount and high biomass production according to their results. N-hexane solvent has been used as an efficient extraction agent of algae crude oil from *Chlorella* sp.

According to this results, the chemical typical structure of esters and refined oil spectra were identified and interpreted using FTIR. This led to the identification of functional groups in the molecules of the biodiesel with the aid of structure correlation chart. Therefore, microalgae *Chlorella* sp. can be considered as a potential crude oil for biodiesel production.

5. ACKNOWLEDGMENTS

Authors wish to thank Dr. Myo Myint, Head of Department of Biotechnology, and Dr. Sint Soe, Rector, Mandalay Technological University, and Mandalay, Myanmar for offering the infrastructure for carrying out the current research. The author expresses the special thanks to her senior teachers and colleagues for their helps, supports and encouragement. Finally, thanks to all who helped for this paper.

6. REFERENCES

- [1] Algae: Emerging Options for Sustainable Biofuels. November, 2009.
- [2] Edwards, M. (2008). Green Algae Strategy - End Biowar and Engineer Sustainable Food and Biofuels. Tempe, Arizona, USA, LuLu Press.
- [3] Sheehan J., Dunahay T., Benemann J. and Roessler P., (1998) Aquatic Species Program. National Renewable Energy Laboratory.
- [4] ALGAE-BASED BIOFUELS: A Review of Challenges and Opportunities for Developing Countries May, FAO 2009.
- [5] Yuanjun Li,(2011).”Inexpensive culturing of freshwater algae in a simulated warm environment using chicken manure mediu” Göteborg, Sweden.
- [6] Usta N, Ozturk E, Can O, Conkur ES, Nas S, Con AH., (2005) Combustion of biodiesel fuel produced from hazelnut soapstock/waste sunflower oil mixture in a Diesel engine. Energy Convers Manage. 46, 741–55.
- [7] Wijffels, R. (2006). Energie via microbiologie: Status entoeekomstperspectiefvoor Nederland. Utrecht, SenterNovem.
- [8] Muthukumar, S. Elayaraja, T. T. Ajithkumar, S. Kumaresan and T. Balasubramanian, “Biodiesel production from marine microalgae *Chlorella marina* and *Nannochloropsissalina*”, Journal of Petroleum Technology and Alternative Fuels Vol. 3(5), pp. 59, October, 2012.
- [9] I.A. Degen (1968) Detection of the methoxy group by infraredspectroscopy. Vol.22. Issue 3,pp.164-166
- [10] Silverstein MR, Bassler CG and Morrill CT, Spectrometric Identification of Organic Compound. 4thEdition, New York. Jhon Wiley and Sons,1981-QD 272.S6S55.
- [11] I. P. Soares, T. F. Rezende, R. C. Silva, E. V. R. Castro, and I. C. P. Forte, “Multivariate calibration by variable selection for blends of raw soybean oil/biodiesel from different sources using Fourier Transform Infrared spectroscopy (FTIR) spectra data,” Energy Fuels, vol. 22, pp. 2079-2083, January 2008.
- [12] Knothe G., (2005) Dependence of biodiesel fuel properties on the structure of fatty acid alkyl esters. Fuel Processing Technol. 86, 1059–1070.

Effects of Salinity on the Hatching Efficiency of Artemia Cysts Decapsulation

Hnin Hnin Htun,
Department of
Biotechnology, Mandalay
Technological University,
Mandalay, Myanmar

Htway Htway San,
Administrative Department,
Computer University
(Taungoo),
Taungoo, Myanmar

Zin Myo Swe
Department of
Biotechnology
Mandalay Technological
University,
Mandalay, Myanmar

Abstract: In this study, hypochlorite (liquid bleach, NaOCl) was used for *Artemia salina* cysts decapsulation as a decapsulation method which saves cost and labor because of increasing the hatching rate and speed. Cysts were removed from hypochlorite solution after 15 min. The stocking density in each hatching systems were 1gm cysts per 1L, replicated three times. The treatments were maintained at 25‰, 30‰, 35‰ and 40 ‰ saline solution and the pH between 7.5 - 8.5 respectively. A uniform temperature of 28°C was maintained for all the treatments throughout the study period. However, among the treated cysts, the best hatching rate (83±1.7%) was achieved in cysts treated with (liquid bleach, NaOCl). Hatching efficiency of the cysts in different salinity levels was studied and described in this paper in salinity range of 25‰ to 40‰. Maximum hatching efficiency was recorded in the water having 30‰. The aim of this paper is to study the hatching efficiency of *Artemia* cysts in varying salinity decapsulation conditions.

Keywords: *Artemia salina*, Decapsulation, Hatching efficiency, Cysts, salinity

1. INTRODUCTION

Among the live diets used in the larviculture of fish and shellfish, nauplii of the brine shrimp *Artemia* constitute the most widely used food item. Annually, over 2000 metric tons of dry *Artemia* cysts are marketed worldwide for on-site hatching into 0.4 mm nauplii. Indeed, the unique property of the small branchiopod crustacean *Artemia* to form dormant embryos, so called 'cysts', may account to a great extent to the designation of a convenient, suitable, or excellent larval food source that it has been credited with. Those cysts are available year round in large quantities along the shorelines of hyper-saline lakes, coastal lagoons and solar salt works scattered over the five continents. After harvesting and processing, cysts are made available in cans as storable 'on demand' live feed. Upon some 24-hr incubation in seawater, these cysts release free-swimming nauplii that can directly be fed as a nutritious live food source to the larvae of a variety of marine as well as freshwater organisms, which makes them the most convenient, least labor-intensive live food available for aquaculture [1].

Live food is necessary for fish larvae, especially in marine species. Undeveloped digestive system of larvae, makes them completely dependent on live food. Live foods have other advantages over the formulated feed including appropriate size, palatability due to high water content, immersion in water column and stimulation of larval predatory behavior (Bengston, 2003). Many fish and other aquatic creatures need to eat living organisms in the first stage of their development, i.e. when they hatch and the yolk sac retreats (Lavens et al. 1986) [2].

Generally, *Artemia* cyst decapsulation depends on many factors like temperature, salinity, pH, cyst quality, aeration etc. Moreover, fixed temperature, cyst density and container's design also play important role in maximal production of *Artemia* cyst (Lavens and Sorgeloos 1996, Sharahi and Zarei 2016) [1], [3].

Decapsulation is a process in which the chorion layer is dissolved and removed. Decapsulated cysts could be used as a

food source for fish larvae, although its application is limited compared to the nauplii. Decapsulated cysts have been used to rear larvae of freshwater catfish (*Clarias gariepinus*), common carp (*Cyprinus carpio*), and marine shrimp (*Penaeus indicus* and *Penaeus monodon*) and milkfish (*Chanos chanos*) (Verreth et al., 1987; Vanhaecke et al., 1990; Stael et al., 1995; Ribeiro and Jones, 1998; Sui, 2000).

But, there was lack of research work of precise temperature and salinity or their combined effect on cyst decapsulation. That is why, an experiment was conducted to find out the influence of salinity and temperature on the decapsulation of cyst. This *Artemia* embryo was completely removed from the cyst by a short-term incubation in saline solution with aeration. This procedure is called decapsulation of cyst (Lavens and Sorgeloos 1996)[1].

Sorgeloos (1976) stated in his study that the highest hatching rate occurs when the water temperature is kept stable at 28°C [8]. Similarly, in the study he conducted in 1980, he stated that quick and maximum amount of hatching of *Artemia* eggs occurs in 30 °C temperature but at 33-40 °C temperature the egg metabolism is delayed and deaths are observed (Sargeloos, 1980)[9]. Vanhaecke et al. (1984) have reported that the optimal salinity for egg hatching is 35‰ [10].

It was determined that larva production from *Artemia* eggs can be carried out in artificially prepared salty waters and the salinity can change between 5-70‰ (Çelikkale, 1978)[11].

Sorgeloos and Persoone (1980) detected that *Artemia sp.* spends a lot of energy for osmoregulation at high salinity and salinity has an effect on physicochemical factors affecting the egg metabolism of *Artemia* and that salinity needs to be under a certain threshold in order for cyst development to begin. In a study they conducted, Güven and Erçetin (1992) have examined the hatching of *Artemia* eggs in different salinities (25‰, 30‰, 32‰ and 35‰) and stated that the difference salinity levels have not found a significant effect on hatching rates [12].

Ahmed *et al.* (1997) performed an experiment on the effect of decapsulation on viability and hatching of *Artemia* cysts at different salinities. They found highest hatching rate ($75.7 \pm 2.5\%$) at 30‰ and lowest ($70.0 \pm 1.7\%$) at 25‰ after 24 hrs of incubation [13].

It is necessary for *Artemia nauplii* used in feeding of fish larvae as live feed to have the smallest size, to hatch at the same time and in a short period, and to be consumed at the stage it has the highest nutritional value (Alpbaz *et al.* 1992) [14]. For this purpose hatching efficiency and hatching rates in different salinity of *Artemia* sp. compared in our study.

2. MATERIALS AND METHODS

2.1 Ultrastructure of *Artemia* Cyst

The hard, dark brown, external layer of a cyst, the chorion (Figure. 1), which can be removed in a hypochlorite solution, is lipoproteinaceous and is impregnated with haematin, a derivative of haemoglobin (Dutrieu, 1960; Linder, 1960; Anderson *et al.*, 1970) [15]. It has numerous interconnected canals which are filled with air and are in contact with the surface of the cortical layer. According to Mathias (1937) this alveolar layer contributes to the buoyancy of the cyst [16].

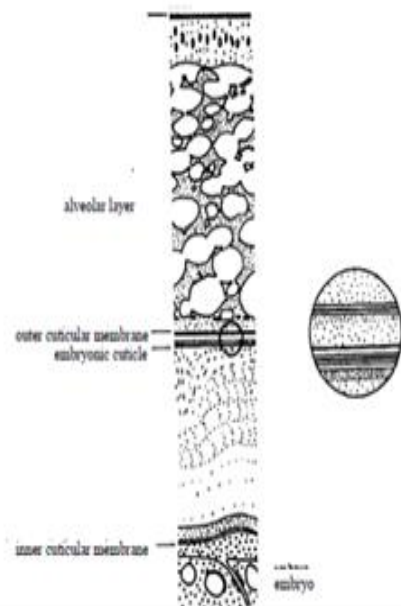


Figure 1. Schematic Diagram of the Ultrastructure of an *Artemia* Cyst. (Modified from Morris and Afzelius, 1967)[17]

2.2 *Artemia* Decapsulation Procedure

1. Cyst hydration: Hydrate 1gm of dried cyst with 100 μm mesh bag in 1 L of tap water in a cup for 15 minutes at room temperature. Examine the cyst under a microscope with top lighting before proceeding. In the figure 2, dry cysts are dimpled, resembling a deflated basketball, whereas fully hydrated cysts are completely spherical in shape. The cysts must be fully hydrated prior to the decapsulation step.

2. Decapsulation: Add the chilled bleach (NaOCl) to the cup and continue with pushing for 15 minutes. When the cysts are 90% orange, stop the reaction and rinsing well with cool tap water.

3. Neutralization of residual chlorine: To neutralize any residual chlorine transfer the mesh bag to a clean 2 L cup and pour the 1.0% sodium thiosulfate (1L) into the bag. Soak the cysts in the sodium thiosulfate solution for ~1 min, then rinse the cysts with dechlorinated tap water. And then, 5mL of the 100 μm mesh bag water sample tested with one drop of otholidine solution. When the sample water appeared light yellow color, it was indicated for presence of chlorine residues and the colorless of water sample was free of chlorine residues.

4. Dehydration for long-term storage: Transfer the cysts back to the cup with 2 L of saturated brine and aerate for 24 hours (save back a filled squirt bottle of saturated brine solution to help transfer cysts to pail). Add granular NaCl (30gm/1L) 30‰ as needed to keep the solution saturated during the dehydration process. Transfer dehydrated cyst 5 L pail and fill with fresh saturated brine 30‰.

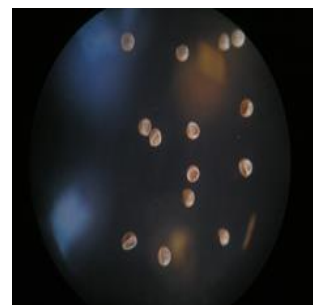


Figure 2. Dry *Artemia* Cysts

3. RESULTS AND DISCUSSIONS

The chorion of the brine shrimp cysts is removed without affecting the viability of the embryos by a process known as decapsulation. The decapsulated cysts can be supplied as feed for shrimp larvae. The process of decapsulation involves hydration of the cysts for 15 minutes in clean water.

For decapsulation of 1gm of cysts, a solution is prepared by dissolving 0.5 g of bleaching powder in water and cysts were removed from hypochlorite solution after 15 min. Thereafter, the cysts were washed with clean water 5 times prior to incubation. Continuous aeration was provided to ensure dissolved oxygen up to 5 ppm and suitable turbulence for cysts.

Four types of decapsulation salinity solution were prepared (e.g. 25‰, 30‰, 35‰ and 40‰). Three replicates were maintained for each treatment. Decapsulation was performed at 28°C. Temperature and salinity of water were checked using a refractometer, and thermometer.

After keeping the solution overnight with aerator (SOBO-348A air pump) at (pH 8.0-8.5), the supernatant was taken for decapsulating the cysts. Hatching rate was recorded at 24hr after incubation and determined by counting and averaging the *nauplii* in three samples (0.1 ml).

Table 1 shows the hatching rates of *Artemia* eggs at 24hr in 28°C and 25‰, 30‰, 35‰ and 40‰ salinity ratios. When the table is examined, it was observed that the hatching rate at the salinity 40‰ was generally lower compared to

other groups. It was detected that the highest hatching rate was at the 24hr, 30‰ salinity, in *Artemia sp.* OUXE(Great Salt Late –Uta USA).

Table 1: Hatching Rates of *Artemia* Eggs at 24 hr in 28°C with 25‰, 30‰, 35‰ and 40‰

Artemia Types	24hr(Hatching Time)			
	25‰	30‰	35‰	40‰
OUXE(Great Salt Late –Uta USA)	73±2.6	83±1.7	71±2.6	63±2

There was general increase in the hatching rate of *Artemia* cysts in different salinity levels. In this study, temperature was uniform (28°C) for all the three salinity levels tested and pH of the rearing medium was (7.7-8.5) for (25‰, 30‰, 35‰ and 40‰) saline solutions respectively.

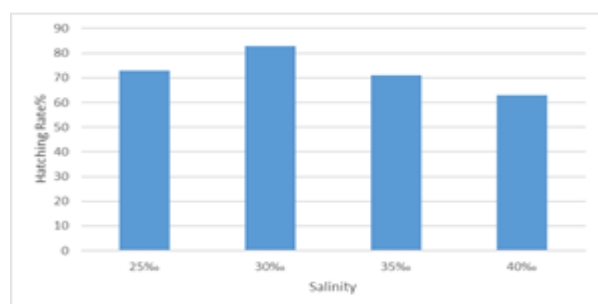


Figure 3. Effect of Salinity on Decapsulation of *Artemia* Cyst at 28°C

Water temperature, and pH is probably the most important environmental variables in *Artemia salina* cultures, because it directly affects metabolism, oxygen consumption, growth, moulting and survival (Herbst, 2001)[18].

The effect of salinity on decapsulation of *Artemia* cyst at 28°C is presented (Figure 3). Highest hatching rate (83±1.7) % was observed in 28°C temperature at 30‰ salinity. Lowest hatching rate (63±2) % was found in 30°C at 40‰. Data are recorded as mean ±SEM. Bar with different letter show significantly difference ($p < 0.05$, analyzed by one way ANOVA). This experiment was conducted to find out the influence of salinity and temperature on the decapsulation of cyst.

4. CONCLUSIONS

The variation of *Artemia* decapsulation rate could be the effect of different above mentioned factors. It can be concluded from the above discussion and the findings of this study that the decapsulation rate of *Artemia* cyst greatly depends on salinity and temperature.

This result, 30‰ salinity and 28°C could be the best combination of higher rate of decapsulation of *Artemia* cyst. Moreover, decapsulation rate decreases above 35‰ and 28°C. The best survival rate is most probably achieved at 30‰. Therefore, we may conclude that 30‰ salinity at 28°C could enhance survival of *Artemia*.

This paper deals with the study of hatching efficiency of *Artemia* cysts in decapsulation condition. *Artemia* cysts found

a direct correlation with the environmental factors, which is supported by the present findings.

5. ACKNOWLEDGMENTS

Authors wish to thank Dr. Myo Myint, Head of Department of Biotechnology, and Dr. Sint Soe, Rector, Mandalay Technological University, and Mandalay, Myanmar for offering the infrastructure for carrying out the current research. The author expresses the special thanks to her senior teachers and colleagues for their helps, supports and encouragement. Finally, thanks to all who helped for this paper.

6. REFERENCES

- [1] Lavens, P. and Sorgeloos, P. 1996. Manual on the production and use of live food for aquaculture FAO Fisheries Technical Paper. No. 361. Rome, FAO. 295 pp.
- [2] Bengston D. A. (2003). Status of marine aquaculture in relation to live prey: Past, present and future. In: J. G. Støttrup, and L. A. McEvoy (Eds.) Live Feeds in Marine Aquaculture, Wiley-Blackwell. pp: 1-16.
- [3] Lavens, P., Leger, P., Sorgeloos, P. (1986). Production, Utilization and Manipulation of Artemia as Food Source for Shrimp and Fish Larvae, Actualities de Biochemie Marine, Oceanis, 9: in pres 1-16.
- [4] Sharahl, A.R. and Zarei, S. 2016. Mutual effect of light and turbidity on hatching of *Artemia franciscana* cysts. International Journal of Fauna and Biological Studies 3(2): 03-06.
- [5] Vanhaecke P., De Vrieze L., Tackaert W., Sorgeloos P. (1990). The use of decapsulated cysts of the brine shrimp *Artemia* as direct food for carp *Cyprinus carpio* L. larvae. Journal of World Aquaculture Society, 21: 257–262.
- [6] Verreth J., Segner H., Storch V. (1987). A comparative study on the nutritional quality of decapsulated *Artemia* cysts, micro-encapsulated egg diets and enriched dry feeds for *Clarias gariepinus* (Burchell) larvae. Aquaculture, 63: 269–282.
- [7] Ribeiro F.A., Jones D.A. (1998). The potential of dried, low-hatch, decapsulated *Artemia* cysts for feeding prawn post-larvae. Aquaculture International, 6: 421-440.
- [8] Sorgeloos, P. (1976). The Brine Shrimps *Artemia salina*; A Bottleneck in Mariculture Pillay T.V.R., Dill. Wm. AAdvens in Aquaculture, Fishing News Boks Ltd. Farnhom, 321-324.
- [9] Sorgeloos, P. (1980). Life History Of The Brine Shrimp *Artemia*, Proceeding of the International Symposium on the Brine Shrimp *Artemia salina*, Corpus Christi, Texas, USA, Univesal Pres, Wetteren, Belgium, 19-23.
- [10] Vanhaecke, P., Siddall, E.S., Sorgeloos, P. (1984). International Study on *Artemia* XXXII. Combined Effects of Temperature and Salinity on the Survival of *Artemia* of Various Geographical Origin, J. Exp. Mar. Biol. Ecol., Vol: 80, pp: 259-275.
- [11] Çelikkale, M.S. (1978). *Artemia salina* nauplii Yumurtalarının Tuzlu Suda Açılımve Normal Suda Yaşama Süreleri Üzerine Bir Araştırma, Ankara Üniversitesi Ziraat Fakültesi Yıllığı, Cilt:28 Sayı:2 Sayfa:447-456.
- [12] Güven, E., Erençin, Z. (1992). Determination of Hatching Rates of the Brine Shrimp, *Artemia sp.*, Depending on the Temperature and Salinity in

Laboratory Conditions, İ.Ü. Su Ürünleri Dergisi, Cilt:6,
Sayı 2, Sayfa:61-70

- [13] Ahmed, S.U., Rahman, M.A., Islam, M.N. and Kamal, M. 1997. Effect of decapsulation on viability and hatching performance of Artemiacysts at different salinity levels. BangladeshFish. Res. 1(2): 67-74.
- [14] Albaz, A., Temelli, B., Özden, O., Korkut, A.K., Güner, Y.(1992).Farklı Orjinli Artemia Yumurtalarının Açılım Oranları Üzerinde Araştırmalar, E.Ü. Su Ürünleri Dergisi, Sayı: 31-32, Cilt: 8 Sayfa: 116-123.
- [15] Dutrieu, J., 1960. Observations biochimiques et physiologiques sur le développement d'Artemiasalina Leach. Arch. Zool. Exp. Gén., 99: 1—134.
- [16] Mathias, P., 1937. Biologie des Crustacés phyllopoies. ActaSci. Ind., 447: 1—107.
- [17] Morris, J.E. and Afzelius, B. A., 1967. The structure of the shell and outer membranes in encysted Artemiasalina embryos during cryptobiosis and development. J. Ultrastruct. Res., 20: 244—259.
- [18] Herbst D.B., (2001). Gradient of salinity stress, environmental stability and water chemistry as a template for defining habitat types and physiological strategies in inland salt waters. Hydrobiologia 466: 209-219.

Performance Analysis of DSR Routing Protocol in MANET

Dr. Khin Khat Khat Kyaw
Associate Professor
Information Technology Department
West Yangon Technological University, Yangon
Myanmar

Abstract: Since the usage of mobile applications gets higher, the availability of MANET needs better performance. The topology of MANET dynamically changes because of mobility. Consequently, the routing protocols used in MANET must be fast and save. Therefore, the performance analysis of MANET routing protocols becomes an interesting case in networking research area. In this paper, the performance of DSR routing protocol has been analysed in term of throughput, end-to-end delay, PDR and packet loss.

Keywords: MANET, DSR, NS2, routing, PDR, throughput

1. INTRODUCTION

Mobile ad hoc network (MANET) is a collection of independent mobile nodes with no centralized administration. Mobility makes network topology unstable and results various changes in connection between two hosts. Routing path can be broken frequently and so its routing is more complex than that of wired networks.

In MANET, to support mobile computing, a mobile host must be able to communicate with other mobile hosts which may not lie within its radio transmission range. Hence routing protocols will need to perform four important functions as determination of network topology, maintaining network connectivity, transmission scheduling channel assignment, and packet routing. Routing protocols in MANETs were developed based on the design goals of minimal control overhead, minimal processing overhead, multi hop routing capability, dynamic topology maintenance and loop prevention[1].

In general, ad hoc routing protocols can be classified into three groups: reactive (on-demand), proactive (table-driven) protocol, and hybrid protocol.

Reactive (on-demand) routing protocols find routes by using the route request packet. It is a bandwidth efficient on-demand routing protocol for Mobile Ad-Hoc Networks. The protocol deals with two main functions of Route Discovery and Route Maintenance. The discovery of new route is decided by Route Discovery function and the detection of link breaks and repair of an existing route is decided by Route Maintenance function. Reactive or on-demand routing protocols route is discovered when required. Distribution of information is not required in reactive protocols. The popular reactive protocols are AODV and DSR. These protocols do not maintain permanent route table. Instead, routes are built by the source on demand.

Proactive protocols maintain the global topology information in the form of tables at every node. These tables are updated frequently in order to maintain consistent and accurate network state information. The well-known examples are DSDV, WRP, and STAR.

A hybrid routing protocol such as ZRP effectively combines the best features of both proactive and reactive routing protocols. The key concept employed in ZRP is to use a proactive routing scheme within a limited zone every node, and use a reactive routing scheme for nodes beyond this zone.

Each protocol type has its specific network behavior. Therefore, the performance analysis of these protocols is a must task to know the behavior and efficiency rate in that environment. Several factors will affect the overall performance of any protocol operating in an adhoc network. For example, node mobility may cause link failures, which negatively impact on routing and quality of service (QoS) support. Network size, control overhead, and traffic intensity will have a considerable impact on network scalability along with inherent characteristics of ad hoc networks may result in unpredictable variations in the overall network performance.

2. RELATED WORK

Dynamic Source Routing(DSR) protocol adapts quickly to routing changes when host movement is frequent, yet requires little or no overhead during periods in which hosts move less frequently[1].

Source routing is a routing technique in which the sender of a packet determines the complete sequence of nodes through which to forward the packet; the sender explicitly lists this route in the packet's header, identifying each forwarding "hop" by the address of the next node to which to transmit the packet on its way to the destination host. When a host needs a route to another host, it dynamically determines one based on cached information and on the results of a route discovery protocol.

To send a packet to another host, the sender constructs a source route in the packet's header, giving the address of each host in the network through which the packet should be forwarded in order to reach the destination host. The sender then transmits the packet over its wireless network interface to the first hop identified in the source route. When a host receives a packet, if this host is not the final destination of the packet, it simply transmits the packet to the next hop identified in the source route in the packet's header. Once the packet reaches its final destination, the packet is delivered to the network layer software on that host.

A host initiating a route discovery broadcasts a route request packet which may be received by those hosts within wireless transmission range of it. The route request packet identifies the host, referred to as the target of the route discovery, for which the route is requested. If the route discovery is successful the initiating host receives a route reply packet listing a sequence of network hops through which it may reach the target.

Dynamic Source Routing (DSR) protocol was extended and termed as Energy Efficient Secure Dynamic Source Routing (EESDSR)[3]. The protocol was based on an efficient, power aware and distributed trust model that enhances the security of Dynamic Source Routing (DSR) protocol. The model identified the nodes exhibiting malicious behaviors like: gray hole, malicious topology change behavior, dropping data packets and dropping control packets.

The performance of optimized dynamic source routing protocol (DSR) was investigated for MANETs. To find the optimal paths between the communicating nodes, traditional DSR algorithm was modified by using the Fire fly algorithm. In recent times, a population based method named as Firefly algorithm was stimulated by the surveillance of real firefly and its brightness behaviour. So firefly algorithm was used for their proposed method on MANET which improved the DSR routing performance with well-organized packets transfer from the source to destination node. Optimal route was found based on link quality, node mobility and end to end delay. Simulations were conducted with 25 nodes and the performance of the traditional DSR, link quality based DSR for selecting a route and proposed firefly algorithm for optimal route finding are compared by the parameters such as throughput, end to end delay, number of retransmitted packets and the number of hops to the destination[4].

Energy Secure Dynamic Source Routing (ESDSR) Protocol has been proposed in [5]. This study analyzes DSR protocol on the basis of energy consumption by using a mechanism in which nodes having less energy will not use in route selection to prolong the life time of network. This Energy Secure DSR (ESDSR) uses basic mechanism of existing DSR with little modification to optimize DSR performance in the sense of energy consumption as well when ESDSR is compared with some additional parameters like delay, throughput and packet delivery ratio and it showed better performance than DSR..

3. SIMULATION DESIGN

The system was implemented in SUMO and NS2 simulation tools. The aim is to evaluate performance parameters of DSDV routing protocol in different conditions.

1) *Simulation Parameters:* The paper focuses on the following parameters: throughput, end-to-end delay, number of dropped packets, packet loss and PDR.

Throughput means the measure of how fast a node can actually sent the data through a network. So throughput is the

average rate of successful message delivery over a communication channel.

$$\text{Throughput} = \frac{\text{number of received packets}}{\text{number of sent data packets}}$$

End-to-end delay is the time taken for an entire message to completely arrive at the destination from the source. The average end-to-end delay is calculated as:

$$\text{End-to-end delay} = \frac{\text{total packet duration}}{\text{total number of packets}}$$

Packet Delivery Ratio (PDR) is the ratio of the total data bits established to total data bits sent from source to destination.

2) *Mobility Parameters Values:* Table 1 shows the mobility parameters that were used in experiment. The test case-1 was implemented for various numbers of nodes: 30, 50 and 100. In these three cases, the number of connection is set the same: 10 TCP connections.

The next case (case-2) was considered for various numbers of TCP traffic: 10 and 20. In this case, the number of nodes is set to constant value 30.

The last case is similar to case- 2 except the number of nodes is set to constant value 100.

Table 1. Parameter Values

Parameter	Value
Number of connection	10,20
Number of nodes	30,50,100
Packet type	TCP
Maximum packet size	1000 byte
Traffic speed	64 kbps

4. SIMULATION RESULTS

NS2 is the most well-known simulator to the development and examining of mobile ad- hoc networking protocols. The mobility model was implemented in SUMO mobility model tool. The following section shows simulation results and discussion on performance of DSR protocol.

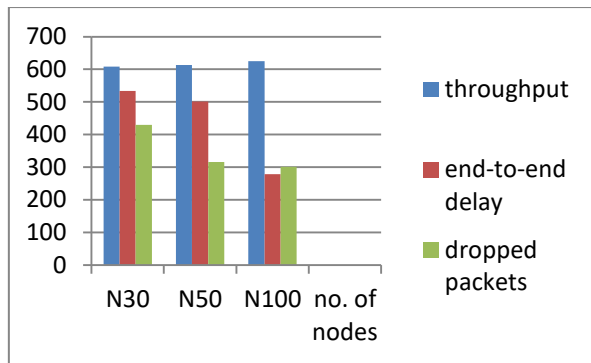


Figure. 1 Performance of DSR in various numbers of nodes

According to Figure1, throughput is nearly similar in all cases. However, end-to-end delay decreases with the increased nodes. The number of dropped packets gets less with the increased number of nodes. Therefore, it can be concluded that DSR provides fast speed for a large number of nodes.

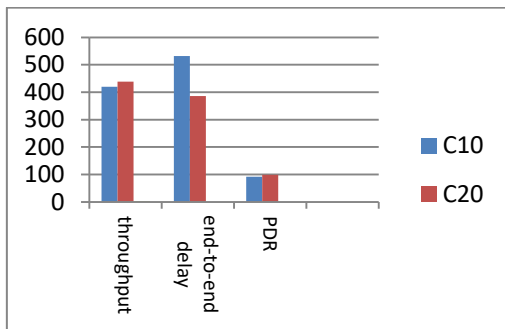


Figure. 2 Performance comparison in various number of connection on 30 nodes

According to Figure 3, the higher connection provides the higher throughput. End-to-end delay decreases with the improved number of connection. The larger traffic produces the higher PDR. Here, it is clearly seen that DSR is a good choice for complex connection.

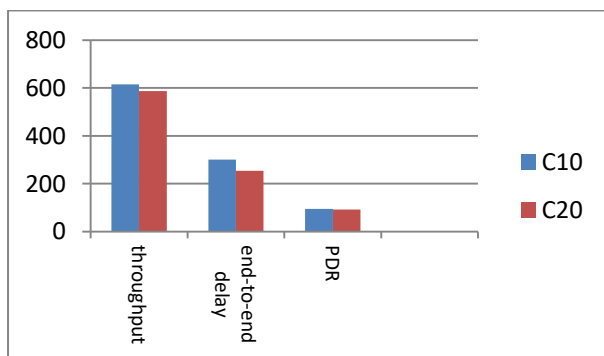


Figure. 3 Performance comparison in various number of connection on 100 nodes

As shown in Figure 3, when the number of traffic increases from 10 connections to 20 connections, throughput decreases, end-to-end delay decreases, and PDR decreases.

6. CONCLUSION

DSR is a famous reactive protocol in MANET routing protocols. This paper implements the mobility and traffic models to observe the performance of DSR protocol. The experiments have done on various numbers of nodes and various numbers of connections. According to the results, DSR is suitable for complex connections in many nodes.

REFERENCES

- [1] Royer E.M.andToh C., A review of current routing protocols for adhoc mobile wireless networks, IEEE personal communications,1999, pp. 46–56.
- [2] David B. Johnson and David A. Maltz, Dynamic Source Routing in Ad Hoc Wireless Networks, <https://www.researchgate.net/publication/2802692>.
- [3] Deepika Kukreja, Sanjay Kumar Dhurandher, and B.V.R. Reddy, Enhancing the Security of Dynamic Source Routing Protocol Using Energy Aware and Distributed Trust Mechanism in MANETs, Advances in Intelligent Systems and Computing 321, DOI: 10.1007/978-3-319-11227-5_8.
- [4] N. Prasath and J. Sreemathy, Optimized dynamic source routing protocol for MANETs, Cluster Comput (2018). <https://doi.org/10.1007/s10586-017-1638-1>.
- [5] Hina Khalid1, Tahir Nawaz2, Energy Secure Dynamic Source Routing (ESDSR) Protocol For (MANET), IOSR Journal of Computer Engineering (IOSR-JCE). e-ISSN: 2278-0661,p-ISSN: 2278-8727, Volume 18, Issue 2, Ver. I (Mar-Apr. 2016), PP 62-75

A Study on COP of Existing Ice Plant

Soe Myat Thu
 Department of Mechanical
 Engineering
 Technological University
 (Mawlamyine)
 Mawlamyine, Myanmar

Thant Zin Win
 Department of Mechanical
 Engineering
 Technological University
 (Mawlamyine)
 Mawlamyine, Myanmar

Hti Lar Tun Kyi
 Department of Mechanical
 Engineering
 Technological University
 (Mawlamyine)
 Mawlamyine, Myanmar

Abstract: Refrigeration is the process of removing heat from substance or space to reduce its temperature and transferring that heat to another substance or refrigeration is providing and maintaining the temperature below that of the surrounding temperature. To produce this effect requires certain machinery, hence, the method is called mechanical refrigeration. One of applications of refrigeration is ice plant. 10 tons per day of block ice plant is studied for COP improvement. This plant is located in Yangon, Myanmar. Design calculation of compressor, evaporator and COP of existing ice plant are determined. Ammonia is used as refrigerant in this plant. To improve COP of ice plant, refrigerant changing can be considered. If R-22 or R-134a is used, COP improvement occurs. COP with R-22 is 3.88. COP with R-134a is 3.94.

Keywords: refrigeration, mechanical refrigeration; ice plant; COP, Ammonia, R-22, R-134a

1. INTRODUCTION

The methods of production of cold by mechanical processes are quite recent. Long back in 1748, William Coolen of Glasgow University produced refrigeration by creating partial vacuum over ethyl ether. But he could not implement his experience in practice. The first development took place in 1834 when Perkins proposed a hand-operated compressor machine working on ether. Then in 1851 came Gorrie's air refrigeration machine, and in 1856 Lande developed a machine working on ammonia.

The pace of development was slow in the beginning when steam engines were the only prime movers known to run the compressors. With the advent of electric motors and consequently higher speeds of the compressors, the scope of applications of refrigeration widened.

2. CLASSIFICATION OF ICE PLANTS

Ice plants are usually classified by the type of ice they produce; hence there are block ice plants, flake ice plants, tube, slice or plate ice plants and so on. A further subclassification may be made of plants depending on whether they produce dry subcooled ice or wet ice. Generally, subcooled ice is produced in plants that mechanically remove the ice from the cooling surface. Most flake ice plants are examples of this type. Wet ice is usually made in plants that use a defrost procedure to release the ice. The defrost partially thaws the ice where it makes contact with the cooling surface and unless the ice has been reduced to a temperature substantially below 0°C (subcooled) the surface will remain wet. Tube ice and plate ice plants are examples of this type.

2.1 Block Ice Plant

The traditional block ice plant forms the ice in cans which are submerged in a tank containing circulating sodium or calcium chloride brine. The dimensions of the can and the temperature of the brine are usually selected to give a 24 hour production time and batches of cans are emptied and refilled in sequence during that period. Ice block weight can range from 12 to 150 kg depending on requirements; 150 kg is regarded as the largest size of block one man can conveniently handle.

The size of tank required is related to the daily production. Table 2 describes the approximate size of the freezing tank (ice-making tank) for 135 kg standard ice cans.

Table. 1 Standard sizes of ice can

Capacity	A (mm)	B (mm)	C (mm)	Standard Freezing Time
11kg (25lbs)	100	260	580	4.5 ~ 5 Hrs
22kg (50lbs)	130	300	815	8 ~ 9
45kg (100lbs)	190	405	815	17~ 20
90kg (200lbs)	290	570	815	40 ~ 48
135kg (300lbs)	290	570	1145	40 ~ 48
135kg (300lbs)	280	560	1250	37 ~ 45

Table. 2 Standard sizes of Freezing Tank

Nominal Daily Ice-making Capacity (ton)	Number of Ice-Cans to be accommodated	Dimensions of Freezing Tank			System
		Length (m)	Width (m)	Depth (m)	
5	10 × 8 = 80	6.30	3.65	1.20	Single-Can
10	12 × 14 = 168	10.30	5.00	1.20	Twin-Can
20	16 × 20 = 320	14.20	6.30	1.20	Twin-Can
30	20 × 24 = 480	16.50	7.85	1.20	Multi-Can
40	26 × 25 = 650	17.50	10.00	1.20	Multi-Can

50	26×31 = 806	21.50	10.00	1.20	Multi-Can
----	-------------------------	-------	-------	------	-----------

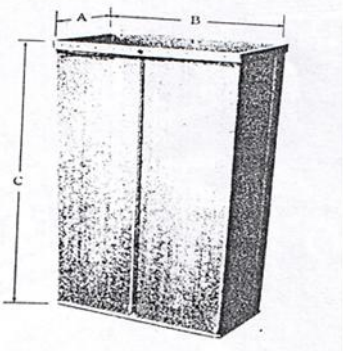


Figure 1. Ice Can

2.2. Flake Ice Plant

A sheet of ice 2-3 mm thick is formed by spraying water on the surface of a refrigerated drum and scrapping it off to form dry subcooled flakes. In some models the drum rotates against a stationary scraper on its outer surface. In others the scraper rotates and removes ice from the inner wall of a double walled stationary drum.

2.3. Tubular Ice – Inside Tube

When ice is produced inside a tube, the freezing cycle is approximately from 13 to 26 min. the tube is usually 20 to 50 mm in diameter, producing a cylinder that can be cut to desired lengths. The refrigerant temperature outside the tube is continually dropping, with an initial temperature of -4°C and terminal suction temperature ranging from -7 to -20°C . At the end of freezing cycle, the circulating water is shut off and the ice is harvested by introducing hot discharge gas into the refrigerant in the freezing section.

2.4. Tubular Ice-Outside Tube

Tubular ice is produced by freezing a falling film of water either on the outside of a tube with evaporating refrigerant on the inside or by freezing water on the inside of tubes surrounded by evaporating refrigerant on the outside.

When ice is produced on the outside of a tube, the freezing cycle is normally from 8 to 15 min with the final ice thickness from 5 to over 13mm following the curvature of the tube. The refrigerant temperature inside the tube continually drops from an initial suction temperature of about -4°C to the terminal suction temperature in the range of -12 to -26°C . At the end of freezing cycle, the circulating water is shut off. Introducing hot discharge gas results in harvest defrost. This type of ice maker operates with refrigerants R-717, R-12, and R-22.

3. PLATE ICE PLANT

Plate ice makers are commonly defined as those that build ice on a flat vertical surface. Water is applied above freezing plates and flows by gravity over the freezing plates during the freezing cycle. Liquid refrigerant at a temperature of between -21 to -7°C is contained in internal circuiting inside the plate. The freezing cycle time governs the thickness of ice produced. Ice thickness in the range of 6 to 20mm are quite common, with freezing cycles vary from 12 to 45 min.

4. REFRIGERANTS

The working medium circulating in a refrigeration machine or heat pump is referred to as the refrigerant. A refrigerant is the substance used for heat transfer in a refrigeration system. It

absorbs heat (latent heat and sensible heat) from the source at a low temperature and pressure and gives up this heat at a high temperature and pressure.

Chlorofluorocarbons (CFCs) have been used as refrigerants since 1930. Hydrochlorofluorocarbons (HCFCs) and hydrofluorocarbons (HFCs) have been introduced later as refrigerants. CFCs and HCFCs are partly responsible for depleting the ozone layer.

A chlorofluorocarbon (CFC) is an organic compound that contains only carbon, chlorine, and fluorine, produced as a substituted derivative of methane and ethane. It is an ozone-depleting compound, which is highly damaging to the environment.

Hydrochlorofluorocarbons (HCFC's) are similar to CFC's but contain hydrogen and have a lower ozone depleting potential. Hydrofluorocarbon refrigerants (HFC's) are composed of hydrogen, fluorine and carbon atoms connected by single bonds between the atoms; they do not deplete the ozone layer because they do not contain chlorine or bromine.

Ammonia is the cheapest refrigerant. R-12 is slightly cheaper than R-22. During the last few years, R-22 has replaced ammonia in the dairy and frozen food industry. The fact that ammonia may attack some food products has been predominant cause for the change from ammonia to R- 22 even in cold storages.

R 134-a is one of the leading candidates to replace R-12 in many of applications employing this refrigerant. R-134a is an HFC and has a zero ozone depletion potential and a low greenhouse effect.

5. SIMPLE VAPOUR COMPRESSION CYCLE

The vapour compression cycle is used for refrigeration in preference to gas cycles; making use of the latent heat enables a far larger quantity of heat to be extracted for a given refrigerant mass flow rate. This makes the equipment as compact as possible. A liquid boils and condenses – the change between the liquid and the gaseous states – at a temperature which depends on its pressure, within the limits of its freezing point and critical temperature. In boiling it must obtain the latent heat of evaporation and in condensing the latent heat is given up.

Heat is put into the fluid at the lower temperature and pressure thus providing the latent heat to make it vaporize. The vapour is then mechanically compressed to a higher pressure and a corresponding saturation temperature at which its latent heat can be rejected so that it changes back to a liquid. The cooling effect is the heat transferred to the working fluid in the evaporation process, i.e. the change in enthalpy between the fluid entering and the vapour leaving the evaporator.

6. MAIN COMPONENTS OF REFRIGERATION SYSTEM

There are four main components in refrigeration system.

- (i) Compressor
- (ii) Condenser
- (iii) Evaporator
- (iv) Expansion Device

6.1. Compressor

The compressors are one of the most important parts of the refrigeration cycle. The compressor compresses the

refrigerant, which flows to the condenser, where its gets cooled.

Compression of the refrigerant to the suitable pressure ensures its proper condensation and circulation throughout the cycle.

6.1.1 Reciprocating Compressors

The reciprocating compressor is the most widely used, being employed in all fields of refrigeration. It is especially adaptable for use with refrigerants requiring relatively small displacement and condensing at relatively high pressures.

Reciprocating compressors are defined as open-type when one end of crankshaft protrudes outside of the crankcase the casing that contains the pistons and the mechanisms inside the compressors.

6.1.2 Rotary Compressors

The rotary compressors are very suitable for refrigerants having moderate or low condensing pressures. Rotary compressor is positive displacement, direct drive machines. Two designs of rotary compressors are rolling piston type and rotating vane type.

6.1.3 Centrifugal Compressors

Centrifugal compressors have a single major moving part, an impeller that compresses the refrigerant gas by centrifugal force. The gas is given kinetic energy as it flows through the impeller. This kinetic energy is not useful itself, so it must be converted to pressure energy. This is done by allowing the gas to slow down smoothly in a stationary diffuser surrounding the impeller.

6.2. Condenser

The condenser is a heat transfer surface. Heat from the hot refrigerant vapour passes through the walls of the condenser to the condensing medium. As the result of losing heat to the condensing medium, the refrigerant vapour is first cooled to saturation and then condensed into the liquid state.

6.2.1 Types of Condenser

There are three types of condensers. The name of each type is determined by the condensing medium.

- (i) Air-cooled condenser uses air as the condensing unit.
- (ii) Water-cooled condenser uses water as the condensing unit.
- (iii) Evaporative condenser uses air and water as the condensing unit.

6.2.1.1 Air-cooled Condensers

The circulation of air over an air-cooled condenser may be either natural convection or by the action of a fan or blower. Where air circulation is natural convection, the air quantity circulated over the condenser is low and relatively large condensing surface is required.

Because of their limited capacity, natural-convection condensers are used only on small applications, principally domestic refrigerators and freezers.

6.2.1.2 Water-cooled Condensers

The several types of water-cooled condensers commonly used included: shell and coil condenser, shell and tube condenser and double tube condenser.

6.2.1.3 Evaporative Condensers

The evaporative condenser is defined as comprising a coil in which the refrigerant is flowing and condensing inside, and its outer surface is wetted with water and exposed to stream of air to which heat is rejected principally by evaporation of water.

6.3. Evaporator

An evaporator is any heat transfer surface in which liquid is vapourized for the purpose of removing heat from a refrigerated space or product. The capacity of any evaporator

or cooling coil is defined as by the rate at which heat will pass through the evaporator walls from the refrigerated space or product to the liquid refrigerant that is vapourizing.

6.3.1 Types of Evaporator by Construction

By construction, the three principle types of evaporator are bare-tube evaporators, plate-surface evaporators and finned evaporators.

6.3.1.1 Bare-tube Evaporators

Bare-tube evaporators are usually constructed of either steel-pipe or copper tubing. Steel pipe is used for large evaporators and to be employed with ammonia. Copper tubing is utilized in the manufacture of smaller evaporators intended for use with refrigerants except with ammonia. Bare-tube coils are available in a number of sizes, shapes and designs.

6.3.1.2 Plate-surface Evaporators

Plate-surface evaporators may be used singly or in banks. The plates may be manifold for parallel flow of the refrigerant or they may be connected for series flow. Plate-surface evaporators provide excellent shelves in freezer rooms and similar applications.

6.3.1.3 Finned Evaporators

Fin sizes and spacing depend in part on the particular type of application for which the coil is designed. The size of the tube determines the size of the fin. Small tubes require small fins. Fin spacing varies from one fin per inch to fourteen fins per inch, depending on the operating temperature of the coil.

6.4. Expansion Devices

The last of basic elements in the vapour compression cycle, after the compressor, condenser, and evaporator, is the expansion device. The purpose of the expansion device is twofold: it must reduce the pressure of the liquid refrigerant, and it must regulate the flow of refrigerant to the evaporator.

7. DESIGN CALCULATION OF COMPRESSOR

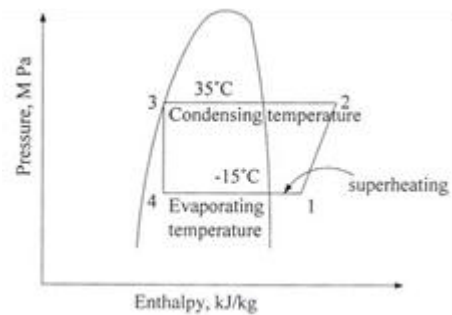


Figure. 2 Pressure Enthalpy Diagram

Open type ammonia reciprocating compressor with four cylinders is used in existing ice plant. Condensing temperature is 35°C and evaporating temperature is -15°C and then 10°C superheat is assumed.

Heat rejected from water, Q_{ice}

$$Q_{ice} = m_{ice} c_p \Delta t + m_{ice} h_1 + m_{ice} c_p \Delta t \quad (1)$$

where

Q_{ice} = heat rejected from water,

m_{ice} = total weight of block, kg,

c_p = specific heat of water

Δt = temperature difference

h_1 = latent heat of fusion

Q_{ice} is calculated from equation (1).

From R-717 chart,

$h_1 = 1590$ kJ/kg, $h_2 = 1900$ kJ/kg, $h_3 = h_4 = 500$ kJ/kg, $v_1 = 0.63$ m³/kg, $v_2 = 0.14$ m³/kg

$$\text{Refrigerant flow rate (m}^\circ\text{R)} = \frac{Q_{\text{evap}}}{h_1 - h_4} \quad (3)$$

Actual volume of suction vapor compressed per minute

$$v^\circ\text{R} = m^\circ\text{R} v_1 \quad (4)$$

$m^\circ\text{R}$ is obtained from equation (3).
To find the bore and stroke, the speed of compressor crankshaft is assumed to be 1000 r.p.m for standard revolution. $L = 0.85 D$ is assumed for open type reciprocating compressor.

$$\text{Piston displacement } V_p = \frac{\pi}{4} \times D^2 \times L \times N \times n \quad (5)$$

D = Bore, L = stroke length, N = no of revolution per minute, n = no of cylinder

Calculated bore dimension is get from equation (5). And standard bore size is chosen.

After choosing standard bore and stroke, V_p is calculated again with choosen condition. Piston displacement with

$$\text{standard size, } V_p = \frac{\pi}{4} \times D^2 \times L \times N \times n$$

$m^\circ\text{R}$ is calculated again by using piston displacement with standard size.

$$\text{Actual intake volume, } V_p = m^\circ\text{R} \times v_1 \quad (6)$$

From equation (6), theoretical $m^\circ\text{R}$ can be calculated.

Theoretical refrigerating capacity, TRC

$$Q_{\text{evap}} = m^\circ\text{R} (h_1 - h_4) \quad (7)$$

Theoretical compressor work done

$$W_{\text{comp}} = m^\circ\text{R} (h_2 - h_1) \quad (8)$$

Motor power required

$$W_{\text{motor}} = \frac{W_{\text{comp}}}{\eta_m} \quad (9)$$

where, η_m = mechanical efficiency

Actual motor power required

$$P_{\text{motor}} = \frac{W_{\text{motor}}}{\eta_e} \quad (10)$$

where, η_e = electrical efficiency

8. CALCULATION FOR EVAPORATOR COIL LENGTH

To obtain the surface area of coil,

$$Q_{\text{evap}} = U A \Delta t \quad (11)$$

where, Q = heat absorbed by evaporator coil, kW, U = heat transfer coefficient, W/m²K, A = effective surface area of coil, m², Δt = log mean temperature difference of brine, K or °F

$$\Delta t = \frac{GTD - LTD}{Ln \frac{GTD}{LTD}} \quad (12)$$

where, GTD = greater temperature difference, K or °F

LTD = lower temperature difference, K or °F

$$A = \pi \times D \times L \quad (13)$$

9. COEFFICIENT OF PERFORMANCE (COP)

The efficiency of refrigeration systems is denoted by its coefficient of performance (COP).COP of refrigeration is calculated by the following equation.

$$\text{COP} = \frac{h_1 - h_4}{h_2 - h_1} \quad (14)$$

For R-22,

$$h_1 = 407.5 \text{ kJ/kg, } h_2 = 450 \text{ kJ/kg, } h_3 = h_4 = 242.5 \text{ kJ/kg}$$

By using equation (14), COP for R-22 can be calculated.

For R-134-a,

$$h_1 = 398.33 \text{ kJ/kg, } h_2 = 436.25 \text{ kJ/kg, } h_3 = h_4 = 248.75 \text{ kJ/kg}$$

By using equation (14) again, COP for R-134a can be calculated.

Table 3. Calculated results of existing ice plant

Heat rejected from water, Q_{ice}	64.3 kW
Refrigeration effect (R.E)	1090 kJ/kg
Actual volume of suction vapor compressede per minute, $v^\circ\text{R}$	2.4 m ³ /min
Calculated bore dimension	97 mm
Choosen standard bore and stroke size	100 mm, 85 mm
Position displacement with standard size, V_p	2.67 m ³ /min
Refrigerant flow rate, $m^\circ\text{R}$	0.071 kg/s
Theoretical refrigerating capacity, TRC	77 kW
Theoretical compressor work done, W_{comp}	22 kW
Motor power required, W_{motor}	28 kW
Actual motor power required, P_{motor}	35 kW
Evaporator coil length	232 m
C.O.P(Ammonia)	3.5

Table 4. C.O.P Comparison with superheating

No	Refrigerants	COP $T_e = 35^\circ\text{C, } T_c = -15^\circ\text{C}$
1	Ammonia (R-717)	3.51
2	R-22	3.88
3	R-134a	3.94

8. CONCLUSION

The study observes COP increase when R-22 and R-134a are replaced. So, R-22 or R-134a can be used for COP improvement instead of ammonia. Accordance with COP, R-134a is the most suitable refrigerant in this plant.

9. ACKNOWLEDGMENTS

The authors would like to thank all people who give their tremendous moral supports during our study.

10. REFERENCES

- [1] Arora, C.P. 1975. Refrigeration and Air Conditioning. Tata McGraw-Hill Company limited. New Delhi.
- [2] C.P. Arora., Refrigeration and Air-conditioning, Third Edition.
- [3] Dossat, R.J. 1997. Principle of Refrigeration Prentice-Hall, Inc. Simon and Schuster/A Viacom Company, New Jersey.
- [4] G.F. Hundy. A.R. Trot. T.C. Welch, Refrigeration and Air-conditioning, Fourth Edition.
- [5] ROY J.DOSSAT, Principle of Refrigeration, Fourth Edition.
- [6] Stoeckes, W.F.1992. Ammonia Data Book. International Institute of Ammonia Refrigeration (IIAR). Washington. DC.
- [7] Waterman, J.J., and Graham, J.1968. Ice in fisheries. Torry Research Station, Aberdeen.U.K.

Routing Overhead Comparison on AODV Based Routing Protocols in Vehicular Adhoc Network

Dr. Khin Khat Khat Kyaw
Associate Professor
Information Technology Department
West Yangon Technological University, Yangon
Myanmar

Abstract: Vehicular Ad hoc Network(VANET) is a specific type of Mobile Ad hoc Network(MANET) in which the nodes(vehicles) are moving with high speeds. VANET is one of important issues in building smart city. The first popular routing protocol for MANET is AODV. After that there are various papers that propose the modification of AODV. This paper focus on routing overhead comparison among AODV based routing protocols. The simulation was done by using Network Simulator 2 (NS2) and MOVE (MObility model generator for VEhicular networks) over SUMO (Simulation of Urban Mobility).

Keywords: VNET, AODV, MOVE, SUMO ,NS2

1. INTRODUCTION

Rather than the Mobile Ad hoc communication the direct communication between vehicles is relatively new approach. The development of VANET provides some attractive services such as comfort applications and safety applications[1].

Comfort application improves passenger comfort and traffic efficiency and/or optimizes the route to a destination. Examples for this category are: traffic information system, weather information, gas station or restaurant location and price information, and interactive communication such as Internet access or music download.

Safety application gives the safety of passengers by exchanging safety relevant information via inter-vehicle Communication (IVC). The information is either presented to the driver or used to activate an actuator of an active safety system. Example applications of this class are: emergency warning system, lane-changing assistant, intersection coordination, traffic sign/signal violation warning, and road-condition warning.

VANET has many challenges including service differentiation, admission control, efficient broadcasting, geographical routing, etc.

The paper is organized as follows: The next section discusses three routing protocols: AODV, MAODV and AOMDV. Section Three shows simulation results. Section Four explains the characteristic simulation tools. Finally, the last section concludes the comparison analysis of those three protocols.

2. RELATED WORK

Several research studies have been carried out to enhance the routing on VANET. The performance analysis of the

protocols is the major step before selecting a particular routing protocol. In fact, path routing and protocol selection are the primary strategies to design any vehicular ad-hoc network considering data delivery, data integrity and especially time delivery.

The authors illustrate the differences between AODV, DSR and DSDV based on TCP and CBR connection with various network parameters[2]. The performance of these three routing protocols shows some differences in low and high node density. Indeed, in low density with low pause time, the PDR of CBR connection for these routing protocols is low. While for TCP connection, the PDR is high for DSR and average for DSDV.

Performance analysis on VANET routing protocols was done to identify which routing method had better performance in highly mobile environment of VANET [3]. The authors conclude that cluster-based routing protocols with short interval values provide better Packet Delivery Ratio, as their routing table is updated quickly and one node is responsible to deliver messages to all nodes of the clusters. They observe that OLSR and AODV routing protocols have higher end-to-end delay than DYMO. MOBIC and AMACAD again outperforms the other routing protocols when the node density increases in this scenario.

3. AODV BASED ROUTING PROTOCOLS

3.1 Ad-hoc On-demand Distance Vector (AODV)

AODV is a combination of on-demand and distance vector i.e. hop-to-hop routing methodology [4]. When a node needs to know a route to a specific destination it creates a ROUTE REQUEST. Next the route request is forwarded by intermediate nodes which also create a reverse route for itself

for destination. When the request reaches a node with route to destination it creates again a REPLY which contains the number of hops that are require to reach the destination. All nodes that participate in forwarding this reply to the source node create a forward route to destination. This route created from each node from source to destination is a hop-by-hop state and not the entire route as in source routing.

3.2 Multicast Ad hoc On-demand Distance Vector Routing Protocol (MAODV)

In [5], the authors extend Ad-hoc On-Demand Distance Vector Routing (AODV), an algorithm for the operation of such ad-hoc networks to offer novel multicast capabilities which follow naturally from the way AODV establishes unicast routes. AODV builds multicast trees as needed (i.e on-demand) to connect multicast group members. Control of the multicast tree is distributed so that there is no single point of failure. AODV provides loop-free routes for both unicast and multicast even while repairing broken links.

3.3 Adhoc Multipath on Demand Distance Vector Routing(AOMDV)

AOMDV, on the other hand, is a multi-path routing protocol[6] . It is an extension to AODV and also provides two main services i.e. route discovery and maintenance. Unlike AODV, every RREP is being considered by the source node and thus multiple paths discovered in one route discovery. Being the hop-by-hop routing protocol, the intermediate node maintains multiple path entries in their respective routing table. As an optimization measure, by default the difference between primary and an alternate path is equal to 1 hop. The route entry table at each node also contains a list of next hop along with the corresponding hop counts. Every node maintains an advertised hop count for the destination. Advertised hop count defined as the “Maximum hop count for all the paths”. Route advertisements of the destination are sent using this hop count. An alternate path to the destination is accepted by a node if the hop count is less than the advertised hop count for the destination.

4. SIMULATION TOOLS

The key concept for VANET simulations is a real world vehicular mobility model which will ensures conclusions drawn from simulation experiments will carry through to real world deployments. Simulation of Urban Mobility (SUMO) allows users to easily generate real world mobility models for VANET simulations[7]. SUMO is conceived to simulate a traffic road network of the size of a city.

As the simulation is multi-modal, which means that not only are car movements within the city modelled, but also public transport systems on the street network, including alternative train networks, the atomic part of the simulation is a single human being. This human being is described by a departure time and the route he/she takes which again is made up of subroutes that describe a single traffic modality.

MOVE [8] tool is used to facilitate users to rapidly generate realistic mobility models for VANET simulations. MOVE is currently implemented in java and is built on top of an open source micro-traffic simulator SUMO. By providing a set of Graphical User Interfaces that automate the simulation script generation, MOVE allows the user to quickly generate realistic simulation scenarios without the hassle of writing simulation scripts as well as learning about the internal details of the simulator. The output of MOVE is a mobility trace file that contains information about realistic vehicle movements which can be immediately used by popular simulation tools such as NS2.

5. SIMULATION RESULTS

Both, routing and data packets have to share the same network bandwidth most of the times, and hence, routing packets are considered to be an overhead in the network. This overhead is called routing overhead. Routing overhead can be calculated the number of packets including sending and receiving packets by sending packets.

Table 1 shows the parameters that were used in simulation.

Parameter	Value
Channel Type	Wireless
Network Simulator	NS2.35
Routing Protocol	AODV, MAODV, AOMDV
Simulation Time	1050s
Number of Nodes	50, 100, 150,200
Mobility Model	MOVE, SUMO
Maximum Average Speed	20 to 50 (km/h)
Packet size	512 bytes

To make tests, city maps are generated using MOVE software. Figure 1 shows the map used for this process.

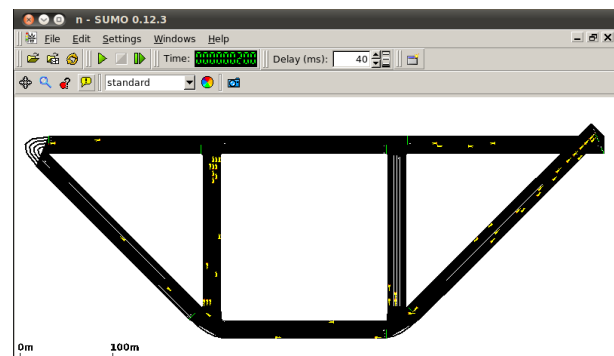


Figure 1. Mobility Model using SUMO

Based on the map shown in Figure 1, the communications between vehicles are implemented in NS2. For implementation, “tcl” script files are written and compiled.

The analysis is taken for three routing protocols: AODV, MAODV and AOMDV. After compiling those script files in NS2, the relevant “nam” files(*.nam) and “trace” files (*.tr) are generated.

The “nam” files can be used to simulate the packet communication between vehicles. The “trace” files are used to generate values of network performance parameters such as packet delivery ratio(PDR), throughput, dropout, etc. The “awk” script file as shown in Figure 2 is written to generate parameter values. With the command “gawk -f parameters.awk *.tr > *.txt”, the output values are produced in “*.txt” file.

```

BEGIN {
    sends=0;
    routing_packets=0.0;
}
{
    time = $3;
    packet_id = $41;
    # CALCULATE PACKET DELIVERY FRACTION
    if (( $1 == "s" ) && ( $35 == "tcp" ) && ( $19=="AGT" )) { sends++; }
    # CALCULATE TOTAL dsr OVERHEAD
    if (( $1 == "s" || $1 == "f" ) && $19 == "RTR" && $35 == "DSDV" )
        routing_packets++;

    RO = routing_packets/sends;    #routing overhead
    printf("RoutingOverheads = %.2f\n",RO);
    #printf("No. of dropped data (bytes) = %d\n",droppedBytes);
}

```

Figure2 . “awk” script to produce routing overhead(RO)

Table 2. Routing Overhead comparison

Number of Nodes/Vehicles	AODV	MAODV	AOMDV
50	23002	24030	24852
100	30021	34178	32873
150	39552	39650	39781
200	43777	43800	45311

The routing overhead comparison between three protocols is shown in Table 2. According to Table 2, AODV has the least routing overhead in various numbers of nodes. MAODV and AOMDV produce more routing overhead than that of AODV. However, the routing overheads are nearly the same when the number of node becomes larger. Since the modified protocols are addressed to reduce transmission time, they can provide high speeds. Therefore the modified protocols are suitable for large, complex traffic area.

6. CONCLUSION

This paper presents the routing overhead comparison of three protocols in VANET. The location area is implemented in SUMO. The simulation and analysis are taken in NS2. According to analysis results, AODV has the least routing overheads among three protocols. However, the routing overheads become nearly the same for the large communication area. It can be concluded that the modified AODV protocols are suitable for large and high speed communications.

REFERENCES

- [1] S. Yousefi, M. S. Mousavi, M. Fathy, Vehicular Ad Hoc Networks (VANETs): Challenges and Perspectives, <https://www.researchgate.net/publication/224761043>
- [2] B. Paul, A. Roy, and S. K. Paul. Comparison of DSR, AODV, and DSDV Routing Protocols with Varying Pause Time and Node Density over TCP and CBR Connections in VANET. IEEE, 2014.
- [3] B.Marzak, M Toumi, E.Benlahmar, T. Mohamed, Performance Analysis of Routing Protocols in Vehicular Ad Hoc Network, <https://www.researchgate.net/publication/309686186>
- [4] Perkins C.E. and Royer E.M, Ad-hoc, “On-demand Distance Vector Routing”, draft-ietf-manet-aodv-02.txt, 1998.
- [5] Royer, E. M. and Perkins, C. E.; Multicast Operation of the Ad-hoc On-Demand Distance Vector Routing Protocol, Proceedings of the 5th Annual ACM/IEEE International Conference on Mobile Computing and Networking (MOBICOM’99), Seattle, WA, USA, August 1999, pages 207-218.
- [6] Mahesh K.Marina and Samir R.Das, Adhoc Multipath on Demand Distance Vector Routing, Published online in Wiley Inter science, 2006. Pages: 969-988.
- [7] Daniel Krajzewicz, Georg Hertkorn, Peter Wagner , Christian Rössel , SUMO (Simulation of Urban MObility), <https://core.ac.uk/download/pdf/30941466.pdf>
- [8] Vaishali D. Khairnar, Dr. S.N.Pradhan, Mobility Models for Vehicular Ad-hoc Network Simulation, International Journal of Computer Applications (0975 – 8887), Volume 11– No.4, December 2010.

Generator Exciter Control for Hydro Power

Kyi Kyi Thein
Department of Electrical Power
Engineering
Technological University
(Thanlyin), Myanmar

Abstract: Myanmar has very rich hydropower resources with a total potential of around 100,000 MW. For obtaining efficient stability and good regulation of generator exciter control in hydropower system, automatic voltage regulators (AVR) are increasingly used. This paper presents the modeling and control of the excitation system with the automatic voltage regulator (AVR) to improve stability on a micro hydro power plant. The objective is to consider a generator AVR system without stabilizer and PID controller and with stabilizer and PID controller. The PID controller automated tuning was used with a view for improving the response of the system and make comparison between the frequency deviation step response. The transfer function controller blocks use linear block model and control techniques in MATLAB/ Simulink environment.

Keywords: Hydropower, Synchronous Generator, Excitation. AVR, Stabilizer, PID controller.

1. INTRODUCTION

Hydro power system performance is affected by dynamic characteristics of hydraulic turbine and its governor system during any disturbance, such as presence of a fault, harmonics on the network, and rapid change of load and loss of a line. An ideal modeling of hydro power plant components, such as synchronous machine, turbine and its governing system is necessary to analysis the power system response during any disturbance on the system.

There are two main types of generators that are used for the hydropower production: (i) synchronous generators (commonly referred as alternators) and (ii) asynchronous generators (referred as induction generators).

Synchronous generators are used in the case of standalone schemes (isolated networks). In case of weak grids where the unit may have significant influence on the network synchronous generator are used. For grid connected schemes both types of generator can be used. In case grid is weak; Induction generators be used if there are two units, one of the unit can be synchronous so that in case of grid failure; supply could still be maintained. Unit size is limited to 250 kW. In case of stronger grids induction generators up to a 2000 kW or even higher can be used. In case of isolated units, small capacity Induction generators with variable capacitor bank may be used up to a capacity of about 20 kW especially if there is no or insignificant Induction motor load less than about 20%.

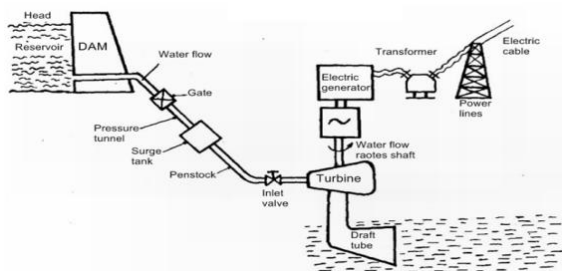


Figure 1. Layout of Hydropower plant

2. EXCITATION CONTROL SYSTEM IN GENERATORS

Types of excitation control system for speed control of the generator are:

- (i) Automatic Voltage Regulator for Generator Excitation Control (AVR)
- (ii) Power System Stabilizer (PSS)
- (iii) PID Controller (PID)
- (iv) AVR-PSS system with PID Controller

Automatic Voltage Regulator (AVR)

The automatic voltage regulator is used to regulate the voltage. It takes the fluctuate voltage and changes them into a constant voltage. The fluctuation in the voltage mainly occurs due to the variation in load on the supply system. The variation in voltage damages the equipment of the power system. The variation in the voltage can be controlled by installing the voltage control equipment at several places like near the transformers, generator, feeders, etc. The voltage regulator is provided in more than one point in the power system for controlling the voltage variations.

Power System Stabilizer (PSS)

With addition of a power system stabilizer (PSS) as a supplementary controller to the AVR, this combined generator excitation control, could eliminate any negative effects on the damping of the post-fault oscillation. The control signal for the power system stability (PSS) is either the speed deviation, or the electric power, or the system frequency as additional feedback signals for introducing a damping torque control component. The speed signal is the most commonly used.

PID Controller

A PID controller is one of the most common controllers which calculates an error value as the difference between a measured process variable and a desired set point. The controller attempts to minimize the error by adjusting the process through use of a manipulated variable.

The PID controller is used to improve the dynamic response as well as to reduce or eliminate the steady-state error. The

derivative controller adds a finite zero to the open-loop plan transfer function and improves the transient response. The integral controller adds a pole at origin and increases the system type by one and reduces the steady-state error due to step function to zero.

AVR-PSS System with PID Controller

The main objective of AVR system is to reduce the error signal to zero or an acceptable value. Proportional - Integral - Derivative (PID) controller, one of the most successful controllers is used in the AVR - PSS system. Using AVR - PSS together with PID controller greatly improves the closed loop system damping ratio.

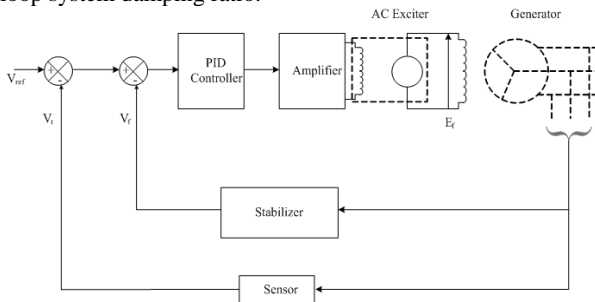


Figure 2. Schematic diagram of Generator Excitation system

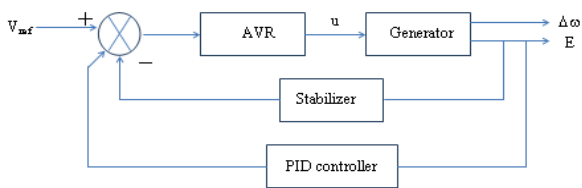


Figure 3. Block diagram of AVR-PSS system with PID

3. MATHEMATICAL MODELLING OF AVR SYSTEM

3.1 Amplifier Model

Transfer function of an amplifier is:

$$TF_A = \frac{K_a}{1 + s\tau_a}$$

where, K_a and τ_a represent the gain and time constant of the amplifier. The values of K_a are in the range of 10 to 40 and τ_a are in the range of 0.02 to 0.1 sec.

3.2 Exciter Model

Transfer function of an exciter is:

$$TF_E = \frac{K_e}{1 + s\tau_e}$$

where, K_e and τ_e represent the gain and time constant of the exciter. The values of K_e are in the range of 1 to 2 and τ_e are in the range of 0.4 to 1.0 sec.

3.3 Generator Model

Transfer function of a generator is:

$$TF_G = \frac{K_g}{1 + s\tau_g}$$

where, K_g and τ_g represent the gain and time constant of the generator. The values of K_g are in the range of 0.7 to 1.0 and τ_g are in the range of 1.0 to 2.0 sec from no load to full load.

3.4 Sensor Model

Transfer function of a sensor is:

$$TF_S = \frac{K_s}{1 + s\tau_s}$$

where, K_s and τ_s represent the gain and time constant of the sensor. The values of K_s are in the range of 0.02 to 1.0 and τ_s are in the range of 0.01 to 2.2 sec.

3.3 Stabilizer Model

Transfer function of a sensor is:

$$TF_F = \frac{K_f}{1 + s\tau_f}$$

where, K_f and τ_f represent the gain and time constant of the sensor. The values of K_f is 1.0 and τ_f are in the range of 0.01 to 0.06 sec.

3.6 PID Controller Model

There are several methods for tuning a PID loop. The most effective methods generally involve the development of some form of process model, choosing P, I, and D based on the dynamic model parameters. Manual tuning methods can be relatively inefficient, particularly if the loops have response times on the order of minutes or longer.

The choice of method will depend largely on whether or not the loop can be taken "offline" for tuning, and on the response time of the system. If the system can be taken offline, the best tuning method often involves subjecting the system to a step change in input, measuring the output as a function of time, and using this response to determine the control parameters.

Transfer function of a PID controller is:

$$TF_{PID} = K_P + \frac{K_I}{s} + K_D s$$

where, K_P , K_I and K_D represent the gain constants of PID controller.

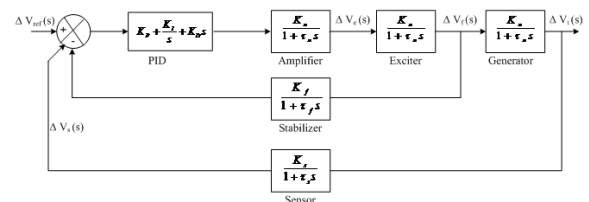


Figure 4. Transfer Function Model of Generator Exciter System with PID Controller

3.7 Calculation of AVR Parameters

For control system stability, the Routh-Hurwitz array was constructed and chooses the amplifier gain constant K_a . Assume AVR parameters as follow:

Amplifier gain constant, K_a	-
Amplifier time constant, τ_a	0.05
Exciter gain constant, K_e	1
Exciter time constant, τ_e	0.4
Generator gain constant, K_g	1
Generator time constant, τ_g	0.5
Sensor gain constant, K_s	1
Sensor time constant, τ_s	0.01

Open-loop transfer function of AVR is

$$G(s)H(s) = \frac{K_a(1)(0.1)}{(1 + 0.05s)(1 + 0.4s)(1 + 0.5s)(1 + 0.01s)}$$

$$= \frac{10000K_a}{s^4 + 124.5s^3 + 2545s^2 + 9600s + 10000}$$

The characteristic equation is

$$1 + G(s)H(s) = 1 + \frac{10000K_a}{s^4 + 124.5s^3 + 2545s^2 + 9600s + 10000} = 0$$

$$\therefore s^4 + 124.5s^3 + 2545s^2 + 9600s + 10000 + 10000K_a = 0$$

The Routh-Hurwitz array for this polynomial is

s^4	1	2545	$10000 + 10000K_a$
s^3	124.5	9600	0
s^2	2467.89	$10000 + 10000K_a$	0
s^1	$504.48K_a - 9095.52$	0	
s^0	$10000 + 10000K_a$		

From the s^1 row, to find K_a for control system stability,

$$504.48K_a - 9095.52 < 0$$

$$K_a < 18.03$$

For $K_a = 18.03$, the auxiliary equation from the s^2 row,

$$2467.89s^2 + 10000 + 10000(18.03) = 0$$

$$s = \pm j8.78$$

Since, for $K_a = 18.03$, a pair of conjugate poles on the $j\omega$ axis, and the control system is marginally stable.

Closed-loop transfer function of AVR is

$$\frac{G(s)}{1 + G(s)H(s)} = \frac{V_t(s)}{V_{ref}(s)}$$

$$= \frac{0.01K_a(s + 100)}{s^4 + 124.5s^3 + 2545s^2 + 9600s + 10000 + 10000K_a}$$

For the system to be stability, the amplifier gain of K_a should be chosen less than 18.03.

Choosing $K_a = 11$, the steady-state response is

$$\square_{\square, \square} = \square \square \square_{\square \rightarrow 0} \square \square_{\square}(\square) =$$

$$V_{t,ss} = \frac{11}{1 + 11} = 0.9167$$

The steady-state error is

$$V_{e,ss} = 1.0 - 0.9167 = 0.0833$$

In order to reduce the steady-state error, the amplifier gain must be increased, which results in an unstable control system. Therefore, choose $K_a = 11$. For the AVR parameters to get the lowest steady-state error, the calculation result shows in Table 1.

Table 1. Calculation result of AVR parameters

Quality	Transfer function	
Amplifier	$TF_A = \frac{K_a}{1 + s\tau_a}$	$TF_A = \frac{11}{1 + 0.05s}$
Exciter	$TF_E = \frac{K_e}{1 + s\tau_e}$	$TF_E = \frac{1}{1 + 0.4s}$
Generator	$TF_G = \frac{K_g}{1 + s\tau_g}$	$TF_G = \frac{1}{1 + 0.5s}$
Sensor	$TF_S = \frac{K_s}{1 + s\tau_s}$	$TF_S = \frac{1}{1 + 0.01s}$
Stabilizer	$TF_F = \frac{K_f}{1 + s\tau_f}$	$TF_F = \frac{0.4s}{1 + 0.04s}$
PID	$G_C(s) = K_P + \frac{K_I}{s} + K_D s$	$G_C(s) = 1 + \frac{0.25}{s} + 0.28s$

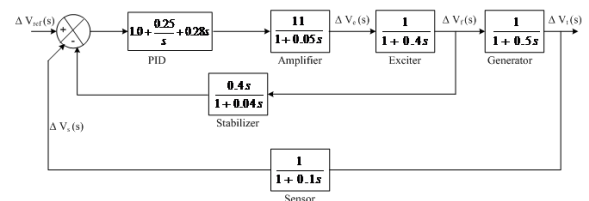


Figure 5. Block diagram of AVR-PSS with PID controller

4. RESULTS AND DISCUSSIONS

4.1 Simulink Model and Result of Simple AVR

Figure 6 shows an AVR system model in MATLAB simulink, where a combined simulation block model was constructed for the amplifier, exciter, and generator cases in order to obtain their respective step response.

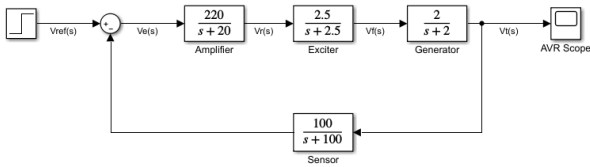


Figure 6 (a) Simulink model of simple AVR system

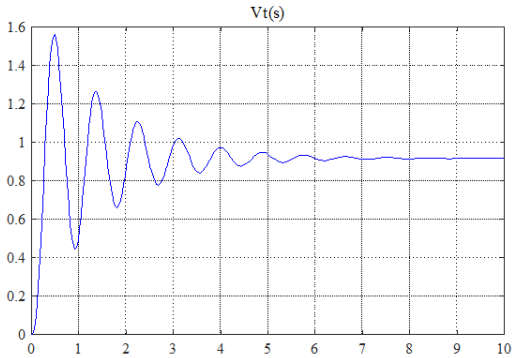


Figure 6(b) Output Waveform of Simple AVR

From Figure (b), the result shows that for an amplifier gain $K_a = 11$, the response is highly oscillatory, with a large overshoot and a long settling time. Since the steady-state error is 8.33%, there is high steady-state error and unsatisfactory transient response.

4.2 Simulink Model and Result of AVR with Stabilizer

Figure 7 shows an AVR with stabilizer in MATLAB simulink, where a combined simulation block model was constructed for AVR and stabilizer cases in order to obtain their respective step response.

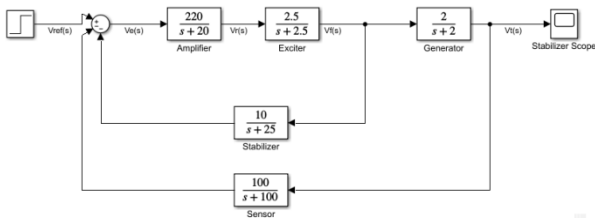


Figure 7(a) Simulink Model of an AVR with Stabilizer

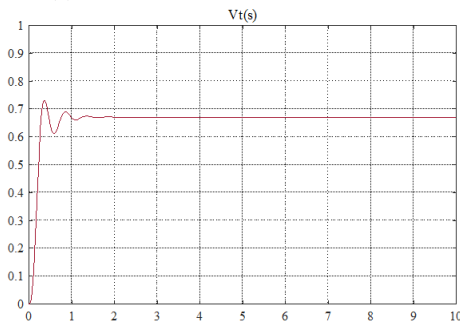


Figure 7(b) Output Waveform of AVR with Stabilizer

From Figure 7(b), the result shows that a very satisfactory transient response with steady state error of 5.4% and a settling time of approximately 2.5 seconds.

4.3 Simulink Model and Result of AVR with PID Controller

Figure 8 shows an AVR system model with PID controller without stabilizer in MATLAB simulink, where a combined simulation block model was constructed for AVR and PID controller cases in order to obtain their respective step response.

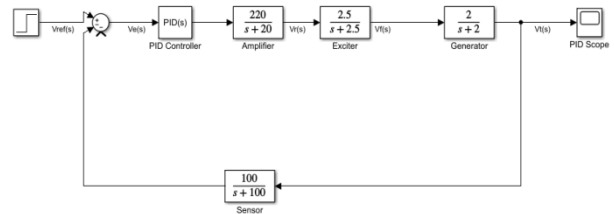


Figure 8(a) Simulink Model of an AVR with PID Controller

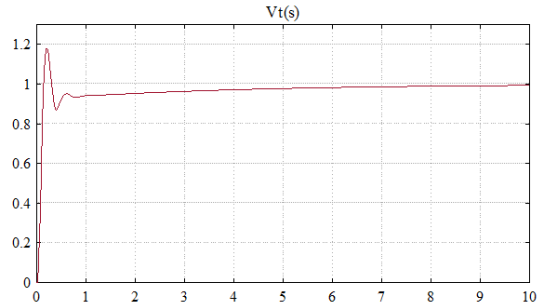


Figure 8 (b) Output Waveform of AVR with PID Controller

From Figure 8(b), the result shows that a very satisfactory transient response with an overshoot and a settling time of approximately 1.7 seconds.

4.4 Simulink Model and Result of AVR-PSS with PID Controller

Figure 9 shows an AVR system model with PID controller and stabilizer in MATLAB simulink, where a combined simulation block model was constructed for AVR, stabilizer and PID controller cases in order to obtain their respective step response.

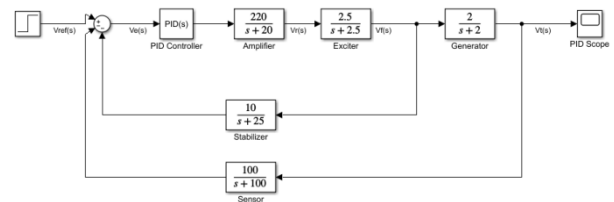


Figure 9(a) Simulink Model of AVR-PSS with PID controller

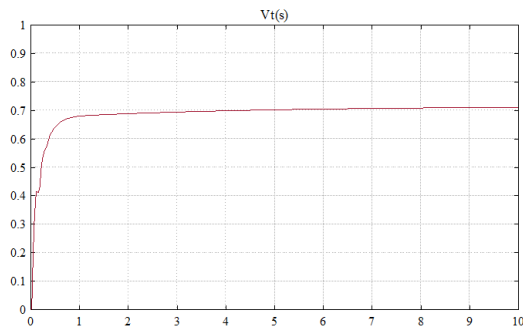


Figure 9(b) Output Waveform of AVR-PSS with PID controller

From Figure 9(b), a proportional gain $K_P = 1.0$, an integral gain of $K_I = 0.25$ and a derivative gain of $K_D = 0.28$ is tuned and it is found to be satisfactory. The response settles in about 2 seconds with no overshoot. The PID controller reduces the steady-state error to zero.

4.4 Simulink Model and Result of Overall AVR System

Figure 10 shows an overall AVR system model with AVR, stabilizer, and PID controller in MATLAB simulink.

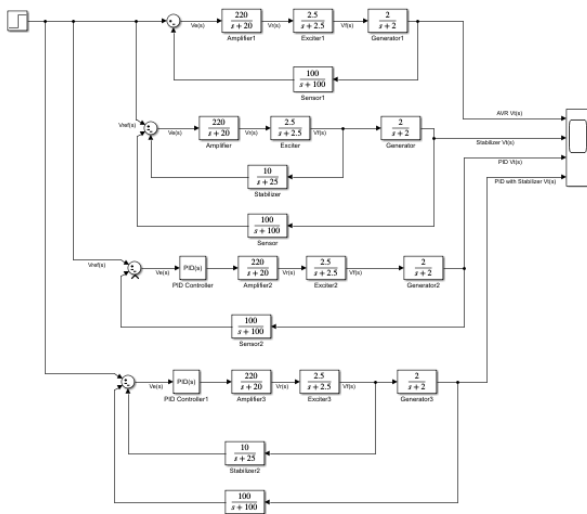


Figure 10(a) Simulink Model of an Overall AVR System

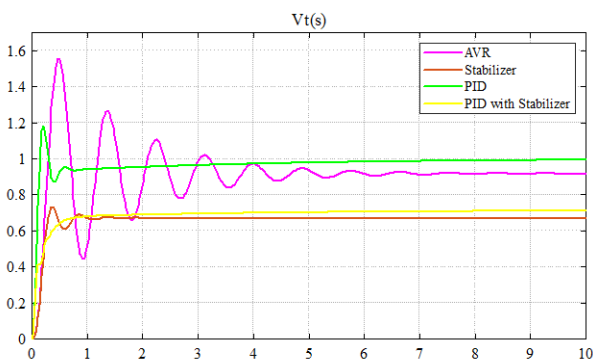


Figure 10(b) Output Waveform for Overall AVR System

The AVR was simulated with stabilizer and PID controller. It was observed that the AVR shows 1 pu output

voltage with PID controller. It also shows that low frequency and less oscillation. The reliability of generating system is determined by its ability for maintaining voltage and frequency within permissible limit. It can be concluded that the generating system for AVR with PID controller shows satisfactory performance.

5. CONCLUSION

In this paper, application of PID controller and stabilizer in exciter control system with variation in its time constant and gain was examined. By using PID controller and stabilizer, not only the system will have an appropriate steady-state error but also provides good dynamic response with a less overshoot for the voltage terminal. Finally, the AVR system was simulated and effects of some parameters were investigated.

The hydraulic transient analysis of the hydropower plant at different values of AVR with PID controller has been carried out. From the obtained results at different values of gain parameters, it is observed that the effect on hydraulic transient is more significant when the AVR with PID controller as compared to simple AVR. Therefore, automatic voltage regulator with PID controller is recommended for stable operation of the hydropower plant.

The aim is to demonstrate the potential advantages of these relatively new techniques for adaptive approach to controller design and simulation, while highlighting some of the limitations and areas of potential difficulty for practical application.

6. ACKNOWLEDGMENTS

First of all, the author would like to express her special thanks to Dr. Myo Thein Gyi, Union Minister of Education, the Republic of the Union of Myanmar, for his encouragement to do research works for regional development and applied science. The author's grateful thanks go to Dr. Thein Gi, Rector of Technological University (Thanlyin) for her kind guidance, suggestion and directions throughout the preparation of research work and valued motivations and encouragement as well. Finally, the author also sincerely thanks to our colleagues from the Department of Electrical Engineering, Technological University (Thanlyin) offered strong moral and physical support.

7. REFERENCES

- [1] Hadi Saadat, 1999. Power System Analysis. McGraw-Hill Inc.
- [2] Gilbert M. Masters, 2004. Renewable and Efficient Electric Power Systems. John Wiley & Sons, Inc.
- [3] Leon Freris & David Infield, 2008. Renewable Energy in Power Systems. John Wiley & Sons, Inc.
- [4] Panagiotis Margonis, 2017. Modeling and Optimization of a Hydroelectric Power Plant for a National Grid Power System Supply. Master Thesis.

- [5] Sonam Dorji, 2016. Modelling and Simulation of Hydro Power Plant. Master Thesis.
- [6] Khin Thi Aye, 2017. The Role of Hydropower in Myanmar. Planning and Statistic Branch, Ministry of Electricity and Energy
- [7] Bill Drury, 2009. The Control Techniques Drives and Controls Handbook. The Institution of Engineering and Technology.
- [8] K. Astrom & T. Hagglund. 1995. PID Controllers: Theory, Design, and Tuning. Instrument Society of America.
- [9] Katsuhiko Ogata. 2002. Modern Control Engineering. Pearson Education International.

Improvement of Fairness in E-cash Protocol

Dr. Khin Khat Khat Kyaw
Associate Professor
Information Technology Department
West Yangon Technological University, Yangon
Myanmar

Abstract: Nowadays ecommerce applications are widely used in the world since it is easier than conventional payment system. The various e-cash protocols have been proposed into the literature in order to get better efficiency. This paper analyses the e-cash protocol that was designed to provide non-repudiation and anonymity. The protocol was checked with AVISPA tool and the results show that it meets weak fairness. Therefore, a modified e-cash protocol is proposed in this paper. The proposed protocol also maintains anonymity and non-repudiation. So, this paper presents analysis of the original e-cash protocol and modified protocol by using AVISPA tool.

Keywords: AVISPA, anonymity, electronic cash, electronic commerce, fairness, non-repudiation

1. INTRODUCTION

Although current e-cash systems can make transactions in a few seconds, they do not fully guarantee the client's privacy. The current systems cannot execute the transactions in a completely anonymous way. For example, the bank or payment provider knows the details of the client's transaction.

Physical cash provides better privacy: the payments are difficult to trace as there is no central authority that monitors all transactions, in contrast to most electronic payment systems. This property is the inspiration for 'untraceable e-cash' systems[1].

To be secure, an e-cash protocol should not only ensure the client's privacy, but must also ensure that a client cannot forge coins which were not issued by the bank. Moreover, it must protect against double spending. Otherwise a client could try to use the same coin multiple times. This can be achieved by using on-line payments, i.e., a seller has to contact the bank at payment before accepting the coin, however it is an expensive solution. An alternative solution, which is usually used to support online payments (i.e., a seller can accept the payment without contacting the bank), is revealing the client's identity if he spent a coin twice. Finally, exculpability ensures that an attacker cannot forge a double spend, and hence incorrectly blame an honest client for double spending.

In so-called payment by instruction type of systems, a payer basically orders the bank to move a sum of money from her account into a payee's account[2]. The central security aspect in these systems is to ensure that only legitimate account holders are able to issue payment instructions. Of course, digital signatures are the solution for doing this over a large, open network such as the Internet. Since digital signatures only make sense if there is an infrastructure for certifying public keys, a lot of effort is devoted to just this.

Prepaid systems are conceptually close to electronic equivalents of cash. The central security aspect in this type of system is to ensure that cards or representations of cash cannot be forged. When forgery happens, the float will ultimately be insufficient to credit all of the payees' accounts

for received payments. Of course, it should also be ensured that only legitimate account holders can reload cash from their accounts. However, this security aspect is now limited to the infrequent withdrawal protocol, and is no part anymore of the more frequent payment protocol.

A basic requirement of a payment protocol is that it allows a payee to receive payments from any payer. A payment can be seen as some sort of authentication of the payer towards the payee. Authentication can be based on secret key cryptography or on public key cryptography.

2. Related Work

The E-cash scheme was the closest to a system that mimicked _at currency with the property that it provided anonymity for users when buying coins from the Bank and spending them when a merchant premises [6].

The authors propose an extension to the E-cash scheme which allows for the anonymous transfer of coins between users without the involvement of a trusted third party. We make use of a powerful technique which allows for distributed decision making within the network - namely the Bitcoin blockchain protocol. Combined with the proof-of-work technique and the classical discrete logarithm problem the proposed protocol is able to continuously reuse coins, and also prevent double-spending of coins without revealing the identities of the users.

The major contribution in [7] is the practical E-cash payment system that provides secrecy and comfortability. The protocol gets security based on X9.59 in which they use Payment Routing Code (PRC) instead of consumer and merchant account/card numbers. It provides security, authentication and integrity.

Non-repudiation is one of the most important security services in electronic commerce. Non-repudiation means that an entity cannot deny its participation in a message exchange. Therefore, non-repudiation protocols provide for undeniable data exchange between two or more principals. Judson Santiago and Laurent Vigneron [8] proposed how to define

non-repudiation properties with the AVISPA tool and explained how they can be automatically verified.

3. RONGGONG SONG AND LARRY KORBA'S PROTOCOL

The following section discusses the e-cash protocol provided in [3].

A. Terminology and Notations

Terminology and notations used in the paper are defined as follows.

- A : a customer
- B : a bank
- ES : an e-commerce store
- IDA : customer A 's identity
- $H()$: one-way hash function
- Z_n : the integers modulo n
- Z_n^* : the multiplicative group of Z_n
- $M \bmod n$: residue of M divided by n
- $Time_A$: time stamp made by customer A
- $Sign_A$: customer A 's signature
- $gcd(m, n)$: greatest common divisor of m and n
- $A \rightarrow B: M$: customer A sends message M to the bank B
- RM : remainder money after A purchases the e-goods
- EMD : e-goods message digest

B. E-cash Issue Protocol

When a customer wants to buy e-goods by using online shopping, he/she first needs to buy some e-cashes. It is issued by the bank using the following protocol where all communications are supported by the SSL security channel.

1. $A \rightarrow B: ID_A, Account_A, PK_A, \alpha, v, Time_A, Sign_A$
2. $B \rightarrow A: ID_A, ID_B, \beta, Time_B, Sign_B$

Step 1: If a customer decides to purchase an e-cash from the bank, he/she first makes a temporary public key (e, n) , and keeps its private key (d, p, q) secret (using RSA public key cryptosystem). Then, the customer selects a random integer r in Z_{nb}^* , and computes $\alpha \equiv (r^{ebv} H(e || n) \bmod nb)$ where $||$ denotes the concatenation symbol, and v contains the following basic information predefined by the bank, i.e. expiration date and money. Then, the customer computes the signature $Sign_A$ as follows.

$$Sign_A \equiv (H(ID_A, Account_A, PK_A, \alpha, v, Time_A))_{dA} \bmod n_A$$

Finally, the customer sends the bank the messages $(ID_A, Account_A, PK_A, \alpha, v, Time_A, Sign_A)$ by using SSL security channel.

Step 2: After achieving the above messages through the SSL security channel, the bank checks whether or not the messages: $Account_A, Time_A, Sign_A$, and v are correct. If they are correct, the bank computes $\beta \equiv (\alpha^{(ebv)-1} \bmod nb)$ and the signature:

$$Sign_B \equiv (H(ID_A, ID_B, \beta, Time_B))_{dB} \bmod n_B$$

Then, it sends the messages $(ID_A, ID_B, \beta, Time_B, Sign_B)$ to the customer through the SSL security channel. In the meantime the bank deducts the money from the customer's account. Finally, after achieving the messages sent by the bank through the SSL security channel, the customer checks whether or not the messages: $Time_B$ and $Sign_B$ are correct. If

they are correct, he/she then computes $s \equiv (r^{-1} \beta \bmod nb)$ as the signature of the bank and gets his/her e-cash (e, nt, v, s) .

C. Online Shopping Protocol

When the customer wants to buy some e-goods like e-book, software, and movie, etc. from the Internet, since it is not necessary for the shipping service, he/she could use the following protocol. When the customer wants to download the licenses of the e-goods and hide his/her identity, he/she could use that online shopping protocol.

1. $A \rightarrow ES: E\text{-goods}, Cost, Account_{ES}, e_t, n_t, v, s, Time_A, Sign_t$
2. $ES \rightarrow B: Cost, Account_{ES}, e_t, n_t, v, s, Time_A, EMD, Sign_t$
3. $B \rightarrow ES: Receipt_{ES}, e_t, n_t, v, s, RM, s', Time_B, Sign_B$
4. $ES \rightarrow A: License, Receipt_A, e_t, n_t, v, s, RM, s', Time_{ES}, Sign_{ES}$

D. Security Analysis

In this system, the bank and merchant do not know anything about the customer except how much money the customer spends for e-cashes. This provides anonymity property for the customers. The owners of the messages signed all transferred messages with their own signatures in the protocol, they can ask a Court to judge it if there is a dispute later. Therefore, the protocol provides the non-repudiation service for the customer, merchant and bank.

However, their protocol still provides weak fairness for the customer. After receiving the correct payment from the bank in step 3, the merchant can deny to send the product decryption key to the customer because the merchant did not send Non-repudiation of Receipt (NRR) to anyone. Therefore, that protocol has weak fairness for customer.

4. PROPOSED ONLINE SHOPPING PROTOCOL

The proposed e-cash system only modifies the online shopping protocol. The e-cash issue protocol remains the same. The modified e-cash system consists of three parties: merchant, customer and bank. The bank is considered as Trust Third Party (TTP).

1. $A \rightarrow ES: E\text{-goods}, Cost, Account_{ES}, e_t, n_t, v, s, Time_A, Sign_t$
2. $ES \rightarrow B: E\text{-goods}, Cost, License, Account_{ES}, e_t, n_t, v, s, Time_A, Sign_t, Sign_{ES}$
3. $B \rightarrow A: License, Receipt_A, e_t, n_t, v, s, RM, s', Time_B, Sign_B$
4. $B \rightarrow ES: Receipt_{ES}, Account_{ES}, Time_B, Sign_B$

Step 1: The protocol starts with the customer (A). The customer downloads an encrypted product from the merchant (ES). Then, A sends ES a purchase order, and computes the following signature $Sign_t$ with the private key corresponding to the temporary public key of the e-cash.

$$Sign_t \equiv (H(Cost, Account_{ES}, e_t, n_t, v, s, Time_A) || H(E\text{-goods}))_{dt} \bmod n_t$$

Then A sends the messages $(E\text{-goods}, Cost, Account_{ES}, e_t, n_t, v, s, Time_A, Sign_t)$ to the ES by using the SSL security channel.

Step 2: After receiving the above messages, the merchant checks whether or not the messages: $Cost, Account_{ES}, Time_A, Sign_t$, and $se_{v_t} \equiv (H(e_t || n_t) \bmod n_t)$ are correct. If they are correct, the merchant forwards the bank the message $(E\text{-goods}, Cost, License, Account_{ES}, e_t, n_t, v, s, Time_A, Sign_t, Sign_{ES})$.

goods, Cost, License, AccountES, e_t , n_t , v , s , $Time_A$, $Sign_t$, $SignES$).

Step3: The bank verifies whether or not the messages: $AccountES$, $Time_A$, and $Sign_t$ are correct. If they are correct, it deducts the money from the e-cash. Then, the bank computes the remainder money RM and the signature:

$$s' \equiv (H(e_t, n_t, v, s, RM))^{db} \bmod n_b$$

$$Sign_B \equiv (H(License, Receipt_A, e_t, n_t, v, s, RM, s', Time_B))^{db} \bmod n_b$$

The bank makes a receipt for the customer and sends the customer the messages ($License$, $Receipt_A$, e_t , n_t , v , s , RM , s' , $Time_B$, $Sign_B$). After achieving the messages, the customer obtains the licenses of the e-goods and his/her remainder ecash.

Step4: Finally, the bank then deposits the money into the merchant's account and the bank makes a statement (receipt) for the merchant and sends the messages ($ReceiptES$, $AccountES$, $Time_B$, $Sign_B$) to the merchant.

$$Sign_B \equiv (H(ReceiptES, AccountES, Time_B, Sign_B))^{db} \bmod n_b$$

The modified version change the step 2,3 and 4. The key idea is that the License for E-goods must be first forwarded to the bank(Trusted Third Party). Therefore, the customer can get the License from the bank even if the merchant deny sending. By this way, the proposed protocol meets the strong fairness for every party.

5. SECURITY ANALYSIS

The formal analysis for the original and modified protocol was done in AVISPA Tool. Automated validation of internet security protocols and applications (AVISPA) [4] is a push button tool for the automated validation of security protocols. A modular and expressive formal language called HLPSSL (High level protocols specification language) [5] is used by AVISPA to specify the security protocol and their properties. HLPSSL language is a role-based language, which means that actions of each participant are defined in a separate module, called a basic role. The security of original protocol is verified by using AVISPA. For this, three basic roles are played as Customer (C), Merchant (M) and Bank (B). Basic roles describe what information the corresponding participant has initially (parameters), its initial state and how the state can change (transitions). The users use channels SND (send) and RCV (receive) for communication. Dolev-Yao (dy) is the intruder model that is assumed for the communication channel.

Security goals of the protocol are presented in HLPSSL language in section called goals. Security goals are actually defined in transition section of basic roles. The definitions of security goals in transition section are called goal facts. The goals section simply describes which combinations of these goal facts indicate an attack. The following goals are considered: (1) the parties (C and M) shall authenticate each other (2) payment information including customer's bank details shall remain secret from any other parties. Therefore, a goal section of the protocol definition can be as follows:

```
goal
    authentication_ on deal
    weak_authentication_ on deal
    secrecy_of order
    secrecy_of payment
end goal
```

Running the AVISPA tool on the original protocol returns the following output.

```
Terminal
File Edit View Search Terminal Help
Linux-55ff:/opt # export AVISPA_PACKAGE=/opt/avispa-1.1
Linux-55ff:/opt # export PATH=$PATH:$AVISPA_PACKAGE
Linux-55ff:/opt # avispa ayedishonestTest.hlpssl --ofmc
% OFMC
% Version of 2006/02/13
SUMMARY
UNSAFE
DETAILS
ATTACK_FOUND
PROTOCOL
/opt/avispa-1.1/testsuite/results/ayedishonestTest.if
GOAL
authentication_on_deal
BACKEND
OFMC
COMMENTS
STATISTICS
parseTime: 0.00s
searchTime: 0.02s
visitedNodes: 0 nodes
depth: 0 plies
```

Figure 1. Security Analysis of the Original Protocol

As shown in Figure 1, the AVISPA tool output provides that

```
SUMMARY
UNSAFE
DETAIL
ATTACK_FOUND
```

This means that the protocol has been found to be unsafe and that an attack has been found. AVISPA tool found *authentication_on_deal* attack. This means that both nonrepudiation of origin and non-repudiation of recipient breaks down. Therefore, fairness breaks down.

The proposed e-cash protocol designed to provide the anonymity service for customers and non-repudiation services for all players in the protocol. In the e-cash issue protocol, the customer sends the bank the message that is signed with the customer's certificate. When the customer repudiates this action, the bank can show the customer's signature. On the other hand, if the customer does not do this, the bank also cannot charge the customer because it cannot give evidence (i.e., signature) to prove it.

The proposed system gives the facility to the user, as the customer can make anonymous payment with the merchant as the merchant cannot know the identification of a customer; the merchant can only receive a coin from the user and verify the validity of the signature but cannot determine the customer's identity. Therefore, the customers get strong privacy protection for the e-cash.

The bank needs only to keep the still-alive e-cashes in its database to prevent double-spending because its database can remove all expired e-cash. Moreover, the modified protocol gives strong fairness property for customer because the bank is considered as TTP.

If the merchant did not send the product decryption key(License) to the customer, the bank would directly send the customer the product decryption key. The proposed protocol analyses in AVISPA tool whether it meets fairness, non-repudiation and anonymity.

As shown in Figure 2, the AVISPA tool output shows that

```
SUMMARY
SAFE
DETAILS
BOUNDED_NUMBER_OF_SESSIONS
```



```
Terminal
File Edit View Search Terminal Help
Linux-55ff:/opt # export AVISPA_PACKAGE=/opt/avispa-1.1
Linux-55ff:/opt # export PATH=$PATH:$AVISPA_PACKAGE
Linux-55ff:/opt # avispa ayeonest.hlpsl --ofmc
% OFMC
% Version of 2006/02/13
SUMMARY
SAFE
DETAILS
BOUNDED_NUMBER_OF_SESSIONS
PROTOCOL
/opt/avispa-1.1/testsuite/results/ayeonest.if
GOAL
as_specified
BACKEND
OFMC
COMMENTS
STATISTICS
parseTime: 0.00s
searchTime: 0.01s
visitedNodes: 2 nodes
depth: 1 plies
```

Figure 2. Security Analysis of Proposed Protocol

This means that the protocol has been found to be safe and an attack has not been found. Therefore, the proposed protocol provides anonymity for customer and non-repudiation for customer, merchant and bank. Moreover, the modified protocol provides strong fairness for all playing parties.

6. CONCLUSION

This paper provides the formal analysis of the original protocol. According to the result, the original protocol does not meet fairness for the customer. Therefore, the modified protocol was proposed in order to guarantee fairness for all parties. In addition, the modified protocol maintains anonymity and non-repudiation.

REFERENCES

[1] Jannik Dreier, Ali Kassem, Pascal Lafourcade. Formal Analysis of E-Cash Protocols. 12th International

Conference on Security and Cryptography (SECRYPT 2015), Jul 2015.

- [2] Berry Schoenmakers, Basic Security of the ecash Payment System, State of the Art in Applied Cryptography, Course on Computer Security and Industrial Cryptography, Leuven, Belgium, June 3–6, 1997, vol. 1528 of Lecture Notes in Computer Science, pp. 338–352. Springer-Verlag.
- [3] Ronggong Song and Larry Korba, “How to Make E-cash with Non- Repudiation and Anonymity” , Proceedings of the International Conference on Information Technology: Coding and Computing, 2004
- [4] Avispa - a tool for automated validation of internet security protocols, <http://www.avispa-project.org>.
- [5] Specification of the problems in the high-level specification language, <http://www.avispa-project.org>.
- [6] Hitesh Tewari and Arthur Hughes, Fully Anonymous Transferable Ecash, <http://www.scss.tcd.ie>
- [7] A. Levi, Ç.K. Koç, CONSEPP: CONVenient and Secure Electronic Payment Protocol Based on X9.59, Proceedings of The 17th Annual Computer Security Applications Conference, pages 286-295, New Orleans, Louisiana, IEEE Computer Society Press, Los Alamitos, California, December 10-14, 2001.
- [8] Judson Santiago and Laurent Vigneron, Study for Automatically Analysing Non-repudiation.

Study and Analysis of Double-Line-To-Ground Fault

Ei Ei Phyu
Department of Electrical Power
Engineering,
Technological University,
(Thanlyin), Myanmar

Abstract: During normal operating conditions, current will flow through all elements of the electrical power system within pre-designed values which are appropriate to these elements' ratings. Any power system can be analyzed by calculating the system voltages and currents under normal and abnormal conditions. Faults could happen as a result of natural events or accidents where the phase will establish a connection with another phase, the ground or both in some cases. Faults can also be defined as the flow of a massive current through an improper path which could cause enormous equipment damage which will lead to interruption of power, personal injury, or death. In addition, the voltage level will alternate which can affect the equipment insulation in case of an increase or could cause a failure of equipment start-up if the voltage is below a minimum level. As a result, the electrical potential difference of the system neutral will increase. Hence, people and equipment will be exposed to the danger of electricity which is not accepted. In order to prevent such an event, power system fault analysis was introduced. In double-line-to-ground fault, two phases to ground will be involved and 10% of all transmission lines faults are under this type of faults. In this paper, double-line-to-ground fault on Thanatpin transmission line is analyzed with Matlab simulation.

Keywords: electric power transmission system; types of faults; double-line-to-ground fault; sequence networks; Matlab simulation.

1. INTRODUCTION

Electric power is generated, transmitted and distributed via large interconnected power systems. This could encounter various types of malfunctions is usually referred to as a Fault.

To prevent such an undesirable situation, the temporary isolation of the fault from the whole system it is necessary as soon as possible. This is accomplished by the protective relaying system. The process of evaluating the system voltages and currents under various types of short-circuits is called fault analysis which can determine the necessary safety measures & the required protection system to guarantee the safety of public.

Faults can be defined as the flow of a massive current through an improper path which could cause enormous equipment damage which will lead to interruption of power, personal injury, or death. In addition, the voltage level will alternate which can affect the equipment insulation in case of an increase or could cause a failure of equipment start-up if the voltage is below a minimum level. As a result, the electrical potential difference of the system neutral will increase. Hence, People and equipment will be exposed to the danger of electricity which is not accepted.

When different types of fault occurs in power system then in the process of transmission line fault analysis, determination of bus voltages and the rms line currents are possible. While consulting with the power system the terms bus voltage and rms current of line are very important. In case of three phase power system mainly two faults occurs, three phase balance fault and unbalance fault on transmission line of power system, such as single line to ground fault, double line to ground fault and line to line fault. The transmission line fault analysis helps to select and develop a better for protection purpose. By using MATLAB simulation in computer, the analysis of transmission line fault can be easily carried out.

In three-phase transmission line of power system; mainly two types of fault occurs, balance fault which is also called

symmetrical fault and unbalance fault called as unsymmetrical fault. In this paper, only deals with the unsymmetrical fault which mainly occurs between two conductors and ground.

To study and analyze the unsymmetrical fault in MATLAB, there is a need of develop a network of positive, negative and zero sequence. In this paper, positive, negative and zero sequence voltage and current of buses at fault situation are analyzed.

2. TYPES OF FAULTS

There are two types of faults which can occur on any transmission lines; balanced faults and unbalanced faults also known as symmetrical and asymmetrical faults respectively. Most of the faults that occur on power systems are not the balanced three-phase faults, but the unbalanced faults. Faults can be classified into four categories. Line-to-ground fault, Line-to-line fault, Double line-to-ground, Three-phase fault. The first three of these faults are known as asymmetrical faults and three-phase fault is known as symmetrical fault.

2.1 Line-to- Ground Fault (LG)

This type of fault exists when one phase of any transmission lines establishes a connection with the ground either by ice, wind, falling tree or any other incident. 70% of all transmission lines faults. This type of fault occurs when one conductor falls to ground or contacts the neutral wire. It

could also be the result of falling trees in a winter storm. This type could be represented as in Figure 1.

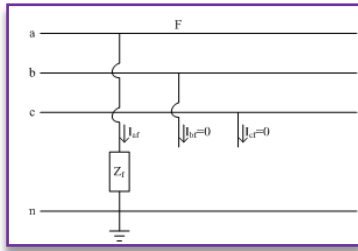


Figure 1. Single Line to Ground Fault

2.2 Line-to-Line Fault (LL)

This type of fault as a result of high winds, one phase could touch another phase and line-to-line fault takes place. 15% of all transmission lines faults are considered line-to-line faults. As in the case of a large bird standing on one transmission line and touching the other, or if a tree branch fall on top of the two of the power lines. This type could be represented as in Figure 2.

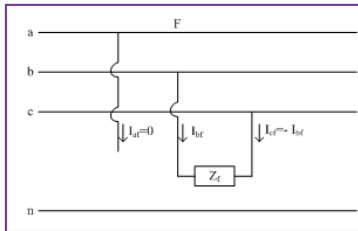


Figure 2. Line to Line Fault

2.3 Double-Line-to-Ground Fault (DLG)

This type of fault is caused by falling tree where two phases become in contact with the ground could lead to this type of fault. In addition, two phases will be involved instead of one at the line-to-ground faults conditions. 10% of all transmission lines faults are under this type of faults. The Double Line-to-Ground fault (DLG) is shown in Figure 3. This can be a result of a tree falling on two of the power lines, or other causes.

In double line-to-ground fault, the two lines contact with each other along with the ground. The probability of such types of faults is nearly 10 %. The symmetrical and unsymmetrical fault mainly occurs in the terminal of the generator, and the open circuit and short circuit fault occur on the distribution system.

In this paper, the calculation of double line to ground fault on 66/33 kV transmission line is emphasized.

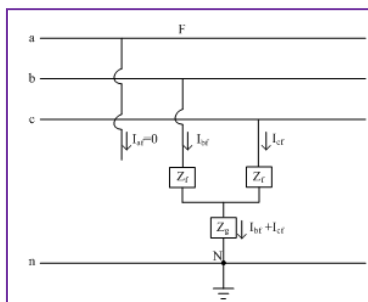


Figure 3. Double-Line-to-Ground Fault

2.4 Three-Phase Fault

In this case, falling tower, failure of equipment or even a line breaking and touching the remaining phases can cause three phase faults. In reality, this type of fault not often exists which can be seen from its share of 5% of all transmission lines faults. The balanced three phase, Figure 4, which can occur by a contact between the three power lines in many different forms.

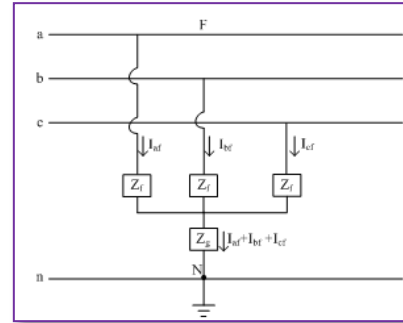


Figure 4. Three Phase Fault

3. DOUBLE-LINE-TO-GROUND FAULT CALCULATIONS

In double-line-to-ground fault, two phases established the connection with the ground.

To calculate the unsymmetrical faults, firstly, the positive sequence component of phase-a has been calculated. Thus, sequence reactances of thevenin equivalent circuits (Z_1 , Z_2 , Z_0) have been calculated. The fault currents of sequences have been determined by using these reactances and phase voltage E_a . The current and voltage values of other phases could be calculated via these components.

$$I_{a1} = \frac{E_a}{Z_1 + \frac{Z_0 Z_2}{Z_0 + Z_2}}$$

$$I_{a2} = -\frac{Z_0}{Z_0 + Z_2} I_{a1}$$

$$I_{a0} = -\frac{Z_2}{Z_0 + Z_2} I_{a1}$$

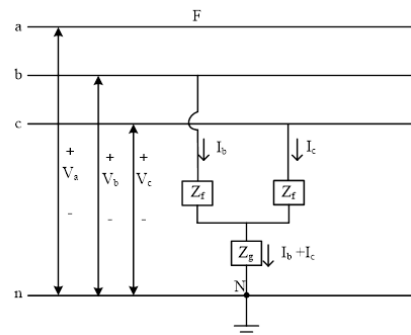


Figure 5 Double Line to Ground Fault Configuration

$$\begin{bmatrix} V_{a0} \\ V_{a1} \\ V_{a2} \end{bmatrix} = \begin{bmatrix} 0 \\ E_a \\ 0 \end{bmatrix} - \begin{bmatrix} Z_0 & 0 & 0 \\ 0 & Z_1 & 0 \\ 0 & 0 & Z_2 \end{bmatrix} \begin{bmatrix} I_{a0} \\ I_{a1} \\ I_{a2} \end{bmatrix}$$

The positive sequence reactance must be calculated from for the time variations of signals.

$$X_1(t) = \left\{ \left(\frac{1}{X_d''} \frac{1}{X_d'} \right) e^{-t/\tau_d''} + \left(\frac{1}{X_d''} \frac{1}{X_d'} \right) e^{-t/\tau_d'} + \frac{1}{X_d} \right\}^{-1}$$

where, X_d'' , X_d' , X_d are direct-axis subtransient, transient and synchronous reactances; τ_d'' , τ_d' are direct-axis fault subtransient and transient time constants; E_a , E are complex and RMS value of phase-a voltage of synchronous machine terminal before the fault occurrence.

3.1 Sequence Network for Double-Line-to-Ground Fault

Faulted power systems do not have three phase symmetry, so it cannot be solved by per phase analysis. To find fault currents and fault voltages, it is first transformed into their symmetrical components. This can be done by replacing three phase fault current by the sum of a three phase zero sequence source, a three-phase positive sequence source and a three phase negative sequence source. Each circuit is solved by per phase analysis called a sequence network. In this section, all the sequence components of fault voltages and currents for double-line-to-ground fault are determined.

Assuming the phase b and c are connected to the ground through the fault impedance Z_f . For double line to ground fault, fault current on phase a is $I_a = 0$.

Fault voltages at phase b and c are:

$$V_b = V_c = Z_f (I_b + I_c)$$

Fault currents in phase b and c are:

$$\begin{bmatrix} I_{a0} \\ I_{a1} \\ I_{a2} \end{bmatrix} = \frac{1}{3} \begin{bmatrix} 1 & 1 & 1 \\ 1 & a & a^2 \\ 1 & a^2 & a \end{bmatrix} \begin{bmatrix} I_a \\ I_b \\ I_c \end{bmatrix}$$

$$I_{a0} = \frac{1}{3} (I_b + I_c)$$

$$V_b = V_c = Z_f 3I_{a0}$$

$$\begin{bmatrix} V_{a0} \\ V_{a1} \\ V_{a2} \end{bmatrix} = \frac{1}{3} \begin{bmatrix} 1 & 1 & 1 \\ 1 & a & a^2 \\ 1 & a^2 & a \end{bmatrix} \begin{bmatrix} V_a \\ V_b \\ V_c \end{bmatrix}$$

$$V_{a0} = V_{a1} = V_{a2}$$

$$I_{a0} + I_{a1} + I_{a2} = 0$$

Since, the zero, positive and negative sequence voltages are equal which imply that the sequence networks must be in parallel.

$$V_{a0} = \frac{1}{3} (V_a + V_b + V_c)$$

Since, $V_b = V_c$,

$$3V_{a0} = (V_a + 2V_b) = V_{a0} + V_{a1} + V_{a2} + 2(Z_f 3I_{a0})$$

Since, $V_{a1} = V_{a2}$,

$$3V_{a0} = V_{a0} + 2V_{a1} + 2(Z_f 3I_{a0})$$

$$2V_{a0} - 2(Z_f 3I_{a0}) = 2V_{a1}$$

$$V_{a1} = V_{a0} - (Z_f 3I_{a0})$$

Fault currents are:

$$I_{a1} = \frac{V_f}{Z_1 + \left[\frac{Z_2(Z_0 + 3Z_f)}{Z_0 + Z_2 + 3Z_f} \right]}$$

$$I_{a2} = -\frac{Z_0 + Z_f}{Z_0 + Z_2 + 3Z_f} I_{a1}$$

$$I_{a0} = -\frac{Z_2}{Z_0 + Z_2 + 3Z_f} I_{a1}$$

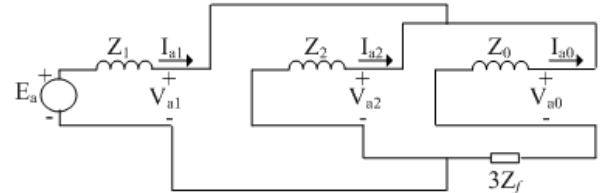


Figure 6. Equivalent Circuit of Double-Line-to-Ground Fault

3.2 Bayargyi Ayethuka Substation Transmission System

In order to do the analysis for a double-line-to-ground fault, 33kV Baryargyi Ayethuka to Thanatpin line is selected from 230 kV Kamanut sub-station.

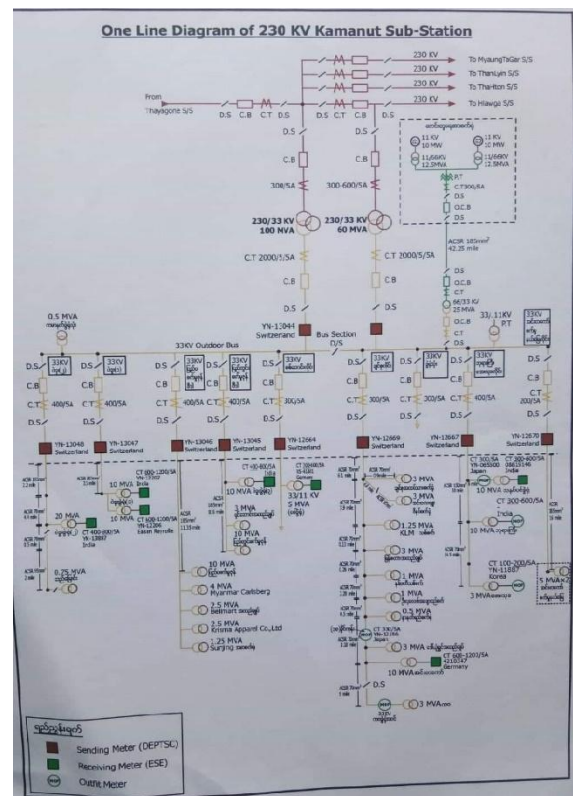


Figure 7 Single line diagram of 230 kV Kamanut substation

3.3 Sequence Impedance Parameters

For 33 kV, 10 MVA Bayargyi Ayethuka substation to Thanatpin line, sequence impedance parameters are shown in Table 1 and 2.

Table 1 Line Parameters

Description	Rating	Voltage Rating	Z1 (Ω)		Z2 (Ω)		Z0 (Ω)	
			R1	X1	R2	X2	R0	X0
Bayargyi Ayethuka substation	10 MVA	33 kV	0	j0.1289	0	j0.1289	0	j0.0309
Thanatpin Line	11 km	33 kV	1.0307	4.3428	1.0307	4.3428	4.1250	8.7362

Table 2 Per Unit Sequence Network Impedance Parameter

Description	Z1	Z2	Z0
Bayargyi Ayethuka substation	j0.032	j0.032	j0.0201
Thanatpin Line	0.2555+j1.0767	0.2555+j1.0767	0.093+j0.1969

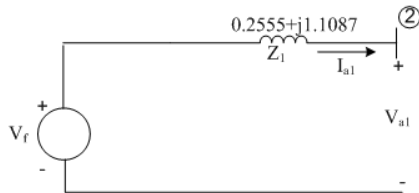


Figure 8 Positive Sequence Impedance Network

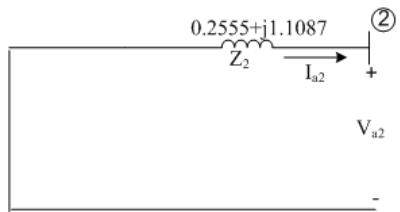


Figure 9 Negative Sequence Impedance Network

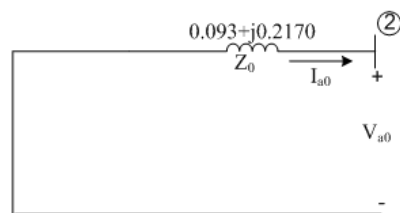


Figure 10 Zero Sequence Impedance Network

3.4 Line Currents and Line Voltages due to Double-Line-to-Ground Fault

For the study of fault analysis, assume that the load is disconnected, and fault impedance is zero (bolted fault). Assume that Bayargyi Ayethuka substation to Thanatpin Line as bus ②, and Thevenin equivalents of the sequence network due to double-line-to-ground fault is shown in Figure 11.

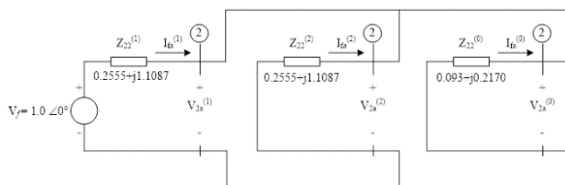


Figure 11 Thevenin Equivalents of the Sequence Networks for Double Line to Ground Fault at Bus ②

Positive, Negative and Zero sequence fault current at bus ②,

$$I_{fa}^{(1)} = \frac{1}{(0.2555 + j1.1087) + \frac{(0.2555 + j1.1087) \times (0.093 + j0.2170)}{(0.2555 + j1.1087) + (0.093 + j0.2170)}} = 0.0299 - j0.6452$$

$$I_{fa}^{(2)} = -(0.0299 - j0.6452) \times \frac{(0.093 + j0.2170)}{(0.2555 + j1.1087) + (0.093 + j0.2170)} = 0.0133 + j0.1107$$

$$I_{fa}^{(0)} = -(0.0299 - j0.6452) \times \frac{(0.2555 + j1.1087)}{(0.2555 + j1.1087) + (0.093 + j0.2170)} = -0.0412 + j0.5345$$

Fault current at bus ②,

$$\begin{bmatrix} I_{fa} \\ I_{fb} \\ I_{fc} \end{bmatrix} = \begin{bmatrix} 1 & 1 & 1 \\ 1 & a^2 & a \\ 1 & a & a^2 \end{bmatrix} \begin{bmatrix} -0.0412 + j0.5345 \\ 0.0299 + j0.6452 \\ 0.0133 + j0.1107 \end{bmatrix}$$

$$= \begin{bmatrix} 0 \\ 1.1818 \angle 153.45^\circ \\ 1.1818 \angle 33.45^\circ \end{bmatrix} \text{ pu}$$

The actual values of current due to double-line-to-ground fault at bus ②,

$$\therefore \begin{aligned} I_{fa} &= 0 \\ I_{fb} &= 1.8609 \text{ kA} \\ I_{fc} &= 1.8609 \text{ kA} \end{aligned}$$

Positive, Negative and Zero sequence fault voltages at bus ②,

$$V_{2a}^{(1)} = V_{2a}^{(2)} = V_{2a}^{(0)} = 1 - [(0.0299 + j0.6452) \times (0.2555 + j1.1087)] = 0.2770 + j0.1317$$

Line-to-neutral fault voltage at bus ②,

$$\begin{bmatrix} V_{2a} \\ V_{2b} \\ V_{2c} \end{bmatrix} = \begin{bmatrix} 1 & 1 & 1 \\ 1 & a^2 & a \\ 1 & a & a^2 \end{bmatrix} \begin{bmatrix} 0.2770 + j0.1317 \\ 0.2770 + j0.1317 \\ 0.2770 + j0.1317 \end{bmatrix}$$

$$= \begin{bmatrix} 0.920 \angle 25.43^\circ \\ 0 \\ 0 \end{bmatrix} \text{ pu}$$

The actual values of phase to ground voltages due to double-line-to-ground fault at bus ②,

$$\therefore \begin{aligned} V_{2a} &= 5.8428 \text{ kV} \\ V_{2b} &= 0 \\ V_{2c} &= 0 \end{aligned}$$

4. RESULT AND DISCUSSION

4.1 Simulink Model for Double-Line-to-Ground Fault in Proposed Line

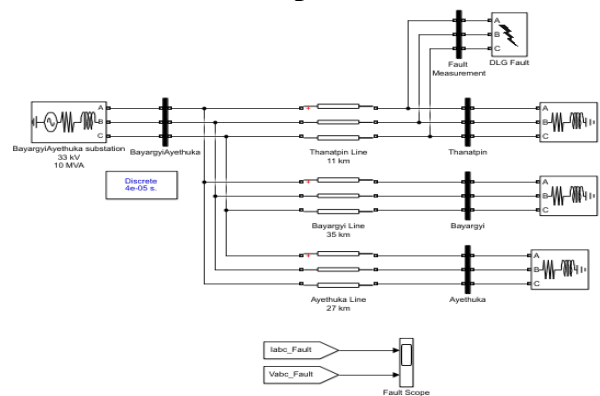


Figure 12 Simulink model of Double-Line-to-Ground Fault near Thanatpin Line

In order to study and analyze the transmission line fault, the simulation circuit arrangements are used which is shown in Figure 12, and bolted double-line-to-ground fault is created near Thanatpin bus.

4.2 Simulation Result and Discussion

Before performing transient tests, the model must be initialized at steady-state condition. For the desired fault, by using the utility of the fault breaker to obtain the double-line-to-ground fault currents and voltages near Thanatpin bus.

Figure 13 shows the current and voltage results of double line to ground fault at faulted bus.

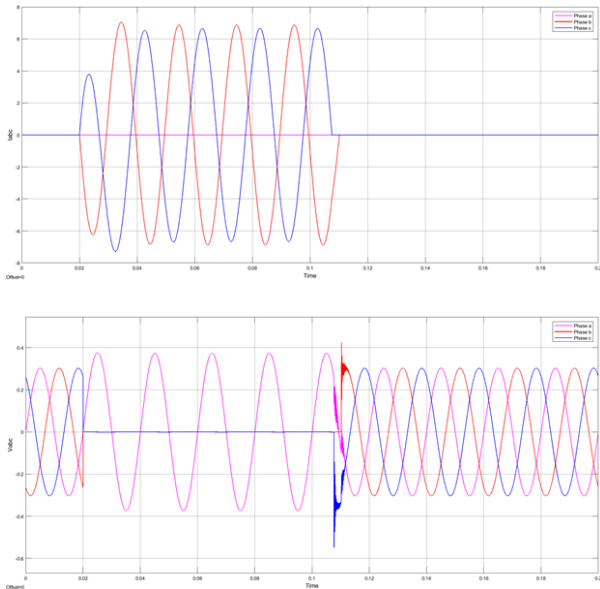


Figure 13 Currents and Voltages output waveforms

The period for creation of fault is of 0.02 to 0.11 second. In double line-to-ground fault simulation, phase b and c currents magnitude 2.35 pu and 2.22 pu respectively and phase a current magnitude is zero during fault period. Phase b and c voltages are zero and phase a voltage magnitude is 1.126 pu during fault. After 0.11 sec, the system is regained in steady-state. All the voltages and currents are in stable condition.

The results were compared with software solutions to validate the accuracy of the hand calculations.

In hand calculation results, the current magnitude values of phase b and c are more than that of simulation results because of the presence of capacitance and magnetization effect in MATLAB simulation. The voltage magnitude values of phase a are nearly the same in both hand calculations and simulation results.

5. CONCLUSION

Most of the faults that occur on power systems are unsymmetrical faults, which may consist of unsymmetrical short circuits, unsymmetrical faults through impedances, or open conductors. Unsymmetrical faults occur as single line to ground faults, line to line faults or double line to ground faults.

Since any unsymmetrical fault causes unbalanced currents to flow in the system, the method of symmetrical components is very useful in an analysis to determine the currents and voltages in all parts of the system after the occurrence of the fault. Faults on a power system are considered by applying Thevenin's theorem, which allows finding the current in the fault by replacing the entire system by a single generator and

series impedance, and the bus impedance matrix is applied to the analysis of unsymmetrical faults can be calculated.

Unbalanced voltages and currents can be resolved into their symmetrical components. Problems are solved by treating each set of components separately and superimposing the results. A knowledge of the positive, negative and zero sequence network is necessary for power flow studies, fault calculations, and stability studies. If the fault calculations or stability studies involve unsymmetrical faults on otherwise symmetrical systems, the negative and zero sequence networks are also needed. Synthesis of the zero-sequence network requires particular care because the zero-sequence network may differ from the others considerably.

This paper investigates the problem of double line to ground fault calculation in three phase power systems. And, the proposed model of three phase transmission line system is simulated with MATLAB software. The hand calculations and the software results are nearly the same corresponding to the same proposed network.

6. ACKNOWLEDGEMENTS

First of all, the author would like to express her special thanks to Dr. Myo Thein Gyi, Union Minister of Education, the Republic of the Union of Myanmar, for his encouragement to do research works for regional development and applied science. The author grateful thanks to Dr. thein Gri, Rector of Technological University (Thanlyin) for her kind guidance, suggestion and directions throughout the preparation of research work, and valued motivations and encouragement as well. Finally, the author also sincerely thankful to our colleagues from the Department of Electrical Power Engineering, Technological University (Thanlyin) offered strong moral and physical support.

7. REFERENCES

- [1] John J. Grainger & William D. Stevenson, Jr., 1994. Power System Analysis. McGraw-Hill Book Inc.
- [2] Hadi Saadat, 1999. Power System Analysis. McGraw-Hill Book Inc.
- [3] J.C.Das, 2002. Power System Analysis Short-Circuit Load Flow and Harmonics. Marcel Dekker Inc.
- [4] Jorge Santamaria, 2011. Analysis of Power Systems Under Fault Conditions. M.S Thesis.
- [5] William Patrick Davis, 2012. Analysis of Faults in Overhead Transmission Lines. M.S Thesis

Comparative Analysis of a SI Engine using Petrol and CNG Fuel with and without Supercharger Review Study

Akari San Win
Department of Mechanical Engineering,
West Yangon
Technological University
Yangon, Myanmar

Abstract: The uses of engine-driven machines are increased and the air is polluted day by day. Thereby, substitution of natural gas (made by the country) in Petroleum would save more money (foreign currency spending), reduce air pollution and much more good benefits could be achieved. However, natural gas- driven engine could produce lesser power output in comparison with petroleum – driven engine. This problem can be solved by setting up the supercharger at the engine inlet that helped the engine to produce higher output, but reduce the air pollution. The comparison of performance of the petrol engine using the fuel of petrol and CNG as alternative fuel with and without supercharger are presented in this paper.

Keywords: Natural gas, Petroleum, Supercharger, Pollution, Engine.

1. INTRODUCTION

The number of cars in the world increases, especially in urban areas. The increase in pollution by hydrocarbons HC, CO₂, CO, and NO_x day by day. Gasoline is the main factor causing environmental pollution. Gasoline is very volatile fuel that contains a combination of hydrogen and carbon and if evaporated due to thermal effects at a higher speed, and then produce the carbon dioxide (CO₂) to pollute the atmosphere. Pollution has a significant impact on the environment and human health. Lead from gasoline not burned, carbon monoxide, compound containing gas and other gases polluting air deadly and harmful to humans, animals, and food crops [1].

To reduce its emissions characteristics, CNG is more suited for an engine internal combustion fuel. Therefore, it is necessary optimize CNG engine with high compression rate resulting in more power, less fuel consumption and emissions. CNG (compressed natural gas) is a mixture of hydrocarbons consisting of approximately 80-90% of methane.

Compressed Natural Gas is a gaseous form of natural gas and is mixture of hydrocarbons. It acts as an alternative fuel due to its substantial benefits compared to gasoline and diesel. It exists in the gaseous state at normal temperature and pressure. CNG is composed primarily of methane. It emits about 70% less carbon monoxide and has much less ozone-forming potential than standard petroleum gasoline. CNG is less expensive than gasoline. Heavy tanks are required to store it and the pressure required (200-300 bar).CNG is colorless, odorless, non-toxic, lighter than air and inflammable. The advantages of CNG are a unique combustion and suitable mixture formation. The engine operates smoothly with high compression ratios without knocking due to high octane number. It will lead to low exhaust emission and fueling operating cost, during lean burning conditions. It has a lower flame speed and causes high engine durability.

Compressed Natural Gas (CNG) engine can be divided into three main types; Dual Fuel Diesel-CNG, Gasoline-CNG and

dedicated/mono fuel. The lack of engine performance is the main problem of CNG engine [2]. Its performance is lower than that of gasoline because of its losses in volumetric efficiency and low flame speed. This will cause the low engine power and torque. It needs to make design modification to achieve a faster burn to optimizing the engine performance [3]. The properties of petrol and CNG are listed in table 1&2.

TABLE I
THERMODYNAMICS PROPERTIES OF PETROL [3]

Stoichiometric ratio	14.2
Octane number	96
Higher heating value(MJ/kg)	45
Lower heating value(MJ/kg)	42.2
Molecular Weight(kg/kmol)	106.2

TABLE II
THERMODYNAMICS PROPERTIES OF CNG [3]

Stoichiometric ratio	15.7
Octane number	120
Higher heating value(MJ/kg)	50.3
Lower heating value(MJ/kg)	45.9
Molecular Weight(kg/kmol)	17.74

The researchers analyzed the comparison of CNG spraying machines with gasoline engines. Their energy can be reduced by about 10 to 15 percent. The two main reasons for this drop when injected into the CNG state are that some air channels may be used by this. And it reduces the volumetric efficiency which will cause the power reducing. Another reason is about air fuel ratio. The number is around 15.7 to 1 for gas and 14.2 to 1 for fuel. This factor has been identified as more necessary

for CNG engines in the air than gasoline engines with air. And the amount of additional air available for the engine can be obtained by overfeeding machines. If the amount of air pressure inlet in the engine can be increased, so it can also increase the amount of inlet air mass to the engine. Mass density of air entering the engine will cause the combustion to be complete which improves the thermal efficiency and therefore to compensate for CNG engines seems to be necessary. Until now, the supercharged engine optimization is done by the researches [4]. There are two methods for increasing the engine power. One of them would be to the proportion of fuel in fuel air mixture. This will increase the engine power but the fuel efficiency cost increase and pollution level also increase. The other method is by increasing the volume of air entering into the cylinder and increasing the fuel intake proportionately, this will increase the engine power the power and fuel efficiency without hurting the environment. In recent years, the motor vehicle industry aims at the small sized and high power density engine, while downsizing (small size and weight saving) and less air pollution. Supercharging is a process which helps to increase the suction of IC engines above the atmospheric pressure [5].

2. SPERCHARGING THEORY

The power output of the engine depends on the amount of air inducted per unit time, the degree of utilization of that air and the thermal efficiency of the engine. Increasing the engine speed or increasing the density of air at intake increase the amount of air inducted per unit time. The engine friction and bearing loads also increase and the volumetric efficiency decreases when the speed is increased. The method of increasing the inlet air density, called supercharging, is usually employed to increase the power output of the engine. This is done by supplying air at a pressure higher than the pressure at which the engine naturally aspirates air from the atmosphere by using a pressure boosting device called a supercharger. The power output can also be increased by increasing the thermal efficiency of the engine, say, by increasing the compression ratio. However, this increases the maximum cylinder pressure. The rate of increase of maximum cylinder pressure is less than rate of increase of break mean effective pressure in case of supercharged engine. This means that for a given maximum cylinder pressure more power can be obtained by increasing the compression ratio. The rate of increase of maximum temperature is also low in case of supercharging. This results in lower thermal loads [6].

The main objective of supercharging is to increase the amount of air per cycle. Due to access amount of air in charge (air-fuel mixture), permits the better combustion of fuel compare to aspirate. Thus the power output of the engine is increased. Purpose of supercharging is to raise the volumetric efficiency above that which can be obtained by normal configuration. The effect of supercharging on the performance of the engine are the power output, mechanical efficiency, volumetric efficiency and the fuel consumption [7]. The PV diagrams of naturally aspirated & supercharged engines are presented as in figure.1.

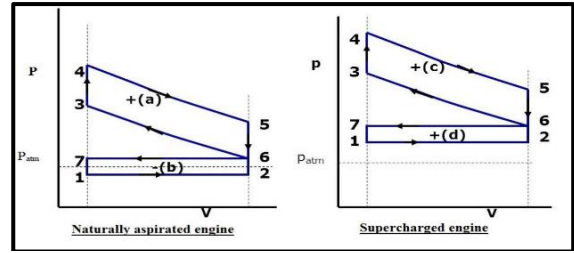


Fig.1. PV diagrams of naturally Aspirated & Supercharged engines

The power output of a naturally-aspirated engine can be increased by supercharging. It is necessary to make some modification of the engine for more suitable to supercharging. These modification include increase in the valve overlap period to allow complete scavenging of the clearance volume and increase in clearance volume by decreasing the compression ratio. The types of superchargers are Root Supercharger, Vane Supercharger and Centrifugal Supercharger. Two different types of supercharging methods are mechanical supercharging and turbocharging. The first limit is the knock for the SI engines and for CI engines the load and thermal stresses limits are reached first [8].

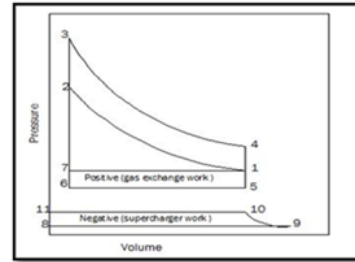


Fig. 2. Thermodynamics Analysis of Supercharged SI Engine [9]

TABLE III
 VARIOUS PROCESS FOR THE SUPERCHARGED SI ENGINE

Process	S. C. Engine
Induction	7→1
Compression	1→2
Heat addition	2→3
Explosion	3→4
Heat rejection	4→1

A. Power Input for Mechanical Driven Supercharge [9]

Assuming adiabatic compression of air, the work done on the supercharger per kg of air is given by

$$\begin{aligned} \dot{\omega} &= - \int v dp = h_2 - h_1 \\ &= C_p (T_2 - T_1) = C_p T_1 \left[\left(\frac{p_2}{p_1} \right)^{\frac{\gamma-1}{\gamma}} - 1 \right] \end{aligned}$$

Where T_1 = initial temperature, p_1 = initial pressure, p_2 = delivery pressure.

And, with the isentropic efficiency of η_c

$$\dot{\omega} = \frac{C_p T_1}{\eta_c} \left[\left(\frac{p_2}{p_1} \right)^{\frac{\gamma-1}{\gamma}} - 1 \right]$$

Thus power required to drive the compressor is given by

$$= \frac{\dot{m}_a C_p T_1 \left[\left(\frac{p_2}{p_1} \right)^{\frac{\gamma-1}{\gamma}} - 1 \right]}{60 \times \eta_c} \text{ kW}$$

Where \dot{m}_a mass of air is supplied by supercharger in kg/min and C_p is specific heat of air in kJ/kg K.

3. THE COMPARISON OF THE PERFORMANCE OF THE PETROL FUELED GASOLINE ENGINE AND THE GASOLINE ENGINE USING THE CNG FUEL

Das and Reddy [10] conducted the experiment on CNG bi-fuel passenger car and predicted the engine performance, fuel consumption and emission to reduce system calibration time as well as the cost of testing. According to their result, the carbon monoxide (CO) on CNG is very lower compared to petrol engine.

E. Ramjee and K. Vijaya Kumar Reddy [3] did an experimental investigations on a single cylinder 4-stroke air cooled type Bajaj-Kawasaki petrol engine to compute performance and exhaust emissions of the test engine. All tests have been carried out under steady state conditions for both petrol and CNG fuels and the results have been compared. They found that for all range of speeds, the volumetric efficiency is reduced and varies between 10-14%; except thermal efficiency the other performance parameters, viz; BMEP, Torque, Power and BSFC are decreased for CNG fuelled engine compared to petrol fuelled engine; except NO_x the other emission characteristics such as CO, CO_2 , and HC are decreased. The experiment tested at full load conditions and the various parameters of performance and emissions are calibrated. Fig.3 shows a graph plotted between volumetric efficiency and engine speed for both fuels.

From the graph, it is observed that the volumetric efficiency of CNG fuelled engine is lower than petrol engine, as the CNG engine occupies more volume of inlet air. The volumetric efficiency for CNG is decreases about 13.3% and it has occur at engine speed 4000 rpm and its average value is about 12.3% throughout the engine speed range. From the Fig. 4 and 5, it is learnt that the engine torque and brake power of CNG fuelled engine are considerably lower than that of petrol engine. This is due to lower volumetric efficiency of CNG fuelled engine.

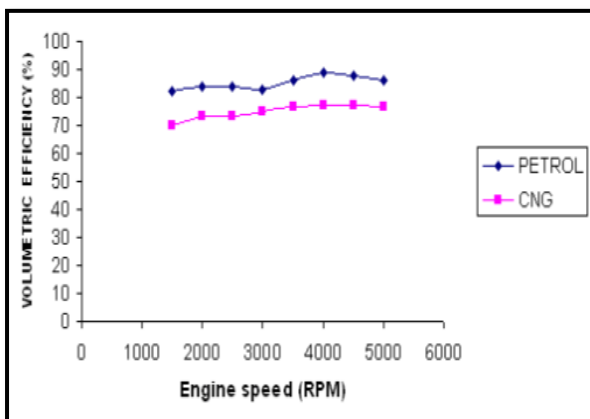


Fig. 3 Variation of volumetric efficiency and engine speed [3]

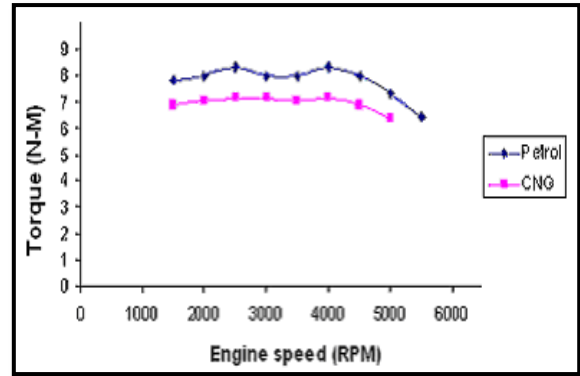


Fig. 4 Variation of Torque and engine speed [3]

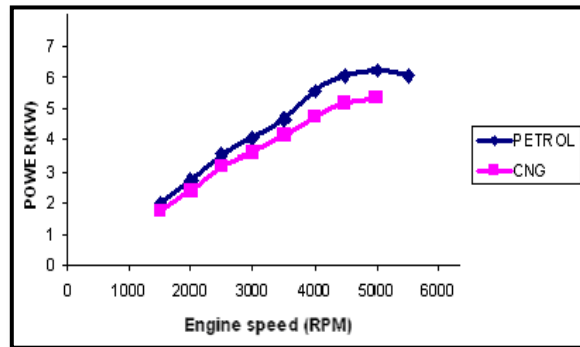


Fig.5.Variation Of Power and engine Speed [3]

Munde Gopal G. [2] reviewed the research paper of compressed natural gas as an alternative fuel for spark ignition engine. According to this reviewed paper, it is studied that the compressed natural gas is a good alternative fuel for SI engine but some disadvantages observed from the studies of the various experimental results are: the engine thermal efficiency and exhaust gas temperature produced by the CNG burning is always higher than that of the petrol. CNG produces less 8 -16% of brake torque, brake power and BMEP compared to gasoline fuel due to reduced volumetric efficiency and lower flame speed of CNG. On average the reduction of CO, CO_2 and HC emission are 20 -98%, 8-20% and 40-87% respectively by CNG. Higher NO_x emission is the main emission concern for CNG as automotive fuel that can be reduced by increasing fuel density and blending small quantities of H_2 .

Musthafah Mohd. Tahir [11] wrote the paper of Performance analysis of a spark ignition engine using compressed natural gas (CNG) as fuel. This study focused on the performance of CNG when used in a single cylinder SI engine. Based from the experiment in this study, compressed natural gas (CNG) produced low performance compared to liquid fuel (petrol). The power of CNG when compared to liquid fuel is reduced to about 18.5 %. The main reason for the lack of power when using CNG is because of the volumetric efficiency. According to this paper, the volumetric efficiency for this test engine is high when liquid fuel was used as the power source. However, when CNG was applied to this engine, it results low volumetric efficiency compare to liquid fuel. The lower volumetric efficiency is due to CNG physical properties, which is gas. During intake, CNG which consist of methane as the main particle does not produce a cooling effect during this condition. This result is due to the CNG is in the gas phase and it is vapor at ambient temperature.

4. COMPARISON OF THE PERFORMANCE OF THE PETROL FUELED GASOLINE ENGINE WITH AND WITHOUT SUPERCHARGER

Comparing performance characteristics of a gasoline and CNG engines and increasing volume efficiency and power using designed turbocharger was studied by Fathollah OMMI [4]. In this study, a one-dimensional model was used to model the XU-7 engine. After Gasoline and CNG engine model, the results of modelling was valid by using the results of engine dynamometer test and functional characteristics were compared between the two engines, and finally given the design parameters of the turbocharger, the engine system was selected for overfeeding. The results were presented in a CNG engine with a significant power reduction compared to gasoline engine. So two systems were modelled on CNG engine for solving this problem. The results were presented that using the designed turbocharger, the volumetric efficiency, braking torque and pressure inside the combustion chamber for overfeeding CNG engine have high level than natural breathing.

Pasala Venkata Satish[12] investigated the research of Performance Analysis of Supercharging a Single Cylinder SI Engine. A test engine, single cylinder 4 stroke air cooled petrol engine (3.7 kW) and vane type 50cc (driven by a belt and pulley) supercharger were set up for this experiment. From this literature the power and torque characteristic of the engine, for both the condition of the vehicle with & without a supercharger, is represented in graphical form.

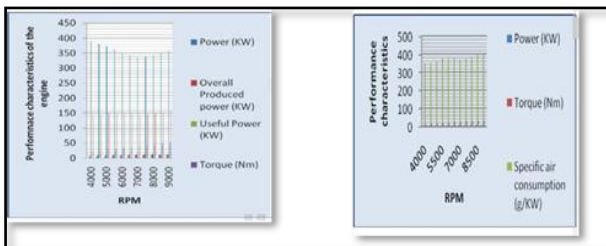


Fig.6 Performance characteristics of SI engine without and with supercharger [12]

From this research paper, it is concluded that the single cylinder SI engine with the supercharger which produce more horsepower on average about 150 % than the original SI engine.

Sujith G [13], did an experimental research of a 125cc Petrol engine with turbocharger. The experiment was carried out air cooled, 4 stroke single cylinder 124.7cc engine. Performance test was done to study and compare its performance under various loads with and without turbocharger. In this research work, it can be seen that the efficiency of the engine can be increased by the turbocharger. This method gives to increase the efficiency and at the same time to reduce the emission from the engine. And also this engine with turbocharger which have more brake thermal efficiency than the normal aspirated engine.

5. CONCLUSIONS

The main focus of this research review is to study the comparative analysis of CNG and Petrol as alternative fuel for SI engine with and without supercharger and as a result, the following conclusions were drawn as follows:

- i. CNG has low volumetric efficiency and reduction in mechanical efficiency.
- ii. CNG has no harmful effect on the engine and it is very adequate for S.I engines.
- iii. CNG burns more completely than petrol and emits lower amounts of exhaust pollutants.
- iv. CNG powered vehicles requires less maintenance, including fewer oil changes and less frequent spark plug replacement.
- v. CNG has higher engine thermal efficiency and exhaust gas temperature.
- vi. CNG produces less than of brake torque, brake power and BMEP compared to petrol due to reduced volumetric efficiency and lower flame speed of CNG.
- vii. CNG has less brake specific fuel consumption (BSFC) compared to petrol.

After referring some of the literature research papers of the SI engine which set up supercharger, it can be seen that the performance of the vehicles improves in terms of power up to 10% to 15% and torque up to 5% to 10%. It also improves mechanical efficiency and volumetric efficiency due to pressurized air are present in the cylinder. The use of the supercharger helps in reducing the emission of carbon monoxide and other hydrocarbons. Supercharger unit can be installed as detachable device.

From the study of this review paper, gas- driven engine could produce lesser power output in comparison with petroleum and the petroleum –driven engine with the supercharger gives more power output than the normal aspirated engine. So the problem (to detect from the power downgrade by using CNG fuel) is solved by setting up the supercharger at the engine inlet to the compressed natural gas-driven engine that helped the engine to produce higher output, but reduce the air pollution.

REFERENCES

- [1] S. Tambari, I. Benjamin, “Evaluation of comparative analysis in the use of petrol and compressed natural gas (CNG) as vehicular fuel,” *IOSR Journal of Mechanical and Civil Engineering (IOSR-JMCE)*, vol 11, issue 4 Aug. 2014.
- [2] M. G. Gopal., Dr. D. S. Rajendra, “Compressed natural gas as an alternative fuel for spark ignition engine: a review” *International Journal of Engineering and Innovative Technology (IJEIT)* vol 2, issue 6, Dec. 2012.
- [3] F. Ramjee and K. V. K. Reddy, “Performance analysis of a 4-stroke SI engine using CNG as an alternative fuel.
- [4] F. Ommi, E. Movahednejad and K. Nekofar. “Comparing performance characteristics of a gasoline and CNG engines and increasing volume efficiency and power using designed turbocharger”.
- [5] G. Sujith, Jishnu S Nair, “Modification and analysis of 125 cc petrol engine with turbocharger” *International Journal of Innovative Research in Science, Engineering and Technology* vol. 5, issue 4, April. 2016.
- [6] Prakash Kumar Sen, Rohit Jaiswal, “Performance analysis of supercharging process in SI and CI engine and application of supercharger”. *International Journal of Advance Research In Science And Engineering* <http://www.ijarse.com> IJARSE, vol. no.4, issue 01, April. 2015.
- [7] Prof.K.P.Agte, Sangram Khairna, Amol Visave, “Performance analysis of supercharging process in spark

ignition engine”, *International Conference on Ideas, Impact and Innovation in Mechanical Engineering*, vol 5. Issue 6. pp. 847 – 851, 2017.

- [8] H. N. Gupta, *Fundamentals of Internal Combustion Engines*, Second Edition.
- [9] V. Ganesan, *Internal Combustion Engines*, Third Edition, IIT Madras, Chennai. The Mc Graw-Hill Companies.
- [10] Das LM and Reddy YV (2000) Exhaust emission Characteristics of a CNG-fuelled engine, Pro 16th Nat cont IC engines combustion Jadavpur Univ.

Some Applications of Eigenvalues in Engineering Problems

Kyaw Kyaw Than
 Department of Engineering
 Mathematics
 Technological University
 Thanlyin, Myanmar

Aye Aye Khine
 Department of Mechanical
 Engineering
 Yangon Technological
 University
 Yangon, Myanmar

Nwe Thazin Wai
 Department of Engineering
 Mathematics
 Technological University
 Thanlyin, Myanmar

Abstract: In this paper, some applications of eigenvalues, which are useful in solving engineering problems, are presented.

Keywords: Mixing problem, Vibrating system.

1. INTRODUCTION

Eigenvalue problems are of practical interest to the engineers, physicists, and mathematicians; we shall see that their theory makes up a paper in linear algebra that has found numerous applications. In this paper we discuss a few typical examples from the range of applications of matrix eigenvalue problems. Matrix eigenvalue problems concern the solutions of the vector equations

$$Ax = \lambda x$$

where A is a given square matrix and vector $x \neq 0$ and scalar λ are unknown. Here x is called the eigenvector of A and λ 's are called the eigenvalues of A .

2. EIGENVALUE

The eigenvalues of a square matrix A are the roots of the characteristic equation of A . Hence an $n \times n$ matrix A has at least one eigenvalue and at most n numerically different eigenvalues.

2.1 Mixing Problem Involving Two Tanks

We consider mixing problem involving two tanks as follows.

Suppose that two tanks are connected as shown in the accompanying figure (1). At time $t = 0$, tank 1 contains 30 L of water in which 2 kg of salt has been dissolved, and tank 2 contains 30 L of water in which 5 kg of salt has been dissolved. Pure water is pumped into tank 1 at the rate of 20 L/min; the saline mixtures are exchanged between the two tanks at the rates shown, the mixture in tank 2 drains out at the rate of 15 L/min, and the mixture in tank 1 drains out at the rate of 5 L/min. We want to find the amount of salt in the two tanks at time t .

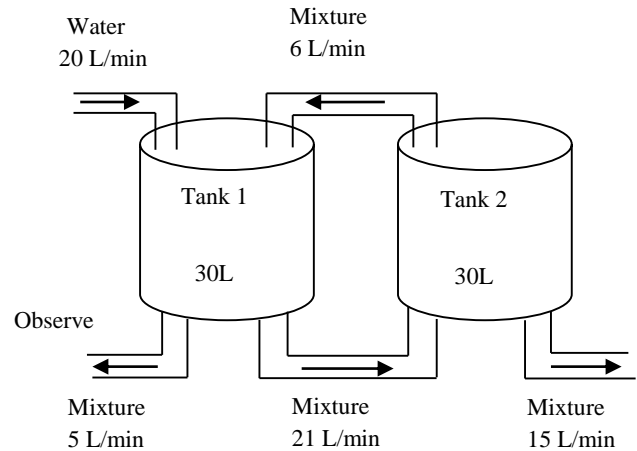


Figure 1. Mixing problem involving two

first that the amount of liquid in each tank remains constant because the rate at which liquid enters each tank is the same as the rate at which it leaves. Thus each tank always contains 30L of liquid.

Now let

$$y_1(t) = \text{amount of salt in tank 1 at time } t,$$

$$y_2(t) = \text{amount of salt in tank 2 at time } t,$$

and let the rates of change be y_1' and y_2' .

Since the rate at which salt enters

$$\text{tank 1} = \left(6 \frac{\text{L}}{\text{min}}\right) \left(\frac{y_2(t) \text{ kg}}{30 \text{ L}}\right) = \frac{y_2(t) \text{ kg}}{5 \text{ min}}$$
 and

the rate at which salt leaves

$$\text{tank 1} = \left(26 \frac{\text{L}}{\text{min}}\right) \left(\frac{y_1(t) \text{ kg}}{30 \text{ L}}\right) = \frac{13y_1(t) \text{ kg}}{15 \text{ min}},$$

the rate of change of $y_1(t)$ is

$$y_1'(t) = \text{rate in} - \text{rate out} = \frac{y_2(t)}{5} - \frac{13y_1(t)}{15}$$

Since the rate at which salt enters

$$\text{tank 2} = \left(21 \frac{\text{L}}{\text{min}}\right) \left(\frac{y_1(t) \text{ kg}}{30 \text{ L}}\right) = \frac{7y_1(t) \text{ kg}}{10 \text{ min}} \text{ and}$$

the rate at which salt leaves

$$\text{tank 2} = \left(21 \frac{\text{L}}{\text{min}}\right) \left(\frac{y_2(t) \text{ kg}}{30 \text{ L}}\right) = \frac{7y_2(t) \text{ kg}}{10 \text{ min}},$$

the rate of change of $y_2(t)$ is

$$y_2'(t) = \text{rate in} - \text{rate out} = \frac{7y_1(t)}{10} - \frac{7y_2(t)}{10}$$

Mixture problem is the system of the first-order ODEs

$$y_1' = -\frac{13}{15}y_1 + \frac{1}{5}y_2$$

(Tank 1)

$$y_2' = \frac{7}{10}y_1 - \frac{7}{10}y_2$$

(Tank 2)

or

$$\mathbf{y}' = \mathbf{A}\mathbf{y} \quad \text{where}$$

$$\mathbf{A} = \begin{bmatrix} -\frac{13}{15} & \frac{1}{5} \\ \frac{7}{10} & -\frac{7}{10} \end{bmatrix} \text{ and } \mathbf{y} = \begin{bmatrix} y_1 \\ y_2 \end{bmatrix}$$

Let $\mathbf{y} = \mathbf{x}e^{\lambda t}$ be solution of $\mathbf{y}' = \mathbf{A}\mathbf{y}$

Then $\lambda \mathbf{x}e^{\lambda t} = \mathbf{A}\mathbf{x}e^{\lambda t}$

$$\mathbf{A}\mathbf{x} = \lambda \mathbf{x} \quad \text{where } \mathbf{x} = \begin{bmatrix} x_1 \\ x_2 \end{bmatrix}$$

which is an eigenvalue problem.

$$-\frac{13}{15}x_1 + \frac{1}{5}x_2 = \lambda x_1$$

$$\frac{7}{10}x_1 - \frac{7}{10}x_2 = \lambda x_2$$

$$\left(-\frac{13}{15} - \lambda\right)x_1 + \frac{1}{5}x_2 = 0$$

$$\frac{7}{10}x_1 + \left(-\frac{7}{10} - \lambda\right)x_2 = 0$$

$$(\mathbf{A} - \lambda\mathbf{I})\mathbf{x} = 0$$

For non trivial solutions,

$$\det(\mathbf{A} - \lambda\mathbf{I}) = \begin{vmatrix} -\frac{13}{15} - \lambda & \frac{1}{5} \\ \frac{7}{10} & -\frac{7}{10} - \lambda \end{vmatrix} = 0$$

$$\left(-\frac{13}{15} - \lambda\right)\left(-\frac{7}{10} - \lambda\right) - \frac{7}{50} = 0$$

$$\lambda^2 + \frac{47}{30}\lambda + \frac{7}{15} = 0 \quad (2)$$

The solutions of quadratic equation are $\lambda_1 = -\frac{2}{5}$ and $\lambda_2 = -\frac{7}{6}$.

$\lambda_1 = -\frac{2}{5}$ corresponding equation are

$$-\frac{7}{15}x_1 + \frac{1}{5}x_2 = 0$$

$$\frac{7}{10}x_1 - \frac{3}{10}x_2 = 0$$

From these two equations, we have $x_2 = \frac{7}{3}x_1$

\therefore we may choose $x_1 = 3$, then $x_2 = 7$.

$$\mathbf{x}_1 = \begin{bmatrix} 3 \\ 7 \end{bmatrix}$$

$\lambda_2 = -\frac{7}{6}$ corresponding equation are

$$\frac{7}{10}x_1 + \frac{7}{15}x_2 = 0$$

$$\frac{3}{10}x_1 + \frac{1}{5}x_2 = 0$$

From these two equations, we have $x_2 = -\frac{3}{2}x_1$

\therefore we may choose $x_1 = -2$, then $x_2 = 3$.

$$\mathbf{x}_2 = \begin{bmatrix} -2 \\ 3 \end{bmatrix}$$

From (1)

$$y = c_1 \mathbf{x}_1 e^{\lambda_1 t} + c_2 \mathbf{x}_2 e^{\lambda_2 t} = c_1 \begin{bmatrix} 3 \\ 7 \end{bmatrix} e^{-\frac{2}{5}t} + \begin{bmatrix} -2 \\ 3 \end{bmatrix} e^{-\frac{7}{6}t} \quad (3)$$

where c_1 and c_2 are arbitrary constants.

Initial condition are $y_1(0) = 2$ and $y_2(0) = 5$.

Therefore,

$$y(0) = c_1 \begin{bmatrix} 3 \\ 7 \end{bmatrix} + c_2 \begin{bmatrix} -2 \\ 3 \end{bmatrix} = \begin{bmatrix} 3c_1 - 2c_2 \\ 7c_1 + 3c_2 \end{bmatrix} = \begin{bmatrix} 2 \\ 5 \end{bmatrix}$$

Then $3c_1 - 2c_2 = 2$ and $7c_1 + 3c_2 = 5$

and hence $c_1 = \frac{16}{23}$, $c_2 = \frac{1}{23}$

$$y = \frac{16}{23} \mathbf{x}_1 e^{-\frac{2}{5}t} + \frac{1}{23} \mathbf{x}_2 e^{-\frac{7}{6}t} = \frac{16}{23} \begin{bmatrix} 3 \\ 7 \end{bmatrix} e^{-\frac{2}{5}t} + \frac{1}{23} \begin{bmatrix} -2 \\ 3 \end{bmatrix} e^{-\frac{7}{6}t}$$

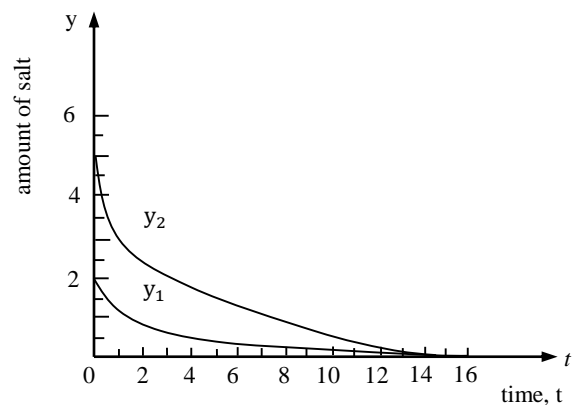


Figure 2. Leaving Salt Vs time graph

In components,

$$y_1 = 2.096e^{-\frac{2}{5}t} - 0.09e^{-\frac{7}{6}t} \quad (\text{Tank 1, lower curve})$$

$$y_2 = 4.87e^{-\frac{2}{5}t} + 0.13e^{-\frac{7}{6}t} \quad (\text{Tank 2, upper curve})$$

2.2 Vibrating System of Two Masses on Two Springs

Mass-spring systems involving several masses and springs can be treated as eigenvalue problems. The mechanical system in figure (3) is governed by the system of ODEs

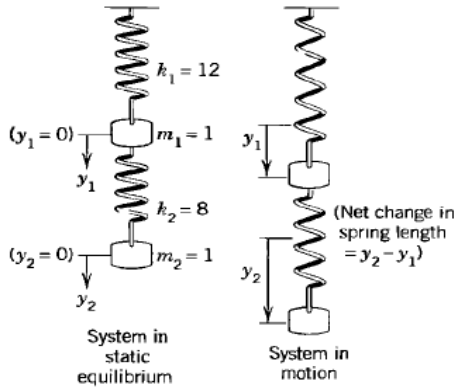


Figure 3. Masses on springs

$$y_1'' = -20y_1 + 8y_2 \quad (1)$$

$$y_2'' = 8y_1 - 8y_2$$

where y_1 and y_2 are the displacements of masses from rest, as shown in figure (3), y_1 and y_2 primes denote derivatives with respect to time t .

$$y'' = \begin{bmatrix} y_1'' \\ y_2'' \end{bmatrix} = \mathbf{A}y = \begin{bmatrix} -20 & 8 \\ 8 & -8 \end{bmatrix} \begin{bmatrix} y_1 \\ y_2 \end{bmatrix} \quad (2)$$

We try a vector solution of the form

$$y = \mathbf{x} e^{\omega t} \quad (3)$$

$$y' = \omega \mathbf{x} e^{\omega t}$$

$$y'' = \omega^2 \mathbf{x} e^{\omega t}$$

Substitution into (2) $\omega^2 \mathbf{x} e^{\omega t} = \mathbf{A} \mathbf{x} e^{\omega t}$

$$\mathbf{A} \mathbf{x} = \lambda \mathbf{x} \quad \text{where } \lambda = \omega^2 \quad (4)$$

$$\mathbf{A} = \begin{bmatrix} -20 & 8 \\ 8 & -8 \end{bmatrix}$$

$$\mathbf{A} \mathbf{x} = \begin{bmatrix} -20 & 8 \\ 8 & -8 \end{bmatrix} \begin{bmatrix} x_1 \\ x_2 \end{bmatrix} = \lambda \begin{bmatrix} x_1 \\ x_2 \end{bmatrix}$$

In components,

$$-20x_1 + 8x_2 = \lambda x_1$$

$$8x_1 - 8x_2 = \lambda x_2$$

Transferring the terms on the right to the left, we get

$$(-20 - \lambda)x_1 + 8x_2 = 0$$

$$8x_1 + (-8 - \lambda)x_2 = 0 \quad (5)$$

$$(\mathbf{A} - \lambda \mathbf{I})\mathbf{x} = 0$$

$$\det(\mathbf{A} - \lambda \mathbf{I}) = \begin{vmatrix} -20 - \lambda & 8 \\ 8 & -8 - \lambda \end{vmatrix} = 0$$

$$(-20 - \lambda)(-8 - \lambda) - 64 = 0$$

$$\lambda^2 + 28\lambda + 96 = 0$$

The solutions of quadratic equation are $\lambda_1 = -4$ and $\lambda_2 = -24$.

Consequently, $\omega_1 = \pm 2i$ and $\omega_2 = \pm 2\sqrt{6}i$. Corresponding eigenvectors are

$$\mathbf{x}_1 = \begin{bmatrix} 1 \\ 2 \end{bmatrix} \quad \text{and} \quad \mathbf{x}_2 = \begin{bmatrix} 2 \\ -1 \end{bmatrix} \quad (6)$$

From (3) we thus obtain

$$\mathbf{x}_1 e^{\pm 2it} = \mathbf{x}_1 (\cos 2t \pm i \sin 2t)$$

$$\mathbf{x}_2 e^{\pm 2\sqrt{6}it} = \mathbf{x}_2 (\cos 2\sqrt{6}t \pm i \sin 2\sqrt{6}t)$$

By addition and subtraction, we get

$$\mathbf{x}_1 \cos 2t, \quad \mathbf{x}_1 \sin 2t, \quad \mathbf{x}_2 \cos 2\sqrt{6}t, \quad \mathbf{x}_2 \sin 2\sqrt{6}t$$

A general solution is

$$y = \mathbf{x}_1 (a_1 \cos 2t + b_1 \sin 2t) + \mathbf{x}_2 (a_2 \cos 2\sqrt{6}t + b_2 \sin 2\sqrt{6}t) \text{ with arbitrary constants } a_1, b_1, a_2, b_2.$$

By (6) $y_1 = a_1 \cos 2t + b_1 \sin 2t + 2a_2 \cos 2\sqrt{6}t +$

$$2b_2 \sin 2\sqrt{6}t$$

$$y_2 = 2a_1 \cos 2t + 2b_1 \sin 2t - a_2 \cos 2\sqrt{6}t - b_2 \sin 2\sqrt{6}t$$

3. CONCLUSION

We had presented the usage of eigenvalues and eigenvectors to solve some engineering problems. There are many applications of eigenvalues and eigenvectors in various fields of engineering and sciences which will be discussed later.

4. ACKNOWLEDGEMENTS

First, the authors would like to acknowledge the support of the papers for their references. The authors are deeply grateful to their adorable benefactor parents and teachers who gave their knowledge, useful discussions, powerful encouragement, invaluable suggestions and interest help through their life.

5. REFERENCES

- [1] Keryszig, E. Advanced engineering mathematics. John Wiley & Sons Inc, 1999.
- [2] Chatelin. F. Eigenvalues of Matrices. New York, Wiley-intersciences, 1993.
- [3] James. G. Modern Engineering Mathematics. Pearson Education Limited, 2007.
- [4] Anton. H. and Busby. RC. Contemporary Linear Algebra. John Wiley & Sons Inc, 2003.

Workspace Analysis of Two-link Planar Manipulator

Thu Zar
Lecturer
Department of Mechanical
Engineering, Technological
University (Thanlyin),
Myanmar

Phyo Wai Lin
Lecturer
Department of Mechanical
Engineering, Technological
University (Meiktila),
Myanmar

Dr. Su Yin Win
Professor
Department of Mechanical
Engineering, Technological
University (Thanlyin),
Myanmar

Abstract: A two link revolute robotic arm is optimized for maximization of work space area covered by its end effector. A mathematical model for optimization is built considering singularities which influence the variation of design variables. Condition number which is the measure of output value (End effector position) for a small change in input value (joint angles) is modelled as the constraint. Joint angle between link2 and link1 and link lengths are considered as design variables. The mathematical model is initially optimized using Semi-infinite Programming technique. Genetic Algorithm using Roulette wheel selection is employed on the nonlinear optimization model for obtaining global optimum value for the objective function. The maximum value of objective function obtained from Genetic Algorithm is found to be considerably higher than the value obtained from Semi-infinite Programming method.

Keywords: Kinematics and Dynamics, Denavit-Hartenberg (DH), 2DOF manipulator, MatLab

1. INTRODUCTION

The objective of designers is to maximize the area covered by the robotic end effectors in their work space. However, their movements are restricted due to kinematic singularities. It is popularly known fact that the Jacobian matrix relates linear velocities of links or end effectors to their joint velocities. At singular positions, the determinant of jacobian becomes zero resulting in infinite joint velocities. Therefore, within these restrictions (singularities), it is area of interest of many researchers to find the global optimum which gives maximum reach for the end effector. A.Morecki et.al (1984) discussed the effect of link length ratios on the distance travelled by end effector.

Position analysis is an essential step in the design, analysis and control of robots. In this article, a basic introduction to the position analysis of serial manipulators is given. This topic is invariably covered in all the textbooks on this subject. Therefore, instead of repeating the standard details of forward kinematics, such as, the designation of the reference frames, determination of the Denavit-Hartenberg (DH) parameters, multiplication of the 4×4 transformation matrices to get the end-effector position and orientation etc., more emphasis is laid on the inverse problem, which is relatively more complicated in such manipulators.

A vertical revolute configuration, a 2-R robot with two degrees of freedom is generally well-suited for small parts insertion tasks for assembly lines like electronic components insertion. Although the final aim is real robotics, it is often very useful to perform simulations prior to investigations with real robots. This is because simulations are easier to setup, less expensive, faster and more convenient to use [2].

In this paper we examine in detail the description of the workspace of a two degree of freedom planar robot

manipulator. We use the technique based on polynomial discriminants described in to characterize the workspace from an algebraic point of view. With the algebraic representation, we can easily investigate the effects of kinematic parameters on the workspace. Most importantly, the algebraic representation of a robot workspace facilitates simple solutions to many problems in the analysis of robot manipulators.

2. MATHEMATICAL MODEL

A 2R planar serial robot is considered as the mathematical modeling for kinematically redundant manipulator. Where l_1 and l_2 are the lengths of the link 1 and 2, and θ_1 and θ_2 are joint variables. P_x and p_y are the position of robot end-effector. The workspace of this planar robot is then all P_x and p_y pairs that the robot is able to reach. Both joints can rotate 360° , the workspace is simply a circle of radius $l_1 + l_2$. When limits exist, the workspace becomes more complex.

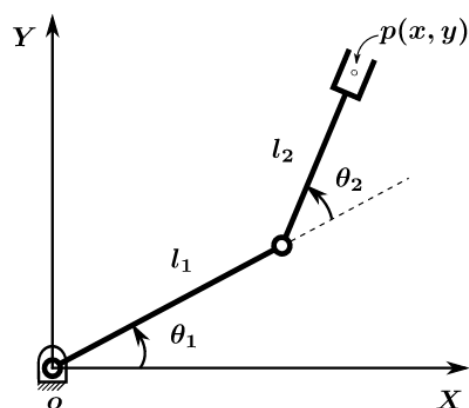


Figure. 1 Two link planar manipulator

Figure. 1 shows a schematic representation of two link planar manipulator with link lengths and link angles.

2.1 Kinematics of 2R planar manipulator

From forward kinematics the following relations connecting end effector positions with joint angles and link lengths are obtained.

$$p_x = l_1 \cos \theta_1 + l_2 \cos(\theta_1 + \theta_2) \quad (1)$$

$$p_y = l_1 \sin \theta_1 + l_2 \sin(\theta_1 + \theta_2) \quad (2)$$

The first kinematic equation in terms of a single joint variable, θ_1 , is obtained by adding the square of equations (1) and (2),

$$g_1(\theta_1) = p_x^2 + p_y^2 - 2l_1 p_x \cos \theta_1 - 2l_1 p_y \sin \theta_1 + l_1^2 - l_2^2 = 0 \quad (3)$$

To obtain the other independent kinematic equation in terms of θ_2 , rewrite equations (1) and (2) as

$$p_x = l_1 \cos \theta_1 + l_2 \cos \theta_1 \cos \theta_2 - l_2 \sin \theta_1 \sin \theta_2 \quad (4)$$

$$p_y = l_1 \sin \theta_1 + l_2 \sin \theta_1 \cos \theta_2 - l_2 \cos \theta_1 \sin \theta_2 \quad (5)$$

Multiplying (4) by $\sin \theta_1$ and (5) by $\cos \theta_1$ and subtracting, equation (6) is obtained.

$$\cos \theta_1 p_y + \sin \theta_1 p_x = l_2 \sin \theta_2 \quad (6)$$

Now equations (3) and (6) are linear equations in $\sin \theta_1$ and $\cos \theta_1$ and can be used to eliminate $\sin \theta_1$ and $\cos \theta_1$ to obtain an expression that relate p_x and p_y and link lengths to θ_2 . Specifically,

$$p_x^2 + p_y^2 = l_2^2 \sin^2 \theta_2 + \left[\frac{p_x^2 + p_y^2 + l_1^2 - l_2^2}{2l_1} \right]^2 \quad (7)$$

which can be simplified to

$$g_2(\theta_2) = p_x^2 + p_y^2 - l_1^2 - l_2^2 - 2l_1 l_2 \cos \theta_2 = 0 \quad (8)$$

Equations (3) and (8) can be verified graphically using in Fig. 1 and they are the two independent kinematic equations on which workspace description is based. Since they are in term of revolute joint variables, substitution

$$x = \tan \frac{\theta_i}{2}$$

or

$$\sin \theta_i = \frac{2x}{1+x^2} \quad \text{and} \quad \cos \theta_i = \frac{1-x^2}{1+x^2} \quad (9)$$

is necessary to remove the periodicity. Then the set of workspace boundary surfaces as required by equation (3), with substitution equation (9), are given by the roots of the characteristic polynomial

$$p_x^2 + p_y^2 - 2l_1 \left(p_x \frac{1-x^2}{1+x^2} + p_y \frac{2x}{1+x^2} \right) = l_2^2 - l_1^2$$

or

$$x^2(p_x^2 + p_y^2 + l_1^2 - l_2^2 + 2l_1 p_x) + x(-4l_1 p_y) + [p_x^2 + p_y^2 - 2l_1 p_x + (l_1^2 - l_2^2)] = 0 \quad (10)$$

(10) is a polynomial in x and has the form $C_2 x^2 + C_1 x + C_0$. Its real roots cease to exist when $C_1^2 - 4C_0 C_2$ is zero, or

$$p_x^2 + p_y^2 = (l_1 + l_2)^2 \quad \text{and} \quad p_x^2 + p_y^2 = (l_1 - l_2)^2 \quad (11)$$

Turning now to the second kinematic equation (8), substitution (9) into (8) results in the characteristic polynomial

$$p_x^2 + p_y^2 - l_2^2 - l_1^2 - 2l_1 l_2 \frac{1-x^2}{1+x^2} = 0$$

or

$$x^2(p_x^2 + p_y^2 - l_1^2 - l_2^2 \pm 2l_1 l_2) + (p_x^2 + p_y^2 - l_1^2 - l_2^2 \pm 2l_1 l_2) = 0 \quad (12)$$

The boundary surfaces defined by θ_2 coincide with those defined by θ_1 . In addition, the boundary surfaces in both cases are two concentric circles with centers at the origin of the x - y plane and with radius of $|l_1 + l_2|$ and $|l_1 - l_2|$, respectively. The second circle degenerates to a point at the origin when the links have the same length. Therefore, the workspace description derived by the algorithm in verifies that which we commonly take for granted.

Additional boundary surfaces are introduced when joint limits are considered. These surfaces are defined by substituting the limit values into the corresponding kinematic equation, equation (3) for joint one and equation (8) for joint two. For the planar robot under investigation, assume

$$\theta_{1\min} \leq \theta_1 \leq \theta_{1\max} \quad \text{and} \quad \theta_{2\min} \leq \theta_2 \leq \theta_{2\max}$$

To derive the additional boundary surface due to joint one limits, rewrite the kinematic equation (3) as

$$(p_x - l_1 \cos \theta_1)^2 + (p_y - l_1 \sin \theta_1)^2 = l_2^2 \quad (13)$$

With either joint one limit substituted into (13), we obtain another circle centered at $(l_1 \cos \theta_{1m}, l_1 \sin \theta_{1m})$, where θ_{1m} is either the minimum or maximum joint limit.

Similarly if one rewrites equation (8) as

$$p_x^2 + p_y^2 = l_1^2 + l_2^2 + 2l_1 l_2 \cos \theta_2 \quad (14)$$

Equation (14) produces tow more circle with centers at the origin and with radius l where

$$l^2 = l_1^2 + l_2^2 + 2l_1 l_2 \cos \theta_{2m}$$

Note that it can be easily shown that

$$(l_1 - l_2)^2 \leq l^2 \leq (l_1 + l_2)^2$$

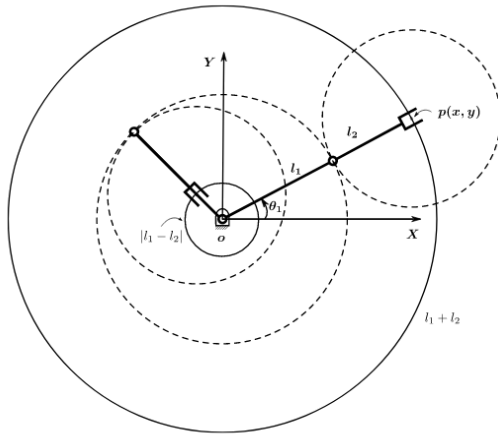


Figure. 2 Singularities and workspace of the 2R planar manipulator

The circles delimit the set of points in the plane that the manipulator can reach. In other words, these circles define the boundaries of the workspace (or more precisely, the reachable workspace) of the manipulator.

3. EFFECTS OF KINEMATIC PARAMETERS ON WORKSPACE

Each workspace boundary surface reveals little of how it relate to other boundary surface. The complete workspace is not simply the intersection of workspaces obtained by considering link and joint constraints individually. For the planar robot, the nature of the workspace depends on six parameters, two link lengths and four joint limits. We take the approach to first consider the simplest situation where joint limits do not exit, and gradually introduce joint limits as additional constraints on the workspace geometry.

Without Joint Limits, the workspace is constrained only by the link lengths. As stated previously, the geometry of the workspace in this case is a ring defined by two concentric circles of radius $|l_1+l_2|$ and $|l_1-l_2|$ with centers at the origin. The inner circle may possible degenerate to a singular point at the origin when the two links are of the same length.

3.1 Consideration of Joint 1 Limits

Two additional boundary surfaces result from limits of joint 1 and they are defined by (21) when the two limits are substituted into it. Part of the two circles will form the boundary of the final workspace. The workspace contribution can be analyzed for three different case, $l_1 > l_2$, $l_1 = l_2$ and $l_1 < l_2$.

Macintosh, use the font named Times. Right margins should be justified, not ragged.

3.2 Consideration of Joint 2 Limits

When joint 1 can rotate a complete revolution while θ_2 is restricted to $(\theta_{2min}, \theta_{2max})$, according to two additional curves, circles in this case. It can possibly form new workspace boundaries, and radii of the two circles are defined by

$$r_{21} = \sqrt{l_1^2 + l_2^2 + 2l_1l_2 \cos \theta_{2min}}$$

$$r_{21} = \sqrt{l_1^2 + l_2^2 + 2l_1l_2 \cos \theta_{2max}}$$

4. RESULTS

Three workspace results presentations are shown in Figure. 2, Figure. 3 and Figure. 4. The workspaces are plotted in MatLab Software using forward kinematic equation for two link planar manipulator.

Case I: $l_1 < l_2$

In this case link 2 is longer than link 1 and the workspace typically has the shape of an apple with its core taken out. A workspace is shown in Fig. 3. Where the set of kinematic parameters are $l_1 = 0.23$ m, $l_2 = 0.17$ m and $0^\circ < \theta_1 < 180^\circ$.

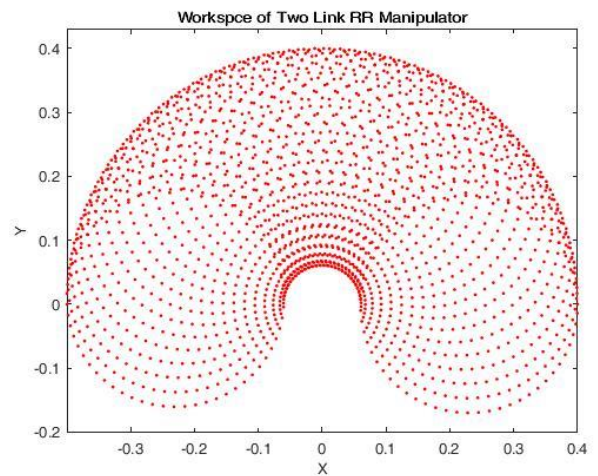


Figure. 3 Workspace with joint 1 limit: Case I

Case II: $l_1 = l_2$

When the two links are of the same length, the workspace looks either like an apple without a core if the range of the joint 1 is greater than or equal to 180° , or like an apple with an oval-shaped core. A workspace is shown in Fig. 4. Where the set of kinematic parameters are $l_1 = 0.20$ m, $l_2 = 0.20$ m and $0^\circ < \theta_1 < 180^\circ$.

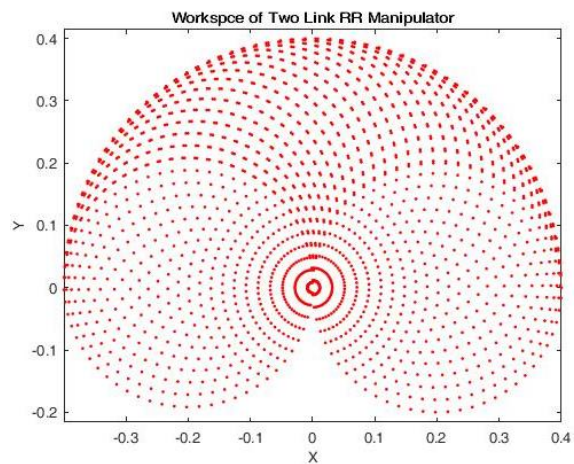


Figure. 4 Workspace with joint 1 limit: Case II

Case III: $l_1 > l_2$

In this case, the workspace looks either like an apple with a

core of a sharp tip pointing to the apple top. A workspace is shown in Figure. 4. Where the set of kinematic parameters are $l_1 = 0.17$ m, $l_2 = 0.23$ m and $0^\circ < \theta_1 < 180^\circ$.

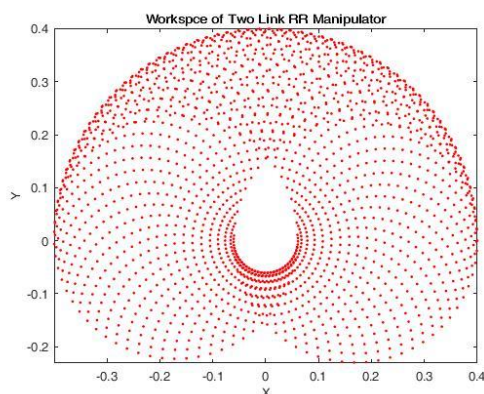


Figure.5 Workspace with joint 1 limit: Case III

5. CONCLUSION

In this paper, the complete mathematical formulation for forward kinematics of two link planar robot manipulator having two degree of freedom is derived. An analytical formulation for determining the robot workspace is presented. This formulation is used to develop the MatLab tool box. The workspace constraint function was formulated in terms of generalized coordinates including, inequality constraints imposed on each joint. For the computational analysis of mathematical formulation of complete forward kinematics of the system MATLAB code are developed in the form of several M-files. The simulated results are also plotted.

6. ACKNOWLEDGMENTS

The authors wish to thank Department of Mechanical Engineering, Technological University (Thanlyin), for permitting to use the facilities to carry out research work.

7. REFERENCES

- [1] Amin A. Mohammed and M. Sunar, “Kinematics Modeling of a 4-DOF Robot Arm”, International Conference on Control Automation and Robotic 2015, IEEE
- [2] Mahmoud Gouasmi, Mohammed Ouali, Brahim Fernini, Mohammed Meghatria, “Kinematic Modelling and Simulation of a 2R Robot Using SolidWorks and Verification by MATLAB/Simulink”, International Journal of Advanced Robotic Systems, DOI: 10.5772/50203
- [3] S K Saha, “Introduction to Robotics”
- [4] Amey V.Sutar, Dr. S. S. Ohol, “Kinematic And Dynamic Analysis Of A Robot Arm Used For All Terrain Robot”, International Journal of Engineering Research & Technology (IJERT), Vol. 3 Issue 5, May-2014
- [5] Tarun Pratap Singh, Dr. P. Suresh, Dr. Swe Chandan, “Forward and Inverse Kinematic Analysis of Robot Manipulator”, International Research Journal of Engineering and Technology (IRJET), Volume: 04 Issue:02, Feb-2017
- [6] Peter Frankovsky, Darina Hroncova, Ingrid Delyova, Peter Hudak, “Inverse and forward dynamic analysis of two link manipulator”, www.sciencedirect.com, Procedia Engineering 48 (2012), 158-163
- [7] Ruthber Rodriguez Serrezuela, Adrian Fernando Chavarro Chavarro, Miguel Angel Tovar Cardozo, Alejandro Leiva Toquica, Luis Fernando Ortiz Martinez, “Kinematic Modelling of a Robotic Arm Manipulator Using MatLab”, ARPN Journal of Engineering and Applied Sciences, VOL.12, No. 7, APRIL 2017
- [8] Vivek Deshpande, P M George, “Kinematic Modelling and Analysis of 5 DOF Robotic Arm”, International Journal of Robotic Research and Developments (IJRRD), Vol. 4, Issue 2, Apr 2014, 17-24
- [9] Javad Enferadi, Mohammad Tavakolian, “Lagrangian Dynamics Analysis of a XY-Theda Parallel Robotic Machine Tool”, Periodica Polytechnica Mechanical Engineering, 61(2), pp-107-114, 2017
- [10] Parham M. Kebria, Saba Al-wais, Hamid Abdi, and Saeid Nahavandi, “Kinematic and Dynamic Modelling of UR5 Manipulator”,
- [11] John J. Craig, “Introduction to Robotics, Mechanics and Control”, Third edition
- [12] Reza N. Jazar, “Theory of Applied Robotics, Kinematics, Dynamics, and Control”, Second Edition

A Vehicle Detecting and Counting Technique Based on Digital Image Processing

Zo Nun Khuma
Department of Information
Technology,
West Yangon Technological
University, Myanmar

Kyu Kyu Than
Department of Information
Technology,
West Yangon Technological
University, Myanmar

Dr. Khaing Myat Mon
Department of Information
Technology,
West Yangon Technological
University, Myanmar

Abstract: Many large cities in Myanmar are suffering from severe traffic problems as their vehicle populations have been being unprecedentedly increase. Nowadays, due to busy schedule of work style, the people are facing heavy traffic problem. This research presents the automatic vehicles counting based on the density of vehicles in a particular road using image processing techniques. In this work, video image processing to extract video frame as input & using detector. The surveillance cameras are fixed at the top view on that road to capture all vehicle motions. Then, frame images are retrieved from the live video and vehicle regions are segmented applying Gaussian Mixture Model and Morphological operations such as opening and closing. After that, motion vehicle regions are appeared as foreground regions and counted. The accuracy of the proposed method will presents with various experiments of different roads.

Keywords: Digital Image Processing, Vehicle Detecting, Vehicle Counting, Gaussian Mixture Model, Morphological operations

1. INTRODUCTION

As digital cameras and computers have become wide-spread, the number of applications using vision techniques has increased significantly. One such application that has received significant attention from the computer vision community is traffic surveillance.

Video camera is a promising traffic sensor because of its low cost and its potential ability to collect a large amount of information (such as the number of vehicles, vehicles speed/acceleration, vehicle class, vehicles track) which can also infer higher-level information (incidents, speeding, origin-destination of vehicles, macroscopic traffic statistics and etc).

The video cameras (CCD or CMOS) are connected to a computer that performs images/video processing, object recognition and object tracking. Numerous research projects aiming to detect and track vehicle from stationary rectilinear cameras have been carried out in terms of measuring traffic performance during the past decades. It is widely recognized that vision-based systems are flexible and versatile in traffic monitoring applications if they can be made sufficiently reliable and robust. Some common and related works of vehicle detection and counting can be summarized as follow.

With respect to vehicle counting, a system of vehicle detection and classification was presented in [1]. The work used a self-adaptive background subtraction technique to separate vehicles from the background. The resulting connected regions are then tracked and counted over a sequence of images using a spatial matching method. The tracked regions are grouped together to form vehicles. Next adaptive background detection method which was also applied to identify vehicles was published in [2]. In this work, the vehicles were detected and counted based on contour extraction. Prewitt filter kernel was used for edge detection. The contour linking method used for connecting separated edge parts of the original object into one closed contour. A contour labelling method is used to mark and calculate the number of vehicles within frames. In [3], feature based vehicle detection and tracking algorithm had been used.

Offline camera calibration had been carried out to detect the parameters such as line correspondences for a projective mapping, detection region and multiple fiducially points for camera stabilization. The projective transformation is necessary as the features are tracked in world coordinates to exploit known physical constraints on vehicle motion. The transformation is used to calculate distance based measures such as position, velocity and density. Another system for vehicle detection and counting was described in [4]. In this work, the Block Matching Algorithm (BMA), which is one of the motion estimation algorithm was applied in the MPEG compression standard video processing. BMA partitions the current frame in small, fixed size blocks and matches them in the previous frame in order to estimate displacement of blocks between two successive frames. BMA provided motion vectors, which are then regularised using a Vector Median Filter. After the regularisation step, motion vectors are grouped based on their adjacency and similarity, and a set of vehicles is identified per singular frame. Finally, the algorithm establishes the correspondences between the vehicles detected in each frames. It considered the BMA output as the basic tracking information associated with each block and combine this information with the already available block-level tracking as a grouped output in order to achieve the desired result.

This paper is intended to detect and count vehicles using some video processing and image processing techniques. In this work, surveillance cameras are fixed at the top view on a particular road to capture all vehicle motions. Then, frame images are retrieved from the live video and vehicle regions are segmented by combining Gaussian Mixture Model based foreground detector and some morphological operations. After that, motion vehicle regions are appeared as foreground regions and counted.

The paper is organized as five sections. Introduction and some of previous works are presented in section 1. Background Theory is shown in section 2. In section 3, the proposed methodology is presented. The section 4 shows experimental results and the last section 5 is conclusion.

2. BACKGROUND THEORY

The proposed technique is one of the vehicle detection and counting to determine traffic congestion on a particular road. In this technique, Gaussian Mixture Model, Morphological opening, closing, filling and regional labeling are used to count the number of vehicles on a particular road. Hence, these theories and operations are discussed as theories background in this section as the following.

2.1 Gaussian Mixture Model

A Gaussian Mixture Model (GMM) is a parametric probability density function represented as a weighted sum of Gaussian component densities. GMMs are commonly used as a parametric model of the probability distribution of continuous measurements or features in a biometric system, such as vocaltract related spectral features in a speaker recognition system. GMM parameters are estimated from training data using the iterative Expectation Maximization (EM) algorithm or Maximum A Posteriori (MAP) estimation from a well-trained prior model.

These component functions are combined to provide a multimodal density. They can be employed to model the colours of an object in order to perform tasks such as real-time colour-based tracking and segmentation [5]. These tasks may be made more robust by generating a mixture model corresponding to background colours in addition to a foreground model, and employing Bayes' theorem to perform pixel classification. Mixture models are also amenable to effective methods for on-line adaptation of models to cope with slowly-varying lighting conditions.

Gaussian mixture models can also be viewed as a form of generalized radial basis function network in which each Gaussian component is a basis function or 'hidden' unit. The component priors can be viewed as weights in an output layer. Finite mixture models can be formulated as follow.

Let the conditional density for a pixel ε belonging to a multi-colored Φ be a mixture with M component densities:

$$p(\varepsilon|\Phi) = \sum_{j=1}^M P(\varepsilon|j)P(j) \quad \text{----- (1)}$$

Where, a mixing parameter $P(j)$ corresponds to the prior probability that pixel ε was generated by component j and where $\sum_{j=1}^M P(j) = 1$. Each mixture component is a Gaussian with mean μ and covariance matrix Σ , i.e. in the case of a 2D colour space:

$$p(\varepsilon|j) = \frac{1}{2\pi|\Sigma_j|^2} \exp^{-\frac{1}{2}(\varepsilon - \mu_j)\Sigma_j^{-1}(\varepsilon - \mu_j)} \quad \text{----- (2)}$$

The Gaussian Mixture models are a semi-parametric alternative to non-parametric histograms [6] and provide greater flexibility and precision in modeling the underlying statistics of sample data. They are able to smooth over gaps resulting from sparse sample data and provide tighter constraints in assigning object membership to colour-space regions. Such precision is necessary to obtain the best results possible from colour-based pixel classification for qualitative segmentation requirements. The following figure shows the three color segmentation from original multi-colored image using GMM.



Figure 1 Description of GMM color segmentation (a) original image and (b) three colored segmented image [9]

2.2 Morphological Opening, Closing and Filling

Morphology: a branch of biology that deals with the form and structure of animals and plants. Morphological image processing is a collection of non-linear operations related to the shape or morphology of features in an image. Morphological operations rely only on the relative ordering of pixel values, not on their numerical values, and therefore are especially suited to the processing of binary images. A morphological operation on a binary image creates a new binary image in which the pixel has a non-zero value only if the test is successful at that location in the input image. The fundamental operations of morphological image processing are dilation and erosion. There are morphological operations by combining erosion, dilation, and simple set-theoretic operations such as the complement of a binary image:

- Opening
- Closing
- Hit-miss transformation
- Thinning
- Regional Filling
- Boundary Extraction and etc.

2.2.1 Opening

In mathematical morphology, opening is the dilation of the erosion of a set A by a structuring element B :

$$A \circ B = (A \ominus B) \oplus B \quad \text{----- (3)}$$

Where \ominus and \oplus denote erosion and dilation, respectively.



Binary image f $f \circ s$ (5x5 square)
 Figure 2 Results of Opening with a Square Structuring Element [11]

Opening removes small objects from the foreground (usually taken as the bright pixels) of an image, placing them in the

background. Opening smooth the contour of an object, breaks narrow strips and eliminates thin protrusions (bulges). Hence, opening is so called because it can open up a gap between objects connected by a thin bridge of pixels. Any regions that have survived the erosion are restored to their original size by the dilation:

2.2.2 Closing

In mathematical morphology, the closing of a set (binary image) A by a structuring element B is the erosion of the dilation of that set,

$$A \cdot B = (A \oplus B) \ominus B \quad \text{----- (4)}$$

Where \ominus and \oplus denote erosion and dilation, respectively.

Closing is so called because it can fill holes in the regions while keeping the initial region sizes. Like opening, closing is dual operation of opening. In image processing, closing is, together with opening, the basic workhorse of morphological noise removal. Opening removes small objects, while closing removes small holes. Closing can sometimes be used to selectively fill in particular background regions of an image. Whether or not this can be done depends upon whether a suitable structuring element can be found that fits well inside regions that are to be preserved, but doesn't fit inside regions that are to be removed.

2.2.3 Regional Filling

Region filling is a Morphological algorithm in image processing, which deals with filling the region in the image with some colours. In a binary image, A denote the boundary points of a region and p is a point inside the boundary. To fill the entire region with 1s,

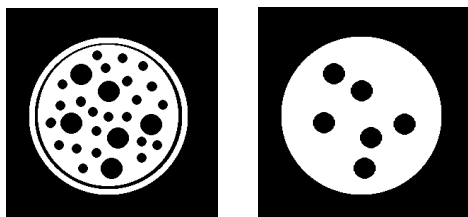
$$X_k = (X_{k-1} \oplus B) \cap A^c \quad \text{----- (5)}$$

Where, $X_0 = p$, B is the structuring element

Algorithm terminates if $X_k = X_{k-1}$ and Union of X_k and A is the region filled.

The image region can be selected in two ways:

- Interior region and
- Boundary region.



Binary image f $f \cdot s$ (22 pixel diameter disk)

Figure 3 Results of closing with a disk structuring element with 22 pixel diameter [12]

Interior regions are defined by assigning the same value to all the pixels inside that region. The algorithms used to change the values of all pixels in the interior regions to new values are FLOOD-FILL algorithms.

Boundary regions are defined by assigning the same value to all the pixels on the boundary of the region. Boundary region pixels and the interior region pixels should not have the same values. The algorithms used to change the value of all pixels

in boundary regions to new value are BOUNDARY-FILL algorithms.

2.2.4 Regional Labeling

Regional is an algorithmic application of graph theory, where subsets of connected components are uniquely labeled based on a given heuristic.

In the labeling process, connected components are scanned in an image and groups its pixels into components based on pixel connectivity, i.e. all pixels in a connected component share similar pixel intensity values and are in some way connected with each other. Once all groups have been determined, each pixel is labeled with a gray level or a color (color labeling) according to the component it was assigned to.

Regional labeling is used in computer vision to detect connected regions in binary digital images, although colour images and data with higher dimensionality can also be processed. When integrated into an image recognition system or human-computer interaction interface, connected component labeling can operate on a variety of information. Blob extraction is generally performed on the resulting binary image from a thresholding step, but it can be applicable to gray-scale and color images as well.

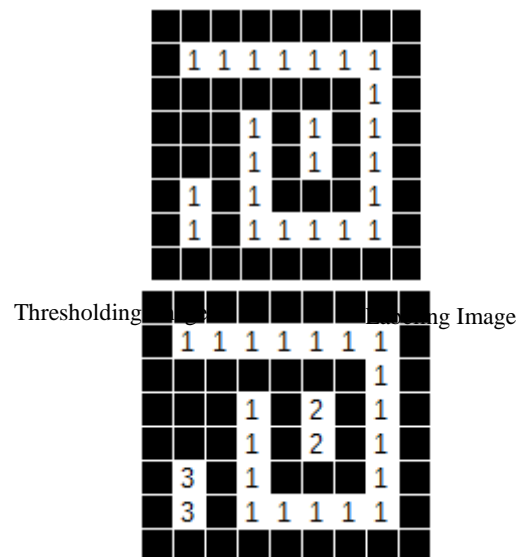


Figure 4 Results of Regional Labeling Process [13]

The above expressions are the fundamental theories of proposed technique in detecting and counting vehicles on a particular road. Using these theories, the following proposed method is implemented.

3. PROPOSED METHOD

This proposed method is divided into three main portions, image acquisition, pre-processing, vehicle detection and counting. The system flow diagram of the proposed method can be summarized as follow figure 5.

3.1 Frame Image Acquisition

Input video is captured by fixed camera which is about 6.5 m above a particular road. It can capture a video using 30 frame per second. Its coverage area is 50 feet of width and 100 feet of length. In this proposed method, not all frame with a second are processed. Only three frames (1st frame, 15th frame and

30th frame) are processed within a second to speed up vehicle detection process. Hence, in every 1/3 second, input frame image is captured by snapshot via camera and it is ready to later process.

3.2 Pre-processing

In detecting motion vehicles on the road, there are many challenges to confuse this detection process. Among them, shadows, light occlusions, dusts and other unwanted motion such as peoples and animals can be confused in detecting actual vehicle motions. To eliminate this unwanted environmental effects, pre-processing is necessary before motion detection.

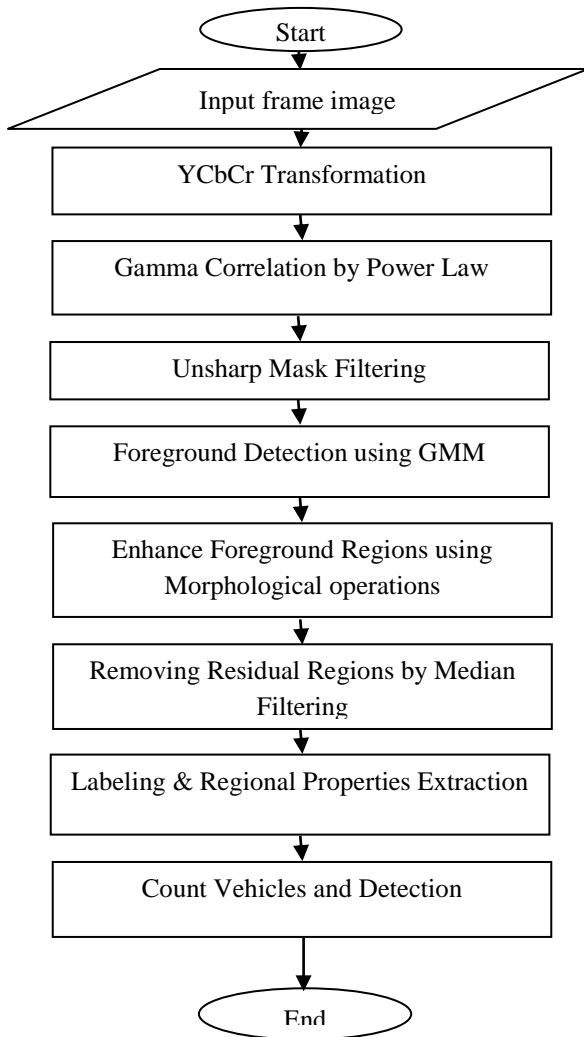


Figure 5 System flow diagram of proposed system

In this proposed system, input color image is converted into luminance Chrominance (YCbCr) color model and only used luminance channel to eliminate unwanted lighting occlusions. This channel image is only presented as intensity image. To eliminate unwanted light shadows and other wrong exposure effect, gamma correlation is adjust by power law transformation. It is very fast and ease technique to remove light shadows and eliminate heavy shadow. After that, to enhance the edges and textures of input image, unsharp mask filtering is applied. This filtering is actually the combination of original image and its edge image. Hence, the filter can give sharper edge image as its output. After finishing these

pre-processing operations, the image is ready for later vehicle detection processes.

3.3 Vehicle Detection and Counting

On the pre-processed frame image, foreground objects are detected and trained using Gaussian Mixture Model of Computer Vision Toolbox. The Gaussian Mixture Model (GMM) is already described in background theory about why it is use in this process.

Next, after the foreground objects detection using foreground detector, the gray scale frame image is changed again edge image. In the edge image, there are unconnected or broken edges and isolated edges. To connect broken edges and remove isolated edges, some morphological image processes are needed to perform. Hence, to modified and enhance the edges, morphological image operations such as “closing” and “opening” are applied. The first “closing” function can connect broken edges and the follower “opening” function can remove isolated edges. Thus, there are all connected edges are remained on the edge image.

Among them, some are closed boundary so they are needed to fill as regions. To fill close boundaries, the morphological operation, “image filling” is used. In the edge image, there may be more than one closed boundaries. These closed boundaries can be seen as regions. In these regions, to remove smaller regions and unwanted residual edges, median filter with larger kernel size (17x17) is used. After finishing the above processes, all of the black background objects except motion region can be removed on the frame image. By this ways, the motion regions are appeared as white regions on the black background.

The next process is to labeling the foreground motion region and produce regional properties, area, BoundingBox and etc. In this proposed system, the Matlab command “bwlabel()” is used to label the foreground regions. The operation of this function has already discussed in theories background section. The command is label all connected components of the foreground regions. The Matlab command “regionprops()” is used to measure each regional properties to point out motion object with BoundingBox. By using these two processes, the proposed system can retrieve geometrical features, regional area, BoundingBox of each foreground region from the static background. The numbers of foreground region can describe the numbers of vehicles. The proposed technique counts the numbers of vehicles by depending on the foreground region and its area. Sometime, the foreground region may be too large when two or more vehicles are very close. Hence, the proposed method is defined as minimum (1800 pixels) and maximum (1900 pixels) threshold area to describe whether a foreground region is a vehicle or not. As above expressions, the proposed method can count the numbers of vehicles for a particular lane on road. The accuracy and performance of the proposed technique can be seen with many experimental results.

4. EXPERIMENTAL FRSLT & DISCUSSION

This section is mainly focus on the performance and accuracy measurement of the proposed technique. The accuracy measurement is estimated by the following formula.

$$Accuracy (\%) = \frac{\text{numbers of correct tests}}{\text{numbers of total tests}} \times 100$$

To measure the performance and accuracy of the proposed technique, there are 20 testing in three different places which are main roads of Yangon. The following are some results images of vehicle detecting and counting.



Figure 6 Some Experimental Results of Vehicle Detection and Counting of the Proposed Technique

In the above figure 6, the first two pair of figures are shown count the numbers of vehicle. In the lower traffic jam figure, vehicles cannot count because these vehicles are very close each other.

Table 1 Accuracy Measurement of Vehicle Counting And Traffic Jam Determination

No	Testing	Actual no; of vehicle	Vehicle counting by proposed system	Accuracy of vehicle counting
1	Test 1	7	7	100%
2	Test 2	5	5	100%
No	Experiment	Actual no; of vehicle	Vehicle counting by proposed system	Accuracy of vehicle counting
3	Test 3	9	7	78%

4	Test 4	6	6	100%
5	Test 5	5	5	100%
6	Test 6	7	6	86%
7	Test 7	3	3	100%
8	Test 8	4	3	75%
9	Test 9	7	7	100%
10	Test 10	9	9	100%
11	Test 11	8	9	88%
12	Test 12	4	4	100%
13	Test 13	6	6	100%
14	Test 14	5	5	100%
15	Test 15	3	3	100%
16	Test 16	7	7	100%
17	Test 17	12	4	33
18	Test 18	16	7	43
19	Test 19	11	7	64
20	Test 20	9	5	65
			Over all accuracy	86.15%

To determine vehicle counting condition, the total lane area is pre-defined as 195086 reference unit (pixels) which is measured from figure. According to the segmented figure, total foreground area is 185328 pixels so it is over 85% of total road area. Hence, the proposed method determine that this situation of the place is occurred traffic jam. The following table show the accuracy of vehicle counting.

According to the above results and accuracy of table 1, the proposed technique achieved 86.15% of vehicle counting accuracy. In vehicle counting, the proposed technique make wrong counts when two or more vehicle are very close each other. At this situation, in the foreground object extraction, the close vehicles are remarked as one region so it gives wrong results. However, vehicles are always moving in every frame image, sequentially so these vehicle can definitely count other frame although current frame give wrong results. By the above 20 testing results, the proposed method give acceptable results and it can be reliable.

5. CONCLUSION

The proposed technique for automatic vehicle detecting and counting has been discussed and presented. According to the experimental results, the proposed technique gives over 86% accuracy in vehicle counting and detection. However, the proposed sometime give wrong results when two or more vehicles are very close together. Furthermore, vehicle counting and detection is based on segmented region so it can confuse and give wrong results whenever camera is shake or sometime light occlusion is occurred. To be more accurate, the vehicle classification method should be used. The research area of Intelligent Traffic Monitoring and Transportation Management is very interesting and currently on demand. Hence, our researches will continue on this area by trying better results and performance.

6. REFERENCES

- [1] Gupte, S. "Detection and Classification of Vehicles", University of Minnesota 2002.
- [2] Atkociunas, E. "Image Processing in Road Traffic Analysis", Vilnius University, 2005
- [3] Coifman, B. "A Real-Time Computer Vision System for Vehicle Tracking and Traffic Surveillance" University of California, 2005.
- [4] Di Stefano, L. "Vehicle Detection and Tracking Using the Block Matching Algorithm", Department of Electronics, Computer Science and Systems (DEIS) University of Bologna, ITALY.
- [5] Raja, Y. McKenna, S. and Gong, S. "Segmentation and tracking using colour mixture models," in Asian Conference on Computer Vision, Hong Kong, January 1998.
- [6] Bishop, C. "Neural Networks for Pattern Recognition," Oxford University Press, 1995.
- [7] <https://kittipatkampa.wordpress.com/2011/02/17/image-segmentation-using-gaussian-mixture-models/>
- [8] <https://www.mmorph.com/html/morph/mmopen.html/>
- [9] <https://homepages.inf.ed.ac.uk/rbf/HIPR2/close.htm>

Introduction to Interpolating Polynomial Curves

Kyaw Kyaw Than
Department of Engineering
Mathematics
Technological University
Thanlyin, Myanmar

Aye Aye Khine
Department of Mechanical
Engineering
Yangon Technological
University
Yangon, Myanmar

Wah Wah Aung
Department of Engineering
Mathematics
Technological University
Thanlyin, Myanmar

Abstract: This paper mentions the convex combinations and the convex hull of a set of points, and a brief and very informal introduction to parametric curves. The first method for curve construction, namely polynomial interpolation, is introduced in this paper.

Keywords:Polynomial interpolation, Cubic interpolating curves.

1. INTRODUCTION

Interpolation polynomials and Interpolating polynomial curves are fundamental tool for “Spline Interpolation”.

2. CONVEX COMBINATION AND CONVEXHULL

2.1 Convex Combination

A convex combination is described as

$$c = (1 - \lambda)c_1 + \lambda c_2 \quad (1.1)$$

c is said to be a convex combination of c_1 and c_2 .

Here, c_1 and c_2 are two given numbers and λ a given weight in the range $[0,1]$. The result of the computation is the number which must lie between c_1 and c_2 as average always do.

2.2 The Convex Hull of a Set of Points

If $c_1 = (x_1, y_1)$ and $c_2 = (x_2, y_2)$, then

(1.1), is usually implemented on a computer by expressing it in terms of convex combinations of real numbers

$$(x, y) = ((1 - \lambda)x_1 + \lambda x_2, (1 - \lambda)y_1 + \lambda y_2), \quad (1.2)$$

where $(x, y) = c$ and the weight λ is some number in the range $0 \leq \lambda \leq 1$.

As λ are all real numbers, the point c in (1.2) will pass through c_1 and c_2 as a whole straight line.

The convex hull, or the set of all weighted averages, of the two points c_1 and c_2 is the part of the line between these two points when $0 \leq \lambda \leq 1$.

$c = \lambda_1 c_1 + \lambda_2 c_2 + \dots + \lambda_n c_n$ is a convex combination of n points $(c_i)_{i=1}^n$

where $\sum_{i=1}^n \lambda_i = 1$, and $0 \leq \lambda_i$ for $i = 1, 2, \dots, n$.

The convex hull of two points is the straight line segment that connects the points, and the convex hull of three points can be identified with the triangle spanned by the points. In general, the convex hull of n points is the n -sided polygon with the points as corners.

3. POLYNOMIAL INTERPOLATION

3.1 Some Fundamental Concepts

The most natural curve to construct from given two points $c_0 = (x_0, y_0)$ and $c_1 = (x_1, y_1)$ is the straight line segment which connects the two points.

Generally, this line segment is expressed as

$$q(t|c_0, c_1; t_0, t_1) = \frac{t_1 - t}{t_1 - t_0} c_0 + \frac{t - t_0}{t_1 - t_0} c_1, \quad \text{for } t \in [t_0, t_1] \quad (1.3)$$

Here, t_0 and t_1 are two arbitrary real numbers with $t_0 < t_1$.

The two coefficients $\frac{t_1 - t}{t_1 - t_0}$, $\frac{t - t_0}{t_1 - t_0}$ add to one and each of them is non-negative as long as t is in the interval $[t_0, t_1]$.

Equation (1.3) is an example of a parametric representation.

If the variable t is denoted as time, the parametric representation $q(t|c_0, c_1; t_0, t_1)$ gives a way to travel from c_0 to c_1 . The parameter t_0 is described as the time at starting point c_0 and t_1 as the time at end point c_1 .

The speed of travel along the curve is given by the tangent vector or derivative $q'(t|c_0, c_1; t_0, t_1) = \frac{|c_1 - c_0|}{t_1 - t_0}$,

while the scalar speed or velocity is given by the length of the tangent vector $|q'(t|c_0, c_1; t_0, t_1)| = \frac{|c_1 - c_0| \sqrt{(x_1 - x_0)^2 + (y_1 - y_0)^2}}{t_1 - t_0}$.

3.2 Quadratic Interpolation of Three Points

The curve is constructed from given three interpolation points c_0, c_1 and c_2 , which is quadratic and also needs three parameters $(t_i)_{i=0}^2$. First, the two straight lines are described as $q_{0,1}(t) = q(t|c_0, c_1; t_0, t_1)$ and $q_{1,2}(t) = q(t|c_1, c_2; t_1, t_2)$

Then, the quadratic curve is

$$q_{0,2}(t) = q(t|c_0, c_1, c_2; t_0, t_1, t_2) \\ = \frac{t_2-t}{t_2-t_0} q_{0,1}(t) + \frac{t-t_0}{t_2-t_0} q_{1,1}(t) \quad (1.4)$$

Att = t_0 ,

$$q_{0,1}(t_0) = \frac{t_1-t_0}{t_1-t_0} c_0 + \frac{t_0-t_0}{t_1-t_0} c_1 = c_0$$

$$q_{0,2}(t_0) = \frac{t_2-t_0}{t_2-t_0} q_{0,1}(t_0) + \frac{t_0-t_0}{t_2-t_0} q_{1,1}(t_0) = q_{0,1}(t_0) = c_0$$

Thus, $q_{0,2}(t_0) = q_{0,1}(t_0) = c_0$

Att = t_1 ,

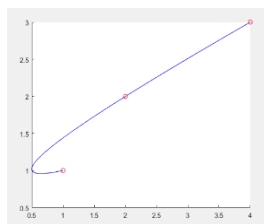
$$q_{0,1}(t_1) = \frac{t_1-t_1}{t_1-t_0} c_0 + \frac{t_1-t_0}{t_1-t_0} c_1 = c_1$$

$$q_{1,1}(t_1) = \frac{t_2-t_1}{t_2-t_1} c_1 + \frac{t_1-t_1}{t_2-t_1} c_2 = c_1$$

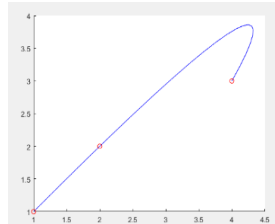
$$q_{0,2}(t_1) = \frac{t_2-t_1}{t_2-t_0} q_{0,1}(t_1) + \frac{t_1-t_0}{t_2-t_0} q_{1,1}(t_1) \\ = \frac{t_2-t_1}{t_2-t_0} c_1 + \frac{t_1-t_0}{t_2-t_0} c_1 = c_1$$

Att = t_2 , $q_{1,1}(t_2) = \frac{t_2-t_2}{t_2-t_1} c_1 + \frac{t_2-t_1}{t_2-t_1} c_2 = c_2$

$$q_{0,2}(t_2) = \frac{t_2-t_2}{t_2-t_0} q_{0,1}(t_2) + \frac{t_2-t_0}{t_2-t_0} q_{1,1}(t_2) = c_2$$



(a) $t = (0, 1.5, 2)$



(b) $t = (0, 0.25, 2)$

Figure 1.1 Some examples of quadratic

Note that the interpolation points are the same in plots (a) and (b). In this case of three points, the result of quadratic interpolation is clearly highly dependent on the choice of parameters. In plot (a) the value of t_1 is being height. Thus, the traveling from c_0 to c_1 takes more time than c_1 to c_2 . In plot (b) the value of t_1 has been lowered leaving more ‘time’ for traveling from c_1 to c_2 than from c_0 to c_1 . This makes the journey between these points longer

and someone traveling along the curve can therefore spend the extra time allocated to this part of the journey.

3.3 General Polynomial Interpolations

The two quadratic interpolants are

$$q_{0,2}(t) = q(t|c_0, c_1, c_2; t_0, t_1, t_2),$$

$$q_{1,2}(t) = q(t|c_1, c_2, c_3; t_1, t_2, t_3)$$

when the given points are $(c_i)_{i=0}^3$ and the choosing four parameters $t = (t_i)_{i=0}^3$.

Then, the cubic interpolant $q_{0,3}(t)$ is

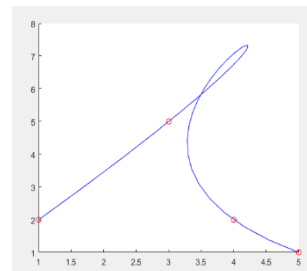
$$q_{0,3}(t) = \frac{t_3-t}{t_3-t_0} q_{0,2}(t) + \frac{t-t_0}{t_3-t_0} q_{1,2}(t)$$

Att = t_0 , $q_{0,2}(t_0) = c_0$

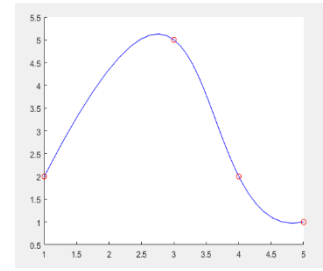
Att = t_3 , $q_{1,2}(t_3) = c_3$

At an interior t_i it is a convex combination of $q_{0,1}(t_i)$ and $q_{1,1}(t_i)$ which both interpolate c_i at t_i . Hence, $q_{0,3}(t_i) = c_i$ for $i = 1$ and $i = 2$ so $q_{0,3}$ interpolates the four points $(c_i)_{i=0}^3$.

Some examples of cubic interpolants are shown in Figure 1.2, and the same interpolation points are used in (a) and (b).



(a) $t = (0, 0.35, 2.75, 3)$



(b) $t = (0, 1.1, 2.25, 3)$

Figure 1.2 Some examples of cubic interpolation

By adjusting the parameters, quite strange behavior can occur, even with these ‘nice’ interpolation points. In Figure (a), there is so much time to ‘waste’ between c_1 and c_2 that the curve makes a complete loop.

In general, given $d + 1$ points $(c_i)_{i=0}^d$ and parameters $(t_i)_{i=0}^d$, the curve $q_{0,d}$ of degree d that satisfies $q_{0,d}(t_j) = c_j$ for $j = 0, 1, \dots, d$ is constructed by forming a convex combination between the two curves of degree $d - 1$ that interpolate $(c_i)_{i=0}^{d-1}$ and $(c_i)_{i=1}^d$,

$$q_{0,d}(t) = \frac{t_d-t}{t_d-t_0} q_{0,d-1}(t) + \frac{t-t_0}{t_d-t_0} q_{1,d-1}(t)$$

Thus, $q_{0,d}(t)$ can be written

$$q_{0,d}(t) = c_0 \ell_{0,d}(t) + c_1 \ell_{1,d}(t) + \dots + c_d \ell_{d,d}(t),$$

where the functions $\{\ell_{i,d}\}_{i=0}^d$ are the Lagrange polynomials of degree d given by

$$l_{i,d}(t) = \prod_{\substack{0 \leq j \leq d \\ j \neq i}} \frac{(t - t_j)}{t_i - t_j}$$

These polynomials satisfy the condition

$$l_{i,d}(t_k) = \begin{cases} 1, & \text{if } k = i \\ 0, & \text{otherwise} \end{cases}$$

which is necessary since $q_{0,d}(t_k) = c_k$.

4. Algorithm (Neville/Aitken Method)

Let d be a positive integer and let the $d + 1$ points $(c_i)_{i=0}^d$ be given together with $d + 1$ strictly increasing parameter values $t = (t_i)_{i=0}^d$. There is a polynomial curve $q_{0,d}$ of degree d that satisfies the conditions

$$q_{0,d}(t_i) = c_i \quad \text{for } i = 0, 1, \dots, d,$$

and for any real number t the following algorithm computes the points $q_{0,d}(t)$. First set $q_{i,0}(t) = c_i$ for $i = 0, 1, \dots, d$, and then compute

$$q_{i,r}(t) = \frac{t_{i+r} - t}{t_{i+r} - t_i} q_{i,r-1}(t) + \frac{t - t_i}{t_{i+r} - t_i} q_{i+r,r-1}(t)$$

for $i = 0, 1, \dots, d - r$, and $r = 1, 2, \dots, d$,

The computations involved in determining a cubic interpolation curve are shown in the triangular table in Figure 1.3.

The computations starts from the right and proceed to the left and at any point a quantity $q_{i,r}$ is computed by combining, in an affine combination, the two quantities at the beginning of the two arrows meeting at $q_{i,r}$. The expression between the two arrows is the denominator of the weights in the affine combination while the two numerators are written along the respective arrows.

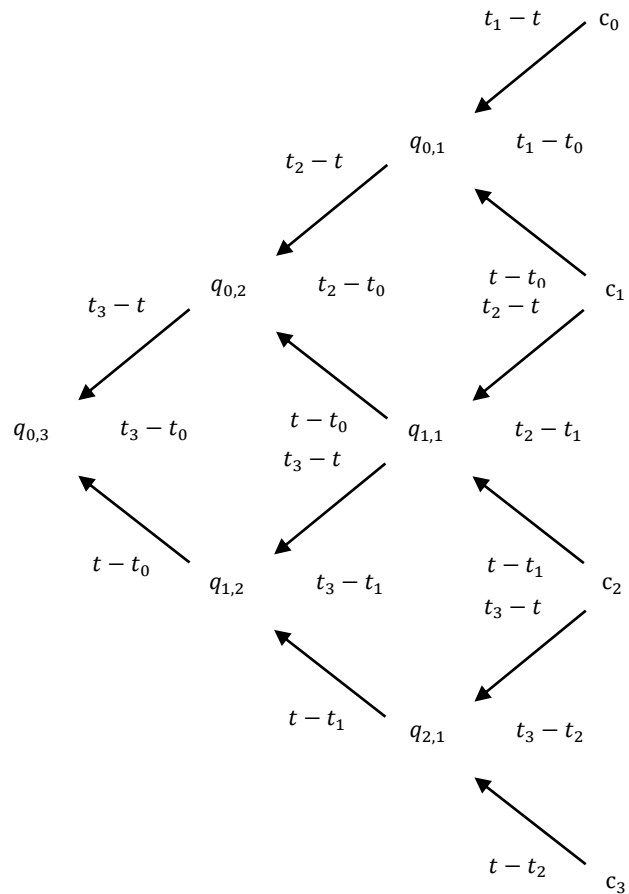
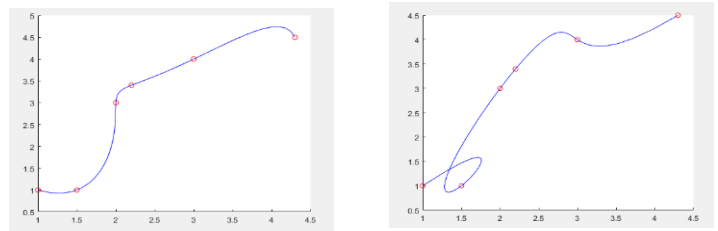


Figure 1.3. Computing a point on a cubic interpolating curve

Two examples of curves of degree five are shown in Figure 1.4, both interpolating same points.



(a) $t = (0, 0.35, 1.9, 2.8, 3.75, 5)$

(a) $t = (0, 1.1, 2.8, 3, 4.2, 5)$

Figure 1.4 Two examples of Interpolation with polynomial curves of degree five

5. CONCLUSION

We had presented polynomial interpolation and cubic interpolating curves that are fundamental background for “Spline interpolation”. Spline interpolation is applied to design the smoothness of shape of automobile, ships, and many others.

6. ACKNOWLEDGEMENTS

First, the authors would like to acknowledge the support of the papers for their references. The authors would like to acknowledge our parents and all our teachers throughout our studies.

7. REFERENCES

- [1] B.P. Demidovich, I.A. Maron, 1973, “Computational Mathematics”, Mir Publisher, Moscow.
- [2] Brian R. Hunt, Ronald L. Lipsman, Jonathan M. Rosenberg, “A Guide to MATLAB for Beginners and Experienced Users”, Cambridge University Press.
- [3] Keryszig, E., 1993, “Advanced Engineering Mathematics”, Eight Edition, John Wiley and Sons, Inc. New York.
- [4] Tom Lyche and Knut Morken, 2002, “Spline Methods Draft”, University of Oslo.

8. APPENDICES

Using the MATLAB, the interpolating curves are easily obtained.

Figure 1.1

```
Inter_curve=[];
t0=0;t1=1.5;t2=2;c0=[1 1];c1=[2 2];c2=[4 3];
for t=0:0.1:2;
    q01=(t1-t)/(t1-t0)*c0+(t-t0)/(t1-t0)*c1;
    q11=(t2-t)/(t2-t1)*c1+(t-t1)/(t2-t1)*c2;
    q02=(t2-t)/(t2-t0)*q01+(t-t0)/(t2-t0)*q11;
Inter_curve=[Inter_curve;q02];
axis on;
hold on;
plot(Inter_curve(:,1),Inter_curve(:,2),'b',[1 2 4],[1 2 3],'ro')
end
Inter_curve=[];
t0=0;t1=0.25;t2=2;c0=[1 1];c1=[2 2];c2=[4 3];
for t=0:0.1:2;
    q01=(t1-t)/(t1-t0)*c0+(t-t0)/(t1-t0)*c1;
    q11=(t2-t)/(t2-t1)*c1+(t-t1)/(t2-t1)*c2;
    q02=(t2-t)/(t2-t0)*q01+(t-t0)/(t2-t0)*q11;
Inter_curve=[Inter_curve;q02];
axis on;
hold on;
plot(Inter_curve(:,1),Inter_curve(:,2),'b',[1 2 4],[1 2 3],'ro')
end
```

Figure 1.2

```
Inter_curve=[];
t0=0;t1=0.35;t2=2.75;t3=3;c0=[1 2];c1=[3 5];c2=[4 2];c3=[5 1];
for t=0:0.1:3;
    q01=(t1-t)/(t1-t0)*c0+(t-t0)/(t1-t0)*c1;
    q11=(t2-t)/(t2-t1)*c1+(t-t1)/(t2-t1)*c2;
    q02=(t2-t)/(t2-t0)*q01+(t-t0)/(t2-t0)*q11;
    q21=(t3-t)/(t3-t2)*c2+(t-t2)/(t3-t2)*c3;
    q12=(t3-t)/(t3-t1)*q11+(t-t1)/(t3-t1)*q21;
    q03=(t3-t)/(t3-t0)*q02+(t-t0)/(t3-t0)*q12;
Inter_curve=[Inter_curve;q03];
```

```
axis on;
hold on;
plot(Inter_curve(:,1),Inter_curve(:,2),'b',[1 3 4 5],[2 5 2 1],'ro')
end
Inter_curve=[];
t0=0;t1=1.1;t2=2.25;t3=3;c0=[1 2];c1=[3 5];c2=[4 2];c3=[5 1];
for t=0:0.1:3;
    q01=(t1-t)/(t1-t0)*c0+(t-t0)/(t1-t0)*c1;
    q11=(t2-t)/(t2-t1)*c1+(t-t1)/(t2-t1)*c2;
    q02=(t2-t)/(t2-t0)*q01+(t-t0)/(t2-t0)*q11;
    q21=(t3-t)/(t3-t2)*c2+(t-t2)/(t3-t2)*c3;
    q12=(t3-t)/(t3-t1)*q11+(t-t1)/(t3-t1)*q21;
    q03=(t3-t)/(t3-t0)*q02+(t-t0)/(t3-t0)*q12;
Inter_curve=[Inter_curve;q03];
axis on;
hold on;
plot(Inter_curve(:,1),Inter_curve(:,2),'b',[1 3 4 5],[2 5 2 1],'ro')
end
```

Figure 1.4

```
Inter_curve=[];
t0=0;t1=0.35;t2=1.9;t3=2.8;t4=3.75;t5=5;c0=[1 1];c1=[1.5 1];c2=[2 3];c3=[2.2 3.4];c4=[3 4];c5=[4.3 4.5];
for t=0:0.1:5;
    q01=(t1-t)/(t1-t0)*c0+(t-t0)/(t1-t0)*c1;
    q11=(t2-t)/(t2-t1)*c1+(t-t1)/(t2-t1)*c2;
    q02=(t2-t)/(t2-t0)*q01+(t-t0)/(t2-t0)*q11;
    q21=(t3-t)/(t3-t2)*c2+(t-t2)/(t3-t2)*c3;
    q12=(t3-t)/(t3-t1)*q11+(t-t1)/(t3-t1)*q21;
    q03=(t3-t)/(t3-t0)*q02+(t-t0)/(t3-t0)*q12;
    q31=(t4-t)/(t4-t3)*c3+(t-t3)/(t4-t3)*c4;
    q41=(t5-t)/(t5-t4)*c4+(t-t4)/(t5-t4)*c5;
    q22=(t4-t)/(t4-t2)*q21+(t-t2)/(t4-t2)*q31;
    q13=(t4-t)/(t4-t1)*q12+(t-t1)/(t4-t1)*q22;
    q32=(t5-t)/(t5-t3)*q31+(t-t3)/(t5-t3)*q41;
    q23=(t5-t)/(t5-t2)*q22+(t-t2)/(t5-t2)*q32;
    q14=(t5-t)/(t5-t1)*q13+(t-t1)/(t5-t1)*q23;
    q04=(t4-t)/(t4-t0)*q03+(t-t0)/(t4-t0)*q13;
    q05=(t5-t)/(t5-t0)*q04+(t-t0)/(t5-t0)*q14;
Inter_curve=[Inter_curve;q05];
axis on;
hold on;
plot(Inter_curve(:,1),Inter_curve(:,2),'b',[1 1.5 2 2.2 3 4.3],[1 1 3 3.4 4 4.5],'ro')
end
```

```
Inter_curve=[];
t0=0;t1=1.1;t2=2.8;t3=3;t4=4.2;t5=5;c0=[1 1];c1=[1.5 1];c2=[2 3];c3=[2.2 3.4];c4=[3 4];c5=[4.3 4.5];
for t=0:0.1:5;
    q01=(t1-t)/(t1-t0)*c0+(t-t0)/(t1-t0)*c1;
    q11=(t2-t)/(t2-t1)*c1+(t-t1)/(t2-t1)*c2;
    q02=(t2-t)/(t2-t0)*q01+(t-t0)/(t2-t0)*q11;
    q21=(t3-t)/(t3-t2)*c2+(t-t2)/(t3-t2)*c3;
    q12=(t3-t)/(t3-t1)*q11+(t-t1)/(t3-t1)*q21;
    q03=(t3-t)/(t3-t0)*q02+(t-t0)/(t3-t0)*q12;
    q31=(t4-t)/(t4-t3)*c3+(t-t3)/(t4-t3)*c4;
    q41=(t5-t)/(t5-t4)*c4+(t-t4)/(t5-t4)*c5;
    q22=(t4-t)/(t4-t2)*q21+(t-t2)/(t4-t2)*q31;
    q13=(t4-t)/(t4-t1)*q12+(t-t1)/(t4-t1)*q22;
```

```
q32=(t5-t)/(t5-t3)*q31+(t-t3)/(t5-t3)*q41;  
q23=(t5-t)/(t5-t2)*q22+(t-t2)/(t5-t2)*q32;  
q14=(t5-t)/(t5-t1)*q13+(t-t1)/(t5-t1)*q23;  
q04=(t4-t)/(t4-t0)*q03+(t-t0)/(t4-t0)*q13;  
q05=(t5-t)/(t5-t0)*q04+(t-t0)/(t5-t0)*q14;  
Inter_curve=[Inter_curve;q05];  
axis on;  
hold on;  
plot(Inter_curve(:,1),Inter_curve(:,2),'b',[1 1.5 2 2.2 3 4.3],[1 1 3  
3.4 4 4.5], 'ro')  
end
```


Analysis of Thyristor Controlled Series Capacitor Performance in Power Flow Control for High Voltage Transmission Lines

Dr. Han Su Yin
Professor

Department of Electrical Power Engineering,
Yangon Technological University
Yangon, Myanmar

Shwe Zan Aung

Project and System Design Engineer
Omega Integration PTE Ltd
Singapore

Abstract: In modern days due to the ever increasing in demand for electric power, the transmission lines are usually required to operate under full load condition and, consequently, there is a higher impact to the power flow in case the large interconnected transmission networks encounter faults due to many factors. Changing loads and atmospheric conditions are unpredictable factors. This paper purposes power flow control between parallel lines by using Thyristor Controlled Series Capacitor (TCSC). It is a series controller from the flexible AC Transmission System (FACTS) family. It consists of back to back Thyristor. By changing the firing angle of this back to back Thyristor it is possible to vary the reactance of the TCSC. In this paper this device is used to regulate the transmission line reactance in order to share power flow if any disturbance occurs during the transfer of electric power. This device can also work continuously by solving the errors in transmission lines. The systematic procedure for modeling and simulation are proposed by using MATLAB/ Simulink. The optimal location of TCSC device is considered for power flow control. The proposed approach is carried out on two area test system.

Keywords: TCSC, FACTS, Power Flow, MATLAB, Thyristor

1. INTRODUCTION

Today's modern interconnected power system is highly complex in nature. One of the most important requirements during the operation of the electric power system is the reliability and stability. [1] Transmission system is very important in Myanmar because the generation system locates far away from load center. Recent development in power electronic introduces the use of flexible AC transmission system (FACTS) controllers in power systems. FACTS controllers are capable of controlling the network condition in a very fast manner. Among them TCSC is one of the important members of FACTS family. It can have various roles in the operation and control of power systems, such as scheduling power flow; decreasing unsymmetrical components; reducing net loss; providing voltage support limiting short-circuit currents; mitigating sub-synchronous resonance (SSR); damping the power oscillation and enhancing transient stability as well as sharing power flow between parallel lines. The main purpose of this paper is to control the equivalent impedance of transmission lines to share power flow among parallel lines under disturbances. [3] The placement of TCSC devices will be determined by using the load flow analysis i.e. Newton- Raphson method. [4]

The transmission system does not have the same power flow when there is a disturbance or increase in load demand or changes in system. This problem can be solved by using TCSC to regulate the power flow in AC transmission line. Power flow in Electrical system can be shared equally by adjusting reactance parameter of the transmission line. Figure 1 show a single line diagram of a simple transmission line with an inductive transmission reactance X_L , connecting to sending end voltage source V_s and receiving end voltage source V_r , respectively.

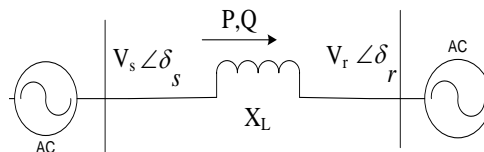


Figure 1. Two-Bus Transmission System [5]

The real power (P) flow at the receiving end is shown in equation (1).

$$P = \frac{V_s V_r}{X_L} \sin(\delta_s - \delta_r) \quad (1)$$

Where, V_s and V_r are the magnitude and δ_s and δ_r are the phase angles of the voltages, respectively. [5]

2. THYRISTOR CONTROLLED SERIES CAPACITOR (TCSC)

All Series Capacitors are installed in series with a transmission line. One of the significant devices from the group is a TCSC, which finds application in solving many problems in the power system. Its properties can increase the power lines transmission capacity, share power flow between the parallel lines and power flow control. TCSC is a FACT device available for application in AC line of voltage up to 500 kV. [1] The capacity is inserted directly in series with the transmission line and the thyristor controlled inductor is mounted directly in parallel with the capacitor. [3]

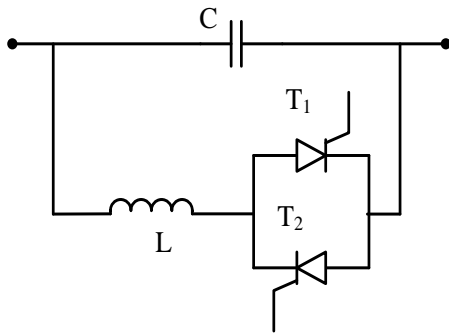


Figure 2. Simple Diagram of TCSC [3]

2.1 Operation of the TCSC

The value of the firing angle is required to be calculated for the operation of TCSC. But, this calculation involves an iterative process. One way to avoid these iterative processes is to use the alternative TCSC Variable Impedance Power Flow model presented in this section. The fundamental frequency equivalent reactance X_{TCSC} of the TCSC module is: [4]

$$X_{TCSC} = -X_C + C_1 \{2(\pi - \alpha) + \sin[2(\pi - \alpha)]\} - C_2 \cos^2(\pi - \alpha) \{ \omega \tan[\omega(\pi - \alpha)] - \tan(\pi - \alpha) \} \quad (2)$$

Where,

$$C_2 = \frac{4X_{LC}^2}{X_L \pi} \quad (3)$$

$$C_1 = \frac{X_C X_{LC}}{\pi} \quad (4)$$

$$X_{LC} = \frac{X_C X_L}{X_L - X_C} \quad (5)$$

$$\omega = \sqrt{\frac{X_C}{X_L}} \quad (6)$$

2.2 Modes of TCSC

There are essentially three modes of TCSC operation. They are Bypassed Thyristor Mode, Blocked Thyristor Mode (Waiting Mode), Partially Conduction Thyristor (Vernier Mode). Furthermore, Vernier Mode has Capacitive and Inductive Vernier Mode. [5]

Mode I (Bypassed Mode): The thyristor is gated for 180 degrees. The susceptance of the reactor is greater than capacitor. Most of the line current passes through reactor and thyristor valves. For protection of capacitor against overvoltage, this mode is used. [2]

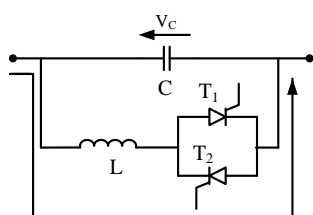


Figure 3. Bypassed Mode [5]

Mode II (Blocking Mode): No current pass through valves and gate pulses are blocked. The reactance of TCSC and fixed capacitor is similar.

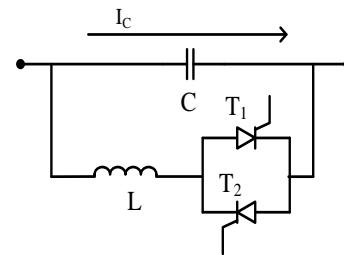


Figure 4. Blocking Mode [5]

Mode III (Vernier Mode): The Thyristor valves are operated by two gate pulses in the two regions, i.e. capacitive vernier region and inductive vernier region. [2]

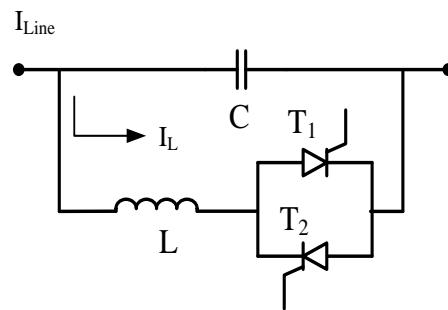


Figure 5. Inductive Mode [5]

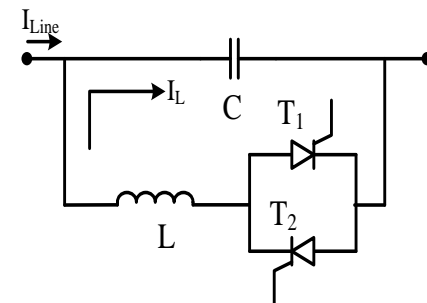


Figure 6. Capacitive Mode [5]

The natural characteristic of the series capacitor of compensated line cannot change by bypassing the series capacitor and high degree of compensation can cause sub synchronous oscillations. [2]

3. CASE STUDY

There are three transmission lines showing under study in Taungdwingyi substation. In this paper Taungdwingyi substation is sending end and Shwedaung substation is receiving end. Among them, 230 kV single Shwedaung line, 230 kV Shwedaung line 1 and 230 kV Shwedaung line 2 are studied. The line length of 230 kV Shwedaung line is 158.43 km and the line length of 230 kV Shwedaung line 1 & 2 is 168.168 km. The size of these cables is 605 MCM. This cable size can carry 773 A.

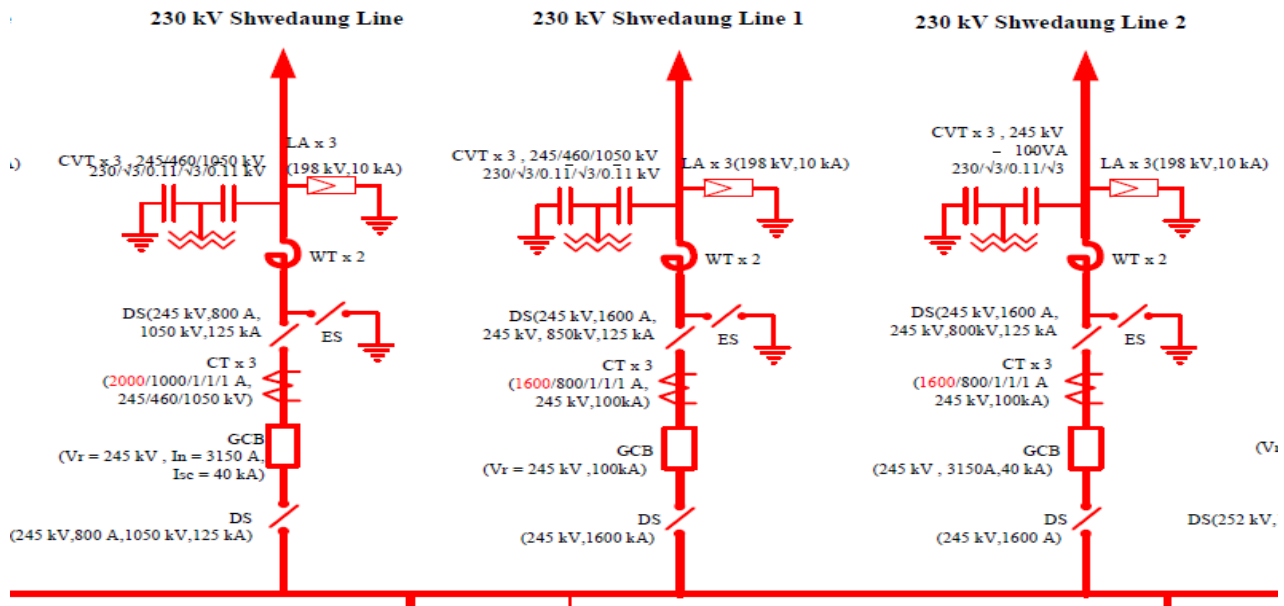


Figure 7. One Line diagram of Taungdingyi Substation showing Transmission Lines under Study

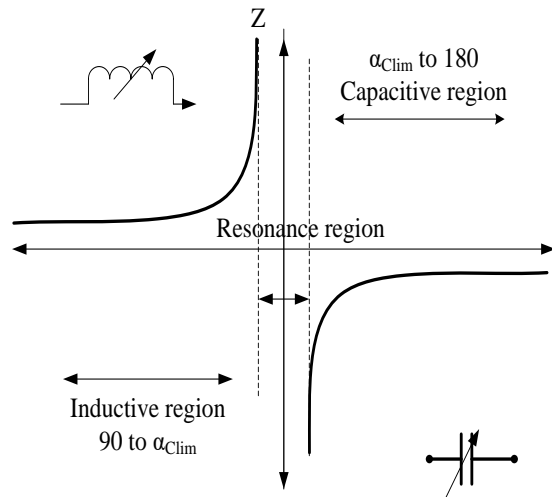


Figure 8. Impedance versus Firing Angle Characteristic of a TCSC [5]

3.1 Data Calculation of Taungdingyi-Shwedaung Old Line and the Existing System

Table 1 shows data calculation of Taungdingyi-Shwedaung old line and TCSC parameter. These data are required to calculate the rating and placement of TCSC. Figure 9 shows the existing system having both sending end and receiving end. These are connected with single old line and doubled new lines.

In proposed area there is unbalance power flow in parallel lines. The old line has higher power flow than new lines. But the power flows of new lines are balance. The purpose of this paper is to share the power flow between parallel lines. In order to share power flow, TCSC is used in proposed area. Figure 10 shows power flow in single old line and double new lines. Reactive power flow in single old line and double new lines is also shown in Figure 11. The magnitude of power in old line is 107.2 MW and the amount of power of new line 1 and 2 is 101.1 MW.

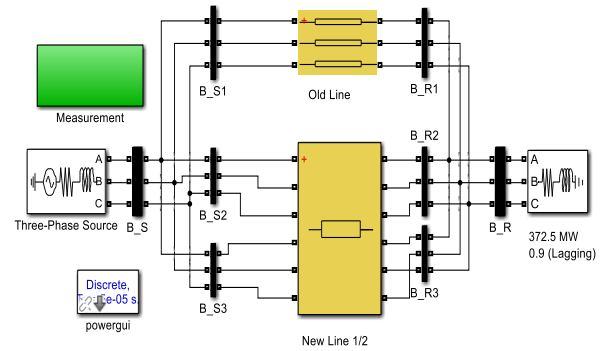


Figure 9. Simulink Model at Existing System

Table 1. Line Flow of Taungdingyi-Shwedaung Transmission Lines Substation

No.	Name	Average Power (MW)	Average Maximum Power (MW)	Average Minimum Power (MW)
1	Old Line	123.188	188.95	34.224
2	New Line1	115.204	188.344	31.814
3	New Line 2	118.113	182.726	31.23

Table 2. Data Calculation of Taungdingyi-Shwedaung Transmission Line and TCSC Parameters

No.	Name	Average Power (MW)
1	Line Reactance (XTCS) in old line	48.4 Ω
2	Capacitance reactance (XC)	18.15 Ω
3	Inductance reactance (XL)	72.6 Ω
4	Capacitance (C)	1.75337 x 10-4 F
5	Inductance (L)	0.23109 H
6	K (Compensation level)	50%

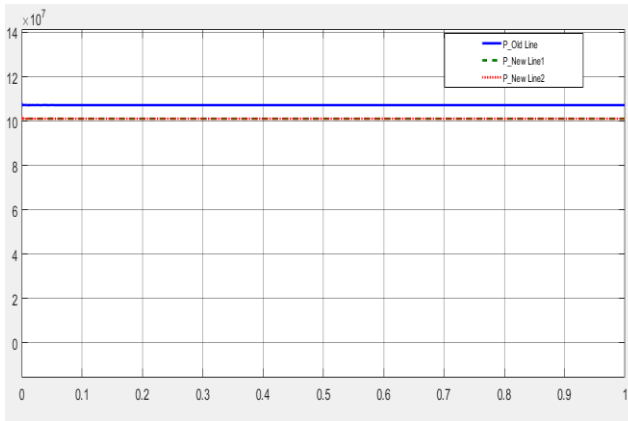


Figure 10. Power Flow Result of Existing System

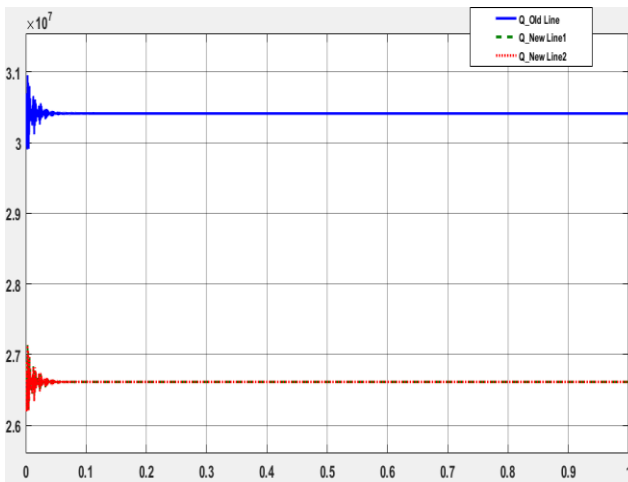


Figure 11. Reactive Power Flow in Existing System

4. TEST SYSTEM SIMULATION MODEL OF TCSC USING MATLAB/ SIMULINK

The source voltages of 230 kV are connected by a 158.43 km transmission old line and 168.168 km double new lines. The loads in area having 372.5 kW are chosen so that the real power flows on the transmission line from Taungdwingyi to Shwetaung. The TCSC used for this model is a phasor model. [1] Figure 12 shows Simulink model of TCSC in old line. To analyze the power control performance of TCSC under fault conditions, the fault is applied at the sending end of new line 2 as shown in Figure 12.

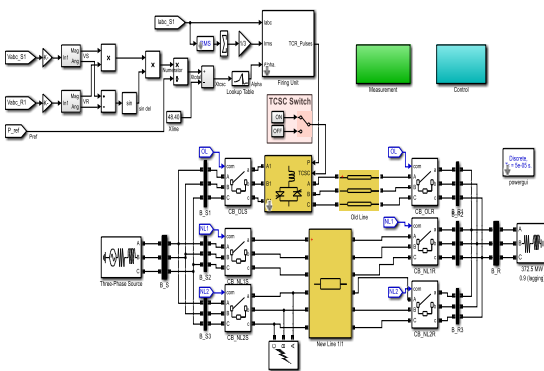


Figure 12. Simulink Model of TCSC in Old Line

4.1 Control Operation of TCSC

The TCSC may appear multi resonant points in 90 degrees to 180 degrees of α . Nevertheless, only one resonant point, namely one capacitive range and inductive range is allowable. Multiple resonant points will reduce the operating range of the TCSC. It is good for operating ω less than 3. Inductive region is from 90 degrees to 97 degrees. From 97.14 degrees to 107.9 degrees is resonant region and capacitive region is between 108 degrees and 160 degrees.

TCSC Controller Design: The TCSC controller consists two main operational blocks. They are an external and internal control. [7]

External Control: The external control may include different control loops depending on the control objectives which is accomplished either automatically with a PI controller or manually through direct operator intervention to regulate the transmitted power. The conventional PI controller attempts to minimize the power deviation (ΔP) which is difference of reference power (P_{ref}) signal and measured power (P_{means}) flowing through line and provides the impedance (X_0). [7]

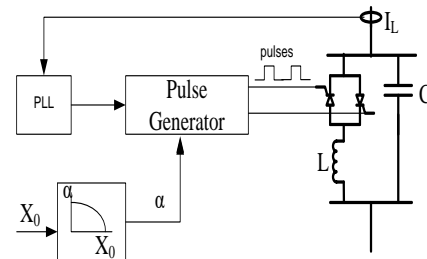


Figure 14. Internal Controller [8]

The internal control is shown in Figure 14. Then Figure 15, Figure 16, Figure 17 and Figure 18 are power flow and reactive power flow under fault condition without TCSC and with TCSC. By using TCSC, when fault occurs in new line 2 of sending end, the powers are shared by the remaining old line and new line 1. When there is fault occurring at the receiving end, power cannot flow through all three lines.

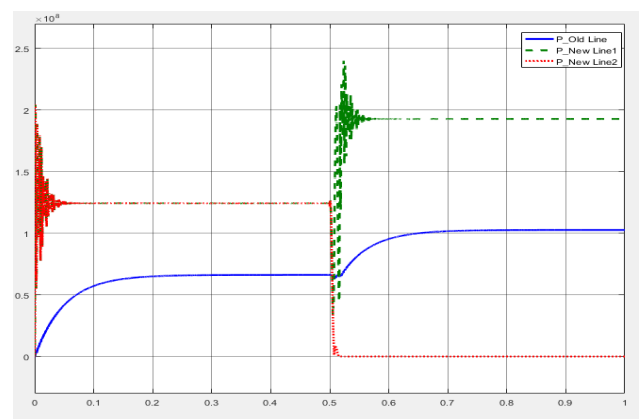


Figure 15. Real Power Flow under Fault Condition without TCSC

Figure 15 shows the real power flow under fault condition without TCSC. Power flows on the lines are not equal under normal condition as well as under fault condition. Power flow unbalance under fault is large. It is about 95.4 MW on old line and about 225 MW on new line 1. These unbalance in power will cause overload on new line 1. The same condition can be observed for reactive power flow without TCSC as shown in Figure 16.

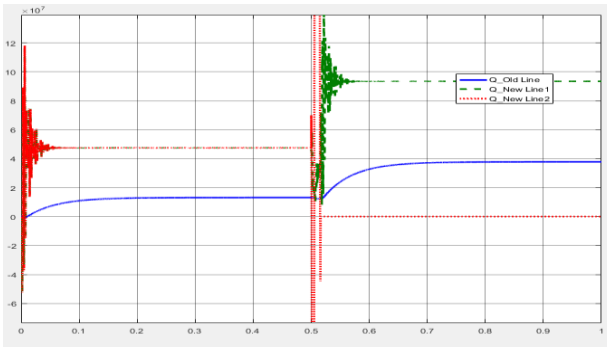


Figure 16. Reactive Power Flow under Fault Condition without TCSC

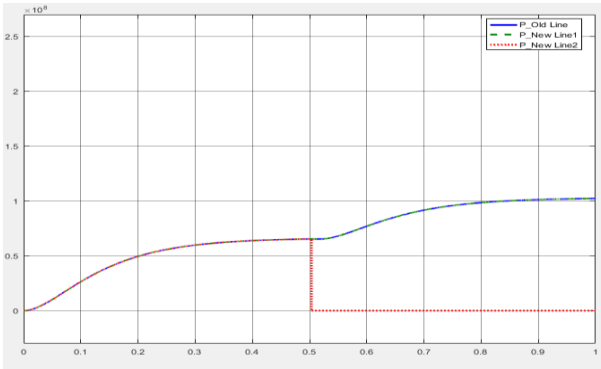


Figure 17. Power flow under Fault Condition with TCSC

To avoid overload on the line, the power flows on lines should be equal. Figure 17 and Figure 18 show the real and reactive power flow under fault condition with TCSC. As shown in these figures, the power flows on three lines are identical before fault condition. The active power is about 64.77 MW and reactive power flow is about 11.76 MVAR on each line before fault. When the fault occurred at new line 2, the active and reactive power flow on this line is drop to zero. Then the transferred power is served by the remaining two lines. With TCSC, the active powers on both remaining lines are equal with 102.3 MW and the reactive power flows are also identical with 11.89 MVAR. Thus the application of TCSC can control power flow under fault condition and overloading on one line is avoided.

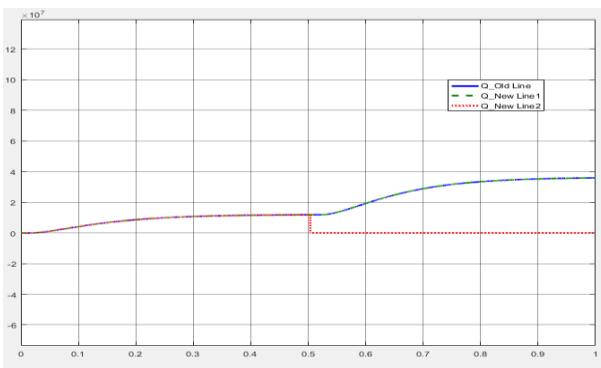


Figure 18. Reactive Power flow under Fault Condition with TCSC

5. CONCLUSION

In this paper, the analysis of power flow control between two ends of the transmission line to maintain power flow is studied. The study of TCSC device shows that this device controls the reactance of the system. The FACTS controller with its classification and performance of TCSC are included in this paper. To observe the power flow control performance

by TCSC, the fault is applied at one of three line and the flows on the remaining two lines are observed. Without TCSC, the old line has higher power flow than new lines and real/reactive power unbalances are about 129.6 MW/ 55.64 MVAR. With TCSC, the power flows of remaining unfaulted lines are balanced and the real/reactive power unbalances are nearly zero. Therefore, the power flow can be shared equally under fault condition by using TCSC.

6. ACKNOWLEDGEMENT

I would like to express my sincere appreciation to Taungdwingyi and Shwedaung Substations for their supports on data collecting. I also would like to acknowledge special thanks to all of my teachers, my seniors and colleagues from Department of Electrical Power Engineering for their support and encouragement towards this paper.

7. REFERENCES

- [1] Priyanka Kathal, Arti Bhandakkar, “Power Flow Control in Power System using FACT Device Thyristor Controlled Series Capacitor (TCSC)”, *Journal of Electrical and Electronics Engineering (IOSR-JEEE)*, Volume 7, Issue 6 (Sep-Oct-2013),72-83.
- [2] Anita Kanwar, Rachit Saxena, “Behavior of TCSC in Transmission Line using MATLAB / Simulation”, *International Journal of Innovative Research In Electrical, Electronics, Instrumentation and Control Engineering*, Volume 3, Issue 5, May 2015, 195-197.
- [3] Ravi Kant Kumar, Sanjeet Kumar, Santan Kumar and K.S.S. Prasad, “Design of Thyristor controlled series capacitor for high voltage controllability and flexibility,” *Middle-East Journal of Scientific Research* 20(1), 2014 134-138.
- [4] Mr. A. Hema Sekhar, Dr. A. Lakshmi Devi, “Performance Improvement of Transmission System using TCSC with Firing Angle Control,” *Journal of Theoretical and Applied Information Technology*, 15th September 2016. Volume 91, 177-188.
- [5] Priyanka Kathal, Arti Bhandakkar, “Power Flow Control in Power System using FACT Device Thyristor Controlled Series Capacitor (TCSC): A Review,” *International Journal of Science and Research (IJSR)*, India, 82-91, 388-395.
- [6] S.Meikandasivam, Rajesh Kumar Nema, Shailendra Kumar Jain, “Behavioral Study of TCSC Device – A MATLAB/Simulink Implementation”, *International Journal Of Electrical and Computer Engineering*, Volume 2, No. 9, 2008, 1958-1963.
- [7] Xiaotian Wang, 2016. “Coordination of Power Flow Control by using FACTS Device and HVDC Transmission System”. (A thesis submitted to Cardiff University in partial fulfillment of the requirements for the degree of MPhil, 2016)

Implementation of Microcontroller Based Smart Room

Thae Hsu Thoung
Lecturer
Technological University
Taunggyi, Myanmar

Aung Myo Htike
Lecturer
Technological University
Pyay, Myanmar

Dr. Zin Ma Ma Myo
Professor
Technological University
Thanlyin, Myanmar

Abstract: This paper describes the comfortable smart room control system. The system consists of room security, lighting control and appliances control. These individual sections can be controlled by simple 3×4 keypad. The proposed system is developed by PIC16F84A microcontroller. Assembly programming language is used to program the microcontroller and Proteus Design Suite 8.0 is used to simulate the design.

Keywords: PIC16F84A, microcontroller, 3×4 keypad, assembly programming language, Proteus Design Suite

1. INTRODUCTION

Fig.1 shows the block diagram of microcontroller based smart room. It is aimed to design a low-cost and ease of access system. The overall system can be divided into room security section, lighting control section and appliances control section. If only the correct password is entered, the door will be opened for room security. Lighting and home appliances can be switched on or off depending on the input key.

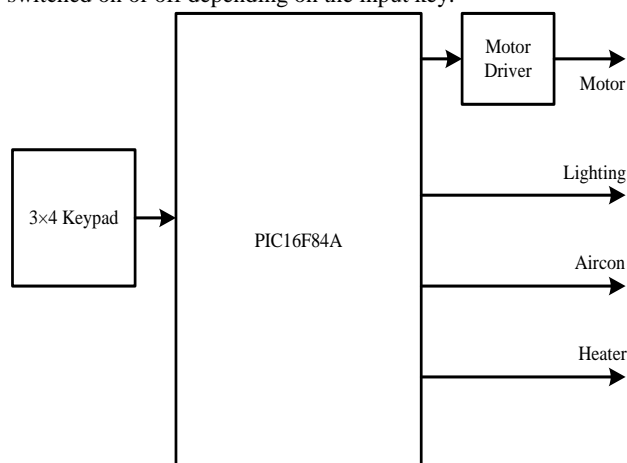


Figure. 1 Block diagram of control system for smart room

2. SYSTEM DESCRIPTION

2.1 Hardware Requirements

- 3×4 Keypad
- PIC16F84A Microcontroller
- Relay Unit
- Power Supply Unit
- Motor Driver
- Motor
- Home Appliances

2.2 Software Requirements

- MPLAB Integrated Development Environment (IDE)
- Proteus Design Suite 8.0
-

3. SYSTEM IMPLEMENTATION

The implementation programs can be categorized as follows:

- Study the relating theoretical background
- Consider the design requirements
- Design the components for the proposed system divided by three sections
- Consider the required assembly language program
- Assemble the program by using MPLAB IDE and correct the errors
- Simulate the overall system by using Proteus Design Suite 8.0

To reduce the number of I/O connections, keypads are usually arranged in a matrix format. A 12-key keypad is arranged in a 3×4 format requiring seven connections. [2] Fig.2 shows the 3×4 keypad.



Figure. 2 3×4 keypad [8]

Table 1 shows the column and row condition for 12-key keypad. Each of the column is connected to RB0, RB1 and RB2 pin of microcontroller. RB3, RB4, RB5 and RB6 are connected to the four rows.

Table 1 12-Key keypad

	Column1	Column2	Column3
Row1, R1	1	2	3
Row2, R2	4	5	6
Row3, R3	7	8	9
Row4, R4	*	0	#

The PIC16F84A belongs to the mid-range family of the PIC microcontroller devices. The program memory contains 1K words, which translates to 1024 instructions, since each 14-bit program memory word is the same width as each device instruction. The data memory (RAM) contains 68 bytes and data EEPROM is 64 bytes. [1]



Figure. 3 PIC16F84A microcontroller [9]

There are also 13 I/O pins that are user-configured on a pin-to-pin basis. Fig.4 shows the pin configuration of PIC16F84A microcontroller. [1]

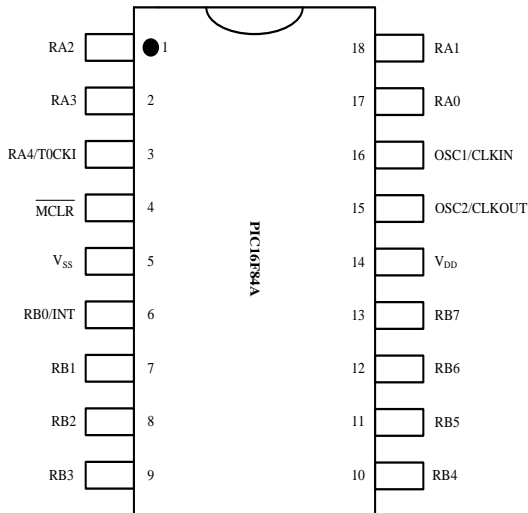


Figure. 4 Pin configuration of PIC16F84A microcontroller

The lighting unit is connected to RA0 via the relay circuit. The aircon unit is connected to RA1 whereas the heater is connected to RA2 pin. RA3 and RA4 pins are connected to motor driver. Fig.5 shows the key specification in program.

```

CHECKSUM: 430F
...
ORG 0
MOVF 0, RA0
MOVF 0, RA1
MOVF 0, RA2
MOVF 0, RA3
MOVF 0, RA4
...

```

Figure. 5 Key specification for lighting and appliances

After writing the assembly language program, converting it to machine language program by using MPLAB IDE assembler.

```

CHECKSUM: 00e2d4
...
MOVF 0, RA0
MOVF 0, RA1
MOVF 0, RA2
MOVF 0, RA3
MOVF 0, RA4
...

```

Figure. 6 Assembly language program

The configuration bits are specified according to the system as in Fig.7. Then the program is built to produce the machine code: HEX file. Fig.8 shows the successful message of building process.

Address	Value	Field	Category	Detail
2000	0000	CONFIGURATION	CONFIGURATION	
		WDT	WDT	WDT Disabled
		POWERUP	POWERUP	Power-up Timer Enabled
		CODE	CODE	Code Protection Disabled

Figure. 7 Configuration bits for the proposed system

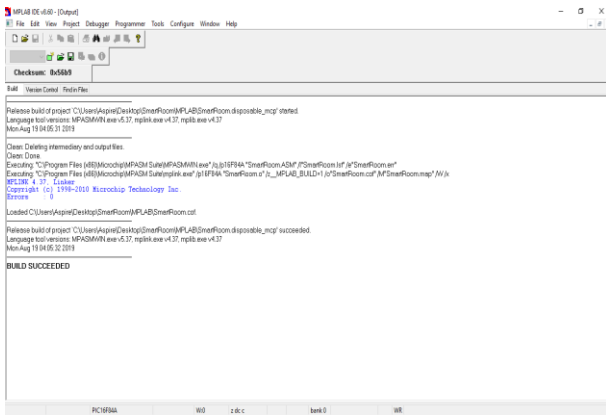


Figure 8 Building process

To simulate the design, sketch the design by using Proteus software. Then the machine code produced by assembler is inserted into microcontroller. Fig.9 shows the schematic diagram of proposed system.

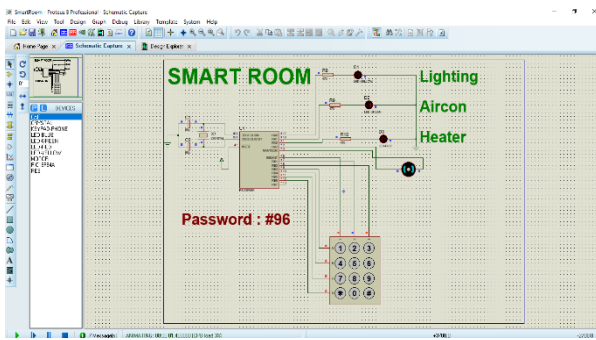


Figure.9 Schematic diagram of proposed system

4. SYSTEM FLOWCHART

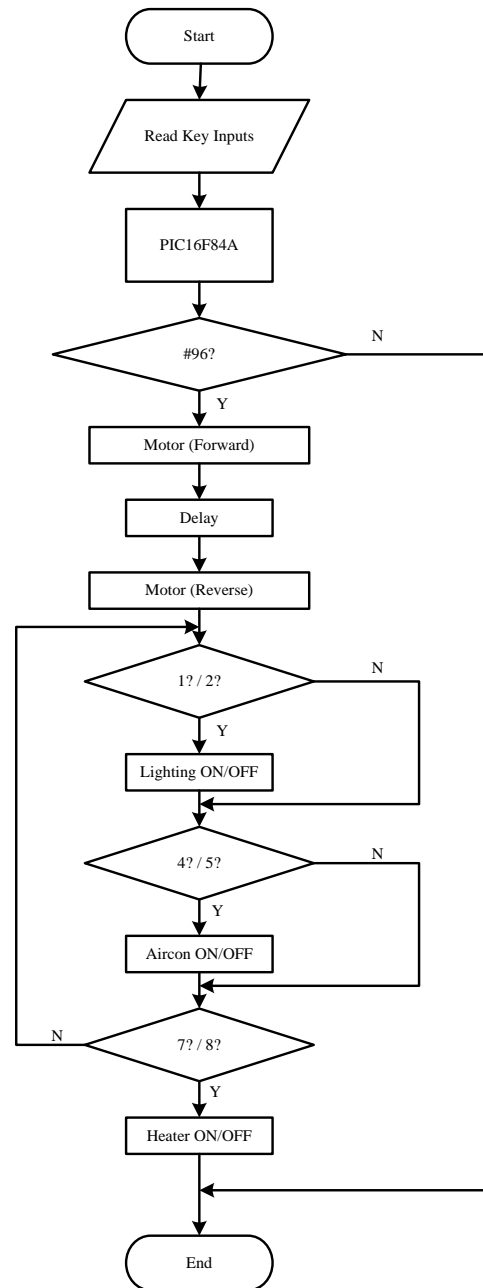


Figure. 10 Flowchart of smart room

The overall flowchart is shown in Fig.10. The security password is #96. The door will be opened only the correct password is entered. Lighting and appliances will be ON or OFF according to the PORTB inputs.

5. SIMULATION RESULTS

If the correct password (#96) is entered, the motor will be rotated in forward direction to open the door. After delay time the door will be automatically closed.

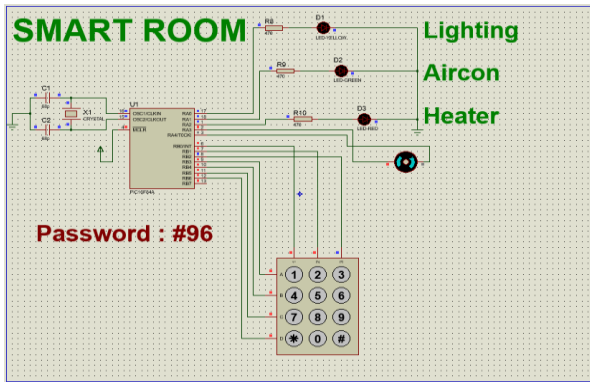


Figure. 11 Motor condition if correct password (#96) is pressed

If key 1 is pressed, the lighting unit will be switched “ON” and it will be switched “OFF” when key 2 is pressed.

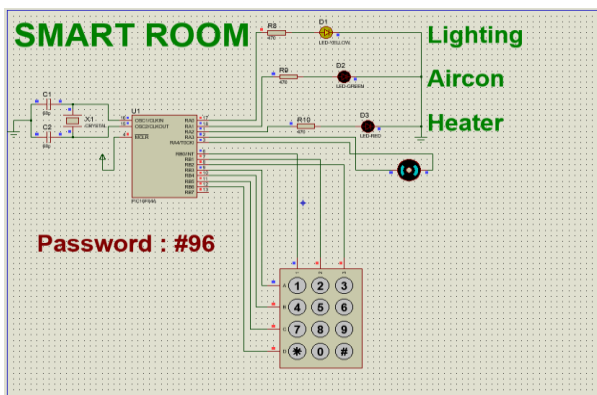


Figure. 12 Lighting condition

If key 4 is pressed, the aircon will be switched “ON” and it will be switched “OFF” when key 5 is pressed.

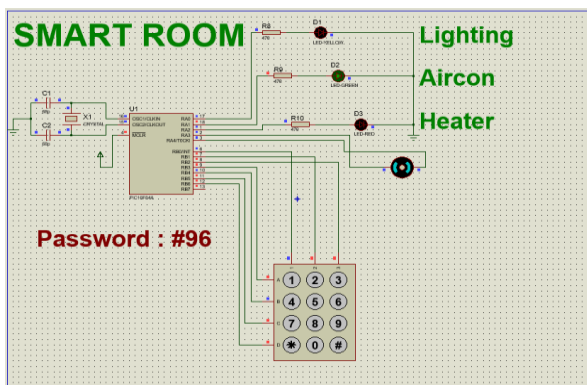


Figure. 13 Aircon condition

If key 7 is pressed, the heater will be switched “ON” and it will be switched “OFF” when key 8 is pressed.

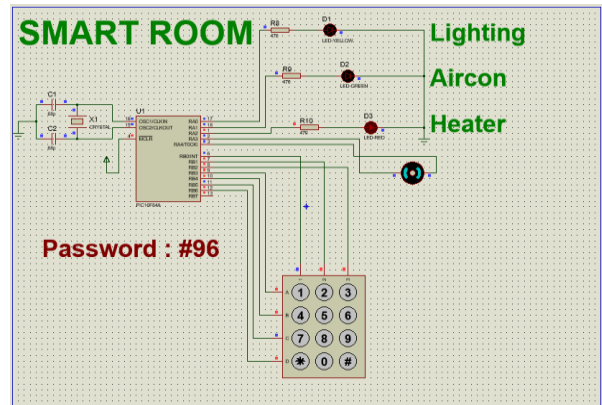


Figure. 14 Heater condition

6. CONCLUSIONS

The control system for smart room was designed and implemented. This system was composed of home security, lighting control and appliance control. It was used microcontroller (PIC16F84A) and keypad. MPLAB IDE was used to assemble the program and Proteus design suite was used to simulate the design.

7. ACKNOWLEDGMENTS

The author wishes to express her deep gratitude to Dr. Zin Ma Ma Myo, Professor and Head, Department of Electronic Engineering, Technological University (Thanlyin), for her permission and the support. The author is also indebted to all of her teachers in the Department of Electronic Engineering, who contributed their knowledge and support during the study and research periods. A special note of thank is also intended to Dr. Thet Mon Aye, Lecturer, Department of Electrical Power Engineering, West Yangon Technological University, who helped her with necessary assistance for her research.

8. REFERENCES

- [1] Microchip Technology Inc. , (2001), “PIC 16F84A Datasheet”
- [2] Di Jasio, Wilmshurst, Ibrahim, Morton, Bates, J.Smith, Hellebuyck, (2008), “PIC Microcontrollers”
- [3] Assaf, M.H, “Sensor based home automation and security system”, Instrumentation and Measurement Technology Conference (I2MTC), 2012 IEEE International
- [4] Usha Devi, Y, (2012), “Wireless Home Automation System Using Zigbee, International Journal of Scientific & Engineering Research ,Volume: 3, Issue: 8
- [5] Lakhya, Inder, Emanuel, Abhijit, Lalan, Debaraj, M. Sujitha, (2012), “Home Automation System Based on Arm and Zigbee”, Undergraduate Academic Research Journal (UARJ), Volume: 1, Issue: 3,4
- [6] Dhawan S. Thakur and Aditi Sharma, (2013), “Voice Recognition Wireless Home Automation System Based on Zigbee”, IOSR – JECE, Volume: 6, Issue: 1
- [7] https://en.wikipedia.org/wiki/Home_automation
- [8] <https://www.sparkfun.com/products/14662>
- [9] <https://www.microchip.com/wwwproducts/en/PIC16F84A>

Performance Analysis of Dynamic Voltage Restorer for Voltage Sag and Swell Compensation in Distribution System

Dr. Han Su Yin
Professor

Department of Electrical Power Engineering,
Yangon Technological University
Yangon, Myanmar

Shwe Zan Aung

Project & System Design Engineer
Omega Integration PTE Ltd
Singapore

Abstract: Nowadays, most of the electrical loads are concerned about the power quality. Power quality problems include voltage sags/swell, transient interrupts and harmonic distortions in sinusoidal waveforms. Modern industrial devices are mostly based on electronic devices such as programmable logic controllers and electronic drives. These electronic devices are very sensitive to disturbances and become less tolerant to power quality problems such as voltage sags, swells and harmonics. Voltage dips are considered to be one of the most severe disturbances to the industrial equipment. In this paper, voltage sag/swell study is carried out for Myaungtagar industrial zone where the steel mills are the main loads. Due to furnaces and large motor drives, the voltage sag/swell is the common problems in this system. To mitigate these voltage sag/swell problems, the Dynamic Voltage Restorer (DVR) is introduced for this system. Dynamic Voltage Restorer (DVR) is a series connected power electronics based device that can quickly mitigate the voltage sag in the system and restore the load voltage to the nominal value. In this paper, modeling and analysis of Dynamic Voltage Restorer (DVR) is presented which will use for voltage sag/swell compensation. Modeling and simulations are carried out with Matlab/Simulink.

Keywords: Voltage regulation, Voltage sag, Voltage swell, Dynamic Voltage Restorer, Hysteresis Control

1. INTRODUCTION

Power distribution systems should provide their customers with an uninterrupted power supply at smooth sinusoidal voltage at the contracted magnitude level and frequency. However, power distribution systems have numerous nonlinear loads which significantly affect the quality of power supplies. The waveform of the supply system may lose purity of sinusoidal due to the nonlinear loads. This ends up producing many power quality problems. Apart from nonlinear loads, some system events, both usual (e.g. capacitor switching, motor starting) and unusual (e.g. faults) could also suffer power quality problems. [1]

In modern distribution system, the substantial pollution and abnormal operating conditions can cause the number of voltage-based power quality (PQ) problems. These power quality problems at point of common coupling (PCC) occur due to the voltage drop in feeders and transformers, faults, use of unbalanced lagging power factor consumer loads, various kinds of disturbances, and so on. Some of these voltage-related power quality problems are surges, flickers, sags, swells, notches, fluctuations, voltage imbalance, waveform distortion, and so on. The active series compensators are extensively used to both inject the voltage of required magnitude and frequency and restore the voltage across the loads to protect the sensitive loads from these voltage quality problems. Solid-state synchronous series compensators (SSCs) and dynamic voltage restorers (DVRs) are known as compensators. [2]

The DVR is a series connected power electronics based device, which can protect the system against the bulk of these disturbances, i.e. voltage sags and swells related to remote system faults. A DVR can compensate for these voltage

excursions, provided that the supply system does not get disconnected entirely through breaker trips. The control systems of a DVR for main considerations are including such as: sag detection, voltage reference generation and transient and steady-state control of the injected voltage. The typical power quality disturbances are voltage sags, voltage swells, interruptions, harmonics and transients. Among the disturbances, voltage sag is considered the most severe since the sensitive loads are very susceptible to temporary changes in the voltage. [3]

2. VOLTAGE REGULATION AND SAG/SWELL IN DISTRIBUTION SYSTEM

Modern power systems operate at some standard voltages. The equipment working on these systems are therefore given input voltages at these standard values, within certain agreed tolerance limits. It is necessary to quantify the drop that takes place inside a transformer when certain load current, at any power factor, is drawn from its output leads. This drop is termed as the voltage regulation and is expressed as a ratio of the terminal voltage. [5] For proper operation of the electrical loads, the voltage regulation should be within $\pm 10\%$ of nominal voltages at distribution level.

$$\text{Voltage Regulation} = \frac{|V_{nl}| - |V_{fl}|}{|V_{nl}|} \quad [5]$$

2.1 Voltage Sag:

The voltage sag is a decrease to between 0.1 and 0.9 pu in rms voltage or current at the power frequency for durations from 0.5 cycle to 1 min [5]. The voltage signal with sag waveform is shown in Figure 1. Sometime, voltage sag last for long duration such prolonged low voltage profile referred as

‘under-voltage’. Voltage sag is further divided in three categories: instantaneous, momentary and temporary sags respectively. [6] In distribution system, voltage sag conditions can be occurred due to occurrence of faults in power system, excessive loads, starting of large induction motors, the electric furnaces and electrical faults. Voltage sag in power system network results in failure of relays and contactor, dim light and fluctuating power.

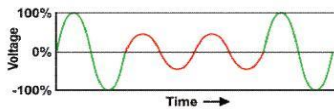


Figure 1. Voltage Signal with Sag Waveform

2.2 Voltage Swell:

Voltage swell is defined as an increase between 1.1 and 1.8 pu in rms voltage or current at the power frequency for durations from 0.5 cycle to 1 min. [5] The voltage signal with swell is shown in Figure 2. Likewise voltage sag, prolonged high voltage profile is referred as ‘over-voltage’. Voltage swell is subdivided as: instantaneous swell, momentary swell, temporary swell. [6] In distribution system, voltage swell conditions can be occurred due to capacitor bank switching, turning on of lightly loaded lines and sudden turning off of large loads as well as Single line to ground fault (SLG) which can result in voltage rise in un-faulted phases and loose connection of neutral wire. Voltage swells results in breakdown of insulation, overheating of electrical equipment and damage to electronic equipment.

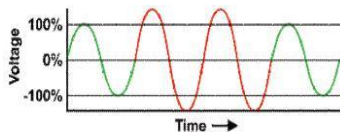


Figure 2. Voltage Signal with Swell Waveform

3. MITIGATION TECHNIQUES FOR VOLTAGE SAG/SWELL

Power devices have proven to be an attractive solution to the voltage sag/swell problem. Different solutions for improving the performance of the power system, as well as the immunity of the equipment, are described. Finally, mitigation devices to be installed at the system-load interface for power quality enhancement are DVR (Dynamic Voltage Restorer), UPS (Uninterruptible Power Supply), D-STATCOM (Distribution Static Synchronous Compensator) and so on.

3.1 Advantages of DVR

DVR is cheaper than D-STATCOM and UPS. UPS requires a lot of maintenance which may be due to problems of battery leakage and replacement. D-STATCOM is more complex to control and maintain than DVR. DVR is smaller in size and is a better power effective device as compared to others link UPS, and D-STATCOM. Therefore, this paper emphasize on the DVR for voltage sag/swell compensation.

4. CONSTRUCTION AND OPERATION OF DVR

A DVR is a custom power device used at distribution level. The DVR is implemented using voltage source converter (VSC) with fast switching power semiconductor devices such as IGBT or IGCT. The voltage injected by VSC in series with distribution feeder is controlled by using Hysteresis control technique. The rapid switching capability provided by IGBT

enables the use of more sophisticated control technique to provide dynamic compensation to sag and swell.

4.1 Basic Structure:

The DVR is a series connected power electronic device used to inject voltage of required magnitude and frequency. The basic structure of a DVR is shown in Figure 3. It contains the following components:

- Voltage Source Converter (VSC)
- DC storage unit
- Filter circuit
- Series Transformer

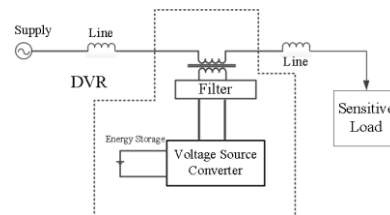


Figure 3. Schematic Diagram of Dynamic Voltage Restorer (DVR)

4.1.1 Voltage Source Converter (VSC):

A VSC is a power electronic system consists of a storage device and switching devices, which can generate a sinusoidal voltage at any required frequency, magnitude, and phase angle. In the DVR application, the VSC is used to temporarily replace the supply voltage or to generate the part of the supply voltage which is missing [7]. The VSC consists of solid state switches like IGBT's or GTO's used to convert the DC input to AC. It is used to inject the AC voltage to compensate the decrease in the supply voltage. The switches of the VSC are operated based on the gate pulses supplied from the drive circuits via PWM or hysteresis controller.

4.1.2 DC Storage Unit:

The storage unit may consist of batteries, capacitors, flywheel, or super magnetic energy storage (SMES). For DVR with internal storage capacity, energy is taken from the faulted grid supply during the sag. Here, a rectifier is used to convert the AC voltage from the grid to DC voltage required by the voltage source converter. [4]

4.1.3 Filter Circuit:

A filter circuit consists of an inductor and capacitor. It is used to filter out the switching harmonic components from the injected voltage. An LC filter is connected at the output of the VSC to filter the harmonics that are present in the output voltage of VSC. Filter has a small rating, approximately 2% of the load MVA connected to delta-connected tertiary winding of the injection transformer. [1]

4.1.4 Series Transformer:

A series transformer is used to connect the DVR with the distribution feeder. In case of three phase system, three single phase transformers are used to connect the DVR with the power network. [4]

4.2 The DVR Operation Modes

The basic operation principle of DVR is measuring the missing voltage by using control unit and injecting the dynamically controlled missing voltage in series to the line and providing the load voltage unchanged during sag. The phase angle and amplitude of the injected voltage are variable during sag. This will allow the control of active and reactive power exchange between the DVR and the distribution system. Generally, the operation of the DVR can be

categorized into three operation modes: protection mode, standby mode (during steady state) and injection mode (during sag).

5. INDUSTRIAL DISTRIBUTION SYSTEM UNDER STUDY

In this paper, the case study area is chosen at Myaungtagar industrial distribution zone. It has seventeen feeders. Eight feeders are connected with 230kV/33kV 100MVA step-down transformer, five feeders are connected with 230kV/33kV, 60MVA step-down transformer, and four feeders are connected with 230kV/33kV, 150MVA transformer respectively.

This paper is emphasized on 100MVA transformer side in which the power quality problem occurs due to industrial loads such as steel mill loads. The single line diagram of case study area is shown in Figure 4. The names of the feeders are Zone 1, Zone 2, Zone 3, Zone 4, Zone 5, Zone 6, Fertilizer 1, and Fertilizer 2 respectively.

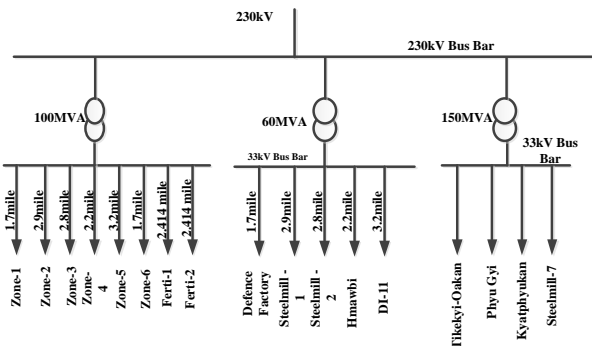


Figure 4. Single Lind Diagram of Case Study Area

6. MODELING OF DVR

Figure 5 shows the demand power of eight feeders for a typical day in the existing system of case study area. According to this load demand graph, power consumption of the system is rising during 8 am to 4 pm in the peak hour of the day. Maximum load consumption is between 11 am to 1 pm as per the graph.

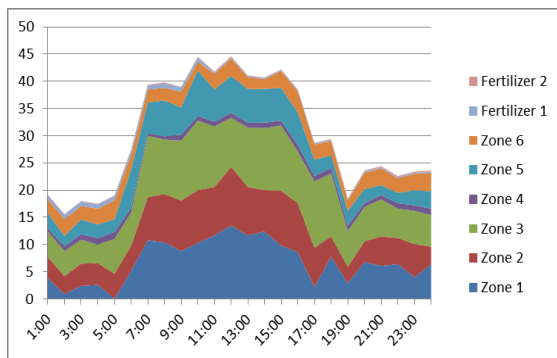


Figure 5. Demand Power of Eight Feeders for a Typical Day

Table 1 describes the parameter of the simulation model for the existing system of the case study area. This table includes the active power, reactive power and line length of each feeder for the case study area. Among the eight feeders, Zone 1, Zone 2 and Zone 3 have the highest load demand. Fertilizer 1 and Fertilizer 2 have the minimum value of the active and reactive power. These data are collected from Myaungtagar

Industrial Distribution Substation base on the load consumption of May, 2018.

Table 1. Parameter of Simulation Model

Feeders	Line Length (km)	Reactive powers (MVAR)	Active powers (MW)
Zone 1	2.735885	3.65998	6.89708
Zone 2	4.6671	4.80004	6.36667
Zone 3	4.50616	4.874777	8.30833
Zone 4	3.540557	0.72029	0.93333
Zone 5	5.1499	3.33267	4.25833
Zone 6	2.73588	1.91355	2.75
Ferti 1	2.41402	0.2179	0.45
Ferti 2	2.41402	0.0605	0.1458

Figure 6 describes the modeling of the existing system when fault occurs at the load side. The case study area of the industrial distribution system source voltage 230kV is connected with 230kV/33kV step down transformer. The outgoing of the step down transformer distribute the voltage for the eight feeders.

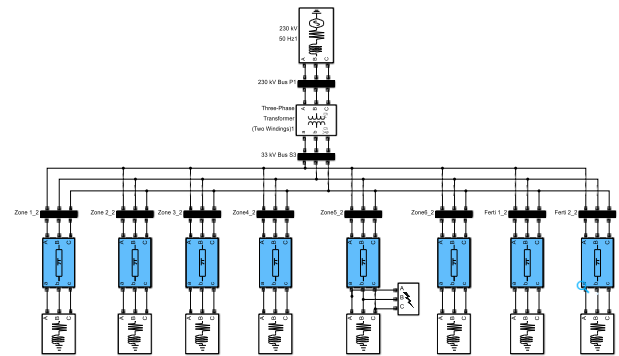


Figure 6. Existing System When Fault occurs at load side

7. PERFORMANCE ANALYSIS FOR SAG/SWELL COMPENSATION

In the performance analysis for the voltage sag/swell simulation of modeling the existing system, we will consider two options. For the voltage sag condition, the system have various fault conditions occurs at the load side and for the voltage swell condition, the capacitive load is connected to the system. For the voltage sag condition, the fault is applied at Zone 5 which is the longest line length and average load among the feeders of the system. Therefore, it has the most chance for the occurrence of fault. For the voltage swell condition, capacitive load, 50MVAR is attached at 33kV transformer side in parallel with the load feeder.

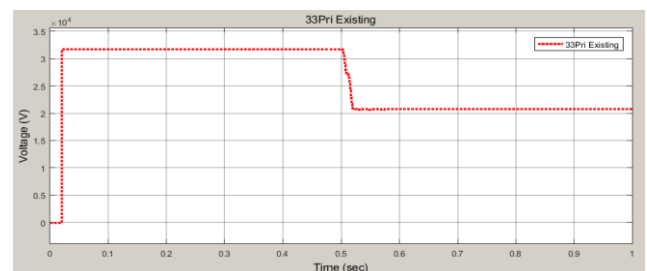


Figure 7. Voltage Profile of the System when Single Line to Ground Fault Occurs

Figure 7, Figure 8, Figure 9 and Figure 10 show the voltage profile of the existing system when the system is suffer from the various fault conditions. The fault is occurred at 0.5 sec and the system voltage decrease lower than 33kV. The voltage sag magnitude are 18.11kV for three phase fault, 11.75kV for line to line fault, 12.225kV for single line to ground fault, and 14.918kV respectively.

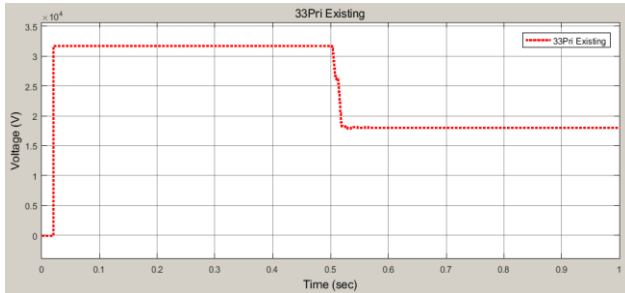


Figure 8. Voltage Profile of the System when Double Line to Ground Fault Occurs

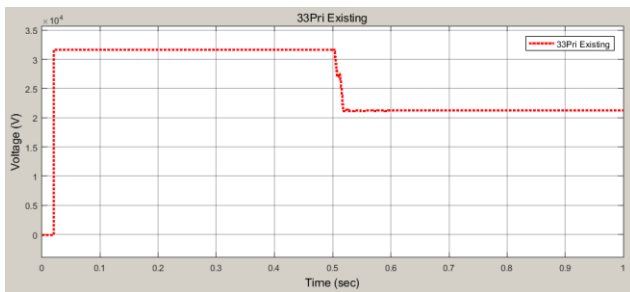


Figure 9. Voltage Profile of the System when Line to Line Fault occurs

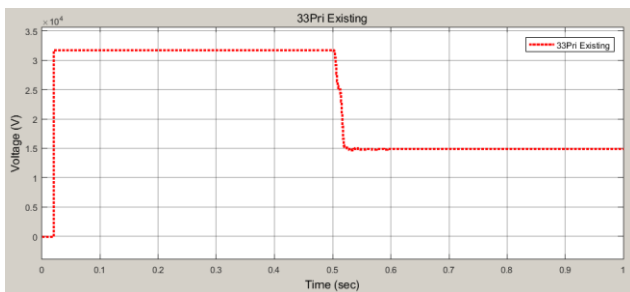


Figure 10. Voltage Profile of the System when Three Phase Fault occurs

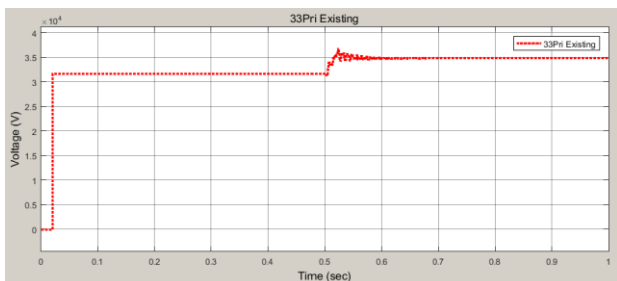


Figure 11. Voltage Profile of the System when the Capacitive Load is connected

Figure 11 shows the voltage profile of the system when the capacitive load is connected. When the capacitive load is connected at 0.5 sec, the system voltage is increased from 33kV to 34.83kV.

Table 2. System Data of the DVR Model

System Voltage	33kV
Series Transformer Turn Ratio	1:3
DC Link Voltage	44.567kV
Filter Inductance	94mH
Total Active Power	30.10954 MW
Total Reactive Power	19.57971 MVAR

To compensate for the voltage sag and swell condition, modeling of the DVR is constructed in the existing system. Table 2 shows the system data of the DVR model.

Figure 12 shows Existing System is connected with DVR when fault occurs at load side. DVR is connected in series with 33kV source side and 33kV load side of the system via three 25MVA, 33kV/11kV, single phase transformers. The secondary side of these single phase transformer are connected with voltage source converter (VSC). DC terminal of Voltage Source Converter (VSC) are connected with Battery.

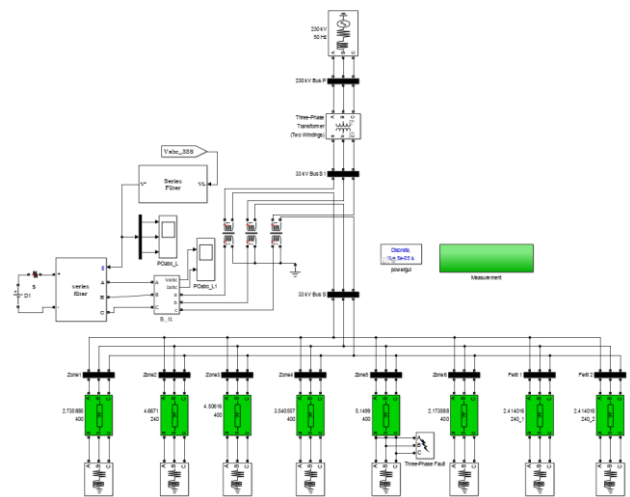


Figure 12. Existing System is connected with DVR when Fault occurs at Load Side

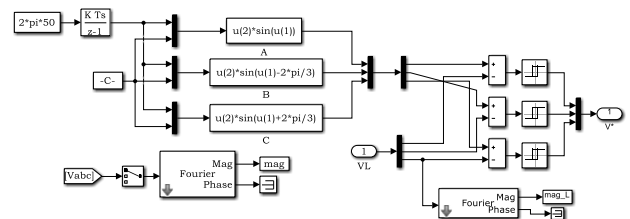


Figure 13. Modelling of Hysteresis Controller

A DVR can compensate the voltage drop or voltage swell across a load by injecting or absorption a voltage through a series transformer with the source voltage. Voltage Source Converter (VSC) is used with hysteresis control for this purpose. In this control, control signal is produced by using error signal which get from the comparing reference voltage and actual voltage with Hysteresis control .Voltage Source Converter (VSC) is operated by the controlled signal which is also get from the Hysteresis control.

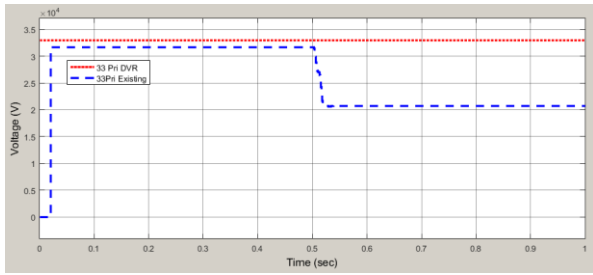


Figure 14. Voltage Profile of the System with and without DVR when Single Line to Ground Fault occurs

Figure 14, Figure 15, Figure 16, and Figure 17 show voltage profile with and without DVR when various fault conditions occurs in the existing system. Without DVR, the bus voltages are significantly reduced below the rated value. With DVR, the bus voltages are maintained at rated values. Thus DVR can restore the bus voltages under various fault conditions.

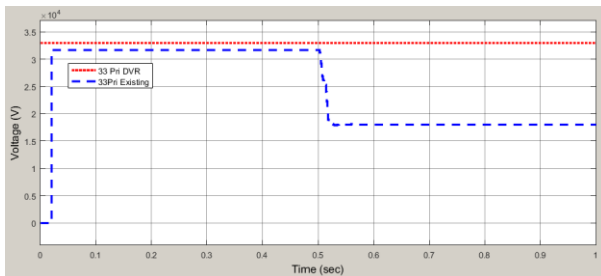


Figure 15. Voltage Profile of the System with and without DVR when Double Line to Ground Fault Occurs

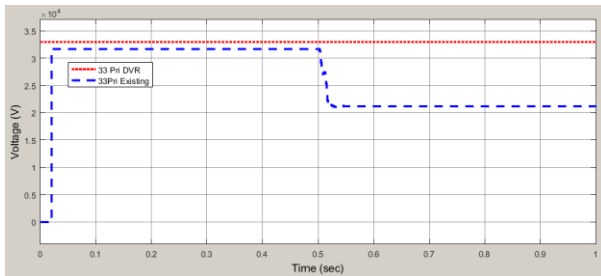


Figure 16. Voltage Profile of the System with and without DVR when Line to Line Fault Occurs

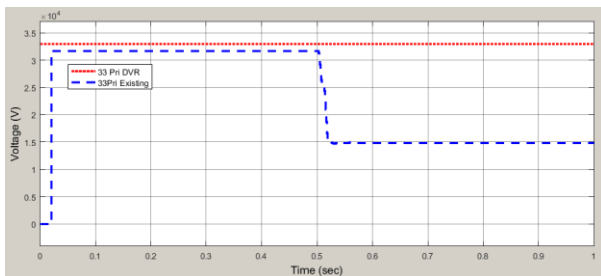


Figure 17. Voltage Profile of the System with and without DVR when Three Phase Fault occurs

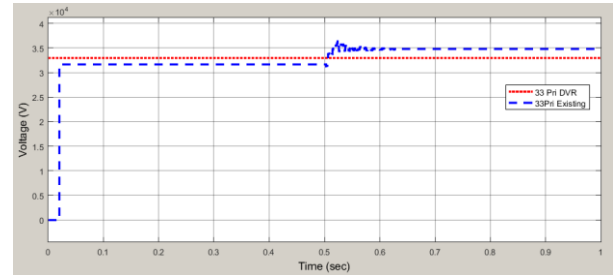


Figure 18. Voltage Profile of the System with and without DVR when Capacitive Load is connected

Figure 18 shows voltage profile with and without DVR when capacitive load is connected in the proposed system. Without DVR, the bus voltage is increased with the application of capacitive load. When DVR is connected with the existing system, the voltage profile is better than without DVR of the system. The simulation results with and without DVR in the existing system are tabulated in Table 3.

Table 3. Simulation Results with and without DVR

Fault Type	Existing System without DVR	Existing System with DVR
Three Phase Fault	14.890266kV	33.0022kV
Line to Line Fault (A &B)	21.2485kV	33.0017kV
Single Line to Ground Fault	20.77545kV	33.00046kV
DL-G Fault (A &B)	18.0823kV	33.00179kV
Capacitive Load Connected	34.832kV	32.9972kV

8. CONCLUSION

The modeling and simulation of a DVR for voltage sag/swell mitigation in industrial distribution system is presented in this paper. Myaungtagar Substation is chosen as case study area where the steel mills are the main loads and the voltage sag/swell is the main problems. Therefore, economical loss and degradation in power quality result due to these voltage deviations. In this paper, DVR is used as a voltage sag/swell mitigation device and use to protect the sensitive loads in the system. The simulation result shows that the voltage sag/swell in the system can be fully mitigated by using DVR. Therefore, the dynamic voltage restorer presented in this paper is efficient and reliable for mitigation of voltage sag/swell in the industrial distribution system.

9. ACKNOWLEDGMENTS

I would like to express my sincere appreciation to Myaungtagar Industrial Distribution Substation for the support on data collecting. I also would like to acknowledge special thanks to all of my teachers, my seniors and colleagues from Department of Electrical Power Engineering for their support and encouragement towards this paper.

10. REFERENCES

- [1] S.Saravanan1, M. Solaimanigandan, T. Tharaneetharan, V. Varunraj, "Dynamic Voltage Restorer for Distribution System", International Journal of Engineering Research and Development e-ISSN: 2278-067X, p-ISSN: 2278-800X, Volume 7, Issue 1 (May 2013), 14-24.
- [2] Bhim Singh, Ambrish Chandra, Kamal Al-Haddad. 2015. Power Quality Problems And Mitigation Techniques,

- [3] Sanjay Haribhai Chaudhary, Mr. Gaurav gangil, “Mitigation of voltage sag/swell using Dynamic Voltage Restorer (DVR)”, IOSR Journal of Electrical and Electronics Engineering (IOSR-JEEE) e-ISSN: 2278-1676,p-ISSN: 2320-3331, Volume 8, Issue 4 (Nov. - Dec. 2013), 21-38.
- [4] Sandeep Kumar N. 2012-2014, Power Quality Issues and its Mitigation Techniques,
- [5] Roger C. Dugan, Mark F. Mc Granaghan, Surya Santoso, H. Wayne Beaty. 2004. Electrical Power System Quality,
- [6] Dev Kumar Taram. 2015. Power Quality Improvement Using Dynamic Voltage Restorer (DVR).
- [7] T.Devaraju1, V. C. Veera Reddy and M. Vijaya Kumar. “Performance of DVR under different voltage sag and swell conditions”, ARPJ Journal of Engineering and Applied Sciences, ISSN 1819-6608, Volume. 5, No. 10, (Oct. 2010), 56-64